CHARLES PANKOW
FOUNDATION
Building Innovation through Research

Low-Cycle Fatigue Effects on the Seismic Performance of Concrete Frame and Wall Systems with High Strength Reinforcing Steel

Stanford University

Kuanshi Zhong

Gregory G. Deierlein

Sponsored by:

The Charles Pankow Foundation

The Concrete Reinforcing Steel Institute

The American Concrete Institute's Concrete Research Council

April 2019

Low-Cycle Fatigue Effects on the Seismic Performance of Concrete Frame and Wall Systems with High Strength Reinforcing Steel

CPF Research Grant Agreement #02-16

Funded by

CHARLES PANKOW FOUNDATION

P.O. Box 820631

Vancouver, Washington 98682

Co-funded by

The Concrete Reinforcing Steel Institute, and

The American Concrete Institute's Concrete Research Council

Principal Investigator: Dr. Gregory G. Deierlein, Stanford University

Graduate Research Assistant: Kuanshi Zhong, Stanford University

Industry Advisory Panel:

Dominic Kelly, SGH, Boston

Ron Klemencic, MKA, Seattle

ACKNOWLEDGEMENT

This project was made possible by funding from the Charles Pankow Foundation, the Concrete Reinforcing Steel Institute, and ACI's Concrete Research Council. The Project benefited greatly from the Industry Advisory Panel members Dominic Kelly (SGH, Boston) and Ron Klemencic (MKA, Seattle) along with research collaborators Dr. Jack Moehle, University of California, Berkeley and his graduate student Dr. Duy V. To; and Dr. Wassim Ghannoum, University of Texas, San Antonio and his graduate students Dr. Drit Sokoli, Albert Limantono, Chase Slavin, and Stephen Zhao; and Dr. Andres Lépage and Dr. Rémy Lequesne, University of Kansas and their graduate students Mohammad Huq, Alexander Weber-Kamin, and Shahedreen Ameen.

Grateful acknowledgment is also made to many other involved individuals for discussion and suggestions including: Ted Lawrence, Dr. Reagan Chandramohan, Dr. Amit Kanvinde, Dr. Masao Terashima, and Andy Ziccarelli. Computing resources for the research were provided by the Blume Earthquake Engineering Center and Sherlock computing cluster at Stanford University.

EXECUTIVE SUMMARY

This is one of several companion projects supported by the Pankow Foundation to support the development of seismic design requirements for the use of high strength reinforcing steel in concrete buildings. In particular, this study examines the effect of high strength reinforcement on the nonlinear system response and risk of bar fracture in concrete moment frames and walls subjected to earthquake ground motions. The risk of reinforcing bar fracture is a particular focus, given concerns raised regarding the difference in cyclic ductility between conventional and high strength reinforcement. The analyses utilize data from cyclic testing of high-strength reinforcing bars to evaluate bar fracture and data from tests of concrete beam, column and wall components to validate the simulations. These models are used to assess the influence of reinforcing bar properties on the seismic performance of special moment frame and wall systems under earthquake ground motions, including the effects of degradation associated with reinforcing bar yielding, buckling and fracture.

Data from over 250 tests of reinforcing bars conducted in a companion project (Ghannoum and Slavin, 2016) is used to calibrate a fatigue-fracture model based on a Manson-Coffin formulation to relate cumulative effective plastic strains to bar fracture. Effective plastic strains are measured over a gage length associated with the bar slenderness based on lateral reinforcing tie spacing, which implicitly includes bar buckling. Statistical regression is used to calibrate three material parameters (α_f, C_f, and ε_f) to capture the correlation of combined buckling and fracture-fatigue resistance to steel yield strength, tensile-to-yield strength ratio, and bar slenderness. The resulting fracture-fatigue damage model is described by a lognormal probabilistic distribution, calibrated to represent the median estimate of fracture with a dispersion of 0.5.

The response of beam, column and flexural wall components is simulated using fiber-type elements that incorporate inelastic behavior of reinforcing steel and concrete and bar slip. Numerical integration points are selected such that the bar strain demands correspond to an 8-inch gage length that is consistent with the effective strains in the bar fatigue-fracture model. The detailed member analyses and reinforcing bar fracture model is validated using data from companion Pankow projects, including tests of beams (To and Moehle, 2017), columns (Sokoli et al., 2017), and T-shaped walls (Huq et al., 2018) with conventional (Gr. 60) and high-strength (Gr. 80 and 100) reinforcement. Overall, the simulated forces, deformations, reinforcing bar strains and fracture indices compare well with the measured test data.

Multi-story moment frame seismic systems are modeled using beam-column members with concentrated hinges, where the resulting member deformation histories are interpreted using the detailed fiber-type elements. The concentrated hinges employ a strength and stiffness degrading hysteretic model which has five backbone-curve parameters and one cyclic deterioration parameter. The backbone curve parameters are determined by aggregating moment-rotation response from fiber-type cross-section analyses with member shear and bar-slip relations. To improve the reliability of these analyses for identifying the influence of reinforcing bar properties on response, the model backbone and cyclic deterioration parameters are calibrated through statistical regression to data from over one hundred previously published tests, including specimens with normal and high strength reinforcement.

The calibrated component and fracture-fatigue models are used in incremental dynamic analyses (IDA) to evaluate the performance of special moment frame and wall systems under strong ground motions. In one set of analyses, the story drifts, cumulative plastic strains, reinforcing bar fracture risks are evaluated under *MCE* ground motions for high-seismic sites in San Francisco and Seattle, where the results are adjusted to account for characteristic ground motion spectral shape and duration. In a second set of analyses, the

FEMA P695 approach is used to evaluate the safety margin against collapse, with and without the effects of reinforcing bar fracture.

Alternative frame and wall designs are compared to evaluate the effects of reinforcing bar strength, tensile-to-yield ratio (*T/Y*), and stirrup spacing. Three *T/Y* ratios are considered for each steel grade (1.3, 1,4, and 1.5 for Gr. 60; 1.2, 1.3, and 1.4 for Gr. 80; 1.1, 1.2, 1.3 for Gr. 100) and three stirrup tie spacings (s/d_b equal to 4, 5 and 6) are considered for each type of steel. This results in 27 different combinations of steel grade, *T/Y* ratio, and s/d_b ratio for each building type. The study includes 4-story and 20-story concrete special moment frames and 8-story and 42-story concrete shear wall systems designed to conform to current seismic design standards.

Key results of the structural component and building archetype analysis studies are as follows:

- As one would expect, replacing Gr. 60 reinforcement with higher strength bars tended to decrease the building stiffness, increase the fundamental period, and increase the earthquake-induced drifts. The moment frames with Gr. 80 and Gr. 100 reinforcing bars experienced maximum story drifts that were about 10% to 20% larger, respectively, than those in the benchmark buildings with Gr. 60 reinforcement. Story drifts in the wall systems with Gr. 80 and 100 reinforcing bars were about 5% to 10% larger, respectively, than the Gr. 60 benchmark design. These results suggest that the design story drifts should be evaluated using models based on transformed section properties, which reflect differences in steel areas for higher grade steels.

- Among the three reinforcing bar material properties and design parameters that were systematically varied in the analyses (yield strength, *T/Y* ratio, s/d_b ratio), the *T/Y* ratio has the most significant effect on the risk of reinforcing bar fracture, followed by s/d_b ratio and yield strength. It should be noted that the characteristic *T/Y* ratios tend decrease with increasing yield strength, so these effects are correlated. But the sensitivity studies indicate that change in fracture behavior is more directly driven by the *T/Y* ratio. Variation in reinforcing bar toughness, beyond that captured in the yield strength and *T/Y* ratio parameters, is treated as a random variable that is reflect in the dispersion of the facture model.

- Comparative studies of frame and wall systems with variable steel reinforcement indicate that structures with Gr. 80 and 100 reinforcing bars with $T/Y = 1.2$ and tie spacing $s/d_b = 5$ have similar cyclic strain demands and probabilities of reinforcing bar fracture (under MCE_R ground motions) to benchmark counterpart systems with Gr. 60 bars with $T/Y = 1.3$ and tie spacing $s/d_b = 6$. In most cases, the reduction in the tie spacing (s/d_b from 6 to 5) tended to offset the increased tendency for fracture in higher strength bars with lower *T/Y* ratios (*T/Y* of 1.2 versus 1.3). Where the *T/Y* ratios and tie spacings were controlled to $T/Y = 1.2$ and tie spacing $s/d_b = 5$, the probabilities of bar fracture under MCE_R ground motions ranged from about 2% to 5% in the moment frames and 42-story shear wall. Considerably larger fracture probabilities of about 10% to 15% where observed in the 8-story shear wall, due to higher cyclic strain demands. In cases where the *T/Y* ratio is reduced to 1.1 and the s/d_b tie spacing is relaxed 6, the bar fracture probability roughly doubles compared to cases with constraints on the permissible bar properties and tie spacing, i.e., $T/Y = 1.2$ and $s/d_b = 5$.

- Comparison between fracture index (*FI*) demands for the frames and walls at story drift ratios up to 4% further confirmed that the fracture probabilities of Gr. 80 and 100 bars are roughly equivalent to the benchmark case (Gr. 60 with $T/Y = 1.3$ and $s/d_b = 6$) by limiting the minimum *T/Y* ratio to 1.2 and maximum spacing s/d_b to 5 (or possibly s/d_b of 4 in the 8-story wall where the fracture demands are largest).

- FEMA P695 Collapse Risk analyses indicated that the risk of collapse under MCE_R motions is comparably between the systems with Gr. 60 versus Gr. 80 or 100 steel, provided that the $T/Y > 1.2$ and tie spacing $s/d_b < 5$ in cases with high strength reinforcing bars. Overall, the risk of collapse under MCE_R motions is negligible (<1%) in the 42-story shear wall and on the order of 5% to 11% in the other systems. As noted previously, control of the T/Y ratio and tie spacing is especially important in the 8-story wall, where the contribution of bar fracture to collapse risk would otherwise increase to values (MCE_R collapse probabilities up to 30%) that are in excess of the specified requirements of ASCE 7.

Contents

LIST OF FIGURES

LIST OF TABLES

1. INTRODUCTION

1.1 Background and Motivation

For seismic design, the ACI-318-14 Building Code limits the use of the high-strength reinforcing steel (with yield strengths greater than 60 *ksi*) to lateral ties for confinement and shear reinforcement and does not permit high strength steel for longitudinal reinforcement in walls and frames. This is in spite of the potential benefits of high-strength reinforcement to improve the cost-efficiency and constructability of buildings, by reducing the quantity of steel, rebar congestion and construction time. The limitations stem from concerns regarding whether high-strength reinforcement has sufficient strain hardening and ductility to resist fracture under inelastic cyclic loading that may occur under large earthquakes.

In response to interest from industry, the National Institute of Standards and Technology (NIST) and the Applied Technology Council (ATC) initiated the project ATC-98 on the *Use of High-Strength Flexural Reinforcement in Reinforced Concrete Seismic Design* to evaluate the use high-strength reinforcement as primary reinforcement in seismic applications (NIST, 2014). Subsequently, the Charles Pankow Foundation (CPF) funded the project ATC-115 (2014), *The Development of a Roadmap on Use of High-Strength Reinforcement in Reinforced Concrete Design*, to identify research needs and set up the milestone for incorporating high-strength longitudinal reinforcement in seismic design standards. Since then, research has been conducted to evaluate material properties of high-strength reinforcement (Slavin and Ghannoum 2015; Zhao and Ghannoum 2016) and structural performance and failure mechanisms of high-strength steel reinforced concrete members (To and Moehle 2017; Sokoli et al. 2017; Huq et al. 2017). These tests have shown that the high strength reinforcement (Grade 80 and 100) generally has lower fracture and fatigue resistance of than Grade 60 reinforcement. In addition, tests of concrete members (Aoyama 2001, Sokoli 2014) indicate that the stress and strain demands of high strength bars may be greater than those in Grade 60 reinforcement for comparably member deformations. As a result of lingering concerns regarding bar fracture resistance from these and other tests, ACI 318-14 has maintained the yield-strength limit of 60 *ksi* on non-prestressed longitudinal steel bars in special moment frames and structural walls for seismic design.

1.2 Behavioral Effects with High Strength Reinforcement

As shown by recent tests to investigate high strength (HS) reinforcing bar properties and their influence on the structural component responses (see Figure 1.1), the major behavioral effects with HS relative to Grade 60 reinforcement, which are considered in this study, are summarized as follows:

1. Lower *T/Y* ratios in HS reinforcement, which tends to inhibit spread of plasticity, potentially leading to more localization of strains.
2. Less fracture toughness in HS reinforcement, which may lead to premature fracture under cyclic loading.
3. Smaller bar sizes in members with HS reinforcement, which may lead to earlier bar buckling (higher bar slenderness for a given stirrup spacing) and more deterioration of bond and development. While bar buckling tends to promote fracture, the deterioration of bond has competing effects. On the one hand, bond deterioration tends to reduce the structural strength and stiffness, but on the other hand, bond slip may improve performance by mitigating the effects of lower *T/Y* ratio on the localization of strain in the reinforcement.
4. Less stiff members with higher yield strains (and curvatures), which tends to increase building drifts but may delay the onset of yielding. On the other hand, if frame designs are stiffness

controlled, then the lower member stiffness could lead to design of members with higher overstrength.

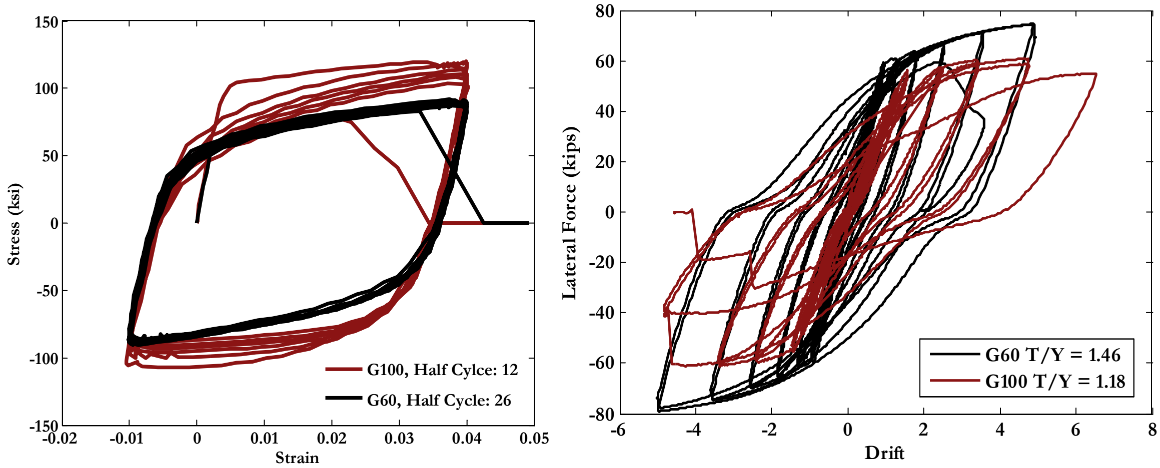

Figure 1.1. The influence of high-strength steel on the structural behaviors. Left: comparison between Gr. 60 and Gr. 100 rebar low-cycle fatigue resistance (Slavin and Ghannoum, 2015); Right: comparison between Gr. 60 and Gr. 100 RC member hysteretic behaviors (To and Moehle, 2017).

The resulting influence of these behavioral effects can be divided into (1) member yielding and cyclic degradation and (2) reinforcing bar fracture. The first of these effects are modeled directly in the nonlinear structural analysis through fiber-type and concentrated hinge type models. For slender wall systems, a fiber-type beam-column model is used, where the effects of bar yield strength, strain hardening (*T/Y* ratio), and cyclic degradation are captured by modeling of inelastic cross-section response that simulates reinforcing bar yielding and buckling, concrete cracking and crushing. Reinforcing bar slip is incorporated by adjusting the reinforcing bar material parameters with semi-empirical bond-slip relationships, and shear deformations are included using equivalent shear stiffness parameters. For moment frame systems, the inelastic effects are modeled using a concentrated plasticity model where the monotonic backbone parameters are also determined by inelastic cross-section fiber analyses, combined with cyclic degradation, and bar-slip elements. The resulting modeling parameters for the slender walls and moment frame members are validated by comparison to tests of members with conventional and high strength reinforcement.

The influence on steel fracture is evaluated as a so-called 'non-simulated' failure mode, where the probability of fracture is evaluated by post-processing of reinforcing bar strain histories using a cyclic fatigue fracture model. Data from monotonic tensile tests and cyclic tests of bare reinforcing bars (Slavin and Ghannoum 2015; Zhao and Ghannoum 2016) are used to calibrate the proposed reinforcement fracture model. Previous tests of concrete wall, beam and column subassemblies (To and Moehle 2017; Sokoli et al. 2017; Huq et al. 2017), where bar fractures were observed, are used to validate the model observing bar rupture failures are used to validate the model accuracy. In the proposed reinforcement fracture model, higher yield strength, lower *T/Y* ratio, and larger bar slenderness are found to result in the reduction of steel fracture capacity which may lead to a lower damage resistance of the reinforced components.

The influence of reinforcing bar properties on structural system performance is evaluated through a series of nonlinear dynamic analyses of archetype models under earthquake ground motions, including 4- and 20-story moment frame and 8- and 42-story shear wall systems. Three grades of longitudinal reinforcing bars are evaluated (Grade 60, 80 and 100), where three characteristic *T/Y* ratios are considered for each steel grade (*T/Y* ratios of 1.3 to 1.5 for Grade 60, 1.2 to 1.4 for Grade 80, and 1.1 to 1.3 for Grade 100). The effect of lateral tie spacing on reinforcing bar slenderness and buckling is evaluated by considering tie spacings of $4d_b$, $5d_b$, and $6d_b$, where d_b is the bar diameter. Therefore, the design space of each archetype system model includes twenty-seven combinations of steel grade, *T/Y* ratios and tie spacings. Building response from the onset of yielding up to collapse is simulated for each case, including the risk of reinforcing bar fracture risk.

1.3 Objectives and Scope

This project aims to help establish acceptance criteria on reinforcing bar properties for use in seismic design of concrete systems, including the combined effects of inelastic member response and cyclic strain demands on the low-cycle fatigue resistance of the steel reinforcement. The building drift response and risk of bar fracture on building safety is evaluated through a reliability-based framework that integrates the effects of (1) reinforcing steel cyclic strain/deformation demands, (2) uncertainty in the fracture/fatigue resistance of reinforcing bars, and (3) local member response and bar fracture damage on the overall system collapse risk.

The scope of work consists of: (1) developing a reliability-based framework to evaluate high-strength bar effects, including fracture, in concrete structures, (2) developing and calibrating a model for reinforcement fracture which translates the rebar plastic strain history to a bar fracture index; (3) calibrating inelastic hinge model to capture variations in reinforcing steel properties (i.e., yield strength, *T/Y* ratio, bar diameter, and bar slenderness) on inelastic response data on beam-columns and slender walls, (4) developing and validating fiber-type beam-column elements to integrate the reinforcing bar fracture model with inelastic member response; (5) investigating the effect of high-strength reinforcing steel (Grade 80 and Grade 100) on the response of reinforced concrete frame and shear wall systems under earthquake ground motions.

1.4 Organization of Report

Chapter 2 provides overview of the proposed reliability-based framework for systematically combining the nonlinear building system response data with the bar fracture model to assess the risk of bar fracture and the combined influence on building collapse risk.

Chapter 3 briefly reviews the monotonic and cyclic rebar test results conducted at the University of Texas (Slavin and Ghannoum 2015; Zhao and Ghannoum 2016), and introduces the proposed reinforcement fracture-fatigue model for evaluating bar fracture risk based on the bar deformation strain histories.

Chapter 4 summarizes the modeling procedure to simulate the inelastic response of concrete beams and columns, including the calculation of the backbone curve and calibration of the cyclic deterioration coefficient for the concentrated hinge model. The inelastic hinge model is calibrated using over 190 previously reported beam and column tests (PEER SPD 2004, Sokoli et al. 2017, To and Moehle 2017), and the resulting fiber-based member and fracture-fatigue model is validated using data from eight beam and column tests conducted at UC Berkeley and the University of Texas (Sokoli et al. 2017, To and Moehle 2017).

Chapter 5 summarizes calculation of model parameters and validation of the resulting fiber-based model to simulate inelastic shear wall response and the risk of reinforcing bar fracture. The model is validated by comparison to four wall tests conducted at the University of Kansas (Huq et al. 2017).

Chapter 6 introduces a method called "hazard-consistent IDA" which is used to adjust the results of incremental dynamic analysis (IDA) results to the earthquake hazard characteristics of specific building locations. In particular, the method adjusts the response to account for differences in ground motion spectral shape and duration between the ground motions used in the IDA and those consistent with the ground motion hazard analysis for the site and return period. The method is similar to the spectral shape adjustment used in the FEMA P695 approach, but with refinements to consider (1) earthquake demand parameters other than collapse, and (2) statistically rigorous measures of spectral shape and ground motion duration that vary with ground motion return period (annual rate of exceedance).

Chapter 7 summarizes the evaluation of moment frame systems, including results for twenty-seven variants of longitudinal reinforcement steel properties for a 20-story archetype and thirteen variants for a 4-story archetype. Chapter 8 summarizes results for shear wall systems, including twenty-one variants of a 42-story archetype and seventeen variants of an 8-story archetype.

Chapter 9 provides an overall summary of observations and resulting conclusions and recommendations regarding the effect of material reinforcing bar parameters and seismic design criteria.

2. OVERVIEW OF RELIABILITY-BASED FRAMEWORK

With the goal to quantify the risk of reinforcement fracture and its implications on building seismic safety, the proposed Framework aims at integrating data from seismic hazard analysis, characteristics of input ground motions, nonlinear structural analyses, behavior of reinforced concrete components, and low-cycle fatigue resistance of reinforcing bars. The Framework is built to utilize and extend the concept of non-simulated failure modes in FEMA P-695, *Quantification of Building Seismic Performance Factors* (ATC 2009), which is the basis of the seismic risk criteria in ACSE 7-16 (ASCE 2017), along with related codes and standards. Alternatively, the Framework also approaches the question by assessing performance under maximum considered earthquake (*MCE*) intensity ground motions, similar to the approach described in the nonlinear dynamic analysis provision of Chapter 16 of ASCE 7-16 and in the PEER TBI performance-based design of tall buildings (PEER 2017).

The FEMA P-695 methodology assesses the seismic collapse safety through nonlinear structural analyses of seismic systems under incrementally scaled ground motions until collapse (i.e., the incremental dynamic analysis, IDA, Vamvatsikos and Cornell 2002). The resulting collapse fragility curve is then shifted by the spectral shape factor (*SSF*) based on the seismic hazard characteristics and the dispersion is modified to account for uncertainties associated with ground motions, structural modeling, implementation of design intent, and uncertainties in structural behavior. The ratio between the median collapse intensity and the *MCE* intensity is the adjusted collapse margin ratio, *ACMR*, which is the primary parameter used to characterize the collapse safety of the structure. The acceptable limit on *ACMR* is specified to limit the collapse at *MCE* intensity to 10%, i.e., P(Collapse | *MCE*) < 10%, which has subsequently been adopted as the collapse risk limit for seismic design criteria in ASCE 7-16 and other associated standards. Where certain deterioration modes, such as rebar fracture, are not explicitly simulated in analyses, FEMA P695 specifies that the effect of these so-called "non-simulated" deterioration modes be incorporated by adjusting the IDA results by imposing additional limits based on the corresponding demand parameters.

The nonlinear dynamic analysis approach in ASCE 7-16 and in PEER TBI take an alternative approach, whereby specific seismic demands and limit states are evaluated under *MCE*-intensity ground motions. Peak story drift ratios are a primary seismic demand considered to help ensure satisfactory performance. Other demands are distinguished between force-controlled and deformation-controlled actions, which are compared to acceptance criteria to limit the chance of significant strength and stiffness degradation in behavioral modes that are not explicitly (or reliably) modeled in the structural analysis. In this study, reinforcing bar strain demands and the associated risk of bar fractures are one of the key parameters considered.

Figure 2.1 shows the proposed reliability-based framework for assessing collapse risks from non-simulated fracture of steel reinforcement. Starting from the bottom of the three information levels, steel strain demands from the nonlinear structural analyses are post processed to determine a fracture index for quantifying the probability of bar fracture. The fracture probability is informative to understand the relative fracture risk between conventional and high-strength reinforcing bars. Following the FEMA P695 approach, the median fracture capacity can be used to conservatively adjust the median collapse intensity determined from the IDA. Alternatively, the bar fracture fragility model can be used to estimate the probability of bar fracture under *MCE* intensity ground motions, and thereby directly estimate the increase in *MCE* collapse probability, above that determined based on simulated deterioration modes.

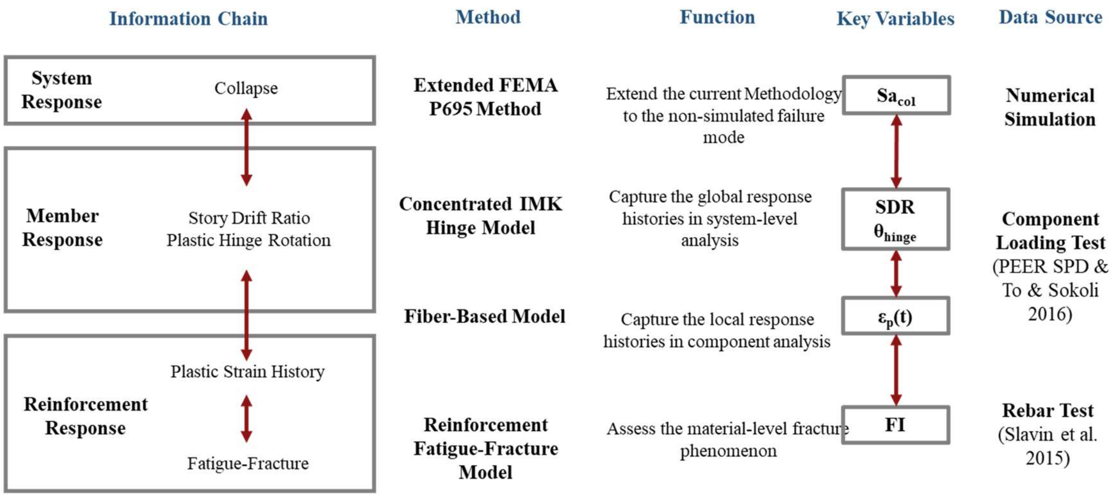

Figure 2.1. Overall reliability-based framework

To elaborate some of the details and key aspects in the reliability Framework, the logical map is shown in Figure 2.2. Corresponding to the three information levels in Figure 2.1, the framework starts from incremental dynamic analysis of structural model at system-level, the recorded story drift ratios (or other structural demand parameters) can be used to estimate the system collapse fragility as a function of spectral intensity. Meanwhile, the recorded lateral deformation history of each beam-column element is used as input to detailed fiber-based beam-column model analyses of each beam and column in the building. The component-level model establishes a link between the global responses (i.e., force-deformation histories) and the local responses (i.e., stress-strain histories). The reinforcing bar strain histories are then used in the fatigue-fracture model (i.e., the material-level) to calculate a fracture index, *FI*, and assess the probability of reinforcing bar fracture. The *FI* obtained from material-level model can be incorporated to adjust the collapse fragility using the FEMA P695, where fracture is treated as a non-simulated failure mode based on median *FI* (corresponding to the expected value, 50% probability, of bar fracture). The story drifts, rebar strains, and fracture indices/probabilities at MCE_R intensity are also evaluated. This evaluation is similar to the approach used in the nonlinear dynamic analysis procedures of ASCE 7-16 and PEER TBI, except that in this study, the variability in demands due to ground motions (record-to-record) and modeling uncertainties are explicitly assessed, as opposed to using the default demand and capacity factors. The MCE_R evaluation utilizes an adjustment of the IDA results to represent the site-specific characteristics of the seismic hazard for locations in San Francisco and Seattle (described further in Chapter 6). Finally, while this framework is described for frame structures, it is adapted for evaluation of wall structures in Chapter 8.

As shown in the lower left box in Figure 2.2, the reinforcing bar fracture index (*FI*) is combined with either the FEMA P695 collapse assessment or the MCE_R demand assessment. Further details of the specific procedures are described in Chapter 6, but the basic concepts are briefly described here. For the FEMA P695 assessment, the maximum fracture index (FI_{max}) in the structure is used to incorporate fracture as a so-called non-simulated failure mode. In this case, the median fracture index, $FI_{max} = 1.0$, is used as a measure to trigger collapse due to reinforcing bar fracture. Thus, combined with the standard peak drift criteria, the collapse intensity is calculated as the minimum of simulated collapse intensity, $Sa(SDR_{max} = 0.1)$, and the fracture intensity, $Sa(FI_{max} = 1.0)$. Separate from the FEMA P695 assessment, the MCE_R demands are evaluated using statistics that account for uncertainties in the analyses and ground motion hazard characteristics. The ground motion characteristics are incorporated through parameters for spectral shape (*SaRatio*) and significant duration ($Ds_{5\text{-}75}$).

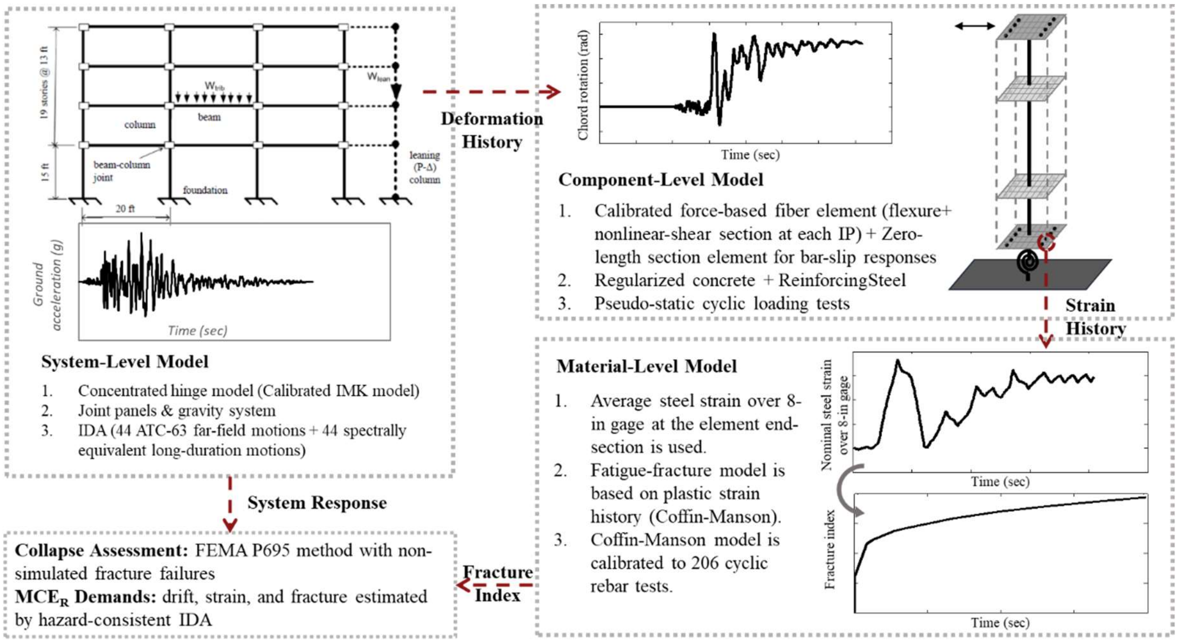

Figure 2.2. Logical map for multi-scale simulations and links to integrated collapse assessment.

Referring to Figure 2.3, as part of this study, the underlying structural analysis and fracture fragility models of the Framework are calibrated to: (1) over 130 tests in the PEER SPD database (PEER SPD 2004) and Charles Pankow Foundation (CFP) tests (To and Moehle 2017; Sokoli et al. 2017; Huq et al. 2017) in Calibration 1 (hinge model calibration) and 2 (fiber-based model calibration), (2) over 200 CPF tests of bare rebar under monotonic and cyclic loading (Slavin and Ghannoum 2015) in Calibration 5 (fatigue-fracture model calibration).

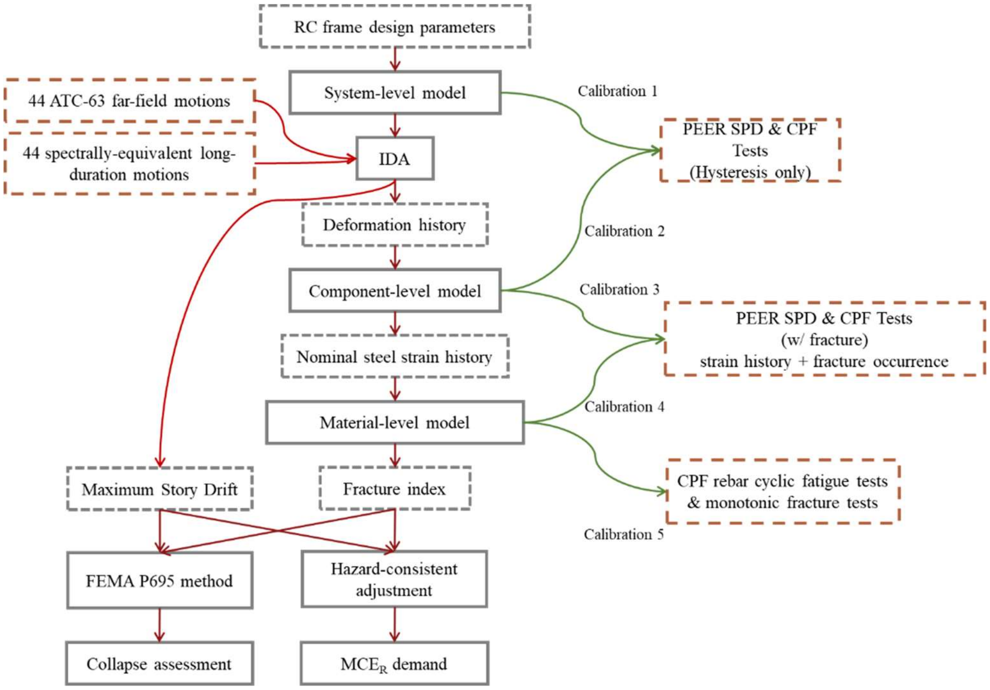

Figure 2.3. Flow chart of proposed Framework and supportive calibrations.

3. MATERIAL-LEVEL FRACTURE MODEL

3.1 Major Preceding Researches on Fatigue Issues

The literature about fatigue of engineering material can be traced back to roughly a century ago (Moore and Kommers 1927). Most fatigue models used for engineering applications are inherently empirical, based on mathematical damage functions that are calibrated to test data. Cyclic fatigue life models for structures operating in the elastic range are widely accepted to depend on the amplitude of cyclic stresses (Palmgren 1924; Langer 1937; Miner 1945). The concept that cyclic fatigue life relies on the strain range was proposed by Manson (1954) to address fracture under inelastic response, where the stress range is not a reliable measure in cyclic strain-hardening/softening material. The strain-based models are supported by the hypothesis that the plastic strains are proportional to the volume of imperfections and irreversible damage that accumulate in a log-log linear manner. The accuracy of Manson's original model has been verified and improved by many subsequent investigations (Coffin 1954; Smith et al. 1963; Weiss 1964; Morrow and Johnson 1965) for low-cycle fatigue problems whose half-cycle number ranges from 10 to 105 (Tavernelli and Coffin 1962). Mean stress and strain effects on fatigue failure were studied to correct the prediction bias under asymmetric loading histories (Smith et al. 1970; Topper and Sandor 1970; Fash and Socie 1982; Lorenzo and Laird 1984; Nihei et al. 1986; Koh and Stephens 1991). Incorporating randomness of extreme loads (e.g., earthquake or wind), stochastic fatigue failure analysis was investigated to provide a probabilistic view and solution (Wirching and Light 1980; Shimokawa and Tanaka 1980; Lutes et al. 1984; Ray 1999). Rain-flow method was developed to count the equivalent amplitudes in random loading histories (Downing and Socie 1982; Rychlik 1987, 1988; Khosrovaneh and Dowling 1990).

Enabled by advances in computational technologies, classical analytic solutions and numerical methods for fracture and fatigue analysis began to converge in in the late 1960's and 1970's. Many new physics-based theorems and models were proposed using failure criteria associated with micro-void growth and coalescence under triaxial stresses and plastic strains (Rice and Tracey 1969; Hancock and Mackenzie 1976; Johnson and Cook 1985; Marini et al. 1985; Benzerga et al. 2004; Kanvinde and Deierlein 2007, 2008). These methods generally require analyzing detailed finite element model to solve the highly nonlinear stress-strain fields that precipitate crack initiation and propagation. The viability of these detailed micro-mechanical models for practical engineering problems depends on many factors, a key one being whether the detailed geometric and material properties can be described reliably at the localized length scales involved in fracture initiation. Nevertheless, the micro-mechanics models provide insights into (1) the effect of stress triaxiality on micro void growth under plastic strains, and (2) distinctions between void growth/shrinkage and localized material damage under positive versus negative plastic strain cycles (which are otherwise treated equally damaging in many of the empirical models).

The modeling approaches described above have been generally applied to a range of situations involving fracture and fatigue in steel materials, with just a few applications to steel reinforcement in concrete structures. At material-level fracture model, Mander et al. (1994) studied the low-cycle fatigue behavior of A615 grade 40 and A722 prestressing reinforcement. Overall 34 rebar specimens were tested with different slenderness and strain ranges. No surface modifications were applied on the deformed bars to represent the real loading conditions. Several existing fatigue models at that time were tested and calibrated: Coffin-Manson model, Koh-Stephens model, Modified SWT model, and Lorenzo-Laird model. A series of hysteric-energy fatigue models were proposed and validated by satisfactory agreement with test results. The test results from large strain amplitudes (1-5%) indicated that mean stress and mean strain have negligible effect on low-cycle fatigue life under strong excitations. They also observed that the rate of crack-propagation following fracture initiation is more rapid in high-strength prestressing bars as compared to the Grade 40 reinforcement. Other similar rebar-level cyclic-fatigue experimental investigations include Aoyama 2001, Adballa et al. (2009), Hawileh et al. (2010), and Trejo et al. (2014).

Brown and Kunnath (2000) conducted an experimental study on the low-cycle fatigue behavior of ordinary reinforcing bars but specifically focused on potential plastic hinge zones. A total of 34 constant amplitude tests were performed covering bar sizes from #6 (#19 in metric) to #8 (#25 in metric). They verified the previously developed fatigue models by Mander et al. (1994) and calibrated updated parameters based on their test results. As expected, they found that buckling leads to localization of cyclic strains and weakening of the material which in turn can reduce fatigue life of reinforcement. They also evaluated the effectiveness of Manson-Coffin model under random earthquake loads for bridge columns, employing several necessary simplifications in structural modeling and rain-flow counting method (Brown and Kunnath 2004).

Most recently, Slavin and Ghannoum (2015) conducted a comprehensive study on the low-cycle fatigue properties, involving reinforcement of three steel grades (Gr. 60, Gr. 80, and Gr. 100) with three different bar sizes (#5, #8, and #11) from two manufacturing processes. Overall 15 categories of reinforcing bars were identified, and 2 to 3 specimens of each group were tested under monotonic loadings per ASTM A370. All monotonic strains used to generate stress-strain relations were measure over an 8-in gage length. These monotonic tension tests were followed by a total of 206 constant-amplitude cyclic tests with various materials, bar sizes, slenderness, and strain ranges. They found that the overall fatigue life of Gr. 80 and 100 bars is shorter but still comparable to Gr. 60 counterparts. However, large variations in fatigue life were observed between different manufacturing processes. Like Brown and Kunnath 2004), their data shows how the post-buckling fatigue life is much shorter than the pre-buckling fatigue life of the same material, due to concentration of strains in the buckled region. Through new optical measurement technologies, they measured the surface strains of a rebar with $6d_b$ clear span and illustrated strain magnifications of up to five times the average bar strain in the buckled region, which helps explain the shortened fatigue life.

At the structural component level, To and Moehle (2017) conducted four cyclic beam tests, three of which used high-strength reinforcement with a cantilever set-up. Of these four tests, two with high-strength steel reinforced failed due to premature bar fractures. Sokoli et al. (2017) conducted four cyclic column tests having a similar test matrix to To and Moehle; but using a full-span fixed-fixed test configuration where axial loads were applied in combination with cyclic shear displacements. All specimens completed at least one full cycle of 5.5% drift ratio before reinforcing bar buckling and fracture. The further observed that the increased concentration of strain demands in the plastic hinge zone of specimens with high-strength reinforcement tended to accelerate the fatigue failure of high-strength reinforcement. Huq et al. (2017) conducted four T-shape shear-wall tests and concluded the lateral drift capacity is highly dominated by the fracture toughness of reinforcement. They found that the lower tensile-to-yield ratios of high-strength reinforcement, which led to higher strain localization, reduced the shear-wall ductility for specimens with high-strength reinforcement as compared to Gr. 60 reinforcement.

3.2 Proposed Reinforcing Steel Fatigue-Fracture Model

For the purposes of this study, fatigue and fracture are treated together as a continuum process in the inelastic cyclic loading process leading to failure of the reinforcement. Damage accumulated from cyclic loadings is assumed to initiates in a fatigue microcrack that propagates and joins with other microcracks under continued cyclic loading until they form a significant crack, at which point the peak bar force starts to drop. The fracture discontinuity in the material results in a highly-nonlinear plastic zone which forms a localized necking phenomenon and precipitate rupture through the reinforcing bar. From a practical standpoint, the last phase of the process (i.e., complete rupture of the bar) is most significant as it impacts the structural capacity of the reinforcing bar and structural member.

Based on observations from prior studies on low-cycle fatigue, there are three major aspects to address in this study: (1) re-calibration of general fatigue/fracture models to represent the unique fatigue-fracture failure mechanism in reinforcing bars; (2) differentiation of cyclic fatigue/fracture based on measurable material characteristics (e.g., yield strength, ultimate strain, *T/Y* ratio) resulting from the different manufacturing processes; (3) differentiation of pre- and post-buckling fatigue/fracture in estimating the fatigue capacity, which can be characterized by the bar slenderness.

With these considerations, we selected the Manson-Coffin model, which as shown in Equation 3.1 relates the cyclic plastic strain amplitude, ε_p, to the number of half cycles at fracture, N_f, through an exponential expression. The model has two material parameters (C_f and a_f), which we the calibrated to parametric expressions of the measurable parameters of the reinforcing bar tests, including yield strength, f_y, tensile-to-yield strength ratio, *T/Y*, and reinforcing bar slenderness, s/d_b, where s is this tie spacing and d_b is the reinforcing bar diameter. In this study, strain demands are defined as nominal engineering strains, based on a consistent gage length of 8-inches, and nominal engineering stress is defined as the measured bar force divided by the nominal bar area (as reported by Slavin and Ghannoum, 2015). Thus, in cases where the reinforcing bars buckled during testing, the buckling effects are considered implicitly in the nominal stress and strain measurements.

$$\varepsilon_p = C_f \left(2N_f\right)^{-\alpha_f} \tag{3.1}$$

Using the normalized stress and strain data, the Manson-Coffin models are calibrated as follows.

> Step 1 – Data reduction. From the available reinforcing bar tests, independent test sets were identified, which are those having same type of steel, slenderness and monotonic/cyclic loading protocols. The mean values of test results within each independent group were calculated and used in the subsequent calibrations and regressions.
>
> Step 2 – Monotonic fracture strain calibration and regression. The monotonic tension fracture strain is an important parameter to anchor the calibration of the cyclic fatigue-fracture model. Based on the tests by Slavin and Ghannoum (2015), monotonic fracture strains are reported for 15 different types of rebar.
>
> Step 3 – Cyclic fatigue-fracture model calibration. Manson-Coffin model was adopted; and the material coefficients C_f and a_f are determined for 32 independent test groups using a total of 206 cyclic tests.
>
> Step 4 – Cyclic fatigue-fracture model regression. The calibrated coefficients C_f and a_f for each of the independent test groups are evaluated and calibrated using statistical regression to the characteristic material/specimen properties, f_y, *T/Y*, and s/d_b.
>
> Step 5 – Fatigue-fracture index and statistical verification. The basic Manson-Coffin model is re-written in the form of fracture index (*FI*) for general applications. The index is then statistically calibrated to the measured results for each test group to determine its median value and dispersion. The *FI* is evaluated through a bias study to examine its sensitivity to different material properties.

The proposed fatigue-fracture model is shown in Equation 3.2, and the resulting damage index is shown in Equation 3.3 (where E_s is the elastic modulus of steel, ε_{pi} is the plastic strain amplitude for each series of *N* cycles). More details will be elaborated in following sections.

$$\begin{cases} \varepsilon_p = C_f \left(2N_f\right)^{-\alpha_f} \\ where, \quad \alpha_f = 0.080 - 0.045 \cdot \left(f_y/60ksi\right) + 0.027 \cdot \left(s/d_b\right) + 0.129 \cdot \left(T/Y\right) \\ C_f = 0.5^{\alpha_f} \cdot \left(\varepsilon_f - f_y/E_s\right) \\ \varepsilon_f = f_y/E_s - 0.043 \cdot \left(f_y/60ksi\right) + 0.128 \cdot \left(T/Y\right) + 0.018 \cdot \left(d_b/1in\right) \end{cases} \tag{3.2}$$

$$FI = \sum_{i=1}^{N} \left(\varepsilon_{pi}/C_f\right)^{1/\alpha_f} \tag{3.3}$$

3.3 Calibration and Regression of Monotonic Fracture Strain: ε_f

Data from 45 monotonic tests (Grade 60, 80, and 100 rebars with different manufacturing processes or bar sizes) conducted by Slavin and Ghannoum (2015) are used in this study to calibrate the ε_f for reinforcing steel. All tests conformed to the procedures specified in *ASTM A370 – Standard Methods and Definitions for Mechanical Testing of Steel Products* and *ASTM E8 – Standard Test Methods for Tension Testing of Metallic Materials*. Mechanical properties of each type are summarized in Table 3.1, where ε_u is the engineering strain at the maximum load and ε_f is the engineering strain at fracture (measured over an 8-inch gage length)

Table 3.1. Monotonic test matrix and the averaged results (Slavin and Ghannoum, 2016).

Bar Size	Manufacturer	Grade	f_y (*ksi*)	f_u (*ksi*)	*T/Y* Ratio	E_s (*ksi*)	ε_u (%)	ε_f (%)
#11	1	60	67	97.1	1.45	28300	11.9	21.7
		100	103.4	128.8	1.27	28300	8.3	11.7
	2	60	62.7	91	1.45	29200	11.4	18.1
		100	99.6	118.9	1.19	28300	6.7	9.9
#8	1	60	63.2	93.7	1.48	26900	11.6	18.8
		80	80.3	110	1.37	27400	10	16.7
		100	101.5	128.5	1.27	30100	8.1	11.6
	2	60	61.5	103.1	1.68	25800	9.5	14.5
		100	104.6	123.8	1.18	31400	6.2	9.8
#5	1	60	68.5	95.8	1.4	30700	10	14.4
		80	83.3	107.1	1.28	26900	9.5	13.7
		100	111	134.9	1.22	26000	8.8	11.6
	2	60	72.4	104.3	1.44	28300	10	15.3
		80	83.6	105	1.26	26900	9.7	13.9
		100	106.8	127.7	1.2	28100	7.6	10.8

Three parameters including (1) yield strength, (2) *T/Y* ratio, and (3) bar diameter are considered in fitting the predictive model for ε_f, given Equation 3.4. Note that with fracture strain decreases with increasing yield strength and increases with the *T/Y* ratio and bar size. As shown in Figure 3.1, the regressed model shows reasonably good fit to observed index with a standard deviation of 0.02.

$$\varepsilon_f = \varepsilon_y - 0.043 \cdot \left(f_y/60ksi\right) + 0.128 \cdot \left(T/Y\right) + 0.018 \cdot \left(d_b/1in\right) \tag{3.4}$$

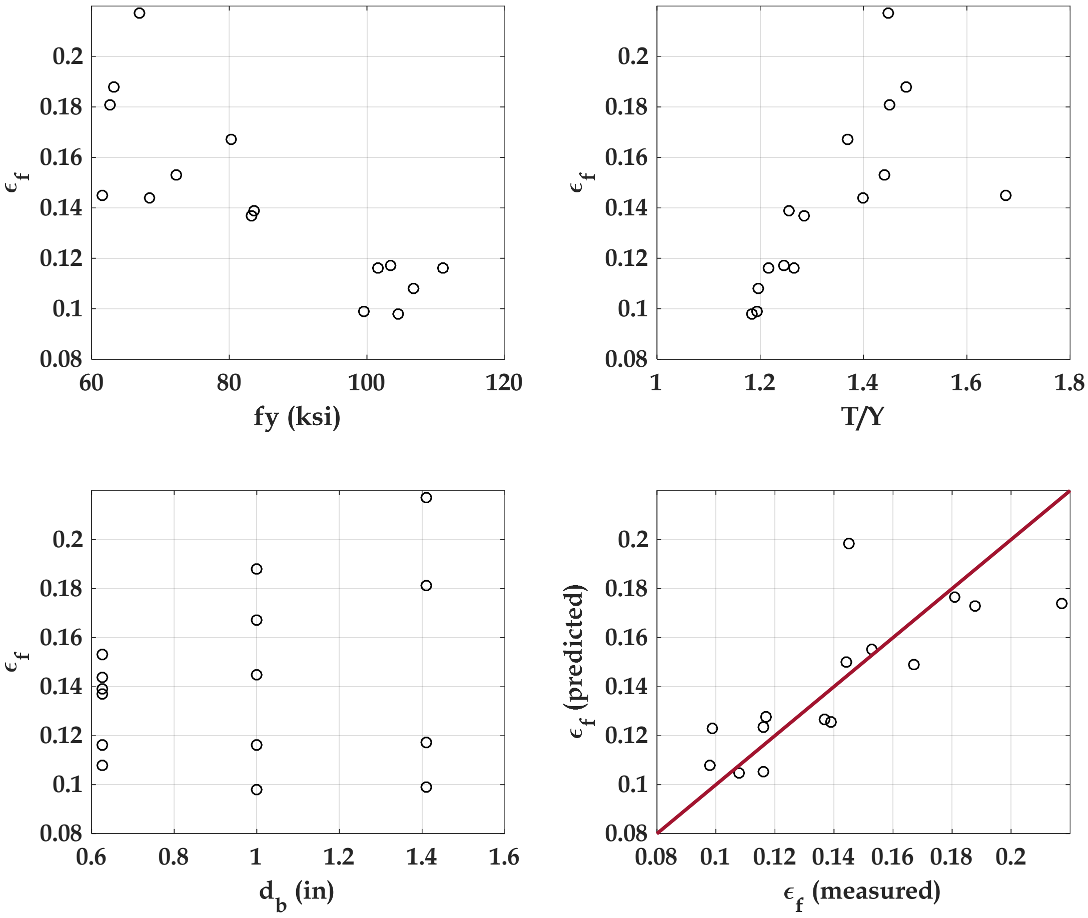

Figure 3.1. Calibration of ε_f.

3.4 Calibration of Cyclic Fatigue-Fracture Model

All the 206 cyclic tests were performed in a universal test machine having two independent hydraulic gripping mechanisms (with 6-in long gripping embedment lengths to provide fixity at both ends). The bars were loaded at a strain rate of approximately 0.001/s and all specimens were first subject to a tension excursion and then cycled between compression and tension strain amplitudes until rupture occurred. The unsupported bar lengths (between grips) was varied based on the desired bar slenderness, s/d_b. The measured displacements over the unsupported length of the bars were used to calculate the reported engineering strains, and engineering stress was computed by dividing the recorded forces by the nominal bar areas. Figure 3.2 shows one comparison between two Gr. 60 and Gr. 100 rebar tests. As reported by Slavin and Ghannoum (2015), the half-cycle number to fracture was counted to the complete rupture point for each specimen. Tables 3.2 to 3.4 summarize the counted half-cycle numbers for all tests.

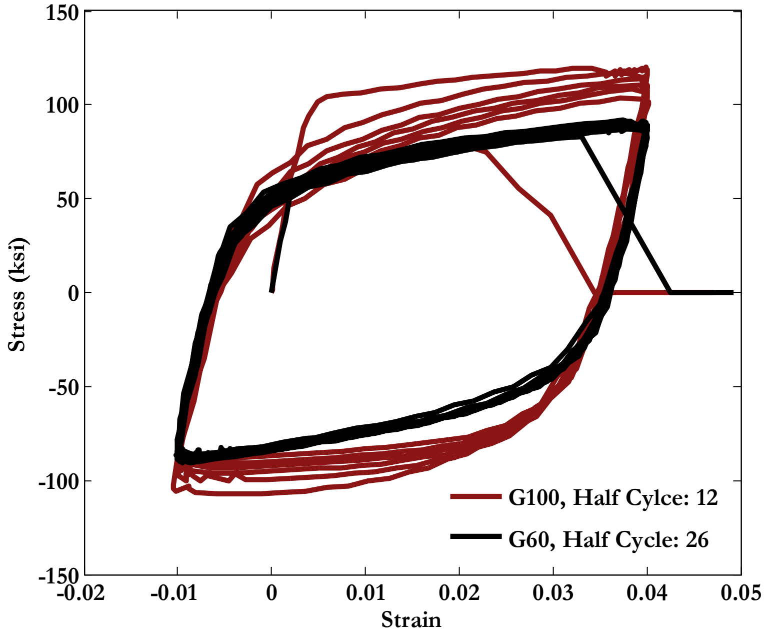

Figure 3.2. Comparison between # 8 Gr. 60 and Gr. 100 rebar cyclic tests (Gr. 60 bar had an unsupported length of $4d_b$; and Gr. 100 had an unsupported length of $6d_b$).

Table 3.2. Mean number of half-cycles to fracture for # 5 bars.

		Strain range		
		4%, 0%		4%, -1%
		Clear-span		Clear-span
Manufacturer	Grade	$5d_b$	$6d_b$	$6d_b$
1	60	30.6	43.2	N/A
	80	N/A	16.0	N/A
	100	39.0	36.5	12.0
2	60	55.0	19.3	N/A
	80	N/A	85.5	N/A
	100	23.0	33.3	14.0

Table 3.3. Mean number of half-cycles to fracture for # 8 bars.

		Strain range					
		2%, -2%			4%, -1%		
		Clear-span			Clear-span		
Manufacturer	Grade	$4d_b$	$5d_b$	$6d_b$	$4d_b$	$5d_b$	$6d_b$
1	60	46.7	44.0	32.0	33.3	25.0	20.0
	80	36.7	N/A	14.7	18.0	N/A	11.3
	100	68.0	42.0	28.5	27.3	18.5	12.7
2	60	69.3	36.0	24.0	25.3	17.3	14.7
	100	57.3	N/A	26.7	28.5	18.0	12.0

Table 3.4. Mean number of half-cycles to fracture for # 11 bars

		Strain range	
		4%, -1%	
		Clear-span	
Manufacturer	Grade	4d_b	6d_b
1	60	25.0	15.6
	100	13.3	6.4
2	60	28.0	10.7
	100	13.5	12.5

The data of the # 8 bars, whose average values are summarized in Table 3.3, are also plotted as in Figure 3.3 to 3.7. Also shown in these figures are the calibrated two coefficients in Manson-Coffin model (Equation 3.1) for each independent test group and the so-called fatigue line (in log-log space). The monotonic test results are included in this calibration, where the corresponding half-cycle number is 0.5 and the strain amplitude is the fracture strain ε_f.

There are two trends seen from these plots: (1) the fracture resistance decreases with increasing yield strength; (2) the fracture resistance decreases with increasing bar slenderness (s/d_b). The first observation reflects the reduced fatigue life of high-strength steel due to bar metallurgy, and the second reflects the impact of pre-fracture buckling. Similar calibrations were applied to all independent test groups with a total number of 206 specimens. Table 3.5 summarizes the basic material properties, bar slenderness, and the two calibrated model coefficients.

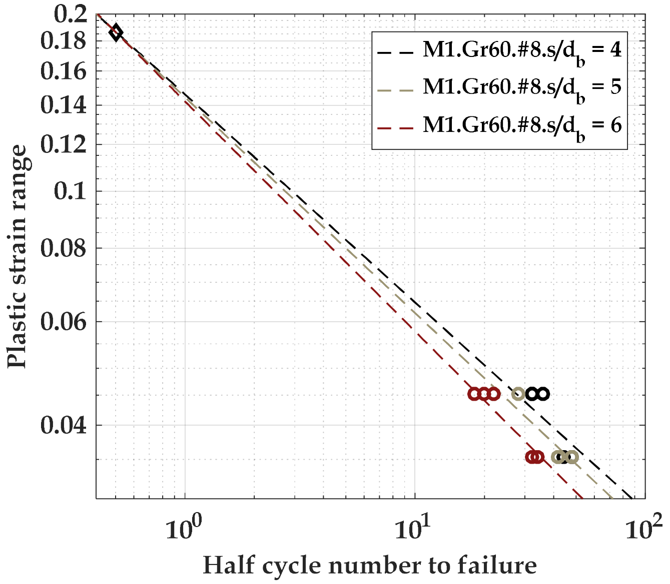

Figure 3.3. Fatigue relations of Gr. 60 reinforcement from Manufacturer 1.

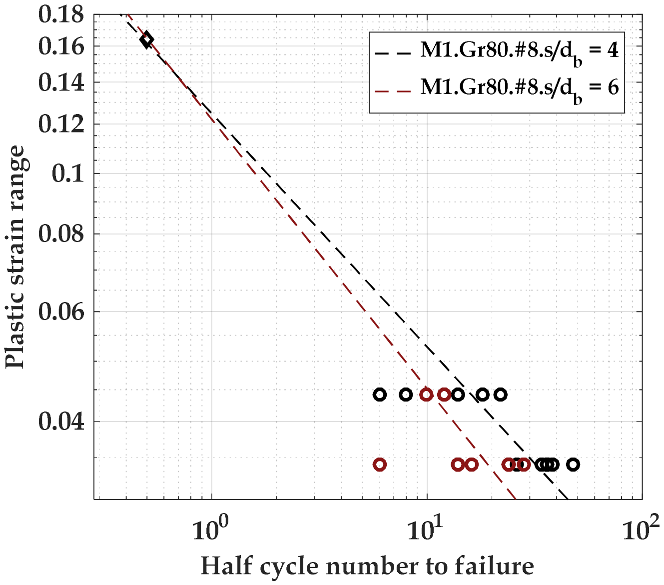

Figure 3.4. Fatigue relations of Gr. 80 reinforcement from Manufacturer 1.

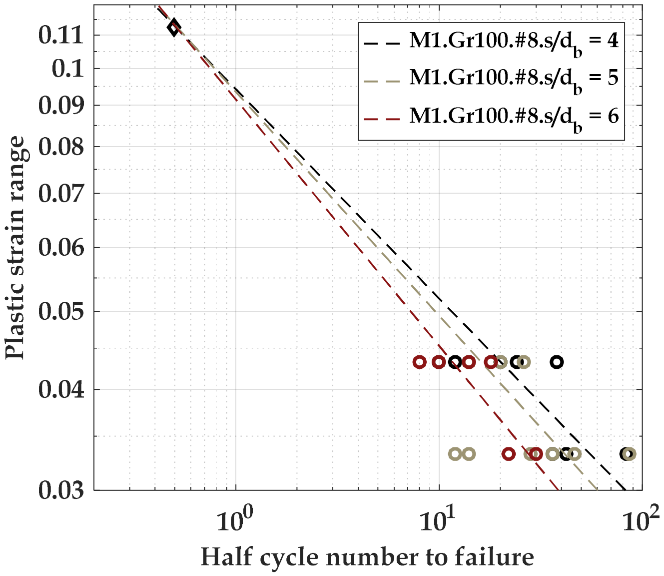

Figure 3.5. Fatigue relations of Gr. 100 reinforcement from Manufacturer 1.

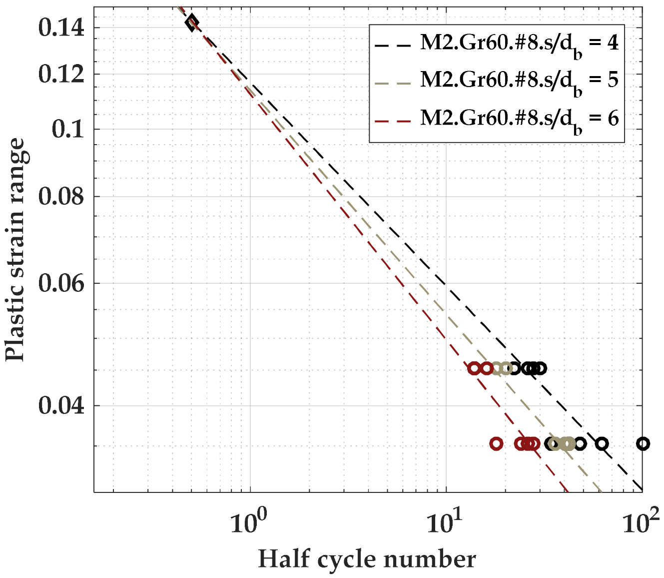

Figure 3.6. Fatigue relations of Gr. 60 reinforcement from Manufacturer 2.

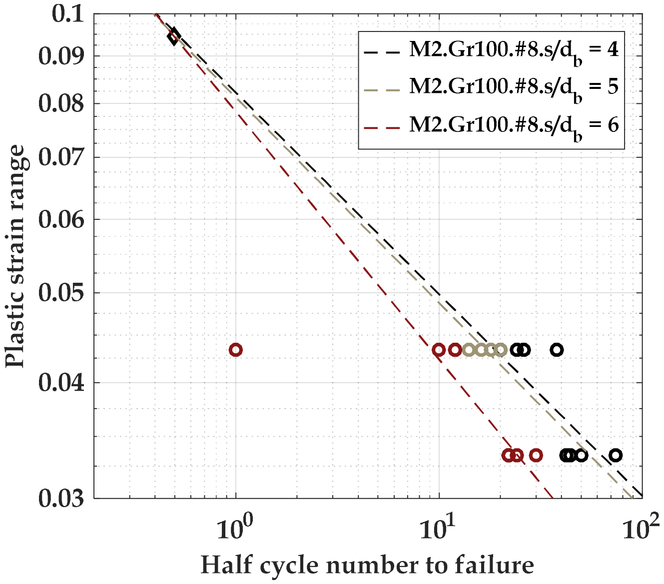

Figure 3.7. Fatigue relations of Gr. 100 reinforcement from Manufacturer 2.

Table 3.5. Calibrated C_f and a_f for all independent test groups.

Group No.	f_y (ksi)	s/d_b	T/Y	d_b (in)	ε_f	ε_{su}	N_{hc}	a_f	C_f
1	67.0	4	1.45	1.410	0.217	0.119	26.0	0.394	0.163
2	67.0	6	1.45	1.410	0.217	0.119	15.2	0.456	0.156
3	103.4	4	1.25	1.410	0.117	0.083	12.5	0.303	0.092
4	103.4	6	1.25	1.410	0.117	0.083	6.3	0.385	0.087
5	62.7	4	1.45	1.410	0.181	0.114	26.0	0.345	0.141
6	62.7	6	1.45	1.410	0.181	0.114	10.0	0.455	0.130
7	99.6	4	1.19	1.410	0.099	0.067	14.4	0.238	0.081
8	99.6	6	1.19	1.410	0.099	0.067	10.7	0.261	0.080
9	63.2	4	1.48	1.000	0.188	0.116	39.7	0.354	0.146
10	63.2	5	1.48	1.000	0.188	0.116	34.5	0.367	0.144
11	63.2	6	1.48	1.000	0.188	0.116	26.5	0.391	0.142
12	80.3	4	1.37	1.000	0.167	0.100	25.0	0.374	0.125
13	80.3	6	1.37	1.000	0.167	0.100	14.7	0.432	0.122
14	101.5	4	1.27	1.000	0.116	0.081	37.4	0.259	0.094
15	101.5	5	1.27	1.000	0.116	0.081	27.8	0.277	0.094
16	101.5	6	1.27	1.000	0.116	0.081	19.3	0.305	0.092
17	61.5	4	1.68	1.000	0.145	0.095	41.9	0.293	0.117
18	61.5	5	1.68	1.000	0.145	0.095	27.9	0.323	0.114
19	61.5	6	1.68	1.000	0.145	0.095	19.3	0.353	0.112
20	104.6	4	1.18	1.000	0.098	0.062	36.7	0.217	0.082
21	104.6	5	1.18	1.000	0.098	0.062	17.0	0.222	0.081
22	104.6	6	1.18	1.000	0.098	0.062	17.0	0.267	0.078
23	68.5	5	1.40	0.625	0.144	0.100	29.3	0.340	0.112
24	68.5	6	1.40	0.625	0.144	0.100	37.3	0.321	0.113
25	83.3	6	1.29	0.625	0.137	0.095	13.8	0.415	0.100
26	111.0	5	1.22	0.625	0.116	0.088	35.1	0.298	0.091
27	111.0	6	1.22	0.625	0.116	0.088	19.6	0.316	0.090
28	72.4	5	1.44	0.625	0.153	0.100	50.3	0.317	0.121
29	72.4	6	1.44	0.625	0.153	0.100	22.0	0.386	0.115
30	83.6	6	1.26	0.625	0.139	0.097	66.7	0.284	0.112
31	106.8	5	1.20	0.625	0.108	0.076	16.7	0.333	0.083
32	106.8	6	1.20	0.625	0.108	0.076	19.8	0.289	0.086

3.5 Predictive Functions for Fatigue-Fracture Model

Using the data from Table 3.5, the next task is to establish relations between the calibrated model coefficients and characteristic reinforcing bar parameters. Figures 3.8 and 3.9 show the trend plots to explore the relationship between the calibrated model parameters, a_f and C_f, against six bar parameters (f_y, s/d_b, T/Y, d_b, ε_f, and ε_u). Note that the manufacturing differences are believed to be well represented by the T/Y ratio and the buckling impact is rationally captured by the slenderness. Some trends observed in these plots include (1) decreasing values of α_f and C_f with increasing yield strength, (2) increasing values of α_f and C_f with increasing T/Y, ε_f, and ε_u, and (3) slightly increasing values of α_f and C_f with increasing s/d_b and d_b. While these trends are somewhat informative, it is difficult to draw firm conclusions since there are inter-variable correlations between the bar parameters and model parameters. Therefore, multi-variate linear regression was performed to isolate the influence from each individual variable on the two model coefficients.

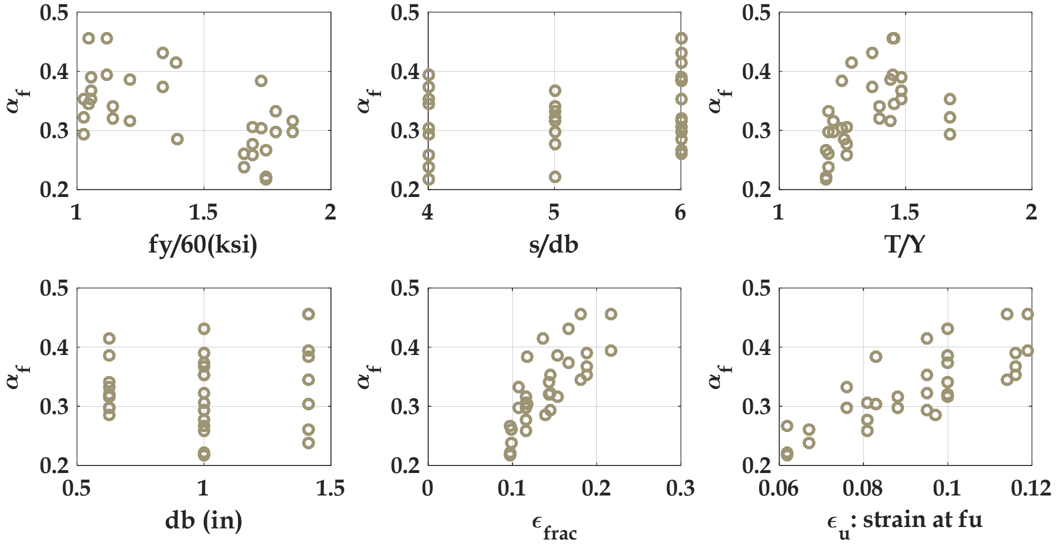

Figure 3.8. Trend plots for calibrated α_f.

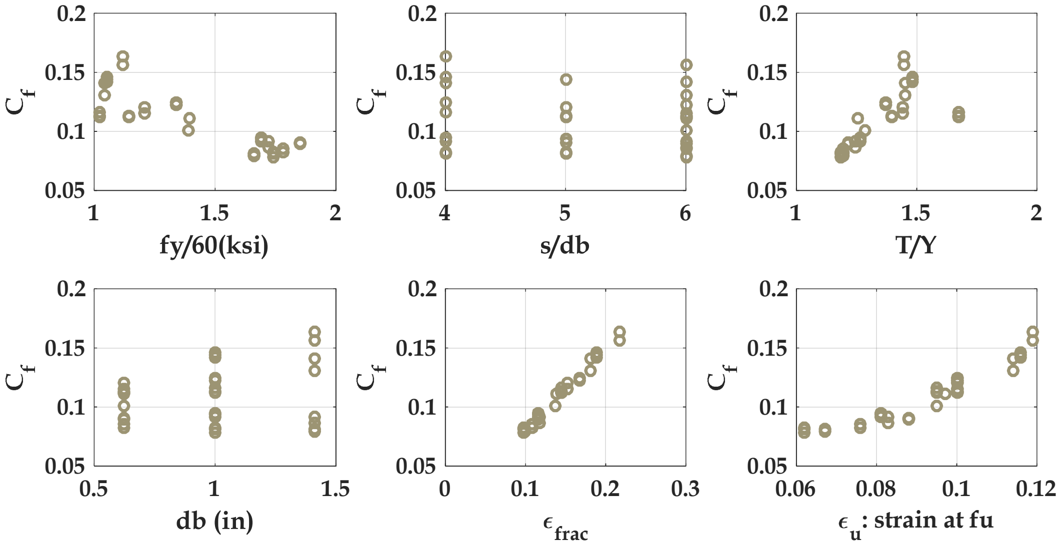

Figure 3.9. Trend plots for calibrated C_f.

The stepwise linear regression algorithm in MATLAB (2012) was used to add or remove predictors based on the statistical significance. Equation 3.5 shows the resulting regressed predictive function for α_f, which reflects a negative correlation with the yield strength and T/Y ratio and a positive correlation with the slenderness. The sum of the squared errors of values determined by Equation 3.5 is 0.07 which is relatively insignificant if compared with the values of a_f, and the R^2 value of 0.63 which is also reasonably good, considering the wide range of steel properties covered in this regression. The largest coefficient in the covariance matrix of the regression is 0.075, which indicates that the four variables in Equation 3.5 have fairly independent predictive relationships with a_f. To avoid introducing unnecessary errors from an additional regression fit for C_f, the coefficient C_f is described by Equation 3.6, which is determined by one realization of Manson-Coffin model from the monotonic tests. Figure 3.10 shows a comparison between the resulting predicted and calibrated (measured) values for a_f and C_f.

$$\alpha_f = 0.080 - 0.045 \cdot \left(f_y / 60ksi \right) + 0.027 \cdot \left(s/d_b \right) + 0.129 \cdot \left(T/Y \right) \tag{3.5}$$

$$C_f = 0.5^{\alpha_f} \cdot \left(\varepsilon_f - f_y / E_s \right) \tag{3.6}$$

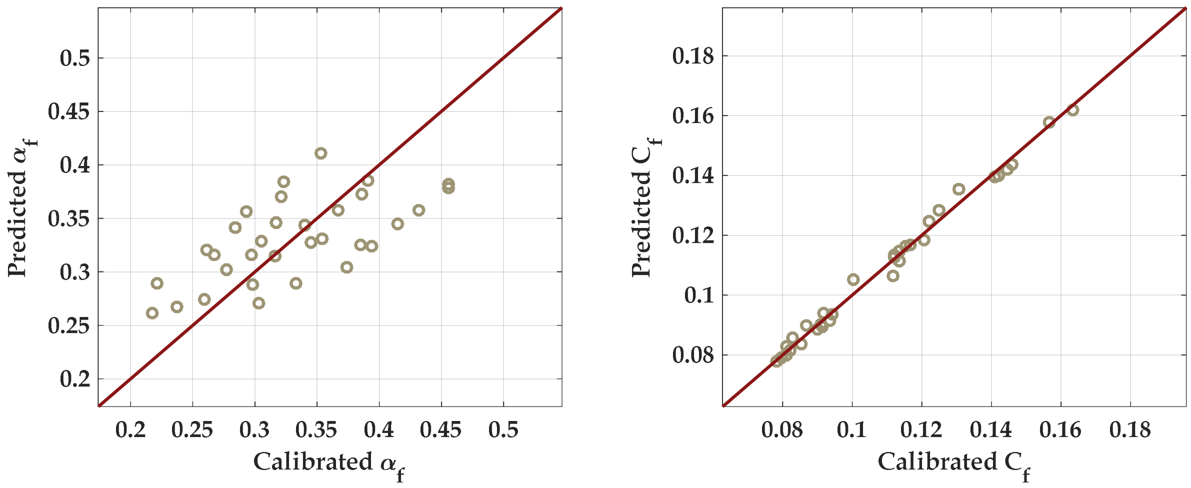

Figure 3.10. Predictions vs. calibrations for a_f and C_f.

3.6 Fracture Index and Verification

The proposed fatigue-fracture model of Equation 3.1 relates the number of half-cycles to fracture with specified plastic strain amplitudes. Before this model can be generally applied to practical applications, two limitations need to be addressed: (1) a strategy is needed to apply the constant strain cycle model to cases with gradually accumulating damage under progressive cycles of different strain histories, and (2) a strategy is needed to apply the model to situations with random strain histories. The second need is addressed through the rain-flow counting procedure discussed in Chapter 4, and the first need is addressed next in this section.

From a practical standpoint, it is useful to have a fracture index that increases continually from zero to its final value to measure the damage accumulation. Miner (1945) proposed a simple model, described by Equation 3.7, that assumes a linear summation of damage as a function of the number of cycles experienced at a specific deformation amplitude.

$$D = \sum_i \left(\frac{1}{2N_{f,i}} \right) \tag{3.7}$$

where, D is the damage index, $N_{f,i}$ is the number of cycles corresponding to the ith excursion for the specified deformation level. Based on this concept, the proposed fracture-fatigue model of Equation 3.1 is rewritten as Equation 3.8 (same as Equation 3.2 shown previously).

$$FI = \sum_{i=1}^{N} \left(1/2N_{f,i} \right) = \sum_{i=1}^{N} \left(\varepsilon_{pi} / C_f \right)^{1/\alpha_f} \tag{3.8}$$

where, FI is the fracture index, N is the half-cycle number corresponding to the ith excursion, and ε_{pi} is the plastic strain amplitude of the ith excursion. Figure 3.11 illustrates application of Equation 3.8 to a constant-amplitude cyclic test.

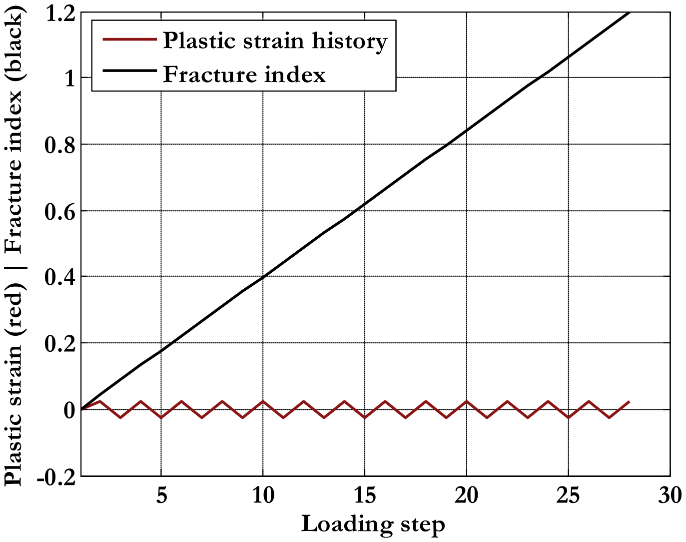

Figure 3.11. Fracture index history under constant-amplitude tests.

To verify the proposed fatigue-fracture model, the fracture index history of each independent test group was back-calculated, where the computed fracture index at the end of the test corresponds to complete rupture. These failure indices are plotted as a counted cumulative probability distribution in Figure 3.12, where the median value has a FI equal to 1.0 (50% fracture probability). This data conforms to a log-normal distribution, which has a calculated dispersion of 0.5 (similar to a coefficient of variation). As shown in Figure 3.12, the range of FI corresponding to observed fractures is from about FI equal to 0.3 up to 2.6.

Shown in Figure 3.13 are so-called bias studies of the fracture index against various yield strength, slenderness, and T/Y ratios. As shown, there is a slight positive bias-trend in f_y, a slight negative bias-trend in T/Y, and practically no bias with respect to s/d_b. By incorporating the yield strength and other bar properties in the calibrated coefficients, the proposed fracture index is applicable to both conventional and high-strength reinforcing steel.

Summarized in Table 3.6 are simulated results for reinforcement with three steel grades (60, 80 and 100) with characteristic T/Y ratios and bar slenderness. The results are based on cycles of 4% strain, where the predicted number of half cycles at fracture (N_{hc}) corresponds to the point when the calculated fracture index FI equals 1 (i.e., the median estimate of fracture). Not surprisingly, the data reflect that the fatigue resistance decreases as T/Y ratio decreases and s/d_b increases. If one considers the least ductile Gr. 60 case (T/Y = 1.3 with s/d_b = 6) as a reference (benchmark), the Gr. 80 and 100 bars can achieve as much fracture resistance with limits of T/Y = 1.2 and s/d_b = 5 (i.e., N_{hc} equals 22 for Gr. 60 and 24 and 22 for the Gr. 80 and 100 cases, respectively).

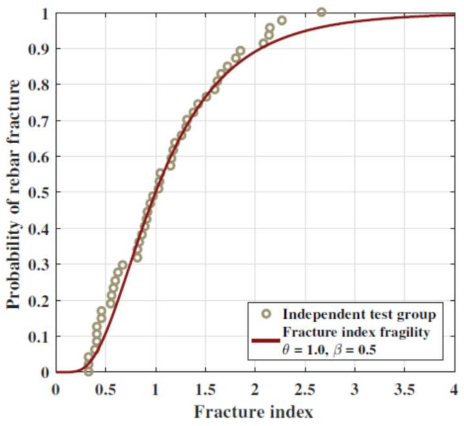

Figure 3.12. Fragility model based on the fracture index.

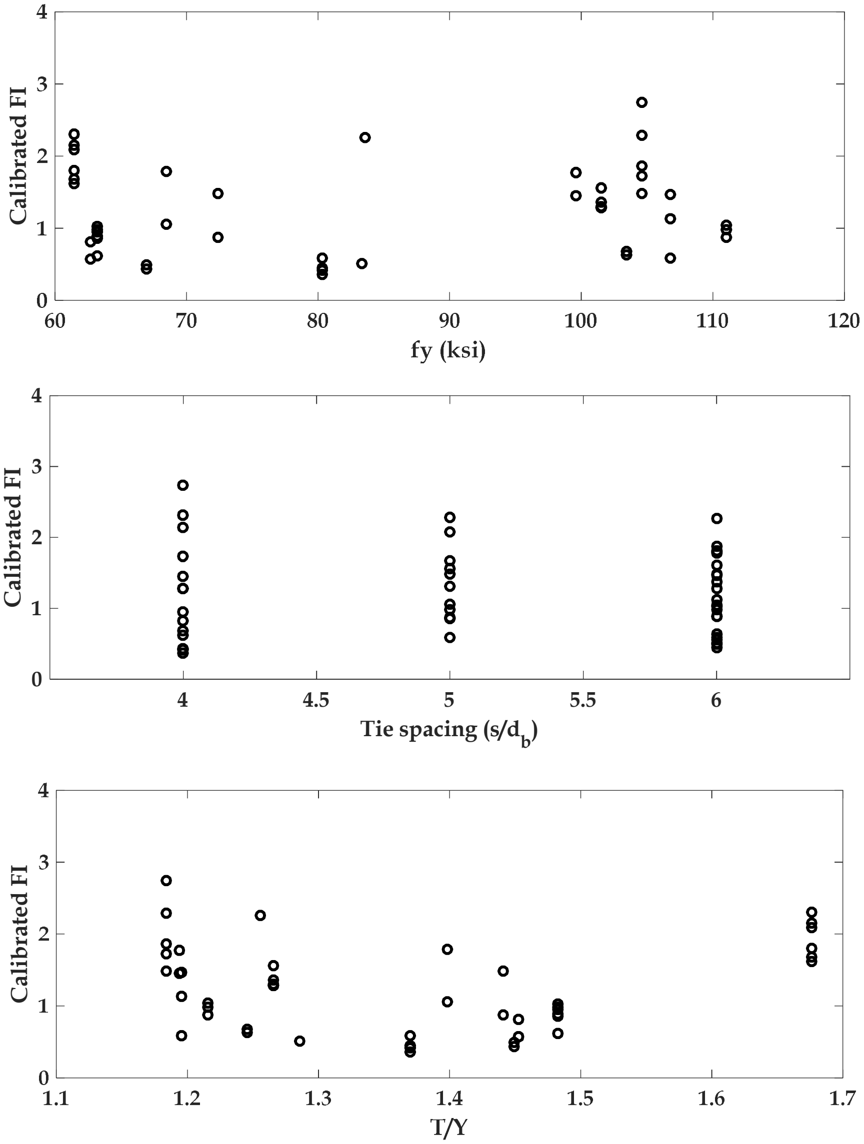

Figure 3.13. Bias studies of the fracture index.

Table 3.6. Calculate half-cycle numbers to fracture (*FI* = 1) under 4% total strain range.

Tag	Grade	T/Y	s/d_b	ε_f	a_f	C_f	N_{hc}
1	60	1.5	4	0.169	0.337	0.133	49
2			5	0.169	0.364	0.130	35
3			6	0.169	0.391	0.128	26
4		1.4	4	0.157	0.324	0.124	46
5			5	0.157	0.351	0.121	32
6			6	0.157	0.378	0.119	24
7		1.3	4	0.144	0.311	0.114	42
8			5	0.144	0.338	0.112	29
9			6	0.144	0.365	0.110	22*
10	80	1.4	4	0.143	0.309	0.113	47
11			5	0.143	0.336	0.111	33
12			6	0.143	0.363	0.109	24
13		1.3	4	0.130	0.296	0.104	42
14			5	0.130	0.323	0.102	29
15			6	0.130	0.350	0.100	21
16		1.2	4	0.117	0.283	0.094	35
17			5	0.117	0.310	0.093	24*
18			6	0.117	0.337	0.091	18
19	100	1.3	4	0.117	0.281	0.093	40
20			5	0.117	0.308	0.091	27
21			6	0.117	0.335	0.090	20
22		1.2	4	0.104	0.268	0.083	31
23			5	0.104	0.295	0.082	22*
24			6	0.104	0.322	0.080	16
25		1.1	4	0.091	0.255	0.073	23
26			5	0.091	0.282	0.072	16
27			6	0.091	0.309	0.071	12

* Assumed Gr. 60 benchmark case and fracture equivalent Gr. 80 and 100 cases

4. BEAM-COLUMN HINGE MODEL

4.1 High-Strength (HS) Reinforcement Hinge Model

4.1.1 Ibarra-Medina-Krawinkler (IMK) model and current predictive modeling equations

The IMK model (Figure 4.1) was developed by Ibarra et al. (2005) to capture monotonic and cyclic deterioration that precipitate sidesway collapse of moment frames under earthquakes. The model is applicable to a broad range of structural members (e.g., reinforced concrete beam-column, steel beam-column, et al). For reinforced concrete beam-column elements, the IMK model uses one backbone curve with several cyclic strength deterioration and stiffness degradation rules to define the behavior of concentrated hinges at the end(s) of a member. Six modeling parameters (yield strength, initial stiffness, hardening ratio, pre-capping plastic rotation, post-capping rotation capacity, residual strength, and cyclic deterioration coefficient) are usually used to define such a specific hinge.

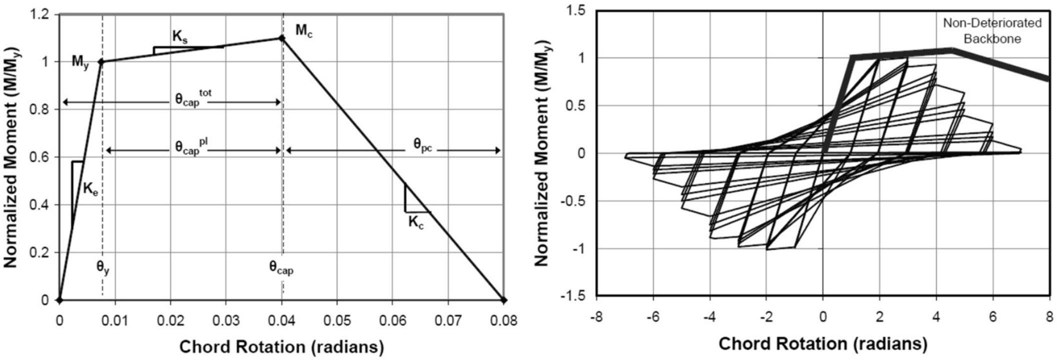

Figure 4.1. Monotonic and cyclic behavior of concentrated hinge model used in study (after Ibarra et al. 2005).

Numerous studies have been conducted to find empirical equations to predict these six modeling parameters as functions of design properties (e.g., material strength, dimensions, et al.) and loading information (i.e., axial load ratio). Most recently, by fitting load-deformation hysteresis to PEER SPD column test data, these six parameters were calibrated for each specimen by Haselton et al., (2008 and 2016). Systematical multivariate regressions were then performed to establish predictive formulas for IMK parameters. For example, the two predictive equations for plastic rotation capacity are shown in Equation 4.1 (full version) and 4.2 (simplified version) where, a_{sl} is a bond-slip coefficient; ν is the axial load ratio; ρ_{sh} is the transverse reinforcement ratio; $c_{unit}f_c'$ is the concrete compressive strength in MPa; s_n is the reinforcing bar slenderness ratio; and ρ is the longitudinal reinforcement ratio.

$$\theta_{cap,pl} = 0.12\left(1+0.55a_{sl}\right)\left(0.16\right)^{\nu}\left(0.02+40\rho_{sh}\right)^{0.43}\left(0.54\right)^{0.01c_{unit}f_c'}\left(0.66\right)^{0.1s_n}\left(2.27\right)^{10.0\rho} \tag{4.1}$$

$$\theta_{cap,pl} = 0.10\left(1+0.55a_{sl}\right)\left(0.16\right)^{\nu}\left(0.02+40\rho_{sh}\right)^{0.43}\left(0.54\right)^{0.01c_{unit}f_c'} \tag{4.2}$$

As reported by Haselton et al., when compared to test data, these two formulas have similar predicted/observed medians (1.02 for both equations) and dispersions (0.54 for Equation 4.1 and 0.61 for Equation 4.2). This hinge model has been applied in previous studies, where nonlinear dynamic analyses have been used to quantify the seismic response of concrete moment frames, including studies that were used in the development of the FEMA P695 guidelines for evaluating seismic response factors for design (Haselton et al. 2008, FEMA 2009).

For the purpose of this study, the hinge parameters developed previously by Haselton et al. do not distinguish hinge response based on the grade, *T/Y* ratio and other parameters of the steel reinforcement that are relevant to this study. Therefore, prior to undertaking frame analyses to evaluate the influence of reinforcing bar properties, we revisited the prior calibration to obtain modeling parameters for IMK hinge model for concrete moment frames.

One of the limitations of Haselton et al.'s calibration (2008 and 2016) is that it does not distinguish between some design variables that relate to the tendency for reinforcing bar fracture. This is partially attributed to the fact that steel fracture is an uncommon potential failure mode in previous experiments of reinforced concrete members. In particular, of the 253 rectangular-section column tests in PEER SPD (2004), which were the basis of Haselton et al.'s calibration, only 16 tests (6% of the entire database) were documented to observe longitudinal bar fracture. With this limited contribution, it is reasonable to see that the influence on response from fracture is statistically insignificant, and thus, related variables would not be reflected in the statistical calibration. As described in Section 4.2, the calibration will be revisited to examine more closely those cases that experienced fracture and to determine with significance of reinforcing bar grade (yield strength) and tensile to yield strength ratio (*T/Y* ratio), both of which are recognized to affect both fracture toughness and spread of plasticity (or localization of strains) in concrete members (e.g., Sokoli et al., 2017).

Since the main scope of previous research is investigating general trends from all available column test data, less effort was made to differentiate potential structural failure modes (e.g., concrete crushing failure and bar buckle failure). Using Equation 4.1 and 4.2 as an example, there are no terms directly related to buckle-induced failure in Equation 4.2, and even though the bar slenderness ratio s_n appears in Equation 4.1, its influence is small relative to other factors (e.g., axial load ratio or concrete strength). The underlying reason is that by treating each test in the column database equally, Haselton et al.'s calibration does not differentiate between local effects and failure modes that may have been the subject of subsets of tests in the database. A good example of this is that, as shown in Figure 4.2, most of the tests in the PEER SPD (2004) database are of columns with regular-strength (Grade 60) reinforcement, which will statistically obscure the influence of the few tests with higher strength steel.

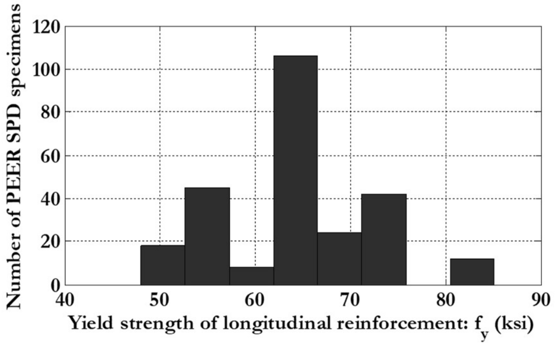

Figure 4.2. Distribution of yield strength of longitudinal reinforcement in PEER SPD (2004).

Aiming to overcome the limitations of existing empirical models of the hinge parameters, we propose to calibrate five of the backbone curve parameters (yield strength, initial stiffness, hardening ratio, pre-capping plastic rotation, post-capping rotation capacity, and residual strength) using fiber-type cross-section analysis, where the material response parameters are more explicitly modeled. We then estimate the sixth parameter (cyclic deterioration coefficient) through a new empirical equation which is calibrated to beam and column test data. This proposed calibration is done in two steps.

Step 1 – Determine the backbone curve: Moment-Curvature (MC) analyses are performed for each test specimen using OpenSees (Mazzoni et al. 2006), whereupon the yield point and peak (capping) point are determined from the MC curve. The yield and peak point curvatures are then converted hinge rotations to generate the Moment-Rotation (MR) curve for each test. Bar-slip is incorporated in the MR curve using the analytical method by Sezen and Setzler (2008), and the MR curve is further adjusted to account for member chord rotations due to member shear deformations using an effective shear modulus. More details regarding these three models will be introduced in Section 4.1.2 to 4.1.5. With these five parameters, the monotonic backbone curve of the IMK hinge is defined for each beam or column test.

Step 2 – Determine the cyclic deterioration factor: This step is conducted by analyzing a cantilever beam-column specimen consisting an end-hinge and an elastic element under the loading history applied in the laboratory test. The IMK end-hinge is defined using the five backbone curve parameters determined in Step 1 and one trial cyclic coefficient. The cyclic coefficient is adjusted and optimized to best fit the hinge hysteresis to test results. Multivariate regression is then applied to find an empirical relationship between calibrated cyclic deterioration coefficients and design properties of each specimen. The resulting predictive equation and parameter sensitivity analyses are introduced later in Sections 4.1.6 to 4.1.7.

4.1.2 Flexural Response: Fiber-Based Cross-Section Analysis

This section describes how the fiber-based cross-section analysis and plastic-hinge length theory are applied to construct the flexural monotonic MR curve.

As mentioned in the previous sections, the total number of tests in the PEER SPD database is 253, among which are monotonic loading tests and many investigations that did not document all of the design properties that are necessary in modeling (e.g., ultimate steel strength, the uniform strain of longitudinal reinforcement). Based on a careful review of the PEER SPD database, 122 specimens were identified and used to calibrate IMK model. In addition, the 4 CPF beam tests (To and Moehle, 2017) and 4 CPF column tests (Sokoli et al., 2017) were included, resulting in a revised database of 130 test specimens. Table 4.1 summarizes the basic information of these 130 experiments.

Table 4.1. Basic information of selected 130 reinforced concrete beam-column tests.

TSN	Test information	b (in)	h (in)	c (in)	L_c (in)	f_c' (ksi)	f_{yl} (ksi)	ν
1	Gill et al. 1979, No. 1	21.65	21.65	1.57	47.24	-5.24	54.39	0.17
2	Gill et al. 1979, No. 2	21.65	21.65	1.50	47.24	-6.00	54.39	0.21
3	Gill et al. 1979, No. 3	21.65	21.65	1.57	47.24	-3.72	54.39	0.35
4	Gill et al. 1979, No. 4	21.65	21.65	1.50	47.24	-4.09	54.39	0.50
5	Ang et al. 1981, No. 3	15.75	15.75	0.96	62.99	-4.11	61.93	0.32
6	Ang et al. 1981, No. 4	15.75	15.75	0.89	62.99	-3.63	61.93	0.21
7	Soesianawati et al. 1986, No. 1	15.75	15.75	0.51	62.99	-8.09	64.69	0.08
8	Soesianawati et al. 1986, No. 2	15.75	15.75	0.51	62.99	-6.38	64.69	0.30
9	Soesianawati et al. 1986, No. 3	15.75	15.75	0.51	62.99	-6.38	64.69	0.30
10	Soesianawati et al. 1986, No. 4	15.75	15.75	0.51	62.99	-5.80	64.69	0.30
11	Zahn et al. 1986, No. 7	15.75	15.75	0.51	62.99	-4.10	63.82	0.22
12	Zahn et al. 1986, No. 8	15.75	15.75	0.51	62.99	-5.82	63.82	0.39
13	Watson and Park 1989, No. 5	15.75	15.75	0.51	62.99	-5.95	68.75	0.50
14	Watson and Park 1989, No. 6	15.75	15.75	0.51	62.99	-5.80	68.75	0.50
15	Watson and Park 1989, No. 7	15.75	15.75	0.51	62.99	-6.09	68.75	0.70
16	Watson and Park 1989, No. 8	15.75	15.75	0.51	62.99	-5.66	68.75	0.70
17	Watson and Park 1989, No. 9	15.75	15.75	0.51	62.99	-5.80	68.75	0.70
18	Tanaka and Park 1990, No. 1	15.75	15.75	1.57	62.99	-3.71	68.75	0.20
19	Tanaka and Park 1990, No. 2	15.75	15.75	1.57	62.99	-3.71	68.75	0.20
20	Tanaka and Park 1990, No. 3	15.75	15.75	1.57	62.99	-3.71	68.75	0.20
21	Tanaka and Park 1990, No. 4	15.75	15.75	1.57	62.99	-3.71	68.75	0.20
22	Tanaka and Park 1990, No. 5	21.65	21.65	1.57	64.96	-4.64	74.11	0.10
23	Tanaka and Park 1990, No. 6	21.65	21.65	1.57	64.96	-4.64	74.11	0.10
24	Tanaka and Park 1990, No. 7	21.65	21.65	1.57	64.96	-4.66	74.11	0.30
25	Tanaka and Park 1990, No. 8	21.65	21.65	1.57	64.96	-4.66	74.11	0.30
26	Ohno and Nishioka 1984, L1	15.75	15.75	1.24	62.99	-3.60	52.50	0.03
27	Ohno and Nishioka 1984, L2	15.75	15.75	1.24	62.99	-3.60	52.50	0.03
28	Ohno and Nishioka 1984, L3	15.75	15.75	1.24	62.99	-3.60	52.50	0.03
29	Wight and Sozen 1973, No. 40.033a(East)	5.98	12.01	0.88	34.49	-5.03	71.94	0.12
30	Wight and Sozen 1973, No. 40.033a(West)	5.98	12.01	0.88	34.49	-5.03	71.94	0.12
31	Wight and Sozen 1973, No. 40.048(East)	5.98	12.01	0.88	34.49	-3.79	71.94	0.15
32	Wight and Sozen 1973, No. 40.048(West)	5.98	12.01	0.88	34.49	-3.79	71.94	0.15
33	Wight and Sozen 1973, No. 40.033(East)	5.98	12.01	0.88	34.49	-4.87	71.94	0.11
34	Wight and Sozen 1973, No. 40.033(West)	5.98	12.01	0.88	34.49	-4.87	71.94	0.11
35	Wight and Sozen 1973, No. 25.033(East)	5.98	12.01	0.88	34.49	-4.87	71.94	0.07
36	Wight and Sozen 1973, No. 25.033(West)	5.98	12.01	0.88	34.49	-4.87	71.94	0.07
37	Wight and Sozen 1973, No. 40.067(East)	5.98	12.01	0.88	34.49	-4.84	71.94	0.11
38	Wight and Sozen 1973, No. 40.067(West)	5.98	12.01	0.88	34.49	-4.84	71.94	0.11
39	Wight and Sozen 1973, No. 40.147(East)	5.98	12.01	0.75	34.49	-4.86	71.94	0.11

Table 4.1. Basic information of selected 130 reinforced concrete beam-column tests (cont.).

TSN	Test information	*b* (in)	*h* (in)	*c* (in)	L_c (in)	*fc* (ksi)	f_{yl} (ksi)	ν
40	Wight and Sozen 1973, No. 40.147(West)	5.98	12.01	0.75	34.49	-4.86	71.94	0.11
41	Wight and Sozen 1973, No. 40.092(East)	5.98	12.01	0.75	34.49	-4.86	71.94	0.11
42	Wight and Sozen 1973, No. 40.092(West)	5.98	12.01	0.75	34.49	-4.86	71.94	0.11
43	Galeota et al. 1996, AA1	9.84	9.84	1.18	44.88	-11.60	62.37	0.30
44	Galeota et al. 1996, AA2	9.84	9.84	1.18	44.88	-11.60	62.37	0.30
45	Galeota et al. 1996, AA3	9.84	9.84	1.18	44.88	-11.60	62.37	0.20
46	Galeota et al. 1996, AA4	9.84	9.84	1.18	44.88	-11.60	62.37	0.20
47	Galeota et al. 1996, BA1	9.84	9.84	1.18	44.88	-11.60	62.37	0.20
48	Galeota et al. 1996, BA2	9.84	9.84	1.18	44.88	-11.60	62.37	0.30
49	Galeota et al. 1996, BA3	9.84	9.84	1.18	44.88	-11.60	62.37	0.30
50	Galeota et al. 1996, BA4	9.84	9.84	1.18	44.88	-11.60	62.37	0.20
51	Galeota et al. 1996, CA1	9.84	9.84	1.18	44.88	-11.60	62.37	0.20
52	Galeota et al. 1996, CA2	9.84	9.84	1.18	44.88	-11.60	62.37	0.30
53	Galeota et al. 1996, CA3	9.84	9.84	1.18	44.88	-11.60	62.37	0.20
54	Galeota et al. 1996, CA4	9.84	9.84	1.18	44.88	-11.60	62.37	0.30
55	Galeota et al. 1996, AB1	9.84	9.84	1.18	44.88	-11.60	62.37	0.20
56	Galeota et al. 1996, AB2	9.84	9.84	1.18	44.88	-11.60	62.37	0.30
57	Galeota et al. 1996, AB3	9.84	9.84	1.18	44.88	-11.60	62.37	0.30
58	Galeota et al. 1996, AB4	9.84	9.84	1.18	44.88	-11.60	62.37	0.20
59	Galeota et al. 1996, BB	9.84	9.84	1.18	44.88	-11.60	62.37	0.20
60	Galeota et al. 1996, BB1	9.84	9.84	1.18	44.88	-11.60	62.37	0.20
61	Galeota et al. 1996, BB4	9.84	9.84	1.18	44.88	-11.60	62.37	0.30
62	Galeota et al. 1996, BB4B	9.84	9.84	1.18	44.88	-11.60	62.37	0.30
63	Galeota et al. 1996, CB1	9.84	9.84	1.18	44.88	-11.60	62.37	0.20
64	Galeota et al. 1996, CB2	9.84	9.84	1.18	44.88	-11.60	62.37	0.20
65	Galeota et al. 1996, CB3	9.84	9.84	1.18	44.88	-11.60	62.37	0.30
66	Galeota et al. 1996, CB4	9.84	9.84	1.18	44.88	-11.60	62.37	0.30
67	Wehbe et al. 1998, A1	14.96	24.02	1.10	91.93	-4.60	64.98	0.08
68	Wehbe et al. 1998, A2	14.96	24.02	1.10	91.93	-3.95	64.98	0.24
69	Wehbe et al. 1998, B1	14.96	24.02	0.98	91.93	-4.31	64.98	0.09
70	Wehbe et al. 1998, B2	14.96	24.02	0.98	91.93	-4.08	64.98	0.23
71	Lynn et al. 1998, 3CLH18	18.00	18.00	1.50	58.00	-3.90	48.01	0.09
72	Lynn et al. 1998, 2CLH18	18.00	18.00	1.50	58.00	-4.80	48.01	0.07
73	Lynn et al. 1998, 2CMH18	18.00	18.00	1.50	58.00	-3.70	48.01	0.28
74	Lynn et al. 1998, 3CMH18	18.00	18.00	1.50	58.00	-4.00	48.01	0.26
75	Lynn et al. 1998, 3CMD12	18.00	18.00	1.50	58.00	-4.00	48.01	0.26
76	Lynn et al. 1996, 3SLH18	18.00	18.00	1.50	58.00	-3.90	48.01	0.09
77	Lynn et al. 1996, 2SLH18	18.00	18.00	1.50	58.00	-4.80	48.01	0.07
78	Lynn et al. 1996, 3SMD12	18.00	18.00	1.50	58.00	-3.70	48.01	0.28

Table 4.1. Basic information of selected 130 reinforced concrete beam-column tests (cont.).

TSN	Test information	b (in)	h (in)	c (in)	L_c (in)	fc (ksi)	f_{yl} (ksi)	ν
79	Sugano 1996, UC10H	8.86	8.86	0.44	17.72	-17.11	57.00	0.60
80	Sugano 1996, UC15H	8.86	8.86	0.44	17.72	-17.11	57.00	0.60
81	Sugano 1996, UC20H	8.86	8.86	0.44	17.72	-17.11	57.00	0.60
82	Sugano 1996, UC15L	8.86	8.86	0.44	17.72	-17.11	57.00	0.35
83	Sugano 1996, UC20L	8.86	8.86	0.44	17.72	-17.11	57.00	0.35
84	Bayrak and Sheikh 1996, ES-1HT	12.01	12.01	0.79	57.99	-10.46	65.85	0.50
85	Bayrak and Sheikh 1996, AS-2HT	12.01	12.01	0.79	57.99	-10.40	65.85	0.36
86	Bayrak and Sheikh 1996, AS-3HT	12.01	12.01	0.79	57.99	-10.41	65.85	0.50
87	Bayrak and Sheikh 1996, AS-4HT	12.01	12.01	0.79	57.99	-10.43	65.85	0.50
88	Bayrak and Sheikh 1996, AS-5HT	12.01	12.01	0.79	57.99	-14.76	65.85	0.45
89	Bayrak and Sheikh 1996, AS-6HT	12.01	12.01	0.79	57.99	-14.78	65.85	0.46
90	Bayrak and Sheikh 1996, AS-7HT	12.01	12.01	0.79	57.99	-14.79	65.85	0.45
91	Bayrak and Sheikh 1996, ES-8HT	12.01	12.01	0.79	57.99	-14.82	65.85	0.47
92	Saatcioglu and Grira 1999, BG-1	13.78	13.78	1.14	64.76	-4.93	66.08	0.43
93	Saatcioglu and Grira 1999, BG-2	13.78	13.78	1.14	64.76	-4.93	66.08	0.43
94	Saatcioglu and Grira 1999, BG-3	13.78	13.78	1.14	64.76	-4.93	66.08	0.20
95	Saatcioglu and Grira 1999, BG-4	13.78	13.78	1.14	64.76	-4.93	66.08	0.46
96	Saatcioglu and Grira 1999, BG-5	13.78	13.78	1.14	64.76	-4.93	66.08	0.46
97	Saatcioglu and Grira 1999, BG-6	13.78	13.78	1.14	64.76	-4.93	69.30	0.46
98	Saatcioglu and Grira 1999, BG-7	13.78	13.78	1.14	64.76	-4.93	66.08	0.46
99	Saatcioglu and Grira 1999, BG-8	13.78	13.78	1.14	64.76	-4.93	66.08	0.23
100	Saatcioglu and Grira 1999, BG-9	13.78	13.78	1.14	64.76	-4.93	62.05	0.46
101	Saatcioglu and Grira 1999, BG-10	13.78	13.78	1.14	64.76	-4.93	62.05	0.46
102	Thomsen and Wallace 1994, B1	6.00	6.00	0.44	23.50	-12.69	66.01	0.00
103	Thomsen and Wallace 1994, B2	6.00	6.00	0.44	23.50	-12.10	66.01	0.10
104	Thomsen and Wallace 1994, B3	6.00	6.00	0.44	23.50	-13.05	66.01	0.20
105	Thomsen and Wallace 1994, C1	6.00	6.00	0.44	23.50	-9.79	69.01	0.00
106	Thomsen and Wallace 1994, C2	6.00	6.00	0.44	23.50	-10.82	69.01	0.10
107	Thomsen and Wallace 1994, C3	6.00	6.00	0.44	23.50	-11.86	69.01	0.20
108	Thomsen and Wallace 1994, D1	6.00	6.00	0.44	23.50	-10.99	69.01	0.20
109	Thomsen and Wallace 1994, D2	6.00	6.00	0.44	23.50	-12.62	69.01	0.20
110	Thomsen and Wallace 1994, D3	6.00	6.00	0.44	23.50	-10.33	69.01	0.20
111	Paultre and Legeron, 2000, No. 1006015	12.01	12.01	0.75	78.74	-13.40	65.41	0.14
112	Paultre and Legeron, 2000, No. 1006025	12.01	12.01	0.75	78.74	-13.53	62.37	0.28
113	Paultre and Legeron, 2000, No. 1006040	12.01	12.01	0.75	78.74	-14.24	58.87	0.39
114	Paultre and Legeron, 2000, No. 10013015	12.01	12.01	0.75	78.74	-13.75	65.41	0.14
115	Paultre and Legeron, 2000, No. 10013025	12.01	12.01	0.75	78.74	-14.17	62.37	0.26
116	Paultre and Legeron, 2000, No. 10013040	12.01	12.01	0.75	78.74	-15.13	65.41	0.37
117	Paultre et al., 2001, No. 806040	12.01	12.01	0.75	78.74	-11.41	64.69	0.40

Table 4.1. Basic information of selected 130 reinforced concrete beam-column tests (cont.).

TSN	Test information	b (in)	h (in)	c (in)	L_c (in)	fc (ksi)	f_{yl} (ksi)	ν
118	Paultre et al., 2001, No. 1206040	12.01	12.01	0.75	78.74	-15.84	64.69	0.41
119	Paultre et al., 2001, No. 1005540	12.01	12.01	0.75	78.74	-15.88	64.69	0.41
120	Paultre et al., 2001, No. 1008040	12.01	12.01	0.75	78.74	-15.11	64.69	0.37
121	Paultre et al., 2001, No. 1005552	12.01	12.01	0.75	78.74	-15.16	58.22	0.53
122	Paultre et al., 2001, No. 1006052	12.01	12.01	0.75	78.74	-15.87	64.69	0.51
123	To et al., 2016, Gr. 60 A706	13.50	24.00	1.25	93.75	-5.34	72.00	0.00
124	To and Moehle, 2017, Gr. 100 *T/Y* = 1.18	13.50	24.00	1.25	93.75	-5.10	110.00	0.00
125	To and Moehle, 2017, Gr. 100 *T/Y* = 1.30	13.50	24.00	1.25	93.75	-5.00	100.00	0.00
126	To and Moehle, 2017, Gr. 100 MMFX	13.50	24.00	1.25	93.75	-5.47	124.20	0.00
127	Sokoli et al., 2017, CH60	18.00	18.00	1.00	54.00	-4.57	64.40	0.17
128	Sokoli et al., 2017, CH100	18.00	18.00	1.00	54.00	-5.21	100.00	0.15
129	Sokoli et al., 2017, CL100	18.00	18.00	1.00	54.00	-5.16	106.40	0.15
130	Sokoli et al., 2017, CM100	18.00	18.00	1.00	54.00	-5.58	124.20	0.14

The OpenSees material model Concrete02 is used to simulate unconfined and confined concrete fibers. For confined concrete, the Concrete02 parameters are established based on the Mander model (Mander et al., 1988). The ReinforcingSteel material is used to model reinforcing bar fibers, where the Dhakal-Maekawa bar buckling model (Dhakal and Maekawa, 2002) is applied to relate strain at buckling to the effective span-ratio and the buckling factor α (Equation 4.3). This buckling factor was calibrated using the 206 reinforcing bar specimens tested by Slavin and Ghannoum (2015) and summarized in Chapter 3. The statistical regression results in a buckling factor α this is described by the following equation as a function of steel yield strength, *T/Y* ratio, and the slenderness of the reinforcement:

$$\alpha = 0.9571 + 0.1209\left(\frac{f_y}{60ksi}\right) + 0.1276\left(\frac{T}{Y}\right) - 0.0698\left(\frac{s}{d_b}\right) \in [0.75, 1] \tag{4.3}$$

Based on a fiber-mesh sensitivity analysis by Limantono (2016), the member cross-sections are divided into a mesh 10 fibers in the confined concrete region and 2 additional layers at both edges for cover concrete. The reinforcing bars are represented by single fibers at the reported bar positions.

One zero-length element of the fiber-section is created for each of the 130 beam-column test specimens and subjected to monotonically increasing curvature, while maintaining the reported applied axial load. All sections are loaded up to a curvature of 0.008 to trace the full range of response. During curvature deformation loading, the applied axial load is maintained using an iterative strategy that begins the with the Newton-Rapson method and then switches sequentially (as needed) to the Initial Tangent, Modified Newton, Modified Newton with Initial Tangent, Broyden, and Newton-Line-Search methods until either convergence is achieved or the analysis fails.

Figure 4.3 shows an example of simulated MC curve of one cross-section (Gill et al., 1979), which is used to explain how the yield and peak (capping) points are determined. For the yield point, four candidate points are considered: (1) first steel yielding in tension, (2) first steel yielding in compression, (3) first cover concrete spalling (when the stress drops to residual strength in the farthest cover concrete fiber), and (4) first core concrete unloading (when the stress starts unloading in the farthest core concrete fiber). Under low- and moderate axial loads, the hinge's yield point is controlled by the steel tensile yielding while under high axial load ratios, the cover concrete may spall first which leads to rapid deterioration in stiffness. The earliest event among these four candidates is deemed to be the component yield point, upon which the calculated yield moment and curvature are based.

Assuming that the curvature linearly increases along the cantilever member from zero at the tip to the yield curvature at the fixed end, the yield flexural displacement of the chord is computed by integrating the curvature *Φ(x)* through the length of the column (Equation 4.4 where *m(x)* is the virtual moment along the column). The equivalent hinge rotation is calculated by dividing the displacement by the length of the column (Equation 4.5).

$$\Delta_{y,f} = \int_0^L m(x)\phi(x)dx = \frac{1}{3}\phi_y L^2 \tag{4.4}$$

$$\theta_{y,f} = \frac{\Delta_{f,y}}{L} = \frac{1}{3}\phi_y L \tag{4.5}$$

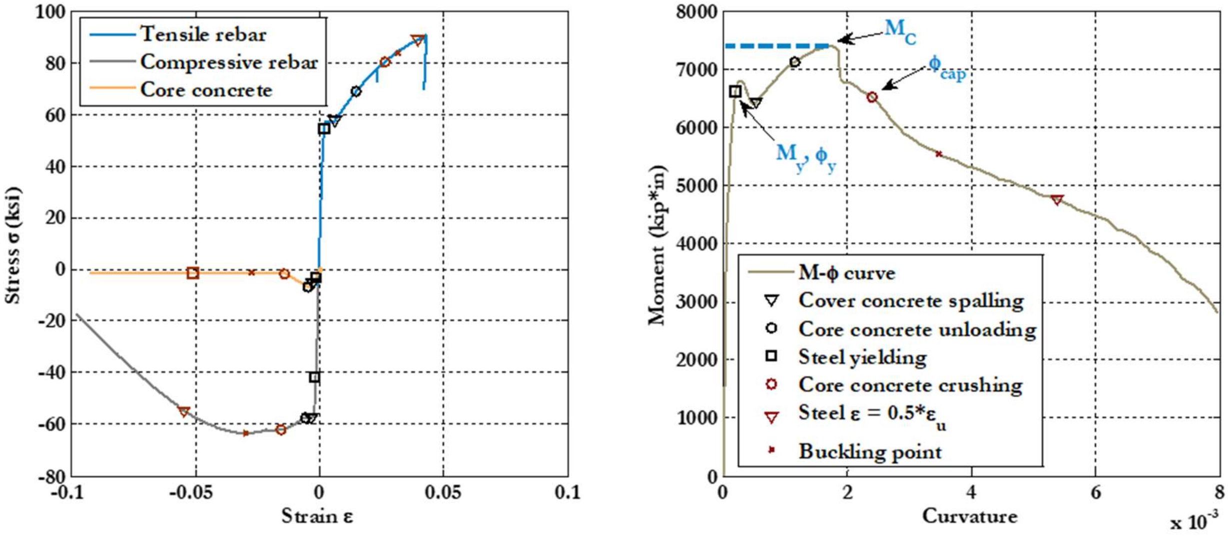

Figure 4.3. Cross-section analysis to find the yield point and the ultimate capacity limits (Test information: Gill et al. 1979, specimen No. 1, measured axial load ratio is about 0.26).

For the peak (or capping) point, the four potential limit states considered are: (1) onset of core concrete crushing (when the stress drops to residual strength at the farthest core concrete fiber), (2) longitudinal reinforcement fracture (when the tensile steel strain first exceeds 0.75 ε_u), (3) longitudinal reinforcement buckling (when the compressive steel fiber starts unloading), and (4) more than 20% strength loss on the MC curve. Since the concrete crushing and bar buckling are explicitly simulated, they can be identified directly from the cross-section analysis based on the underlying material models. On the other hand, the steel fracture point 0.75 ε_u is not included in the material model and follows a suggestion by Paulay and Priestley (1992), based on the assumption that the compressive strain amplitude, which adds to the total strain range, is approximately about ¼ of the tensile strain amplitude. Although this value is considered to be conservative under strain histories with a few cycles of large amplitude excursions, it is obviously unconservative for low-cycle fatigue where bar fracture is observed to occur at lower strain demands in the bare reinforcing bar tests. To account for instances of fatigue-fracture, this limit state is treated as a so-called "non-simulated" failure mode, which is evaluated by post-processing of the strain history data (as described later in Section 4.2).

Similar to determination of the yield point, the peak (or capping) point is defined based on the earliest occurrence of the four limit states mentioned above. In the IMK hinge model, this deformation corresponds to the onset of strain softening (in-cycle negative stiffness) in the backbone curve. The curvature is related to hinge rotation by the plastic hinge length, L_p, suggested by Paulay and Priestley (1992), according to the following equation:

$$\theta_{cap,f} = \phi_{cap} L_p = \phi_{cap}\left(0.08 L_s + 0.15 f_y\left(ksi\right) d_b\right) \tag{4.6}$$

4.1.3 Bar-Slip Response: Analytical Model

Reinforcing bar slip is considered to occur due to (1) deterioration of bond resistance at the rebar-concrete surface in plastic hinge regions where significant flexural/shear cracking occurs, and (2) in beam-column joints and column footings, where the bond-transfer demands are very large and exceed the bond resistance. Many studies have been conducted on modeling bar-slip responses in RC components under lateral loads. Two main directions have been explored at different scales: (1) micro-scale modeling that involves detailed finite element analyses with local contact models to simulate bar-slip behaviors; (2) macro-scale modeling that condenses the bar-slip response into a nonlinear spring with appropriate force-deformation models. Both approaches require calibration of modeling parameters. For reasons of practicality and scope, this study adopts macro-scale model which is considered sufficient for analyzing overall member and structural system response.

Saatcioglu et al. (1992) developed a hysteretic bar-slip macro-model and validated it using seven tests of members that exhibited significant slip response. They modeled the gradually increasing bond stress over the development length with four piecewise functions, with a set of rules defining unloading and reloading branches. Lehman and Moehle (2000) developed a bond-slip response envelope based on their test data. Their proposed envelope is based a local bond stress-slip relationship by Eligehausen et al., 1983, which they simplify into a bi-uniform bond stress relationship along the development length. Following the similar concept, Sezen and Setzler (2008) proposed a macro-level bar-slip model, which is determined by integrating the strains over the development length. By comparing simulated response curves to data from seven test specimens, Sezen concluded that all of three of the aforementioned models produced reasonably accurate results. In this study, we adopted the model by Sezen and Setzler to compute the bar-slip contribution to hinge rotation, θ_{bs}, according to the following equation.

$$\theta_{bs} = \begin{cases} \dfrac{\varepsilon_s l_d}{2\left(b_c - d_b\right)} & \varepsilon_s \le \varepsilon_y \\ \dfrac{\varepsilon_y l_d + \left(\varepsilon_s + \varepsilon_y\right) l_d^{'}}{2\left(b_c - d_b\right)} & \varepsilon_s > \varepsilon_y \end{cases} \tag{4.7}$$

Where ε_s is the longitudinal steel strain; ε_y is the steel yield strain; b_c is the height of the cross-section; d_b is the depth of the bar; and, l_d and l_d' are the development lengths for the elastic and inelastic portions of the reinforcement, respectively, defined as follows:

$$l_d = \frac{f_s d_b}{4 u_b},\ l_d^{'} = \frac{\left(f_s - f_y\right) d_b}{4 u_b^{'}} \tag{4.8}$$

where u_b and u_b' are the uniform bond stresses (Equation 4.9) for the elastic and inelastic portions, respectively. Previous research has found that bond stress can be determined by the compressive strength of the surrounding concrete, f_c'. The model proposed by Lehman and Moehle (2000) is adopted in this study.

$$u_b = 1.0\sqrt{f_c^{'}}\,Mpa = 12\sqrt{f_c^{'}}\,psi\ ,\ u_b^{'} = 0.5\sqrt{f_c^{'}}\,Mpa = 6\sqrt{f_c^{'}}\,psi \tag{4.9}$$

Based on this model, the evolving bar-slip hinge rotation is evaluated based on the evolving longitudinal bar steel strain. Therefore, by substituting the bar strains at the yield and peak (capping) points into Equation 4.7, the hinge rotation values are computed. As the bar-slip response parallels the flexural response, the corresponding moment at these two points are the same as the yield and peak moments in flexural model. Note that the adopted bond-slip model incorporates the effect of bar diameter (Equations. 4.7 and 4.8) along with the *T/Y* ratio (implicit in the yield and peak moments) on the behavior.

4.1.4 Shear Response: Linear Elastic Model

Shear deformation is a small but not insignificant contribution to beam-column member deformations. In the four Pankow supported column tests, Sokoli et al. (2017) report that shear contributes about 10% of the total lateral drift, which is similar to values cited in other studies. For this study, shear deformation is incorporated into the calibrated hinge models, assuming that the beam-column members are well-designed to avoid premature shear failure. The contribution of shear to the hinge (member chord) rotation is calculated based on an effective linear shear model according to the following equation:

$$\theta_{sh} = \frac{6V}{5G_{eff}A_g} \tag{4.10}$$

where V is the shear demand, A_g is the gross cross section area, and the effective shear modulus G_{eff} is taken as 0.2 E_c (E_c is concrete compression modulus) to account for concrete cracking, based on Elwood and Eberhard (2009).

4.1.5 Monotonic Backbone Curve: Aggregation of Flexure, Bar Slip, and Shear

The total hinge response for the RC components is obtained by combining models for flexural, bar-slip, and shear response by the following equation;

$$\theta_{tot} = \theta_f + \theta_{bs} + \theta_{sh} \tag{4.11}$$

By aggregating three response models introduced in previous sections, the total backbone curve of RC hinges is obtained. The yield moment (M_y) and the hardening-ratio (M_c/M_y) can be directly obtained from the cross-section analysis. The bar-slip hinge rotation at the yield and peak (capping) point are computed by substituting the steel stress and strain from section analysis into Equation 4.7. The shear contribution can be computed by substituting the associated shear forces into Equation 4.10. The initial stiffness ratio (EI_{stf}/E_g) can be back-calculated by Equation 4.12. Ideally, the post-peak (capping) rotation capacity can be calibrated to the tests, similar to the peak (capping) rotation, however, because the beam-column database has limited data on in-cycle stiffness degradation tests, the Haselton et al.'s predictive equation for θ_{pc} (Equation 4.13) is used.

$$\frac{EI_{stf}}{EI_g}=\frac{M_y L_{col}}{3EI_g\left(\theta_{y,f}+\theta_{y,bs}+\theta_{y,sb}\right)} \tag{4.12}$$

$$\theta_{pc}=(0.76)(0.031)^{\nu}\left(0.02+40\rho_{sh}\right)^{1.02}\leq 0.10 \tag{4.13}$$

Shown in Figure 4.4 is one example of the backbone curve, computed using the proposed model, as compared to the cyclic test data, for the column test shown previously in Figure4.3. All 130 computed backbone curves are attached in Appendix A and the six model parameters are summarized in Table A.2.

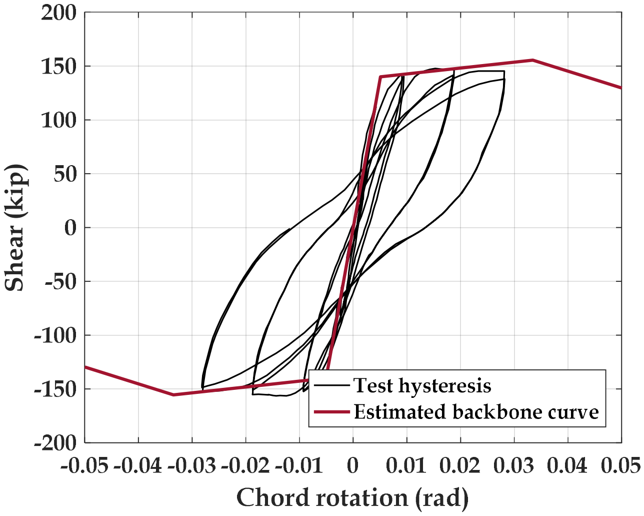

Figure 4.4. Calibrated backbone curve (Test information: Gill et al. 1979, specimen No. 1, measured axial load ratio is about 0.26).

4.1.6 Cyclic Deterioration Coefficient: Calibration and Regression

In IMK model, the following four cyclic deterioration modes may be activated once the deformation demand exceeds the yield point in at least one direction: basic strength, post-capping strength, unloading stiffness, and reloading stiffness deterioration. As recommended by Ibarra et al. (2005), the cyclic deterioration rates are controlled by the rule developed by Rahama and Krawinker (1993), which is defined by the ratio between the hysteresis energy dissipated in current excursion and the residual hysteresis energy capacity of the specimen according to the following equation:

$$\beta=\left(\frac{E_i}{E_t-\sum_{j=1}^{i}E_j}\right)^c\in(0,1) \tag{4.14}$$

where c is the exponent index defining the change rate of the deterioration rate per cycle. To reduce complexity, Haselton et al. (2007) suggest setting c to 1.0 to achieve an almost constant deterioration rate. E_t is the reference hysteretic energy dissipation capacity which is defined as function of the elastic strain energy at yield, according to the following equation:

$$E_t=\lambda F_y\delta_y=\lambda M_y\theta_y \tag{4.15}$$

where λ is a cyclic deterioration coefficient which is dependent on structural characteristics of each specimen, and the cyclic energy dissipation capacity is proportional to λ, which is inversely proportional to the rate of deterioration. Since there is no theoretical function to determine λ it is calibrated to the observed response by fitting the value to the response of each specimen and then regressing the results on relevant design parameters.

Figure 4.5 shows an example of the cyclic responses with the calibrated λ for the tested column shown in Figure 4.3.

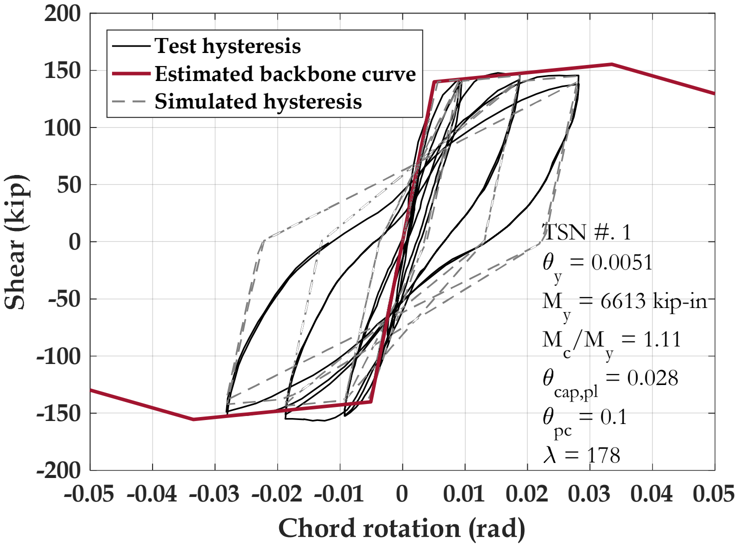

Figure 4.5. Calibrated cyclic response (Test information: Gill et al. 1979, specimen No. 1, measured axial load ratio is about 0.26).

Among the 130 tests used in this calibration, several include specimens with identical for similar design parameters. Since the aim of the regression is to evaluate the dispersion of the calibrated λ relative to the design parameters, before performing the regression, we reduced the data set to 104 tests, where the fitted λ from similar ("duplicate") tests were first averaged together. This process also included averaging of λ values from hinges at each end of a single member, where the moment-rotation data was reported separately in the test data report. Figure 4.6 shows the resulting distribution of main design variables for the 104 data points, and Figure 4.7 shows the scatterplots for the cyclic deterioration coefficient. The data from Figure 4.7 are replotted in the log-log coordinate system in Figure 4.8, where s/h is the tie spacing versus the section depth; and s_n is the bar slenderness (s/d_b) multiplied by square of normalized steel yield strength; L_s/h is the shear span ratio; and ρ_{sh} and $\rho_{sh,eff}$ (as $\rho_{sh}f_y/f_c'$) are original and effective lateral reinforcement ratios, respectively.

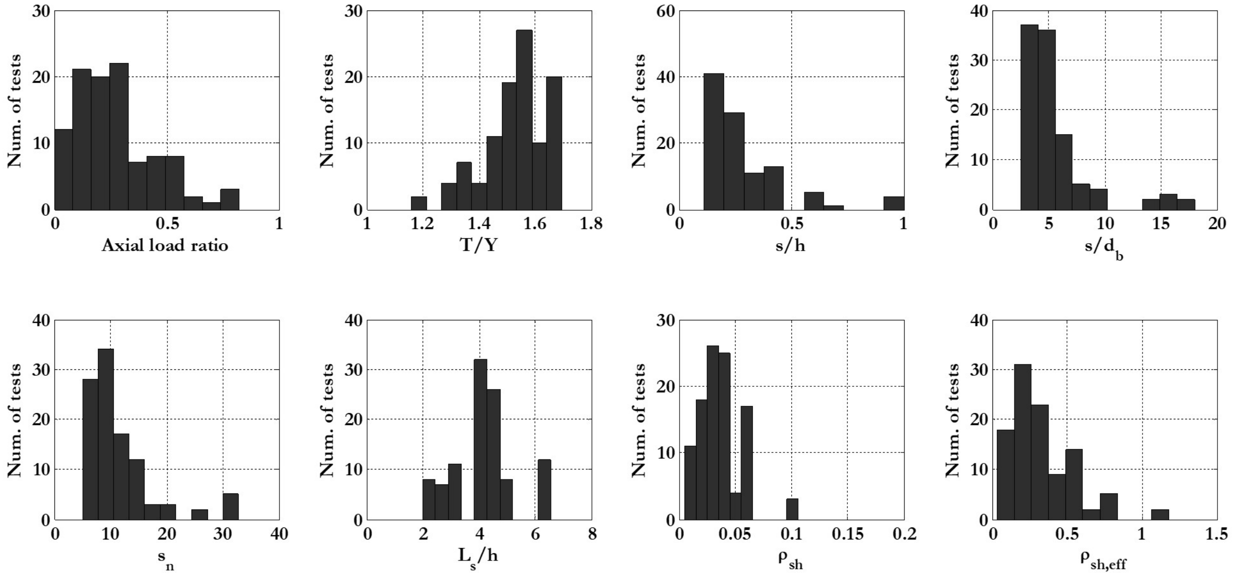

Figure 4.6. Histogram of design properties of reduced database.

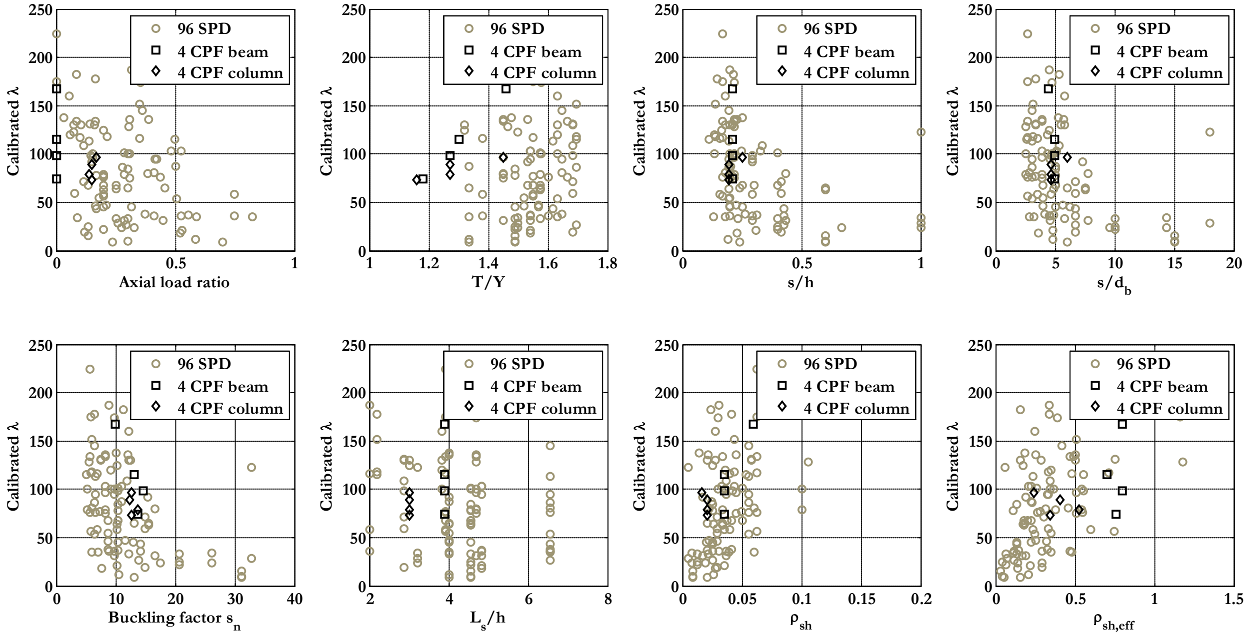

Figure 4.7. Data trends between calibrated λ and design properties.

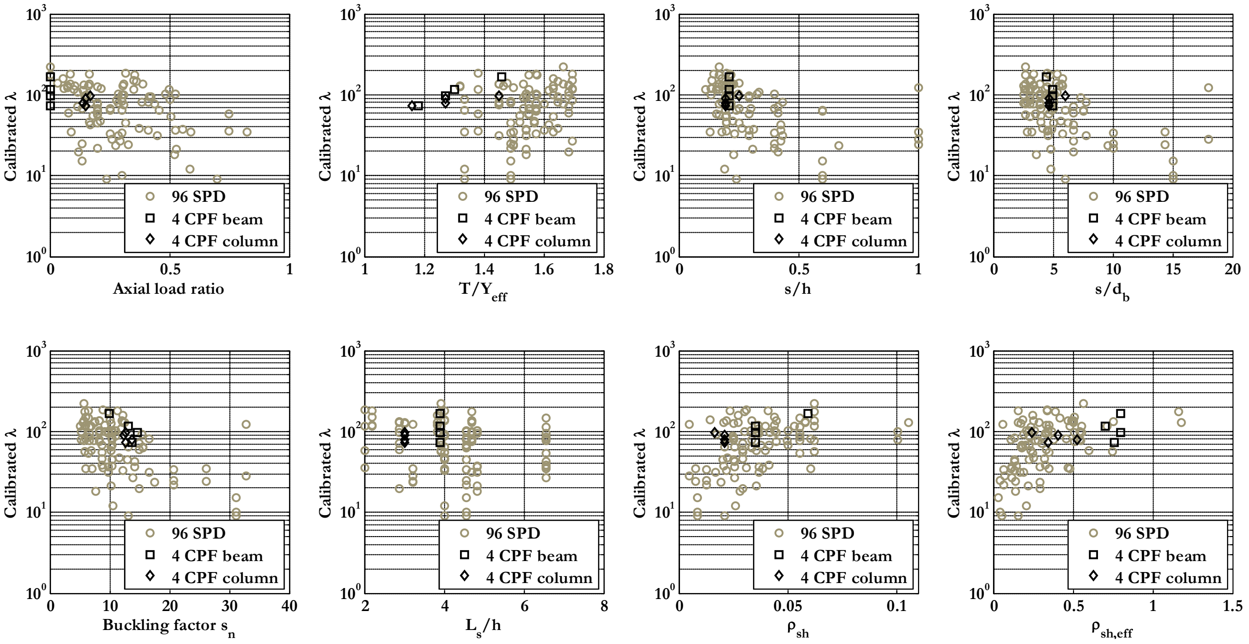

Figure 4.8. Data trends in log-log coordinate between calibrated λ and design properties.

Taken in their entirety, it is difficult to discern clear trends directly from the plots in Figures 4.7 and 4.8 since multiple parameters change from case to case. But we could look at the four recently-tested beams (To and Moehle 2017) or four columns (Sokoli et al., 2017), shown by the black square and triangle points in these figures, as examples in which only the steel property changes. These reveal a clear positive correlation between λ and the *T/Y* ratio, implying that larger *T/Y* ratios will result in higher energy dissipation capacity. This is consistent with the test observations that the plastic hinge region is longer (more distributed yielding) in specimens in higher *T/Y* ratios. Moreover, there is also a clear negative correlation between λ (energy dissipation capacity) and the bar slenderness (s/d_b) or the bar buckling factor (s_n).

After balancing the observation from above trend plots and the knowledge of factors effecting RC member energy dissipation, ten design parameters and member properties are selected for the multivariate regression. These ten parameters include the eight variables shown in Figure 4.7, plus the steel yield strength and the steel uniform strain (ε_{su}). Using multivariate linear regression between logarithmic λ and logarithmic design variables, the predictive formula shown in Equation 4.16 is determined. The ratio of the median calibrated to predicted value is 1.0, and the standard deviation of the error term is 0.49. Upon further evaluation, the contribution from steel uniform strain in Equation 4.15 is negligible compared to other factors. Accordingly, Equation 4.15 can be further simplified by dropping the last term (Equation 4.16), with essentially no change (up to the third decimal place) in the median and standard deviation.

$$\lambda = (253.09)(0.17)^{\nu}(0.92)^{L/h}(1.10)^{T/Y}(1.38)^{\rho_{sh,eff}}(0.94)^{s_n}(1.02)^{\varepsilon_{su}} \tag{4.15}$$

$$\lambda = (253.09)(0.17)^{\nu}(0.92)^{L/h}(1.10)^{T/Y}(1.38)^{\rho_{sh,eff}}(0.94)^{s_n} \tag{4.16}$$

Figure 4.9 shows the scatterplot of calibrated and predicted λ against the diagonal perfect fit line, where 90% of the predicted values are constrained within 35% of calibrated values. Data from only the eight recently tested specimens (4 CPF beam and 4 CPF columns), which have more significance in this study, all fall within a 25% margin of the perfect fit line.

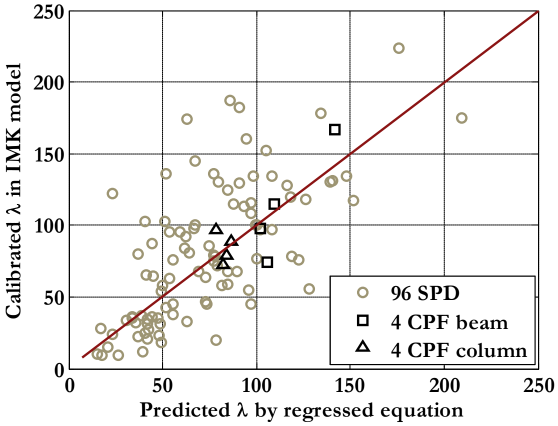

Figure 4.9. Comparison: predicted λ vs. calibrated λ.

To further examine the accuracy of the prediction, both calibrated and regressed values are fed back to IMK for comparative analyses. The cyclic responses based on calibrated and predicted λ are compared for the 4 CPF beams and 4 CPF columns in Figures 4.10 and 4.11. The hysteresis behaviors are very close to each other, and even in the worst λ-fitting case (UCB #2), there are only minor differences between cyclic response curves.

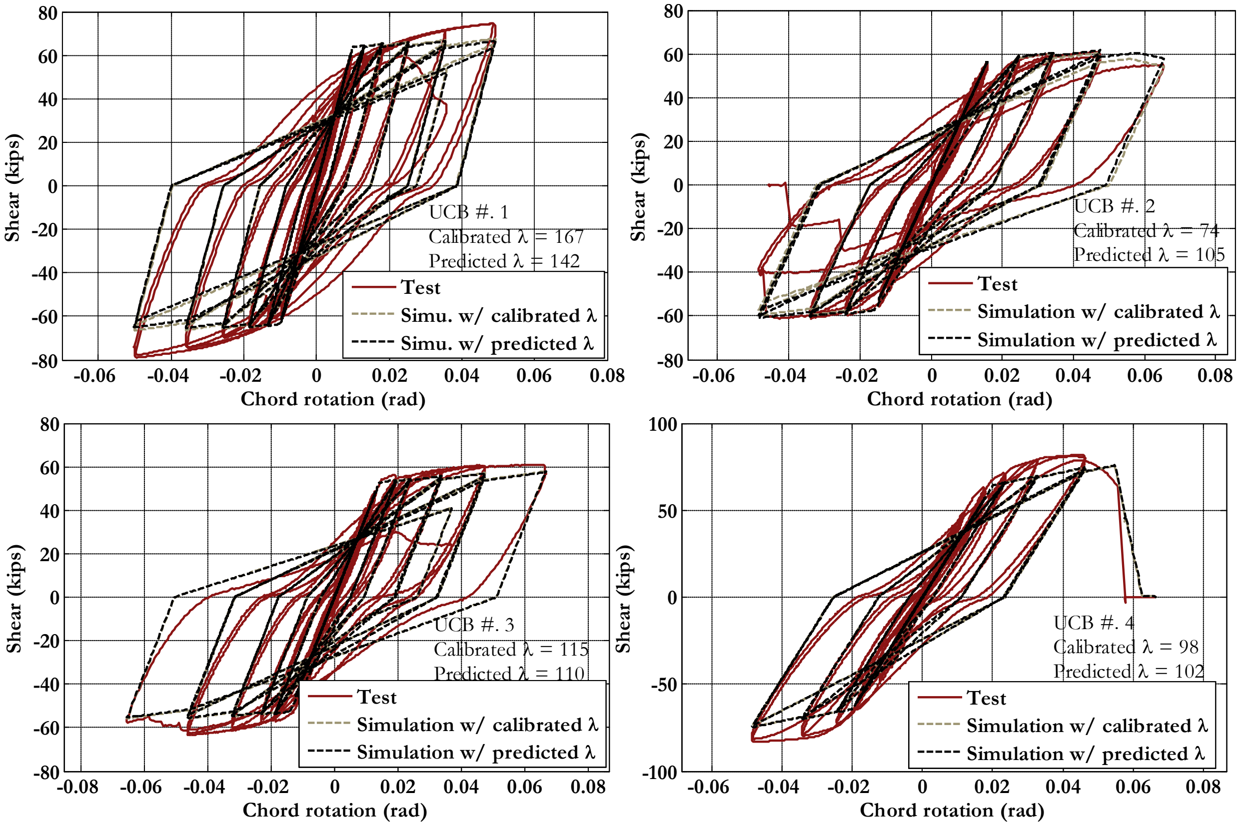

Figure 4.10. Comparison of cyclic responses using calibrated and predicted λ: 4 CPF beams.

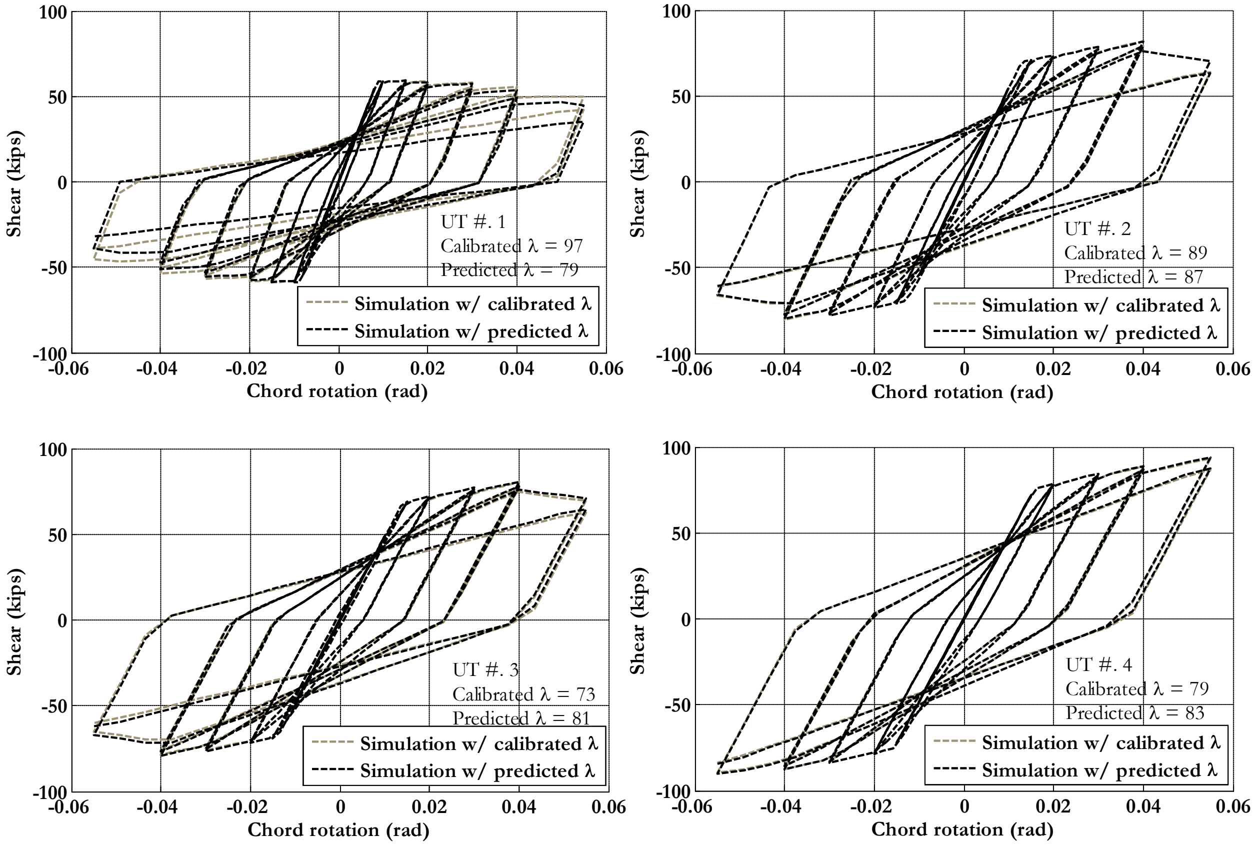

Figure 4.11. Comparison of cyclic responses using calibrated and predicted λ: 4 CPF columns.

4.1.7 Sensitivity of Proposed Hinge Model

This section provides results from the sensitive analysis on the proposed new RC-member hinge-modeling method. Six comparative studies are made, where each is run with three variants of key design variables (steel grade, *T/Y* ratio, ε_{su}, s/d_b, and d_b) are varied between their expected boundaries, from low to high (Table 4.2). All specimens are analyzed under the same loading history, shown in Table 4.3, which is the same FEMA-461 protocol as used in the CPF column tests (Sokoli et al., 2017). Figure 4.12 shows the comparative study on the *T/Y* ratio for columns with Gr. 100 steel. The three specimens have the same properties except for the *T/Y* ratio which varies from 1.1 to 1.3. As shown in Figure 4.12, the hardening ratio (M_c/M_y) increases as *T/Y* increases. Moreover, higher *T/Y* ratio is beneficial to both the monotonic rotation capacity (as it increases the $\theta_{cap,\mathrm{pl}}$) and the energy dissipation capacity (as it increases the λ). The overall effect from *T/Y* ratio includes (1) delaying the occurrence of in-cycle stiffness unloading (*T/Y* =1.1 vs. the other two), and (2) reducing cyclic strength loss. Figure 4.13 shows the comparative study on the steel uniform strain ε_{su} for three beam configurations. The three cases have the same properties except for the ε_{su} which varies from 0.084 to 0.112. As discussed in Section 4.1.2, the ε_{su} controls the monotonic steel fracture failure mode, which is usually not the dominant failure mechanism in columns. Comparative analyses of columns (which are not shown here) confirm that there is no difference for column configurations with different ε_{su}'s. Figure 4.14 shows the comparative study on the slenderness of reinforcement (s/d_b). The three specimens have the same properties except for the s/d_b which varies from 3.5 to 4.5. Comparative analyses (not shown here) confirm that there is no difference in beam response with the variation in s/d_b, but, as shown in Figure 4.14, the column response is influenced by s/d_b. Smaller s/d_b is found to be beneficial to both the monotonic rotation capacity (as it increases the $\theta_{cap,\mathrm{pl}}$) and the energy dissipation capacity (as it increases the λ). The overall effect from s/d_b is to (1) delay the occurrence of in-cycle stiffness unloading (s/d_b = 4.5 vs. the other two), and (2) reduce cyclic strength loss.

Table 4.2. Design properties of specimens in comparative studies.

ID	Grade	T/Y	E_s (ksi)	ε_{su}	Bar size	s/d_b	Axial load ratio	L (in)	b (in)	h (in)	f_c (ksi)
C-1	100	1.3	29000	0.084	#9	3.5	0.1	57	32	42	7.2
C-2	100	1.2	29000	0.084	#9	3.5	0.1	57	32	42	7.2
C-3	100	1.1	29000	0.084	#9	3.5	0.1	57	32	42	7.2
C-4	100	1.2	29000	0.084	#9	4.0	0.1	57	32	42	7.2
C-5	100	1.2	29000	0.084	#9	4.5	0.1	57	32	42	7.2
C-6	100	1.2	29000	0.084	#10	3.5	0.1	57	32	42	7.2
C-7	100	1.2	29000	0.084	#11	3.5	0.1	57	32	42	7.2
C-8	60	1.5	29000	0.110	#11	3.5	0.1	57	32	42	7.2
C-9	80	1.3	29000	0.098	#10	3.5	0.1	57	32	42	7.2
B-1	100	1.2	29000	0.084	#9	5.0	0.0	99	32	42	6.0
B-2	100	1.2	29000	0.098	#9	5.0	0.0	99	32	42	6.0
B-3	100	1.2	29000	0.110	#9	5.0	0.0	99	32	42	6.0
B-4	60	1.5	29000	0.110	#11	3.5	0.0	99	32	42	6.0
B-5	80	1.3	29000	0.098	#10	3.5	0.0	99	32	42	6.0
B-6	100	1.2	29000	0.084	#9	3.5	0.0	99	32	42	6.0

Table 4.3. Loading protocol for sensitive analyses.

Amplitude level	1	2	3	4	5	6	7	8	9	10	11
Lateral drift (%)	0.2	0.3	0.4	0.6	0.8	1.0	1.5	2.0	3.0	4.0	5.5
Number of cycles	2	2	2	2	2	2	2	2	2	2	2

Figure 4.15 shows the comparative study on the longitudinal rebar size (d_b). The three specimens have the same properties, including similar s/d_b ratios, except for the d_b which varies from 1.128 in to 1.41 in (#9 to #11 bars). As shown in Figure 4.15, the column cyclic responses are influenced by d_b, where larger d_b is found to be beneficial to both the monotonic rotation capacity (as it increases the $\theta_{cap,pl}$) and the energy dissipation capacity (as it increases the λ). Presumably, this is due to the tendency for the increased bar slip (with larger d_b) to reduce flexural hinge rotation demands, and thereby reduce cyclic strength loss. Obviously, there may be a point where too much bar slip may negatively impact the structural system response, but that did not occur in this example. The overall effect from HS reinforcement on cyclic responses of RC members are presented in Figure 4.16 (beams) and 4.17 (columns). One interesting observation in Figure 4.16 and 4.17 is that, although the predicted monotonic rotation capacity ($\theta_{cap,pl}$) may decrease dramatically between specimens (by up to 30%), the cyclic response and degradation tend to have much smaller differences. Similar situations are observed in the CPF tests (To and Moehle, 2017 and Sokoli et al., 2017), where more notable cyclic deteriorations are observed in the HS reinforcement specimens, but only slight differences are observed in the peak load, before the onset of strain softening (post-peak response).

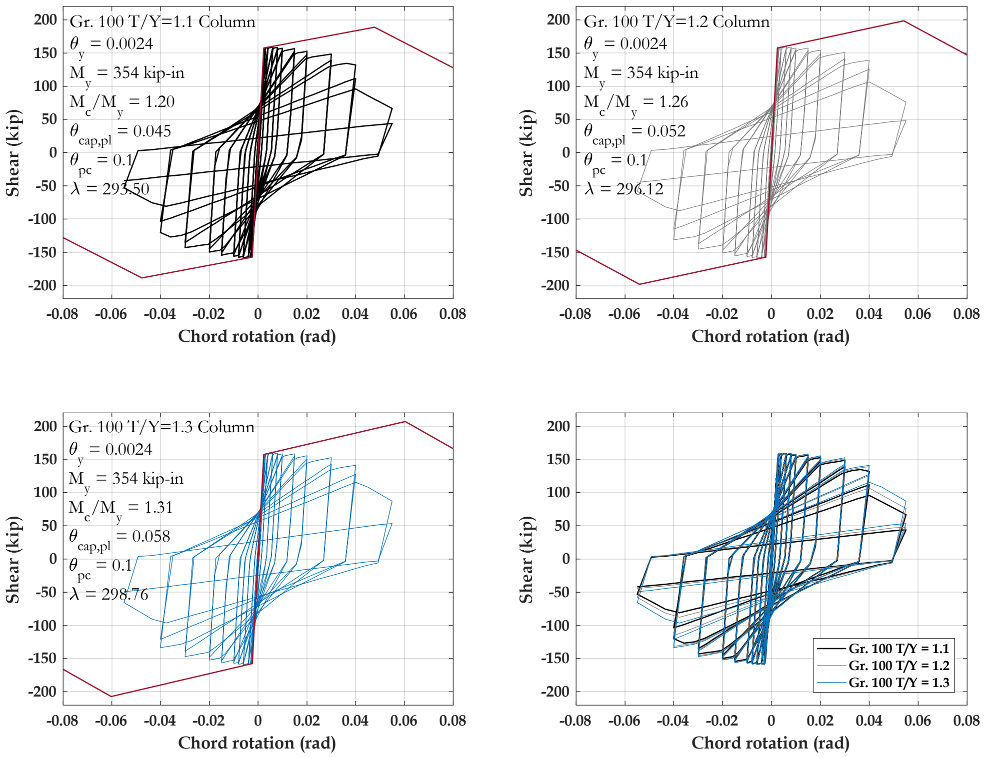

Figure 4.12. Influence of *T/Y* ratio on cyclic behaviors (C-1, C-2, and C-3).

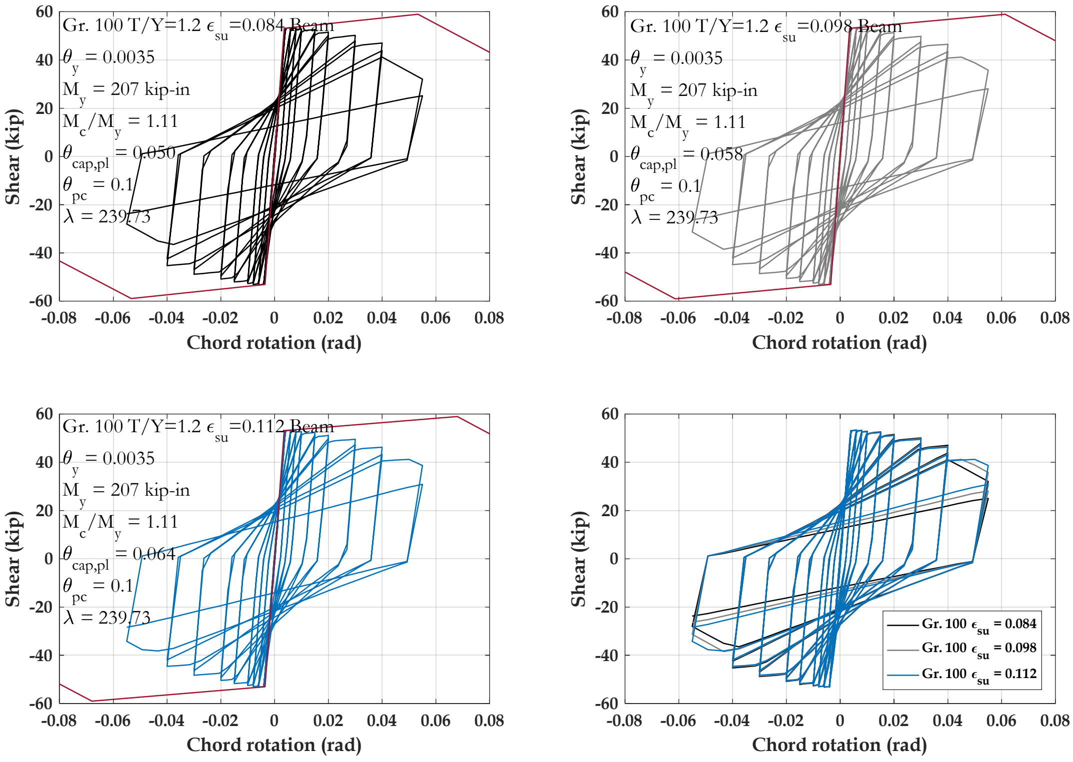

Figure 4.13. Influence of ε_{su} on cyclic behaviors (B-1, B-2, and B-3).

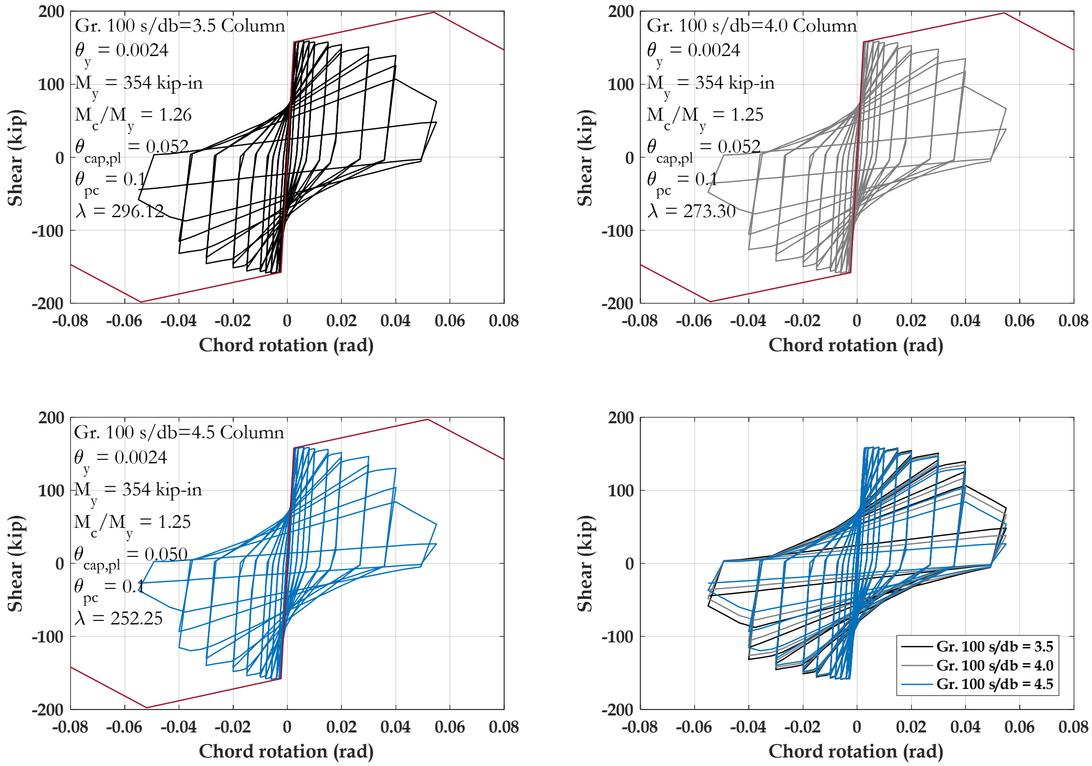

Figure 4.14. Influence of *s/d*b on cyclic behaviors (C-2, C-4, and C-5).

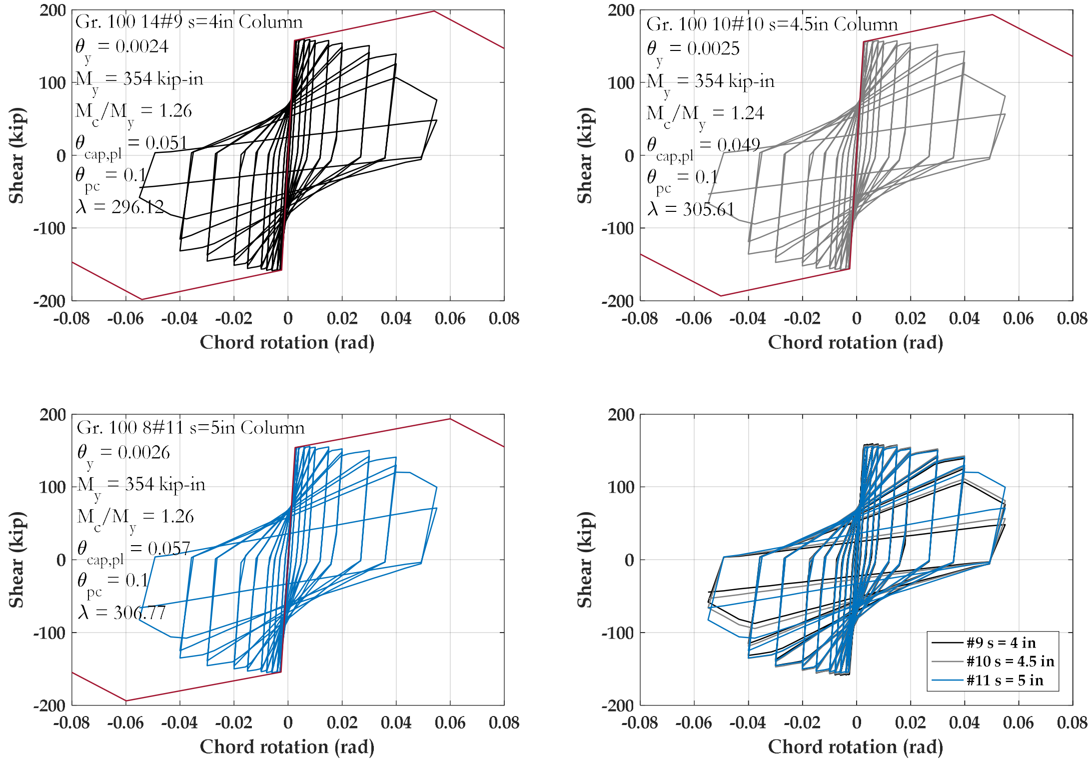

Figure 4.15. Influence of *d*b on cyclic behaviors (C-2, C-6, and C-7).

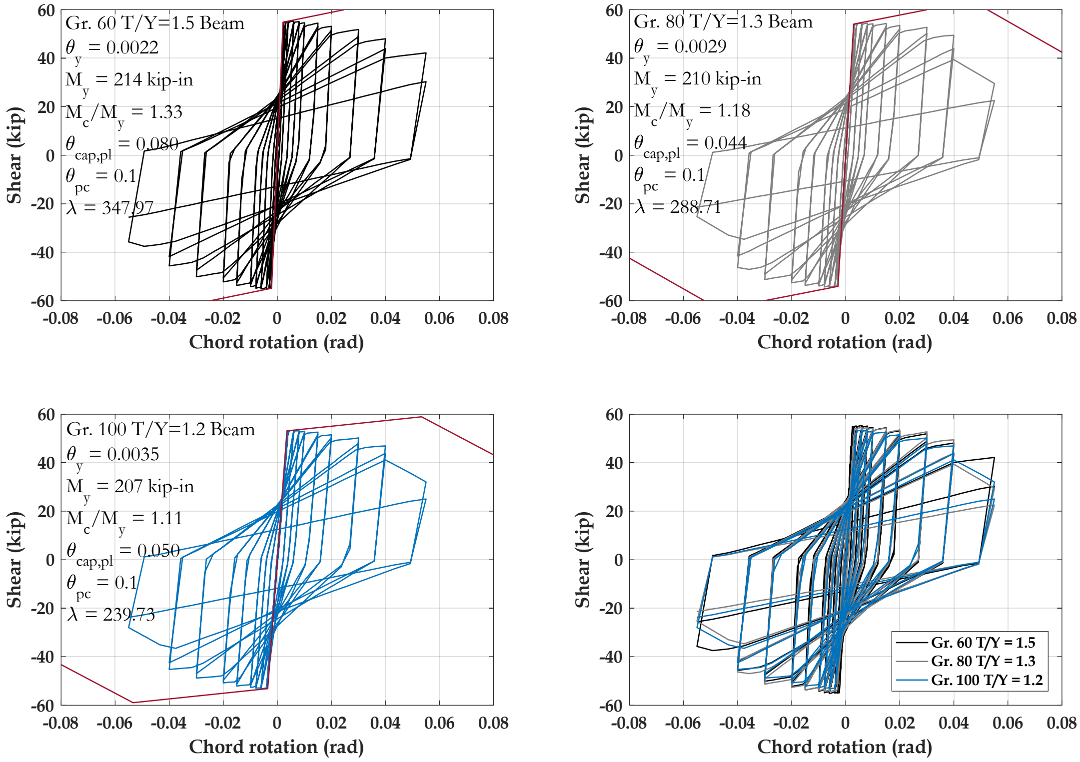

Figure 4.16. Integral influence of HS reinforcement on cyclic behaviors (B-4, B-5, and B-6).

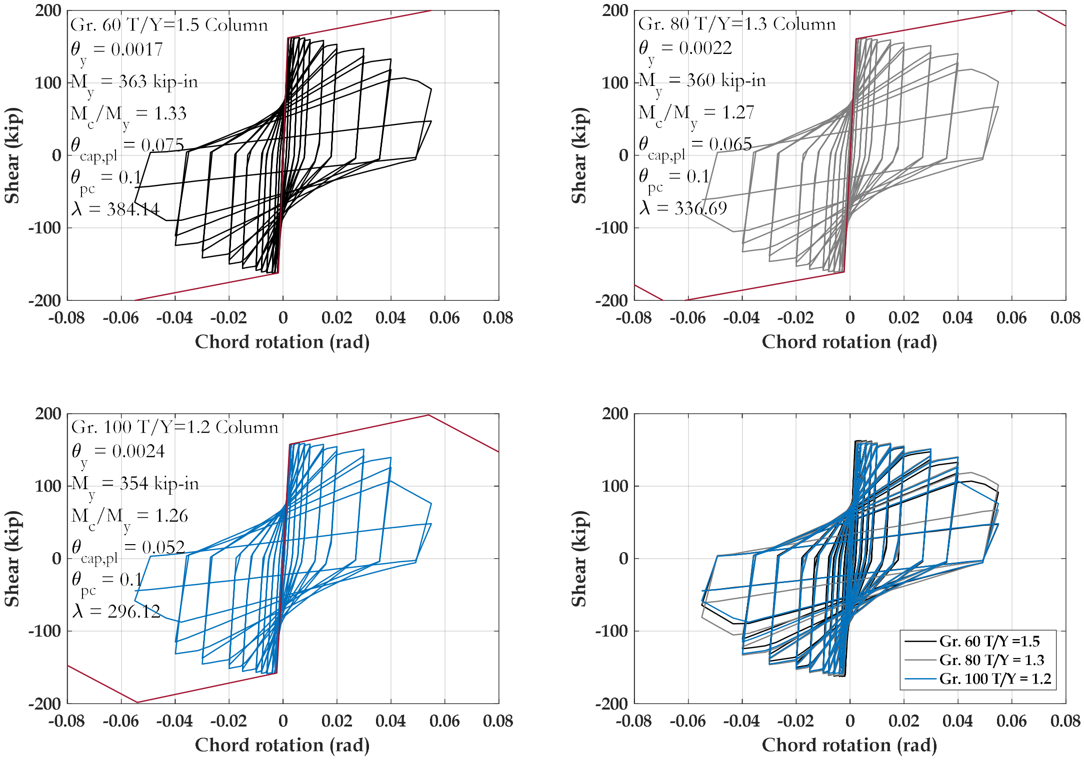

Figure 4.17. Integral influence of HS reinforcement on cyclic behaviors (C-8, C-9, and C-2).

4.2 High-Strength (HS) Reinforcement Fiber-Based Model

4.2.1 Overview and Background on Fiber-Based Model

While the plastic hinge model described in the previous section provides an efficient means to assess overall moment frame response, the hinge model does not have sufficient resolution to evaluate reinforcing bar fracture based on detailed reinforcing bar strains. As illustrated previously in Figure 2.2, member deformation demands from the moment frame system analyses are applied to fiber-based models of beam and column members to evaluate reinforcing bar strains and fracture. As shown in Figure 4.18, the fiber-based model is configured as a cantilever, with a fiber-based beam-column element and a zero-length section to capture bar-slip behavior. This section provides details of the fiber-based model for simulating the reinforcing bar strain demands in beam-columns and flexural dominant shear walls. The bar fracture damage state is then evaluated using the fracture model described in Chapter 3 of this report, and results obtained from the fiber-based models are compared to data from CPF beam (To and Moehle, 2017) and column (Slavin and Ghannoum, 2016) tests. Comparisons to CPF wall tests (Huq et al., 2017) are reported in Chapter 5 as part of the shear wall study.

The fiber-based approach used to evaluate fracture employs concepts previously introduced in research on bridge columns by Chang and Mander (1994) and Brown and Kunnath (2000). Chang and Mander introduced hysteretic and damage modeling techniques for reinforcing steel bars and concrete with the aim to simulate fatigue failures. They adopted Miner's linear accumulation model (Equation 3.7) and rain-flow counting as the basis of cumulative damage model for reinforcing bars and compared the simulated results to tests of bridge columns. Brown and Kunnath (2000) subsequently evaluated several strain-based models (i.e., Kon-Stephens model, Manson-Coffin model, and Lorenzo-Laird model) again 48 tests of bare reinforcing bars. They then examined both total-strain and plastic strain Manson-Coffin models for random loading cases and found both models can provide reasonable predictions with the assistance of the rain-flow counting method. Similar in some respects to the approach used in this study, Brown and Kunnath determined the strain demands in moment frames based on a simplified plastic-hinge model and linear-strain profile assumption, following Paulay and Priestley (1992).

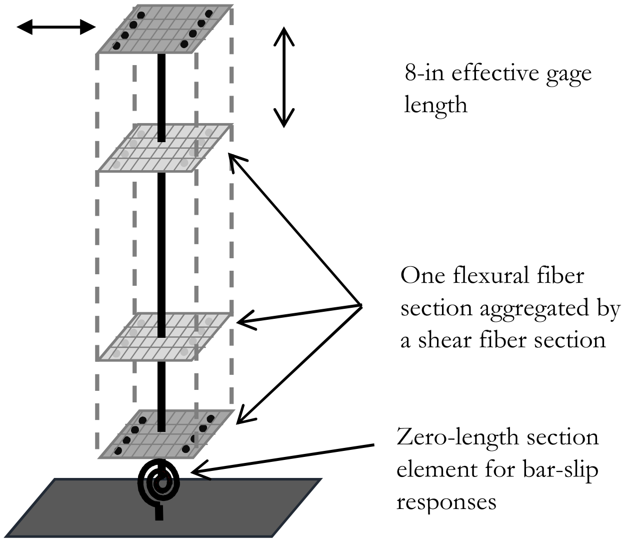

Figure 4.18. Concept plot of the fiber-based element including flexural, shear, and bar-slip responses.

4.2.1 Description of Fiber-Based Beam-Column Model

The fiber-based beam-columns were modeled and analyzed in OpenSees (Mazzoni et al., 2006). Concrete 02 (Yassin, 1994). The fiber-based element for an individual cantilever RC member u includes two sub-elements: (1) one force-based fiber element and (2) one zero-length section element at the fixed end which represents bar-slip responses. The force-based fiber element is constructed by sections located at integration points. Each integration point has one aggregated fiber-section which includes one flexural fiber-section using regularized materials and one shear fiber-section using the nonlinear shear model recommended by ATC 114 (2017). The Park-Kent concrete model (Kent and Park, 1971) was adopted in computing stress-strain relations for cover and core concrete fibers. The OpenSees ReinforcingSteel material (Mohle and Kunnath, 2009) was used to model the reinforcing bar fibers. Since reinforcing bar buckling and fracture are not explicitly simulated in fiber-based model that is used to determine the bar strain history, only basic monotonic and cyclic steel properties are considered in the model. The zero-length section element (Fig 4.19) adopted for bar-slip responses was first proposed for beam-column elements by Zhao and Sritharan (2007) but was also validated for T-shaped walls by Waugh (2009).

To help avoid strain localization and mesh dependency, the concrete fiber model parameters used in this study employs (1) an approach described by Coleman and Spacone (2001) to regularize the concrete post-peak tensile stress-strain response model using the concrete fracture energy (G_f) in combination with a mesh-dependent characteristic length, and (2) recommendations by Pugh, Lowes and Lehman (2015) to use $2f_c'$ N/mm for the unconfined concrete crushing energy (G_{fc}) and 1.7 times G_{fc} as the crushing energy for confined concrete (G_{fcc}).

The fiber model uses the Gauss-Lobatto integration method, where the integration points are closer towards the end of the member, including points at the member ends. Each integration point has an associated location and weighting factor, such that the effective gage length for each point is computed as the product of its normalized weight ($w_i/\Sigma(w_i)$) and the total element length. For consistency between the computed bar strain demands and the fracture model, the Gauss-Lobatto integration points are elected such that the effective gage length for the end integration point is about the same as that used to define the bar fatigue-fracture model. As described in Chapter 3, the gage length is fixed at 8-in in monotonic bar tests and varies from $4d_b$ to $6d_b$ in cyclic bar tests. To the extent that strain localization is not severe before fatigue-fracture occurs in the cyclic bar tests, the number of Gauss-Lobatto integration points are chosen such that the end integration point has an approximate effective gage length of 8 inches. Once the effective integration point length (L_{IP}) is determined, the regularized concrete strain at the 20% residual compressive strength is estimated by Equation 4.18.

$$\varepsilon_{20u} = \frac{G_{fc}}{0.6 f_c' L_{IP}} - 0.8\frac{f_c'}{E_0} \tag{4.18}$$

where E_0 is the elastic modulus in compression of concrete and other terms were defined previously.

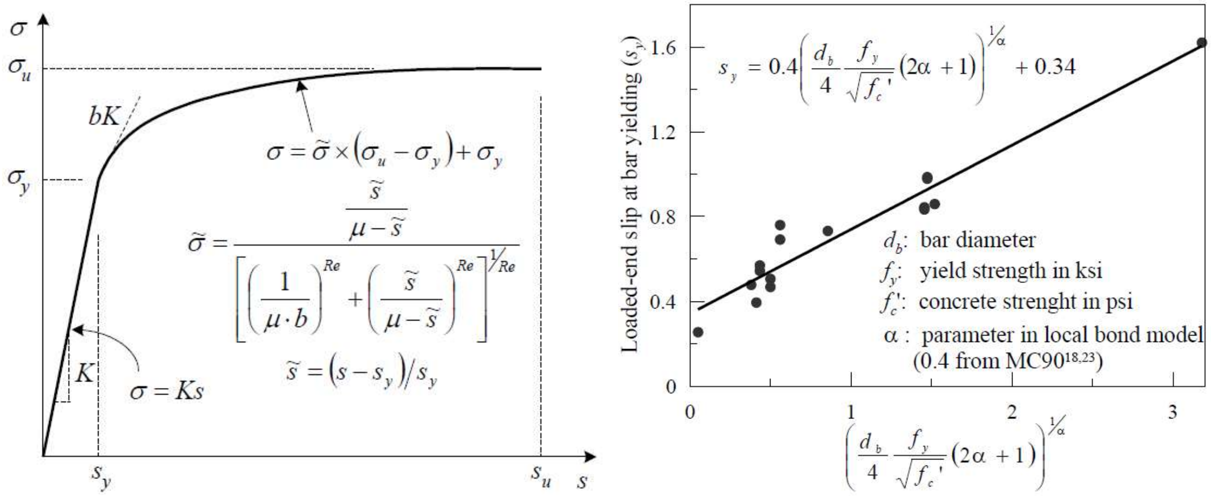

Figure 4.19. Bar-slip strain-penetration model (after Zhao and Sritharan, 2007, units in metric).

Three features were identified to evaluate the fitness of the simulation to experiment: (1) initial stiffness, (2) ultimate strength, and (3) unloading and pinching effects. No additional adjustments for flexural and shear fiber model were made during calibrations. In the bar-slip element, the hardening coefficient b was taken as 2·(*T*/*Y*-1); the yield slip S_y was computed by Equation 4.19; and the ultimate slip S_u was adjusted within the range of 30~50 S_y per Zhao and Sritharan's suggestion to best fit the test results.

$$S_y(in) = 0.1 \cdot \left[\frac{d_b(in)}{4000} \cdot \frac{f_y(psi)}{\sqrt{f_c'(psi)}} \cdot (2\alpha + 1)\right]^{1/\alpha} + 0.013(in) \tag{4.19}$$

where d_b is the bar diameter, f_y is the yield strength; and f_c' is the concrete compressive strength. Figures 4.20 and 4.21 present the comparisons between tested and simulated response of the four CPF beams and four CPF columns, respectively. Overall, the fiber-based model simulations show good agreement with test results, including agreement between the initial, unloading and reloading stiffness and the pinching effects. Since the fiber-based elements do not explicitly model the strength deterioration associated with reinforcing bar buckling or fracture, the member-level strength degradation in the simulations was only from concrete softening and crushing.

Figures 4.22 and 4.23 summarize the isolated cyclic drifts of flexural, bar-slip, and shear behaviors. As expected, member shear effects contributed less than about 10% to the total lateral deformation. Flexure contributed about 50%~60% to the total drift, and bar slip contributed the remainder. The bar-slip for high strength reinforcement was larger than for conventional Gr. 60 steel under similar drift levels, which might be beneficial to ease the strain concentration and tendency for bar fracture. Simulated steel strains are plotted against total lateral drifts in Figures 4.24 and 4.25 for the beam and column tests, respectively.

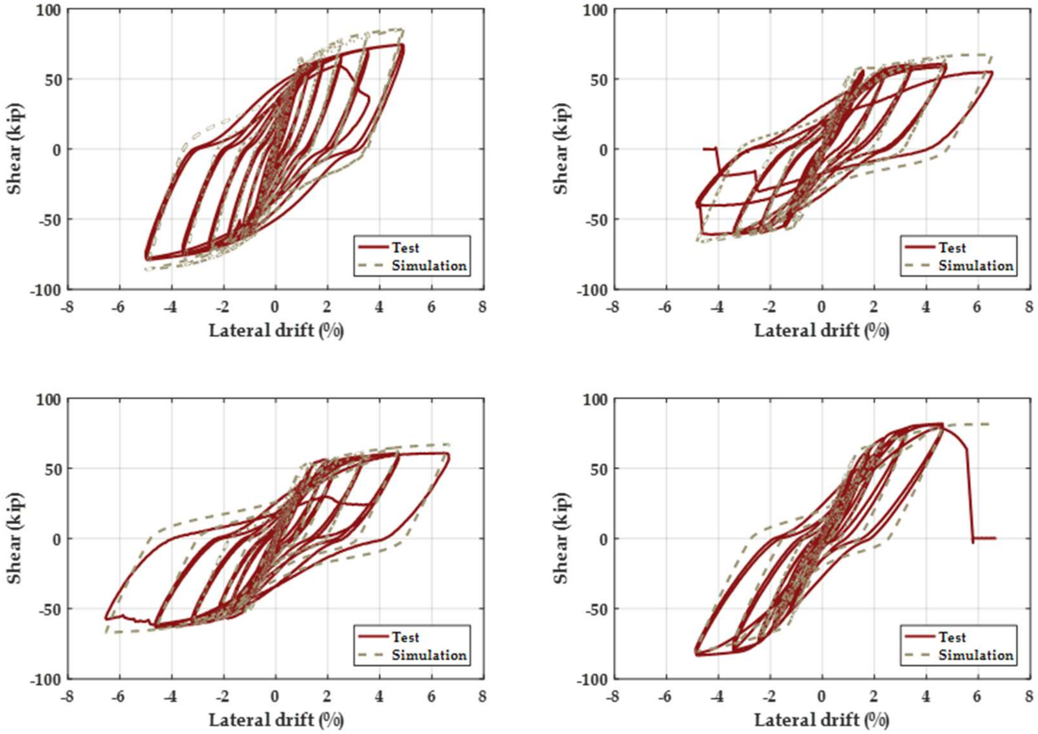

Figure 4.20. CPF beam hysteresis calibrations for the fiber-based approach (top-left: Gr. 60 *T/Y* = 1.46, top-right: Gr. 100 *T/Y* = 1.30, bottom-left: Gr. 100 *T/Y* = 1.18, bottom-right: MMFX Gr. 100 *T/Y* = 1.27).

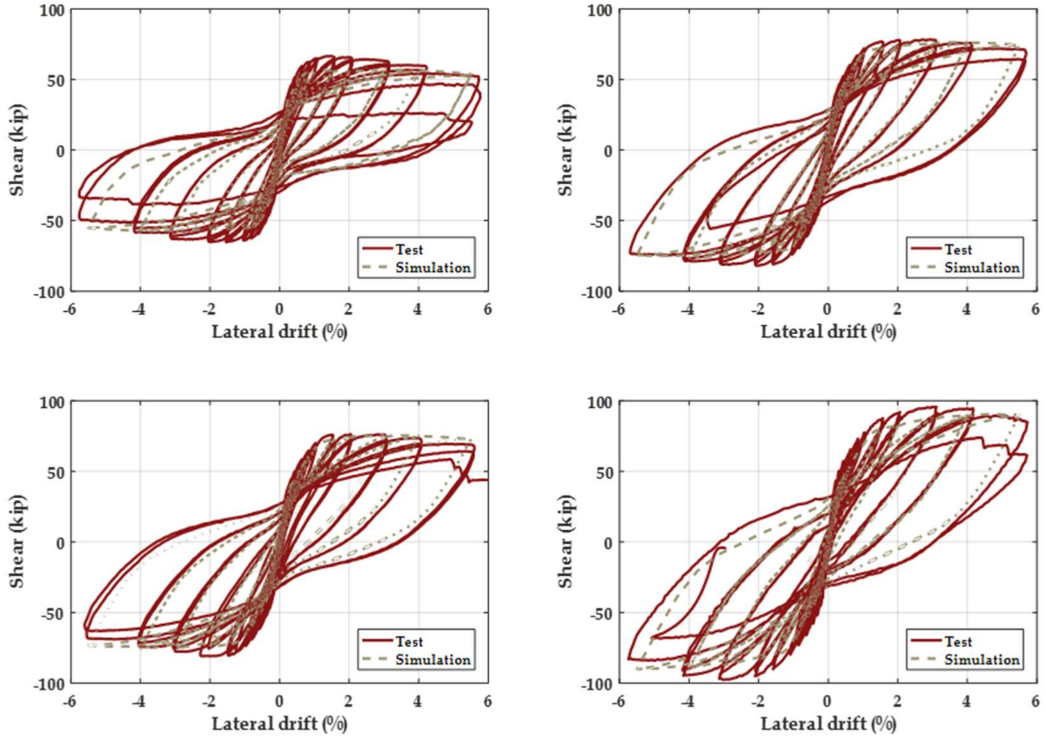

Figure 4.21. CPF column hysteresis calibrations for the fiber-based approach (top-left: Gr. 60 *T/Y* = 1.45, top-right: Gr. 100 *T/Y* = 1.27, bottom-left: Gr. 100 *T/Y* = 1.16, bottom-right: MMFX Gr. 100 *T/Y* = 1.27).

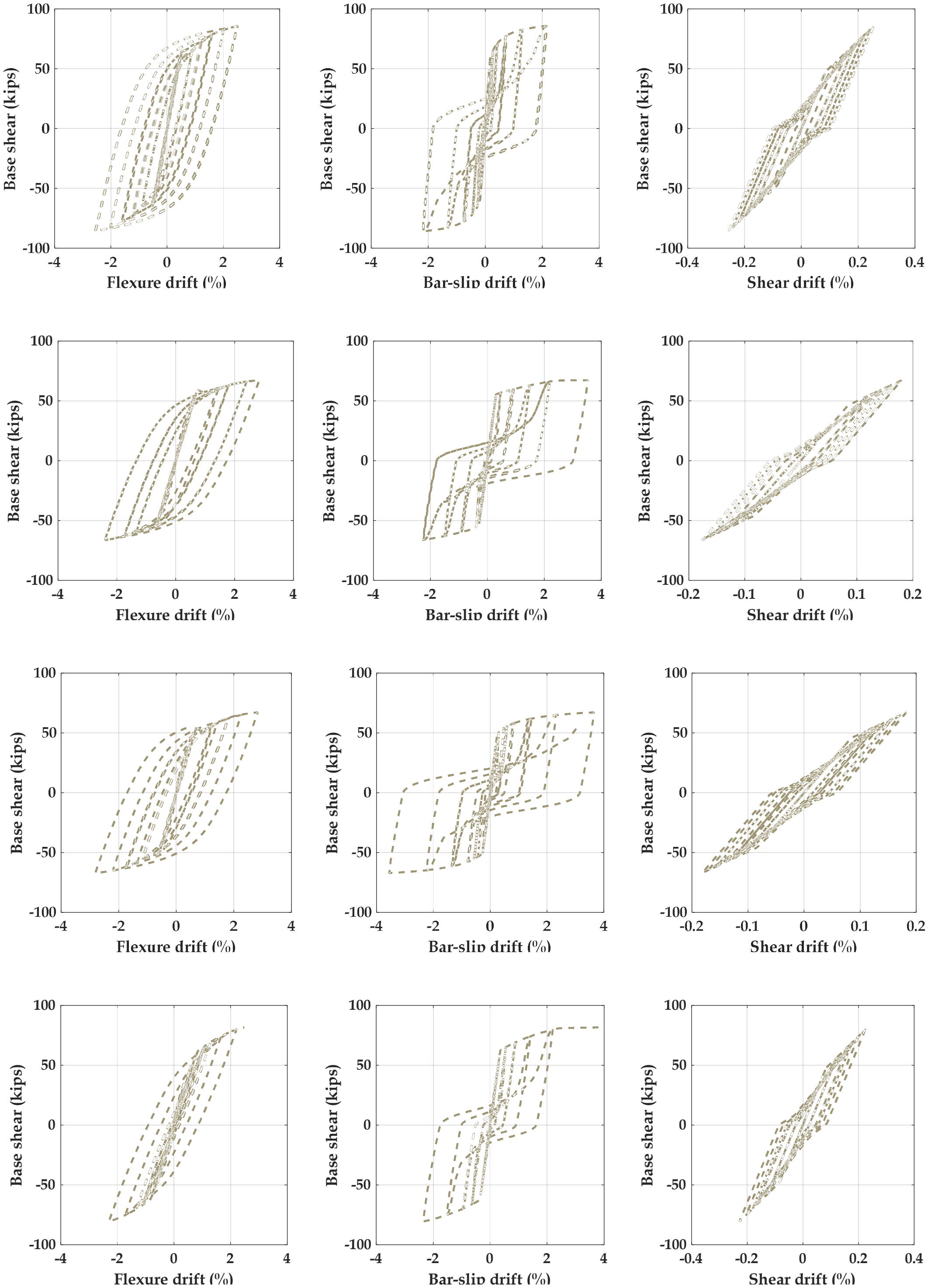

Figure 4.22. Simulated cyclic behaviors of three components in CPF beam specimens (from top to bottom: Gr. 60 *T/Y* = 1.45, Gr. 100 *T/Y* = 1.30, Gr. 100 *T/Y* = 1.18, MMFX Gr. 100 *T/Y* = 1.27).

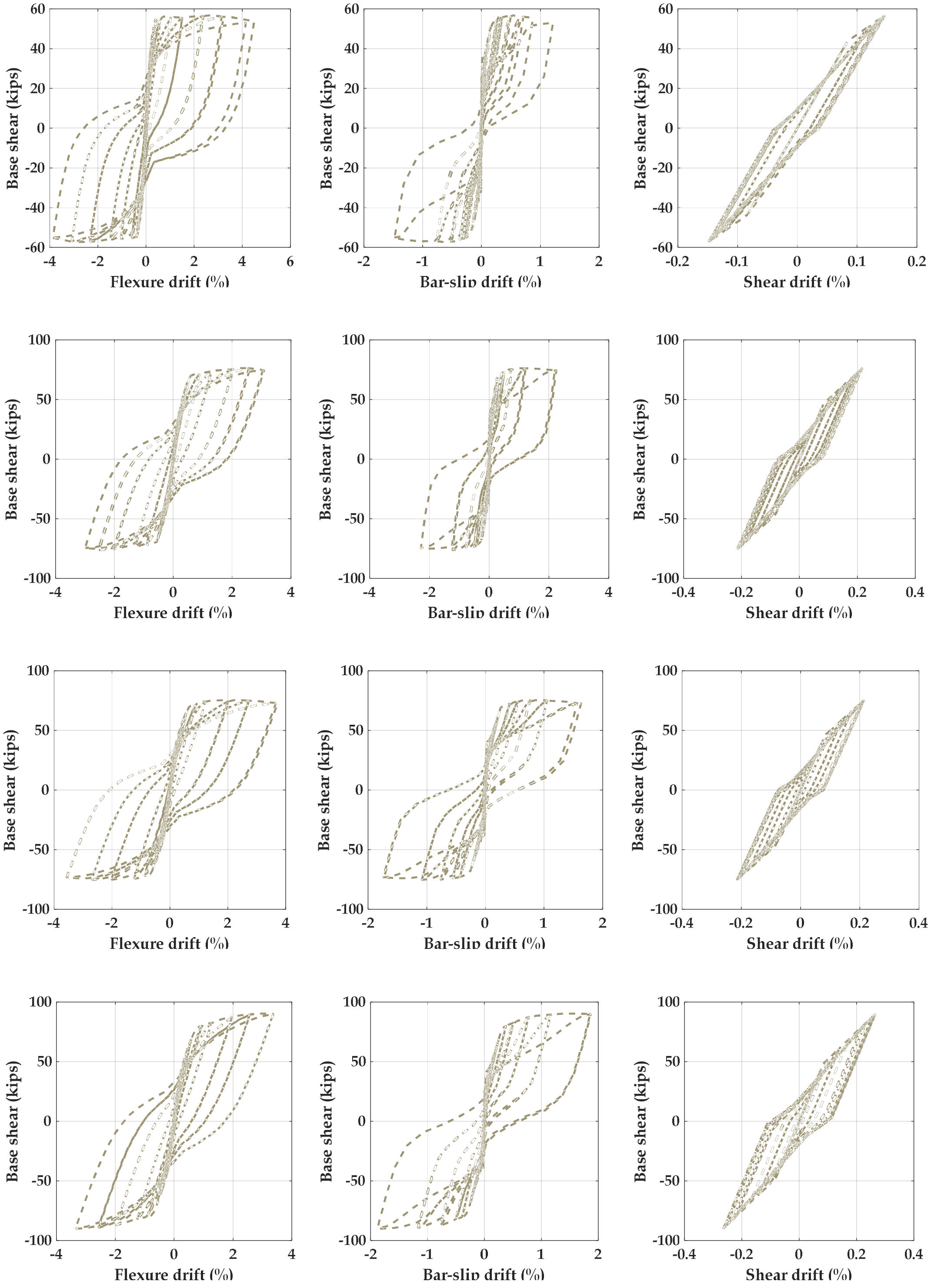

Figure 4.23. Simulated cyclic behaviors of three components in CPF column specimens (from top to bottom: Gr. 60 *T/Y* = 1.45, Gr. 100 *T/Y* = 1.27, Gr. 100 *T/Y* = 1.16, MMFX Gr. 100 *T/Y* = 1.27).

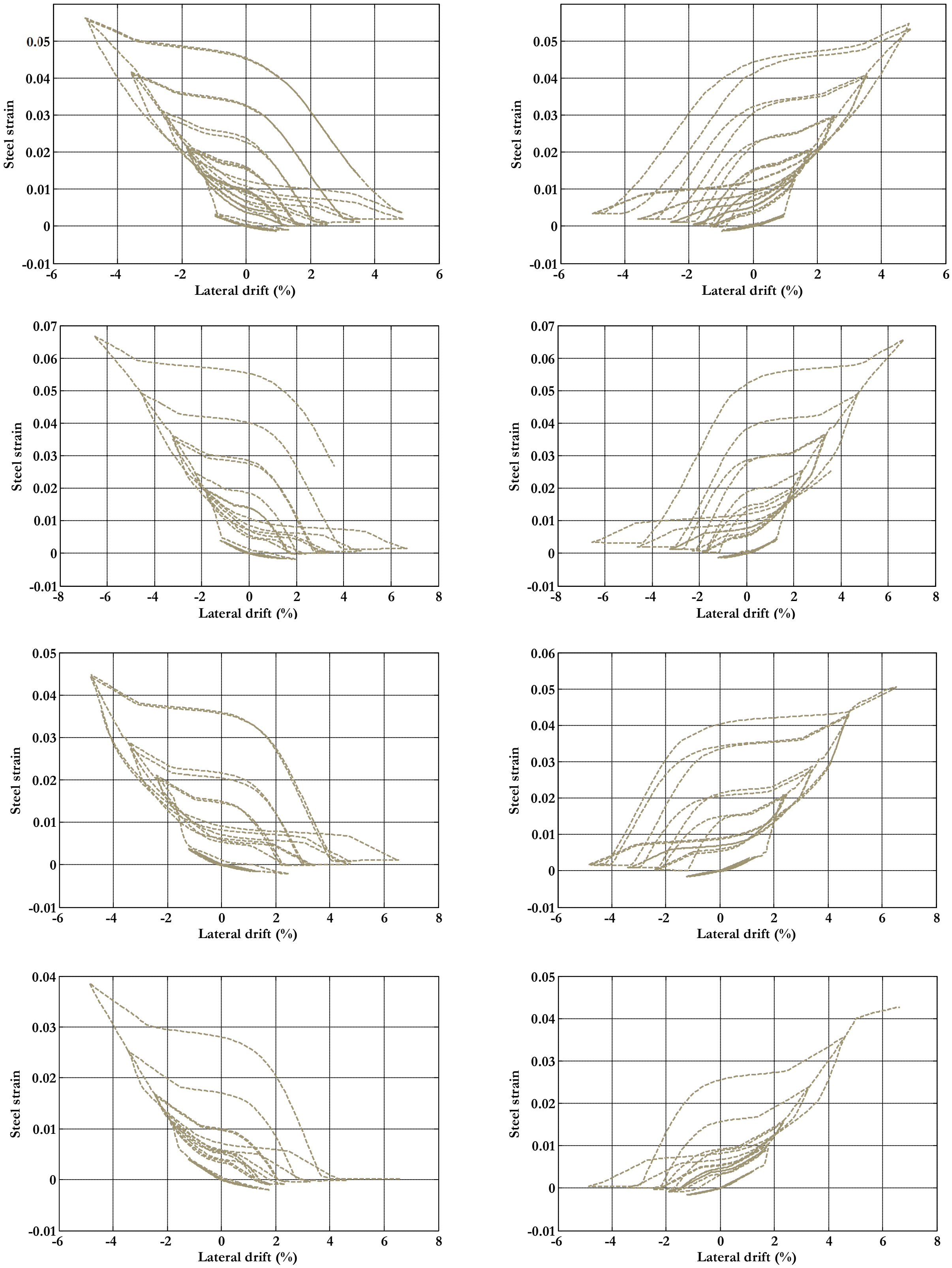

Figure 4.24. Simulated cyclic steel strain-total drift relation in CPF beam specimens (from top to bottom: Gr. 60 *T/Y* = 1.45, Gr. 100 *T/Y* = 1.30, Gr. 100 *T/Y* = 1.18, MMFX Gr. 100 *T/Y* = 1.27).

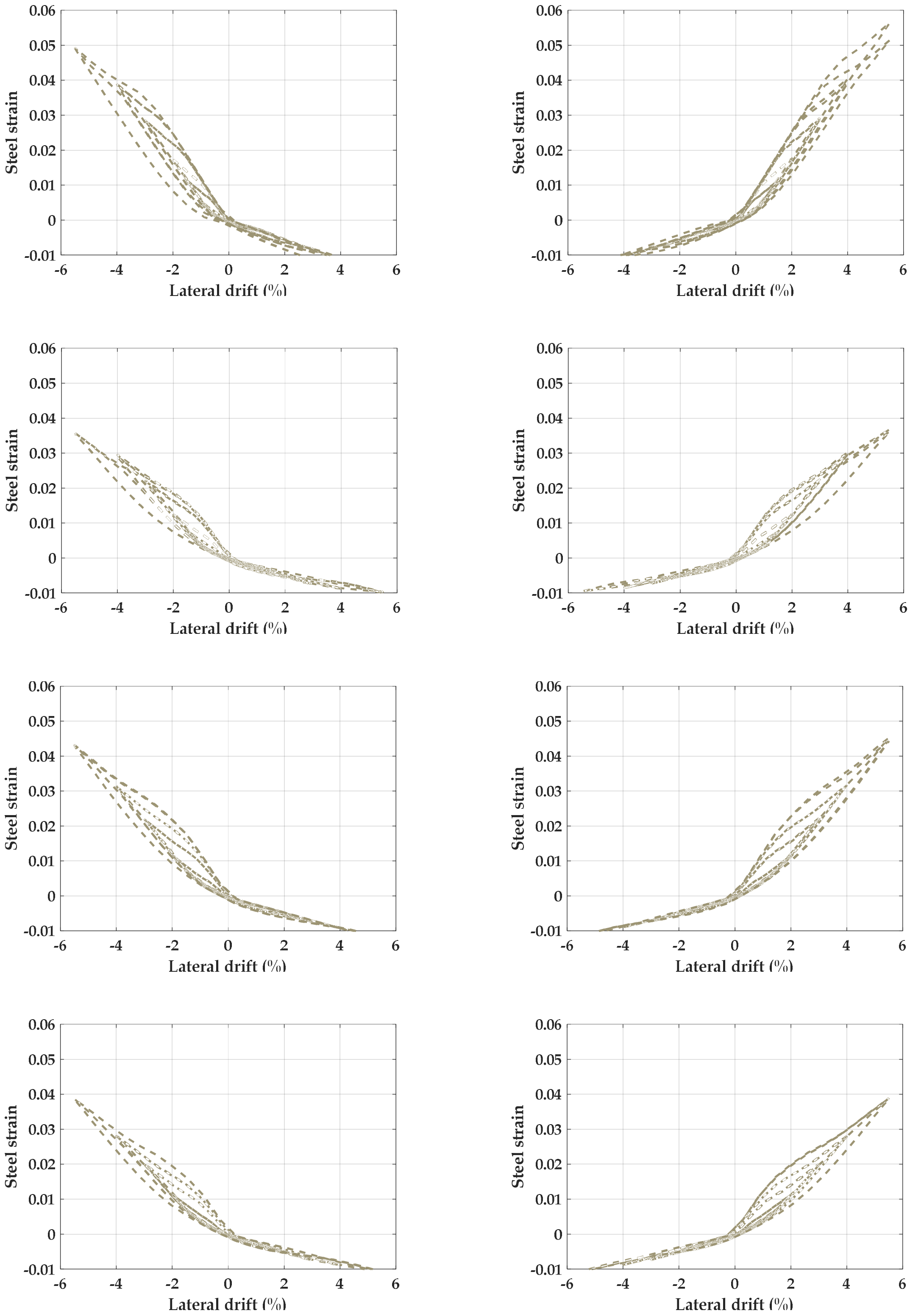

Figure 4.25. Simulated cyclic steel strain-total drift relation in CPF column specimens (from top to bottom: Gr. 60 *T/Y* = 1.45, Gr. 100 *T/Y* = 1.27, Gr. 100 *T/Y* = 1.16, MMFX Gr. 100 *T/Y* = 1.27).

4.3 Application of Fracture Index in Fiber Beam-Column Member Analysis

4.3.1 Validation of Fracture Index Using Simulated Strains from Member-Level Analysis

Strain demands from the fiber-based element analyses are used as input to the fracture-fatigue model of Chapter 3 to estimate probability of bar fracture. As noted previously, the strains recorded in the simulations are the average strain demands over the integration interval whose effective gage length is set to about 8-in, which is consistent with the gage length from the bare bar tests.

Figure 4.26 shows the recorded strain histories at the end IP in the CPF beam (Gr. 60, *T/Y* = 1.45), along with the resulting fracture index histories and estimated fracture probabilities. The top three figures are results for reinforcing bars at the top of the member cross-section, while the bottom three figures are results for the bottom bars. The beige dots in left two plots are recorded strain data at each loading step. The red dots correspond to the reduced data of peak deformations that are used as input to the fatigue-fracture model. Using Equation 3.2 to calculate the material-dependent fracture coefficients and substituting the peak strain history strain into Equation 3.3, the fracture index history is calculated and shown in the middle two plots of Figure 4.26. Mapping the *FI* history through the fracture fragility model (Figure 3.12), the probability of fracture is shown in right two plots. Note that the maximum computed *FI* in this test is about 0.6 corresponding to about 12% probability of fracture. This relatively very low fracture probability is consistent with the fact that no fracture was observed in the test specimen.

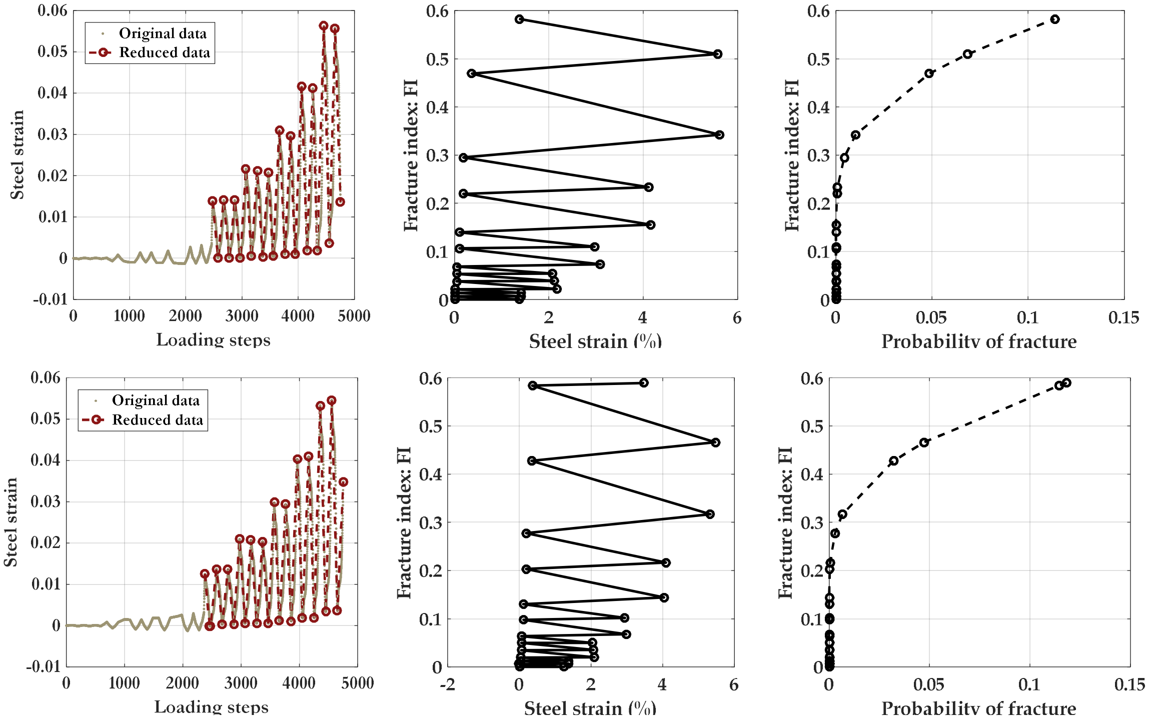

Figure 4.26. Cyclic steel strain and fracture index history of CPF beam Gr. 60 *T/Y* = 1.45 (top and bottom steel).

The simulated strain histories, fracture index histories, and fracture probabilities of the other seven CPF beam and column tests are plotted in Figures 4.27 to 4.33. The observed fractures are indicated by the solid-red dots for comparison. In general, these data confirm that the model predications are fairly accurate, where the calculated fracture index at the observed fracture points range from *FI* equal to 1.0 to 1.5 (with corresponding fracture probability estimates of 50% to 80%) during the tensile loading cycles.

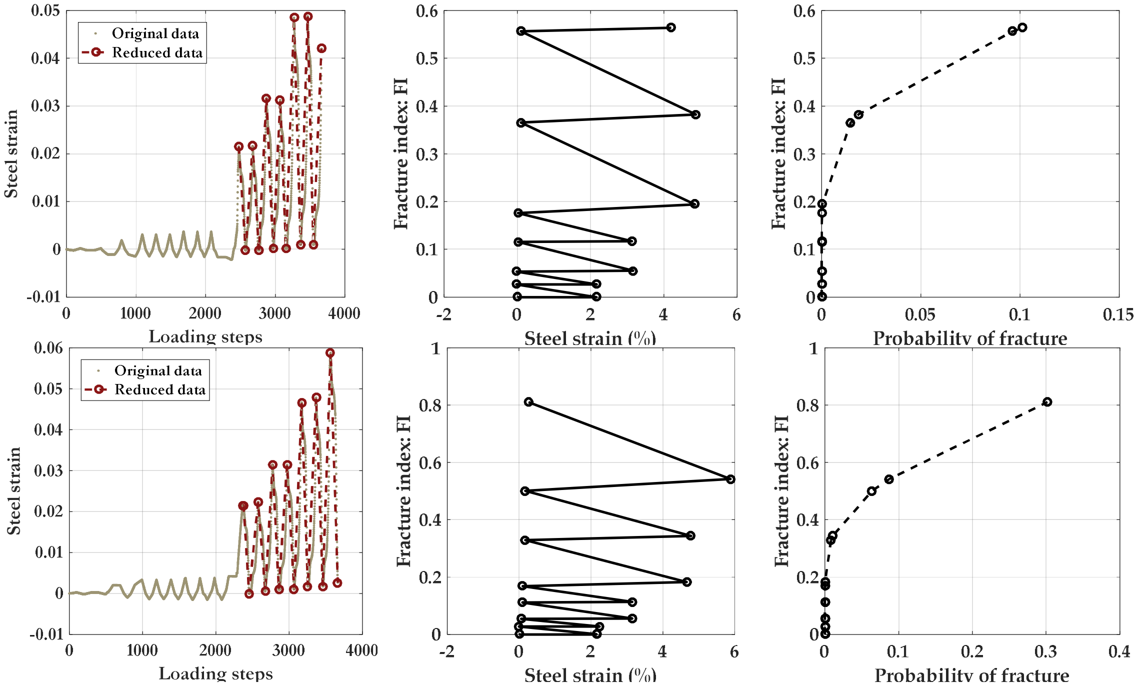

Figure 4.27. Cyclic steel strain and fracture index history of CPF beam Gr. 100 *T/Y* = 1.30 (top and bottom steel).

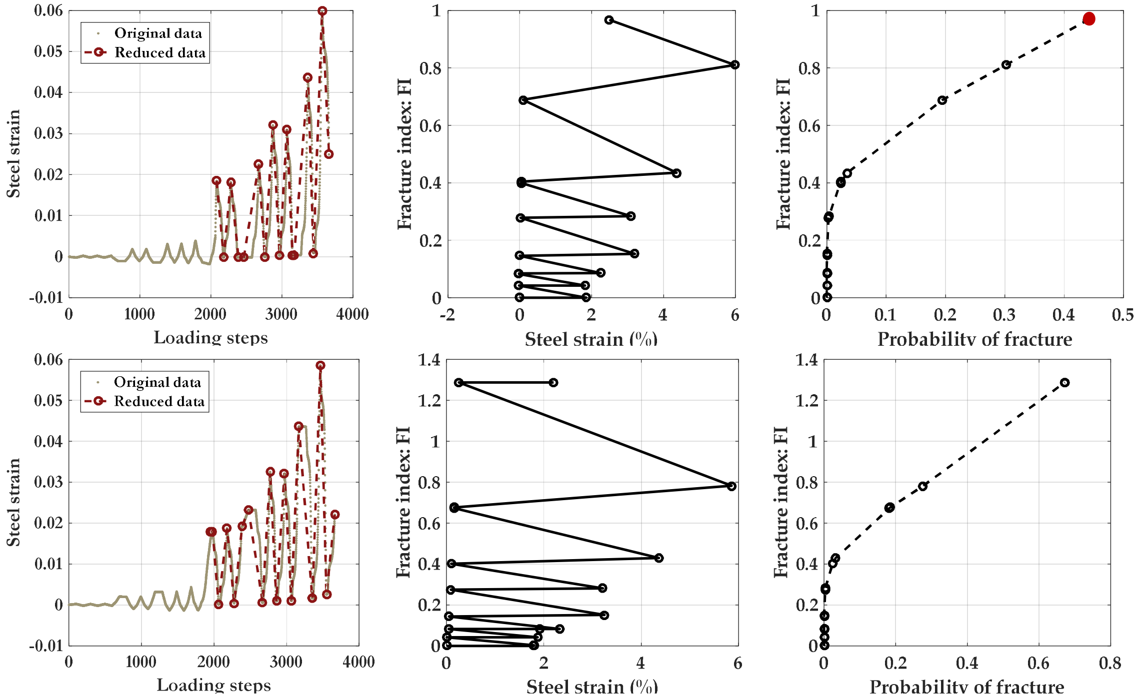

Figure 4.28. Cyclic steel strain and fracture index history of CPF beam Gr. 100 *T/Y* = 1.18 (top and bottom steel).

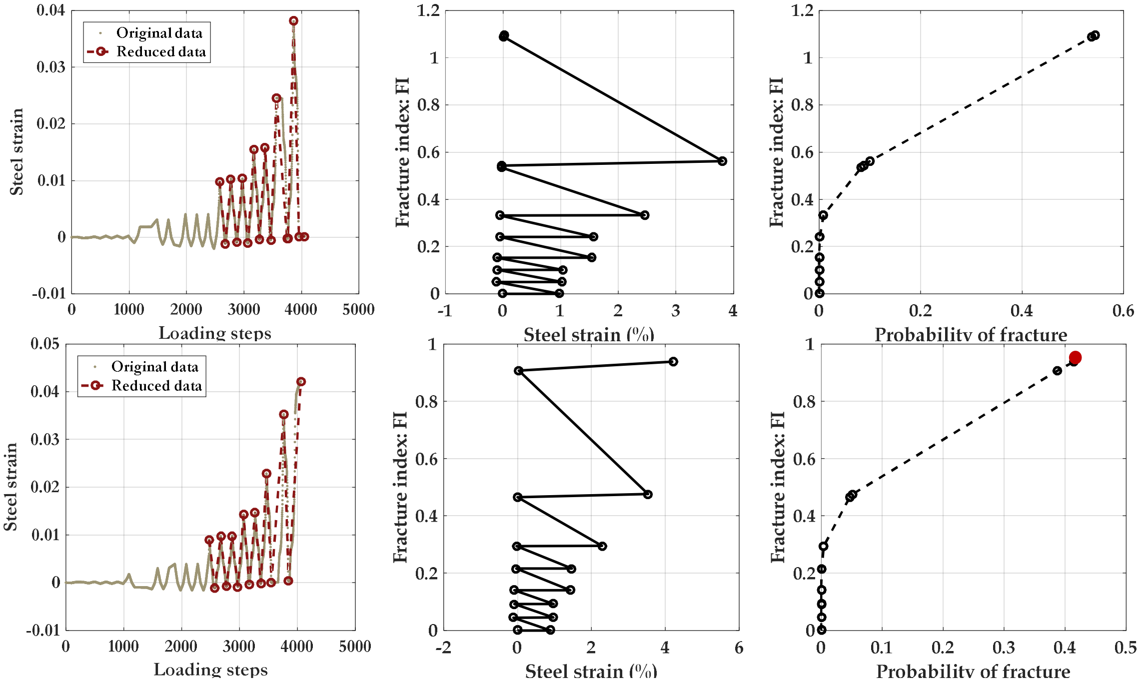

Figure 4.29. Cyclic steel strain and fracture index history of CPF beam MMFX Gr. 100 (top and bottom steel).

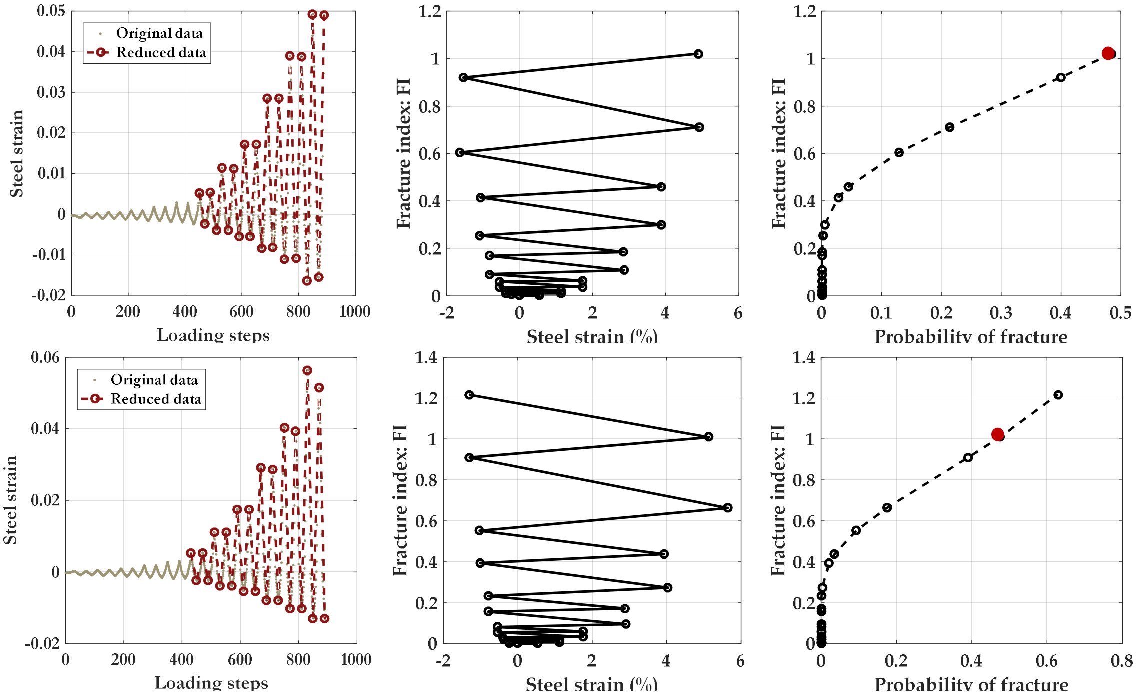

Figure 4.30. Cyclic steel strain and fracture index history of CPF column Gr. 60 *T/Y* = 1.45 (top and bottom steel).

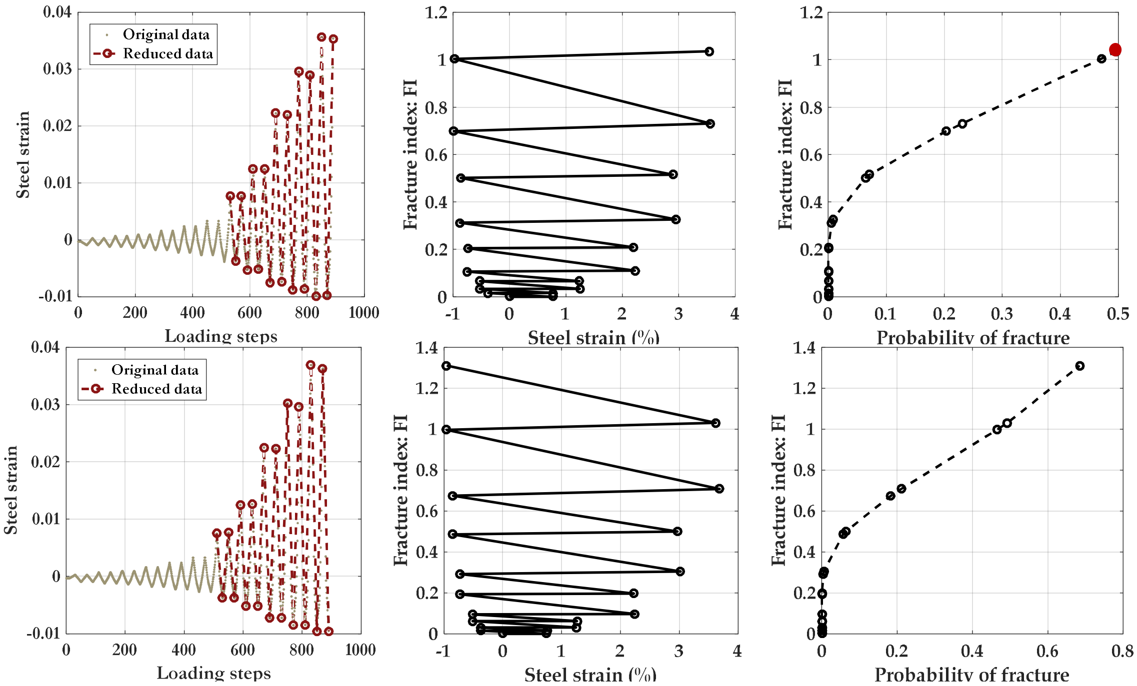

Figure 4.31. Cyclic steel strain and fracture index history of CPF column Gr. 100 *T/Y* = 1.27 (top and bottom steel).

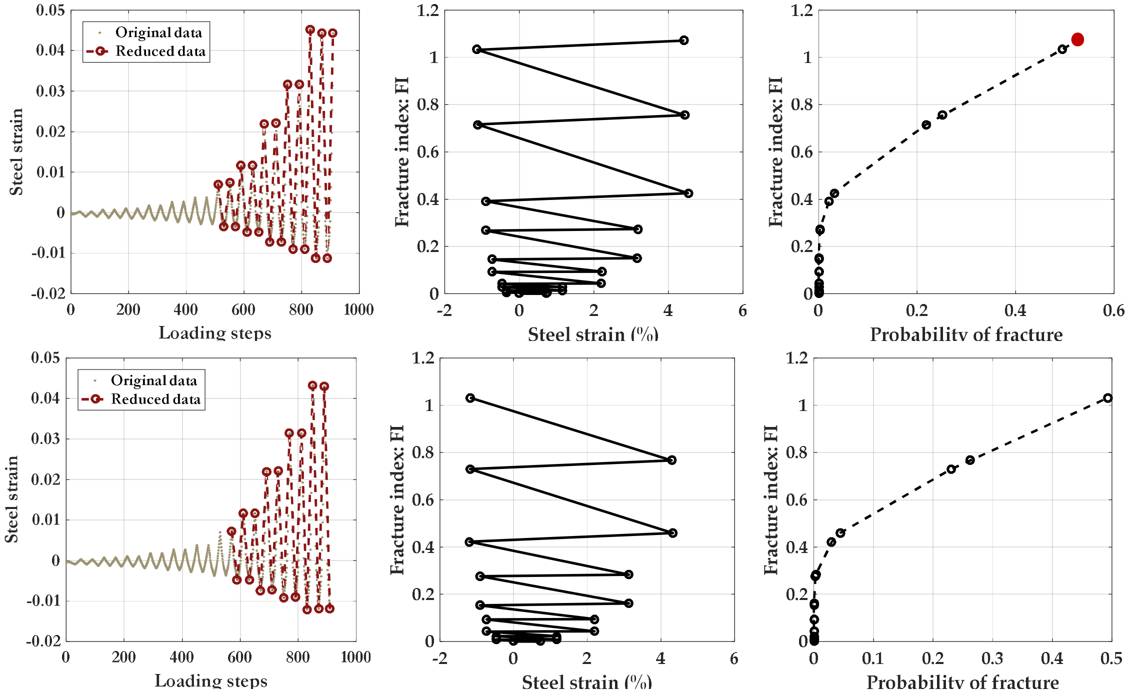

Figure 4.32. Cyclic steel strain and fracture index history of CPF column Gr. 100 *T/Y* = 1.16 (top and bottom steel).

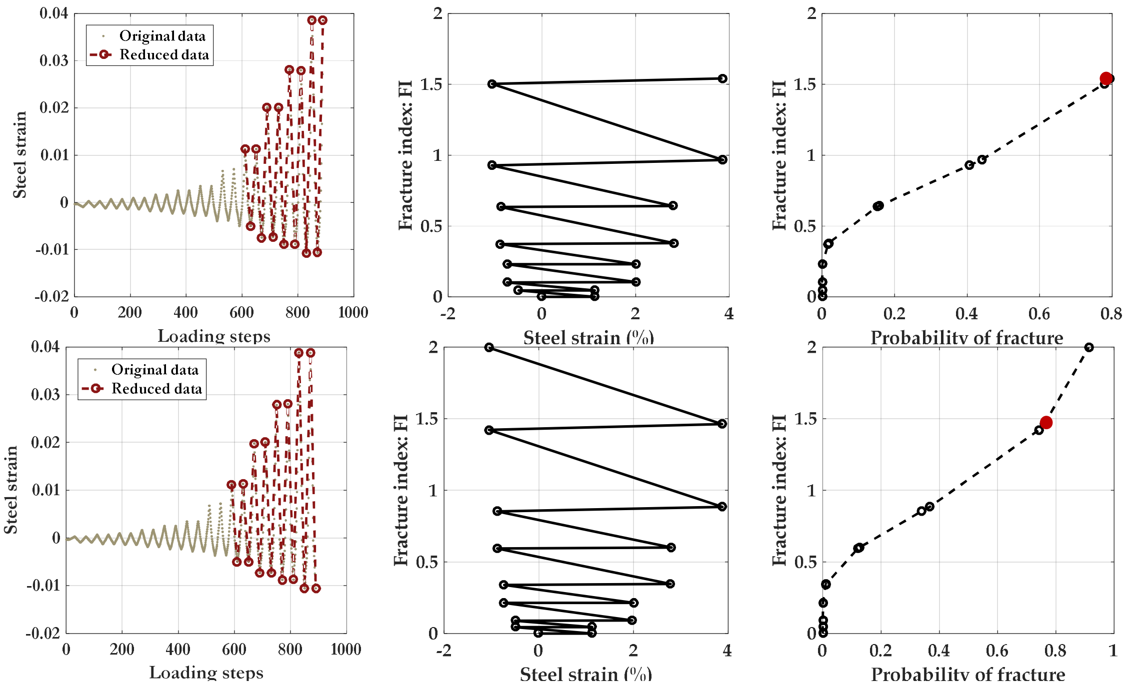

Figure 4.33. Cyclic steel strain and fracture index history of CPF column MMFX Gr. 100 (top and bottom steel).

4.3.2 Transition from Regular Loading Protocol to Random Loading History: Rules and Example

The last two sections compare the simulated and measured member response and fracture observations for the CPF beam and column tests under cyclic loading. In this section the fatigue-fracture evaluation is extended to consider random loading associated with structural members in building systems subjected to earthquake ground motions. The evaluation method follows an approach previously used by Brown and Kunnath (2000) to evaluate reinforcing bar fracture in concrete bridge piers. They then examined total strain and plastic strain variations of the Manson-Coffin model, where the rain-flow counting method is used to relate strain demands from random loads to the fracture index.

The rain-flow algorithm was first demonstrated by Downing and Socie (1982) to count half cycles in wide-band signals. The so-called wide-band signals are data streams having multiple local peaks and valleys before switching signs. This method has been widely used in cumulative damage predictions for mechanical and civil engineering applications. The counting rules used in this study are concluded as follows (Figure 4.34):

Step 1 – All local peaks and valleys are collected from original data stream to form the reduced data stream.

Step 2 – Rotate the data stream by 90 degrees to let the strain history start from top and end at bottom.

Step 3 – Starting rule: A rain flow is started at each peak and trough.

Step 4 – Marching rule: a rain flow proceeds down, detaching from zig-zag cyclic strain plot at each peak.

Step 5 – Ending rule: each rain flow excursion stops when (1) it detaches at a peak point which is the maximum in that wide-band half cycle (e.g., Path 1-8), (2) the peak which is more positive than the one the current flow started from (e.g., Path 2-3); and (3) the location intercepted by an earlier path (e.g., Path 5-5a).

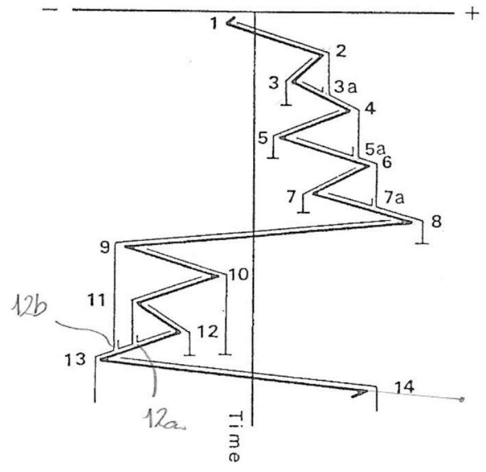

Figure 4.34. An example for rain-flow counting algorithm (after John Wægter, 2009)

To illustrate the proposed fatigue-fracture evaluation for random loading, the loading history from one external column in the 20-story RC moment frame building is considered. More details about the structural modeling and hazard-consistent incremental dynamic analysis (HC-IDA) of the frame are included later in Chapter 6, and only the reinforcing bar strain data and related post-processing results are plotted and discussed here.

The left two plots in Figure 4.35 are the total strain histories experienced by the top and bottom reinforcing bars during the seismic excitation of the 20-story frame, where black dots are the original data at each time step and red dots are so-called "reduced data" only counting local peaks and valleys. The red curves in two right plots are the plastic strain histories, and the individual beige bars represent the value of plastic strain range starting from that peak/valley according to the rain-flow counting algorithm. The horizontal axes in the plots on the right are half-cycle number, which corresponds to the number of strain-cycle reversals. Note that while the steel strain maintains a relatively high amplitude level during the last 100 time-steps (~140 to 240), the plastic range amplitude is relatively small per rain-flow counting. This is because only small oscillations occurred around the peak strain level during these steps. In contrast, the large (damaging) effective strain-pulse was identified to start from much earlier peaks (i.e., from the 11th peak/valley in bottom steel and the 7th peak/valley in the top steel).

Figure 4.36 shows similar calculations for a long-duration motion, recorded during 2011 Tohoku earthquake. It is obvious that significantly more half cycles were seen in strain histories under the long-duration motion compared with the moderate-duration case. Furthermore, instead of a main pulse followed by 3~5 secondary cycles, there are more strain-pulses which are considerable and distributed through the entire loading history.

Figure 4.37 shows the lateral displacement history of the column from which the strain histories in Figure 4.36 (under the Tohoku ground motion). Comparing the plots in Figure4.36 and 4.37, although there are some similar features in the column-drift and steel-strain histories, the steel strain peaks are not always synchronized with the drift peaks, and the top and bottom reinforcing bars have very different strain demands. The differences are due to the fact that the damage-accumulation rate of the entire member includes both concrete deterioration, steel degradation, and other factors (debonding/shear damage), which do not accrue at the same pace as the accumulative steel strain history. Moreover, where residual drifts occur, distinct differences arise between the bars on each side of the column.

Shown in Figures 4.38 and 4.39 are the fracture index histories and estimated fracture probabilities, obtained by substituting the plastic strain range from Figures 4.35 and 4.36 into the fatigue-fracture model. The fracture probability histories indicate that the damage tends to propagate relatively slowly early in the earthquake loading and accelerates after the first significant strain excursion and during the following cycles. Note that in this example from the 20-story frame, the cumulative strain demands, fracture indices and probabilities of fracture are very low. As described later in Chapter 7, this is not always the case, where for example the strain and fracture demands are much larger in the 40-story frame example.

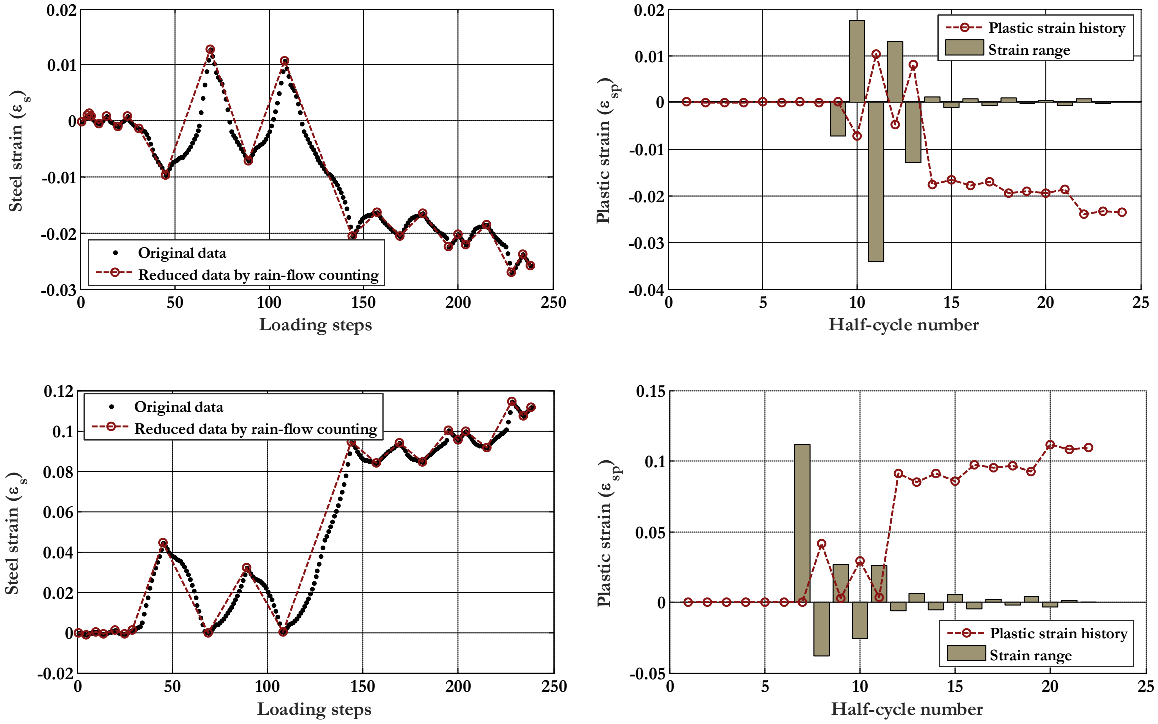

Figure 4.35. An example for rain-flow counting in random loading cases. The strain history was recorded in the bottom and top steel in one external column at 4th story of one RC 20-story frame under Elcentro140.th with a scaled *Sa* (T_1) of 0.87 g.

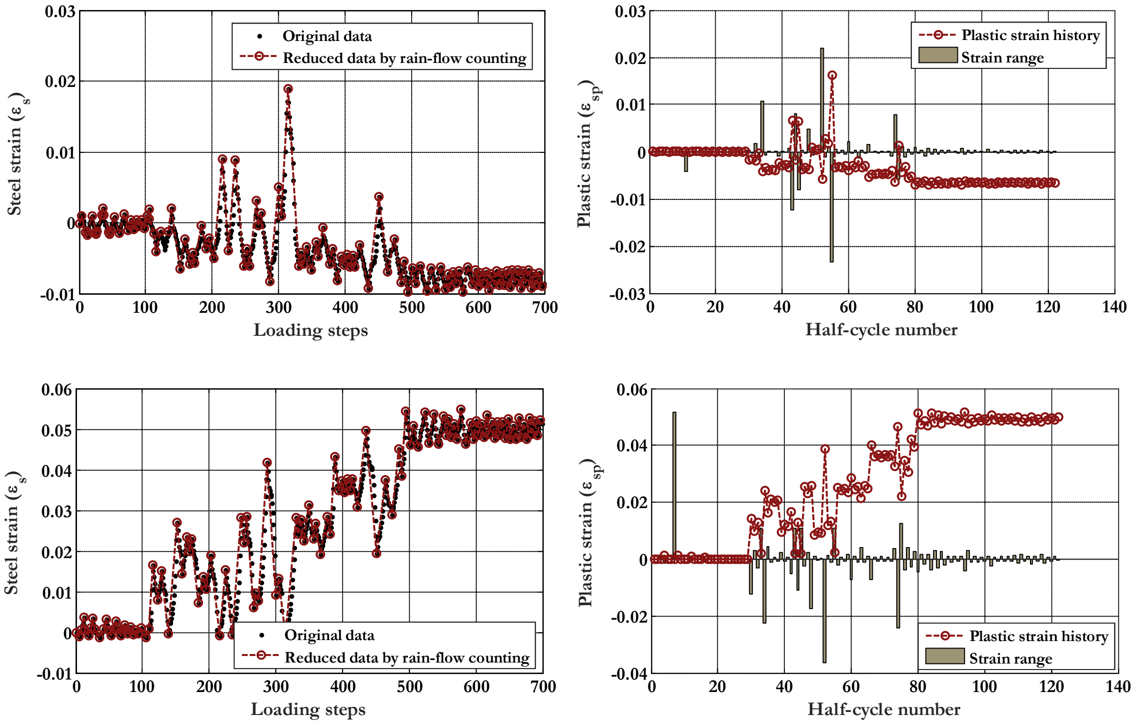

Figure 4.36. An example for rain-flow counting in random loading cases. The strain history was recorded in the bottom and top steel in one external column at 4th story of one RC 20-story frame under Tohoku_FKSH_H2.th with a scaled *Sa* (T_1) of 0.61 g.

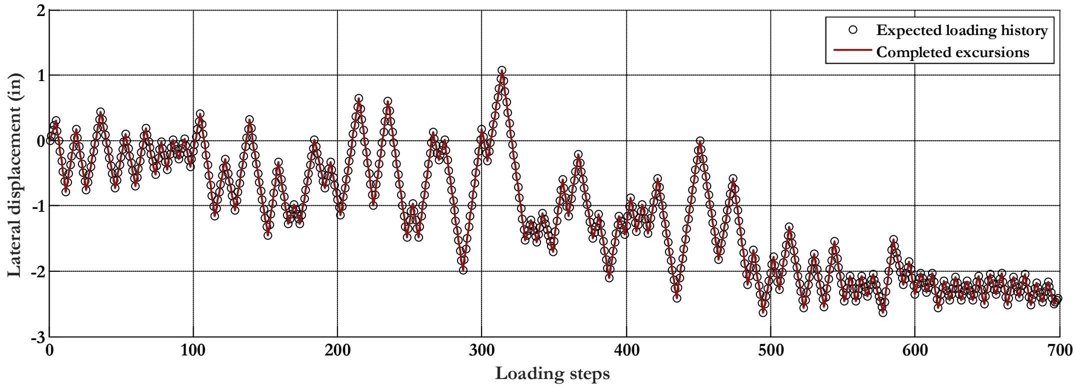

Figure 4.37. The lateral displacement history of the column studied in Figure 4.36.

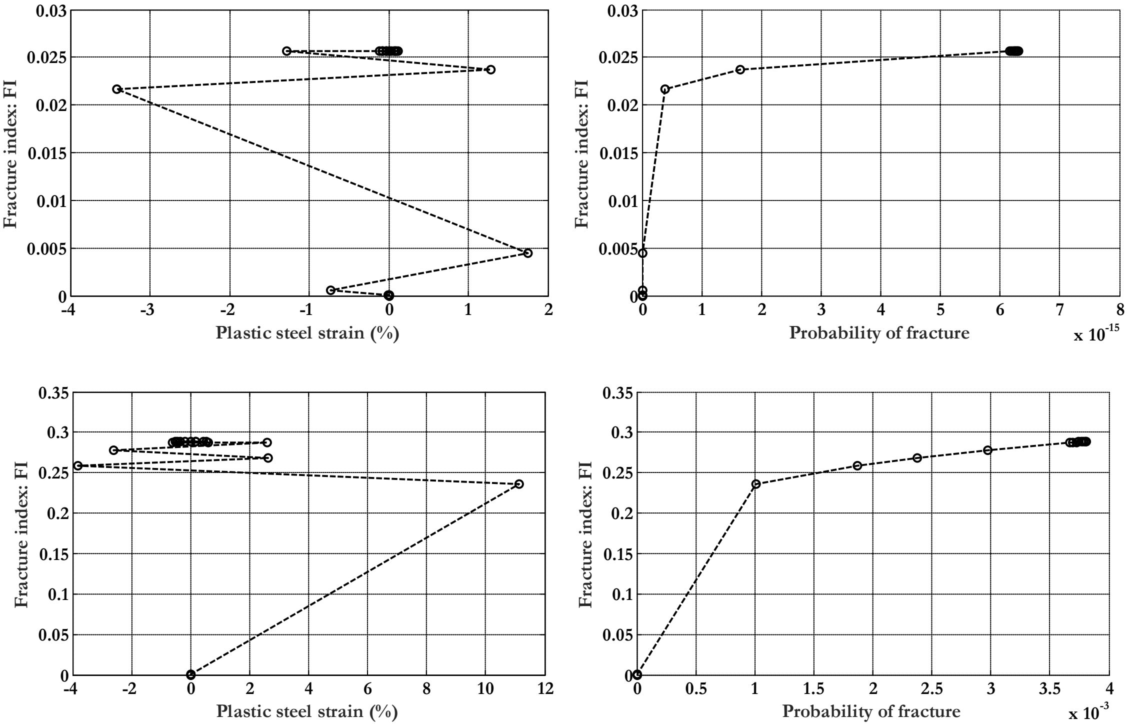

Figure 4.38. Fracture index histories and estimated fracture probability in the bottom and top steel in one external column at 4th story of one RC 20-story frame under Elcentro140.th with a scaled *Sa* (*T*$_1$) of 0.87 g.

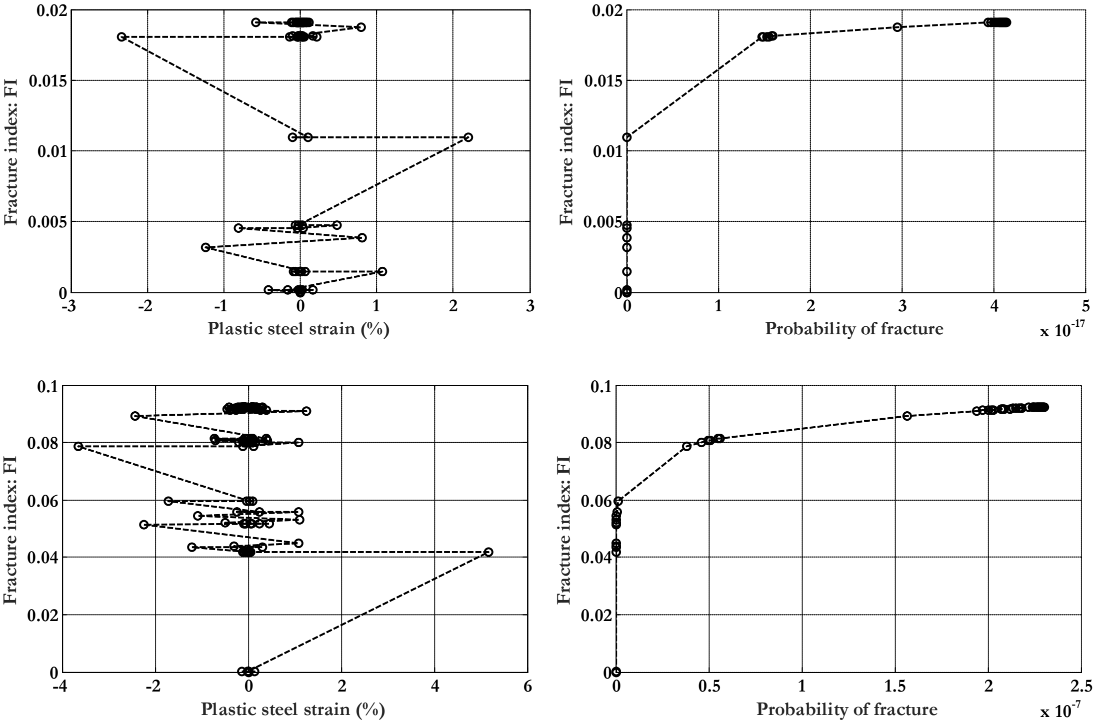

Figure 4.39. Fracture index histories and estimated fracture probability in the bottom and top steel in one external column at 4th story of one RC 20-story frame under Tohoku_FKSH_H2.th with a scaled *Sa* (*T*$_1$) of 0.61 g.

5. FIBER-BASED WALL MODEL

5.1 Overview of Wall Modeling, Analysis, and Assessment

The nonlinear behavior of the flexure-controlled RC walls can be simulated by various approaches. Among the possible structural analysis model types described in *NEHRP Seismic Design Technical Brief No. 4*, this study adopts a fiber-based beam-column model, similar to that described in Chapter 4 for modeling beams and columns, where conventional (plane sections remain plane) flexural section (Figure 5.1) and a nonlinear shear section model (Figure 5.2) are aggregated together. At the bottom of the wall specimen, a zero-length section element is inserted to capture the strain penetration from reinforcing bar bond slip.

The shear walls are discretized into one member per story, following an approach recommended in Chapter 7 of NIST GCR 17-917-45 (FEMA, 2017). For instance, for the CPF 2-story wall test specimen (Huq et al., 2017), the wall is idealized as 2 elements with 5 integration points along the length of each element. At each integration point, fiber sections are defined based on the cross-section properties. The reinforcing bars are modeled by using the Reinforcingsteel material in OpenSees (Mohle and Kunnath, 2010), and the unconfined and confined concrete are modeled by Concrete02 with Kent-Park constitutive model (Filippou, 2010). The unloading branches in concrete constitutive models are regularized following the study by Pugh (2012) to reduced mesh dependent localization of strains. The zero-length bond slip section at the base support is defined in the same manner as previously described for beam-columns (Chapter 4), except that for walls the steel is modeled by Bond_SP01 (Zhao and Sritharan, 2007) with calibrated coefficients.

The trilinear backbone curve (Figure 5.2, based on Birely 2012) is used to simulate the shear response of flexure-controlled shear walls, where V_n is the ACI 318 nominal shear strength. In OpenSees, the shear model was implemented using the Hysteretic material with pinching factors of 0.9 and 0.1 (Table 5.1). Complete wall shear failure is not explicitly simulated, and is checked during post-processing of the response data.

While the beam-column model does not capture shear lag across flange in the C-, I-, or T-shaped walls, this is not considered to be a significant limitation for the cases analyzed in this study. Hassan and El-Tawil (2003) have shown that the effect of shear lag on the effective flange width reduces with correlated axial load and increases with wall lateral drift. Specifically, when the axial load ratio is less than 5% and lateral drift ratio greater than 0.5%, the effective width is greater or equal to wall length. In this study, all non-planar specimens (including T-shape walls and the C-shape 42-story walls) have length-to-width ratios greater or equal to 1.0; and are subject to moderate axial load ratios (0~8%). Moreover, since this study focuses on post-yield strain demands, the drifts of interest are larger than 0.5%, which implies large effective flange widths. In addition, in the T-shape walls, the critical reinforcing bar strains occur in the wall stem, which is much less affected by shear lag. Nevertheless, one should keep this modeling limitation in mind when assessing the response of walls with smaller aspect ratios, higher axial loads, and smaller drift demands.

For analyzing quasi-static wall tests, the recorded displacement histories are used to define the loading protocol, where the OpenSees DisplacementControl integrator is used in analysis with adaptive numerical algorithms starting with Newton method but switching to Newton with initial stiffness, Modified Newton method, Broyden method, and Newton with linear search method in sequence until results converge.

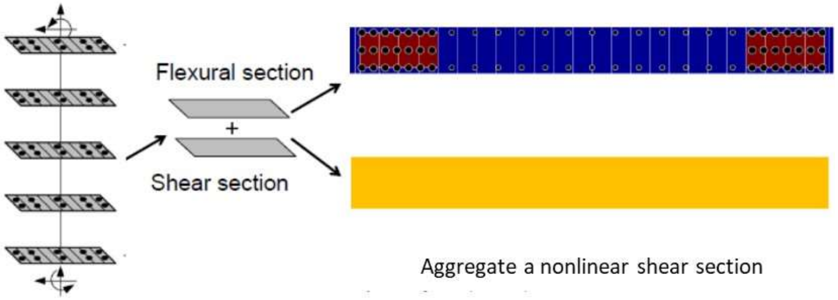

Figure 5.1. The fiber section containing the flexural section and the aggregated nonlinear shear section (after Pugh 2012).

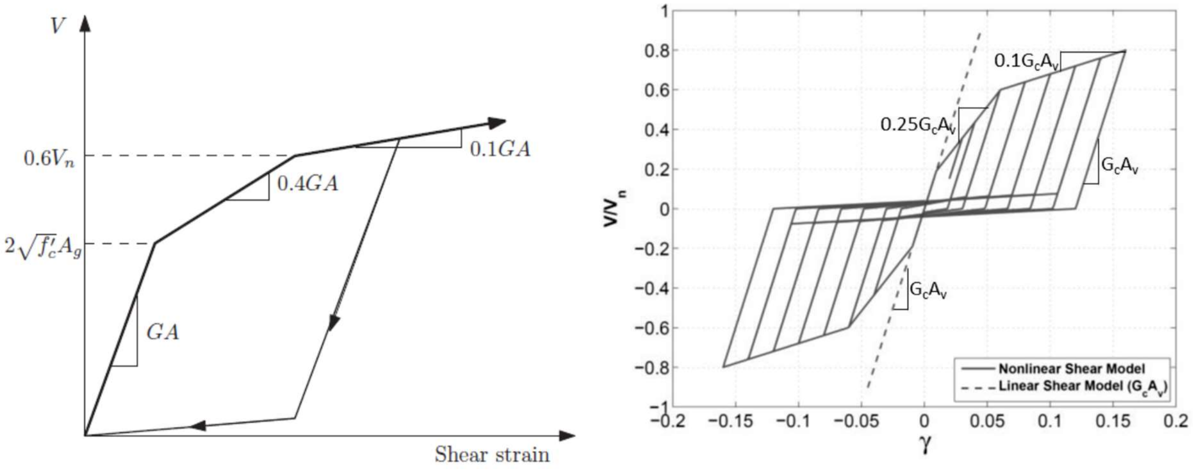

Figure 5.1. Nonlinear shear model. Left: backbone curve (after Birely, 2012); Right: hysteresis (after ATC-114).

5.2 Validation of Fiber-Based Model to Test Data

As part of the CPF project, Huq et al. (2017) conducted four tests of T-shape shear-wall specimens with Gr. 60 and Gr. 100 reinforcement to investigate the implications from rebar-fracture on the wall's ductility and lateral drift capacity. The overall geometries of the specimens are nominally identical (see Figure 5.3), with a slenderness (height-to-section-depth ratio) of 3.0. The wall is designed to have shear stress less than $3.5\sqrt{f_c'}$ so that flexural behavior will dominate the lateral response. As summarized in Table 5.1, one test had Gr. 60 reinforcement and three had Gr. 100 reinforcement, where the *T/Y* ratio varied from 1.15 to 1.35. The Gr. 100 specimens were designed with fewer longitudinal reinforcing bars to maintain a steel strength ratio, $\rho_l f_y$, comparable to the specimen with Gr. 60 reinforcement.

The wall specimens were subjected to cyclic lateral loading, following the protocol recommended by FEMA 461, and without axial loads. Testing was terminated when either severe strength loss occurred, or the drift capacity of the loading equipment was reached. The Gr. 60 T1 specimen was found to withstand lateral loadings up to 6% drift ratio, even after a slight load drop that occurred when two reinforcing bars fractured at about 4% drift. In contrast, reinforcing bar fractures and significant strength loss occurred at lower drifts in the other Gr. 100 tests. Assuming that the drift capacity is defined as the maximum lateral drift ratio before a 25% strength drop occurs, the three specimens with Gr. 100 steel had lower drift capacities (T2: 2%, T3: 3%, and T4: 4%) compared to the Gr. 60 case (T1: 6%). Referring to Table 5.1, the reduction in drift capacities paralleled the differences in *T/Y* ratios, where bars with lower *T/Y* ratios fractured at lower drifts. The typical failure mechanism observed in tests T1, T3, and T4 began with concrete crushing, bar buckling, and subsequent fracture in reinforcement at the extreme fiber of the web in the T-shaped wall. In contrast, in specimen T2 the reinforcing bars in the unconfined region of the wall flange (close to the web-flange intersection) fracture at 2% drift. This poor performance was attributed by Huq et al. to strain localization associated with the low *T/Y* ratio (~1.15) of the reinforcement in T2.

Table 5.1. Summary of tested specimens (after Huq et al., 2017).

Wall	Yield Strength (f_y) (ksi)	*T/Y*	Concrete strength (f_c') (ksi)	Drift Capacity
T1	60	1.35	8	6%
T2	100	1.15	8	2%
T3	100	1.25	8	3%
T4	100	1.35	8	4%

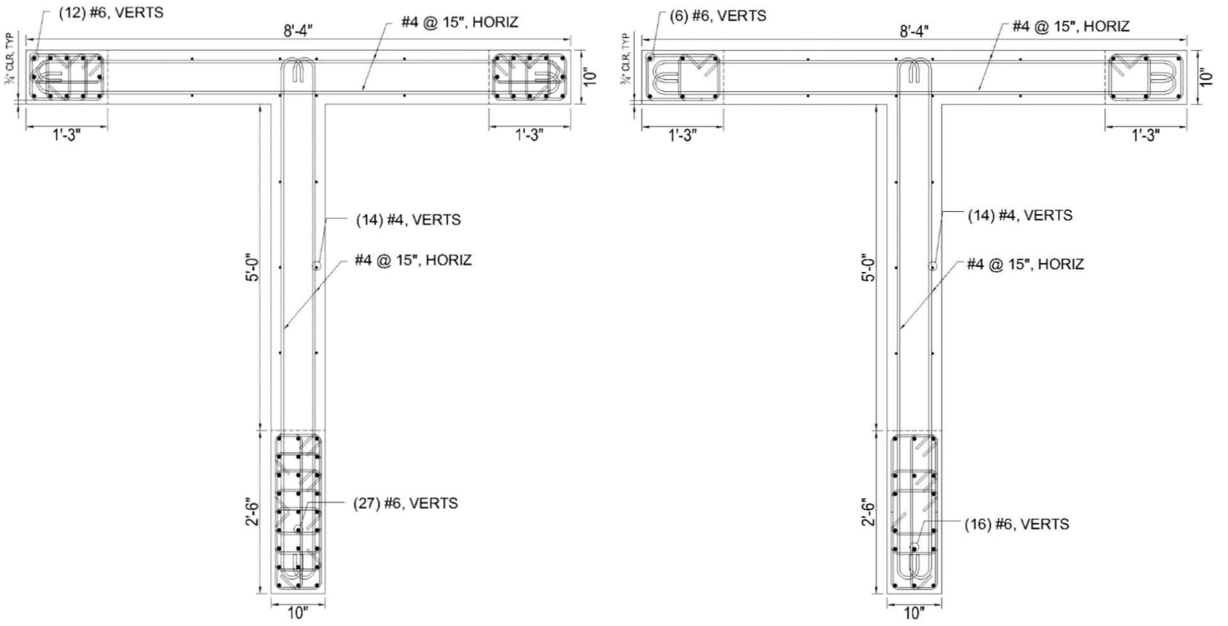

Figure 5.3. Reinforcement schemes for tested T-shape walls. Left: Gr. 60 specimen (T1). Right: Gr. 100 specimen (T2, T3, and T4) (after Huq et al., 2017)

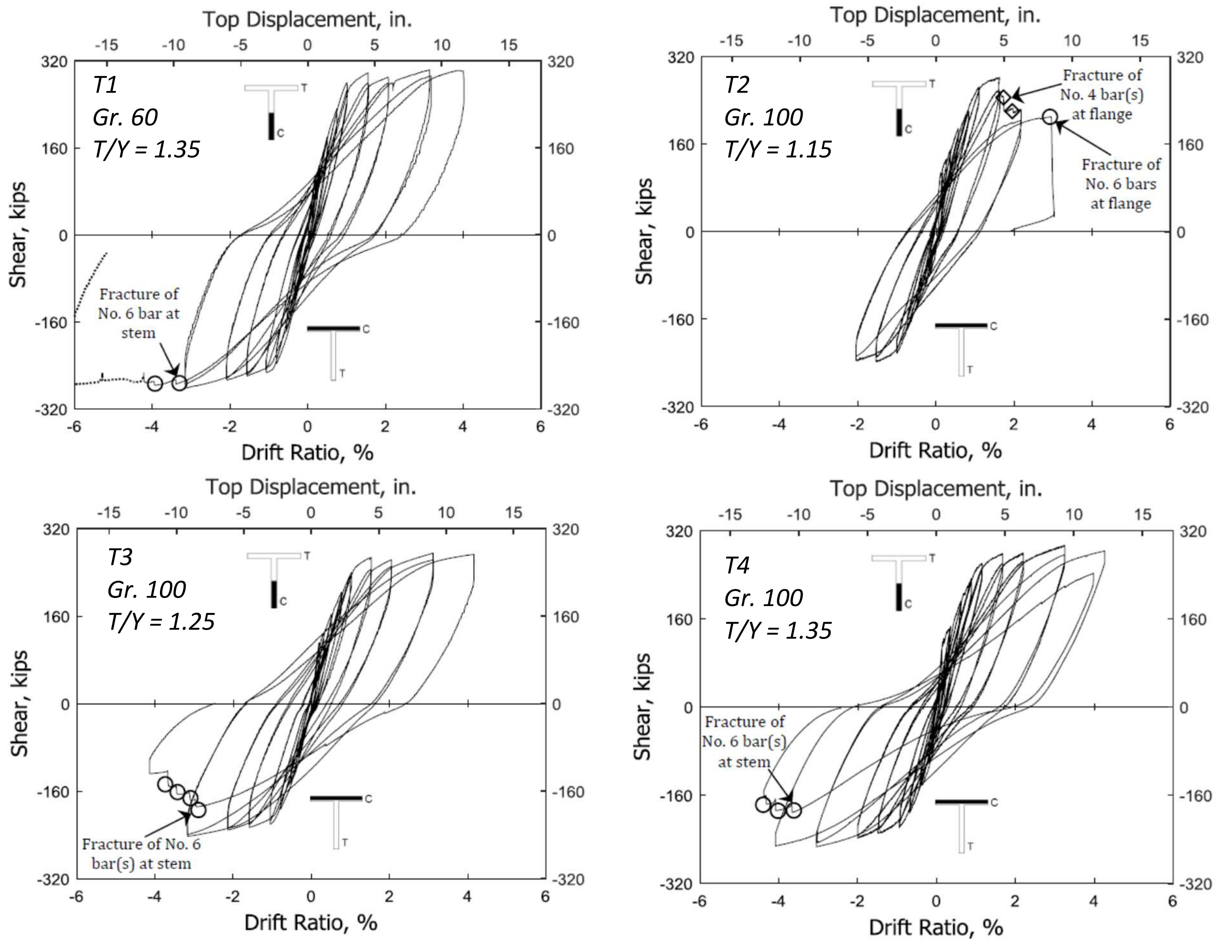

Figure 5.4. Cyclic behaviors of 4 tested T-shape walls (after Huq et al., 2017).

Table 5.2. Shear- and slip-related modeling parameters for the T-shaped wall tests.

	Bond_SP01				**Shear Hysteretic**		
Wall	*a*	*b*	*Su*/*Sy*	*R*	PinchingX	PinchingY	Unloading *β*
T1 (Gr. 60, *T/Y* =1.35)	0.4	0.2	40	0.5	0.9	0.1	0.4
T2 (Gr. 100, *T/Y* =1.15)	0.4	0.1	50	0.5	0.9	0.1	0.4
T3 (Gr. 100, *T/Y* =1.25)	0.4	0.1	50	0.5	0.9	0.1	0.4
T4 (Gr. 100, *T/Y* =1.35)	0.4	0.1	50	0.5	0.9	0.1	0.4

Using the modeling approach introduced in the previous section, 2D fiber-based elements are analyzed in OpenSees for all four tests. Figure 5.5 compares the simulated global hysteretic response versus the measured response of the four wall tests. In general, the simulated results (including initial stiffness, unloading and reloading stiffness) are in good agreement with experimental data. At larger deformations, the measured and simulated results begin to deviate after reinforcing bar buckling and fracture, which is expected since these two failure modes were not directly modeled in the nonlinear analyses.

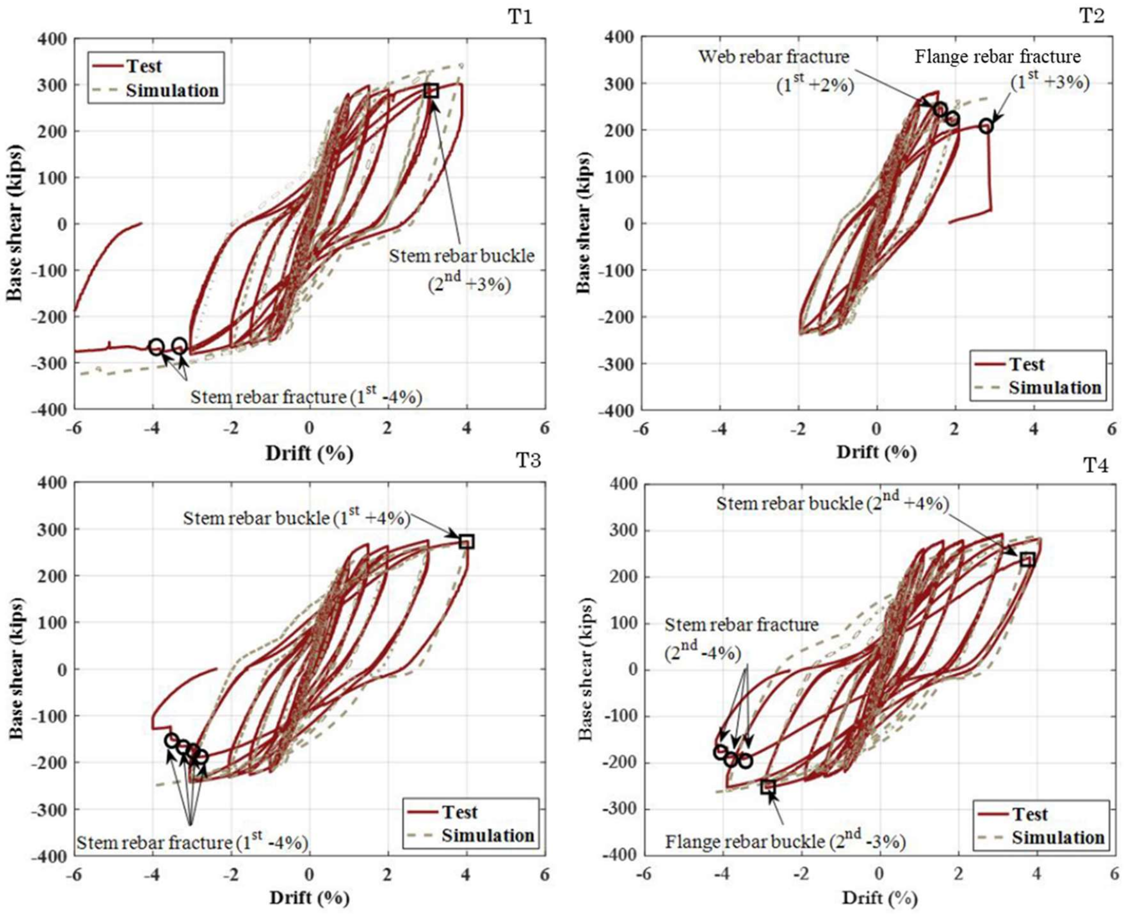

Figure 5.5. CPF shear wall cyclic tests, simulated by the fiber-based approach.

Figure 5.6 shows the simulated shear and bar-slip responses. In T1 specimen, the simulated bar-slip and shear each contributed about 15% of the total lateral drift. In T2 specimen, simulated bar-slip contributed 15%~20% in the total drift, while the shear contribution was about 10%. In T3 and T4 specimen, simulated bar-slip contributed about 25% to the total drift, while the shear only contributed about 5% to the total drift. Generally, for comparable total drift ratios, the specimens with Gr. 100 bars tend to have larger bar-slip responses compared to the specimen with Gr. 60.

Figure 5.7 provides comparisons of simulated stem rebar strains at bottom of four specimens. The maximum tensile strain demand of Gr. 60 bar in T1 is roughly 0.04 and 0.06 for wall drifts of 2% and 3%, respectively. The Gr. 100 bar in T4 (with *T/Y* = 1.35) has similar strain demands as the Gr. 60 bar. Because the confinement steel in T4 is Gr. 100, the confined concrete strength and stiffness in T4 would be greater than the confined concrete strength and stiffness in T1 (using Gr. 60 confinement). So, under the last cycle, the simulated steel strain in T4 is even lower than the steel demand in T1. Comparing T2, T3, and T4 where the *T/Y* of rebar increases from 1.15 to 1.35, the maximum tensile strain demand at 2% are 0.055, 0.047, and 0.040, respectively. This indicates that higher *T/Y* ratios tend to have less strain-concentration at the base of the wall.

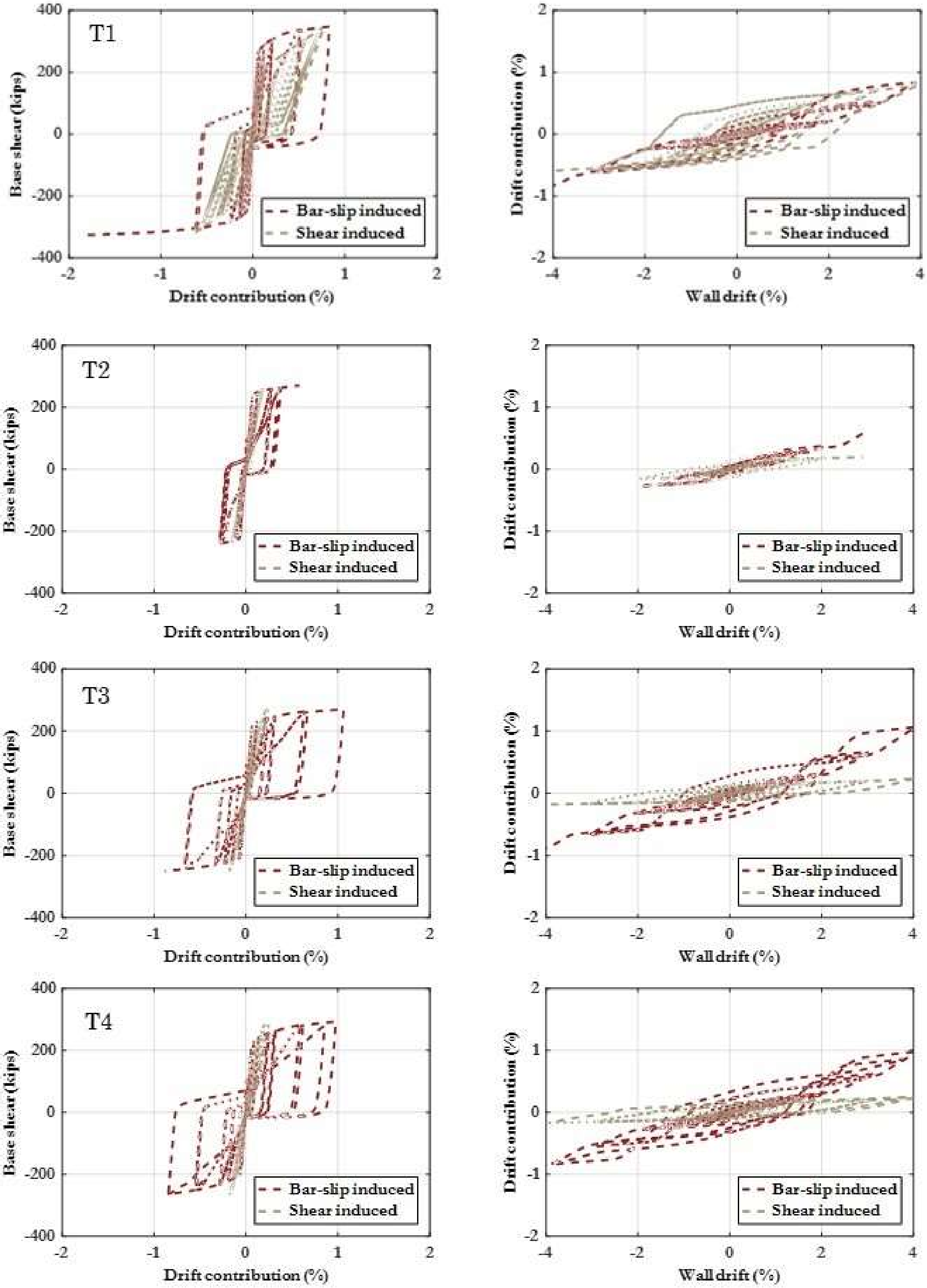

Figure 5.6. Simulated shear and bar-slip responses.

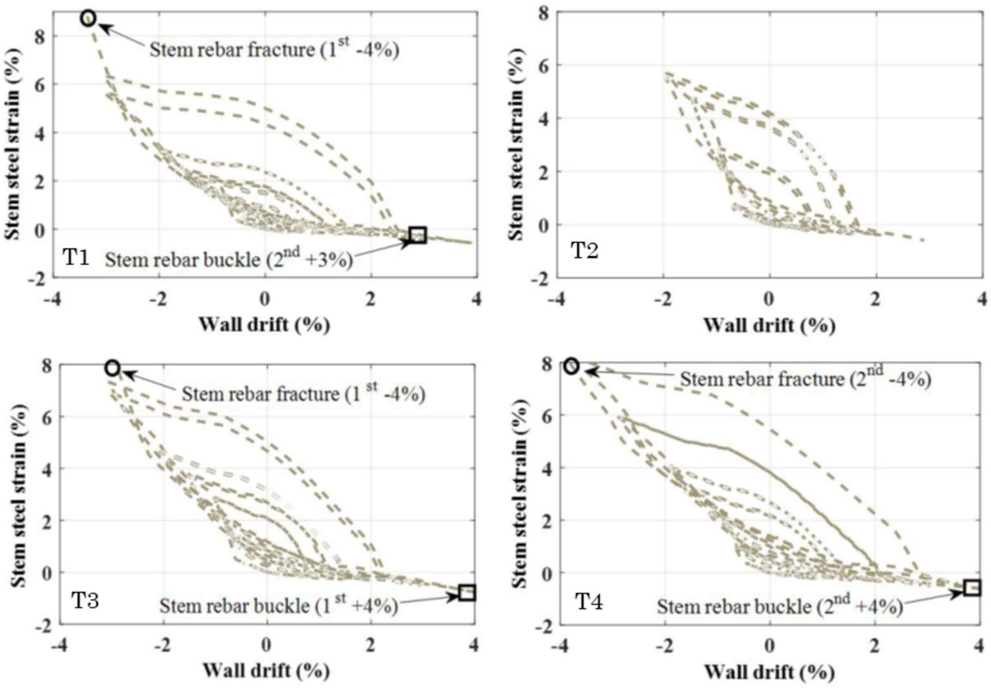

Figure 5.7. Simulated strain-drift relation.

5.3 Validation of Fatigue-Fracture Model in Wall Tests

Figure 5.8 to 5.11 show the simulated strain histories of the most highly strained rebar at the wall stem at the IP located at the base support of the fiber element along with the resulting fracture index histories and estimated fracture probabilities (using the proposed equations 3.2 and 3.3). The red dots in left plots are simulated strain data at each loading step. Since only plastic peak strains are used in the fatigue-fracture model, the red dots are the reduced data as post-yield strain milestones. Using Equation 3.2 to determine the two material coefficients and substituting these strain data into Equation 3.3, the fracture index history can be calculated. The middle plots are the computed *FI* histories. Mapping the *FI* history through the fracture fragility model (Figure 3.13), the probability of fracture is shown in right plots. The red crosses in the plots indicate the reported initial fracture point in tests. The corresponding *FI* values when fractures are observed in tests T1, T3, and T4 are 1.00, 1.19, and 1.16, respectively. In test T2, the early fractures in the flange rebars led to termination of the test before fractures could occur in the wall stem, which is consistent with the wall stem fracture data in Figure 5.9.

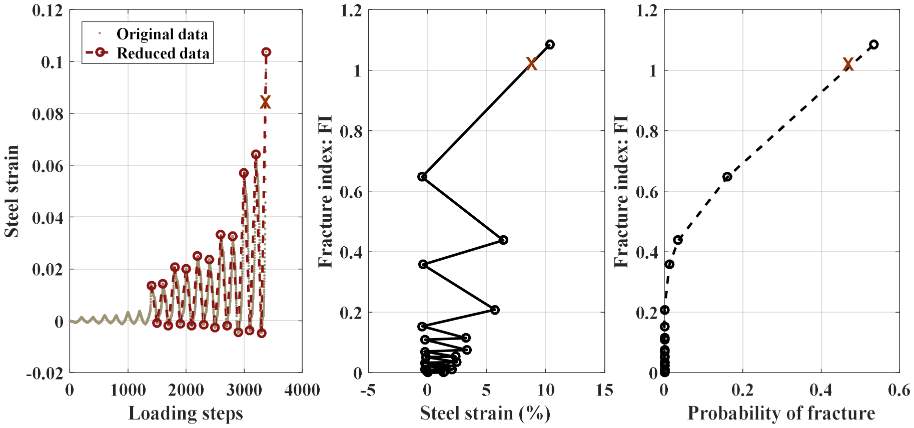

Figure 5.8. *FI* history and estimated fracture probability of the worst rebar at the wall stem (T1: Gr. 60 *T/Y* = 1.35).

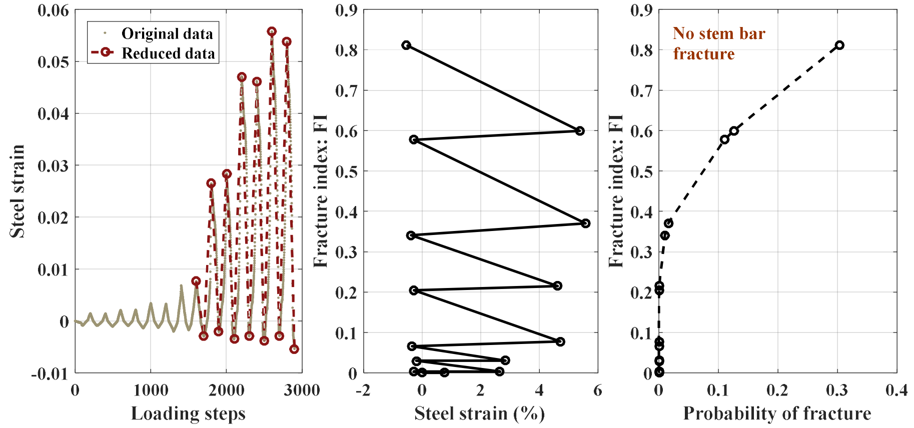

Figure 5.9. *FI* history and estimated fracture probability of the worst rebar at the wall stem (T2: Gr. 100 *T/Y* = 1.15).

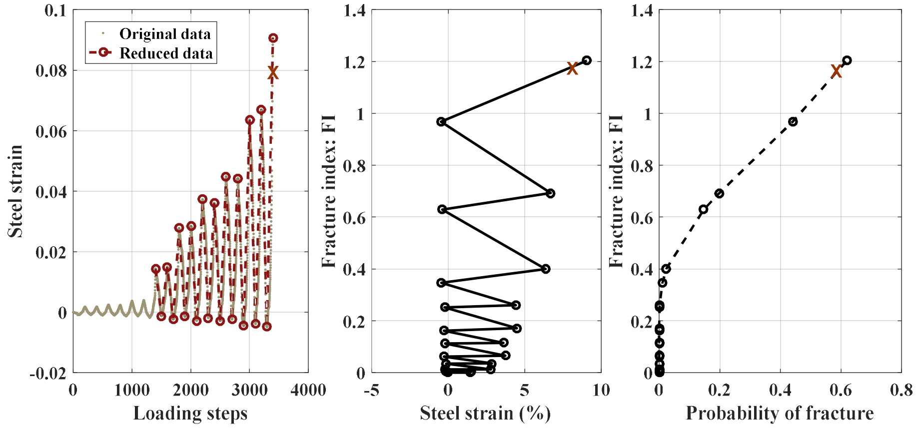

Figure 5.10. *FI* history and estimated fracture probability of the worst rebar at the wall stem (T3: Gr. 100 *T/Y* = 1.25).

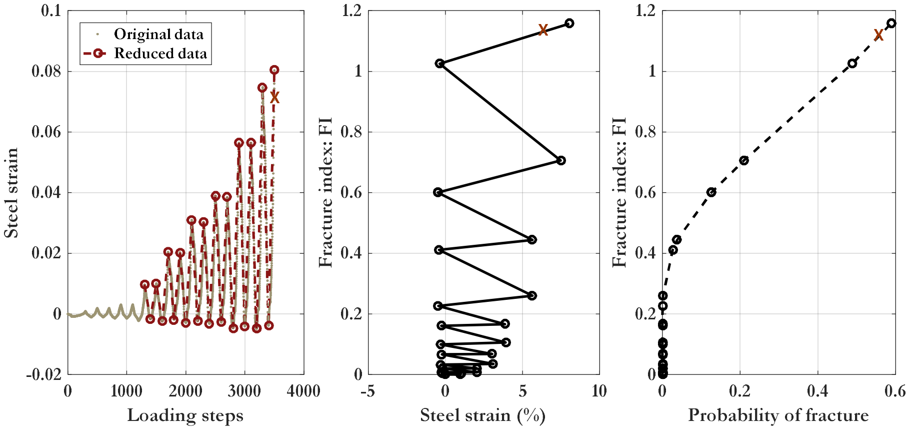

Figure 5.11. *FI* history and estimated fracture probability of the worst rebar at the wall stem (T4: Gr. 100 *T/Y* = 1.35).

6. RELIABILITY INTEGRAL FOR SEISMIC DEMAND PARAMETERS

6.1 Overview of Reliability Considerations

In general, the seismic safety depends on both the structural properties and earthquake hazard. From Chapter 3 to Chapter 5, we focus on capturing the different structural responses and potential failure modes related to the use of high-strength reinforcement. This chapter address how the earthquake hazard characteristics are accounted for in the performance assessment based on incremental dynamic analyses (IDA). Specifically, methods are described for post-processing interpretation of the demand parameters to account for specific ground motion characteristics that are not otherwise considered in the IDA.

In IDA, the structure is analyzed under a generic set of ground motions that are incrementally linearly scaled up in intensity until the structural analysis model reaches its collapse limit state. Since the frequency content (spectral shape) and duration of these ground motions are not necessarily consistent with the characteristics of the target hazard (either for a specific building location or assumed condition), the structural demands and collapse intensities calculated from the IDA need to be adjusted. In FEMA P695, the collapse fragility curve determined from an IDA is adjusted by modifying the median collapse capacity by a spectral shape factor (*SSF*) that is calibrated to the spectral shape for a high intensity *MCE* hazard (e.g., Seismic Design Category D_{max}). More recently, Chandramohan, Baker, and Deierlein (2016a, 2016b) proposed an alternative approach to adjust the collapse fragility that is more statistically rigorous and can adjust to the hazard characteristics at any specific building site. In addition to adjustments for spectral shape, the Chandramohan et al. procedure adjusts for earthquake ground motion duration, which can influence structural collapse and cumulative deformation and strain demands. The duration adjustment is particularly important since fatigue-fracture of reinforcement is controlled by cumulative rebar strain demands.

This chapter summarizes the methods used to adjust IDA results by effects from spectral shape and duration. Collapse assessment is performed by the FEMA P695 methodology (Section 6.2), where bar fracture is treated as a non-simulated failure mode and spectral shape is addressed through the *SSF*. The MCE_R demands (i.e., story drifts, rebar strains, and fracture indices) are estimated by the hazard-consistent adjustment (Section 6.3), where structural demands are adjusted for spectral-shape and duration measures.

6.2 Collapse Fragility by FEMA P695

A key challenge in treating reinforcing bar fracture as a 'non-simulated' collapse mode is in deciding how to relate the local bar fracture indices to the overall collapse behavior. This is a similar challenge to the one faced when interpreting the component limit states in ASCE 41-17 (ASCE 2017), i.e., how does exceeding the CP limit in any one component relate to the overall structural system performance. As observed in experimental test specimens of reinforced concrete beams, columns and wall, significant strength drops generally occur soon after the first reinforcing bar ruptures. However, the degradation depends on the member size and number of reinforcing bars in the member, and the strength deterioration observed in a quasi-static cyclic test does not necessary carry over to dynamic response. For instance, in a shake table test of a large concrete bridge column (Schoettler et al. 2010), the specimen survived beyond the first reinforcing bar fracture (under the 8th ground motion) followed by fractures of a few other bars, during the 9th ground motion before "collapse" under the 10th ground motion.

Upon consideration of several alternatives, for this study we are assuming that collapse due to reinforcing bar fracture occurs when the maximum fracture index (FI) in any column of the concrete frame or in any shear wall first exceeds its median value of $FI = 1.0$. As $FI = 1.0$ is the median (or expected value) of the fracture index, this implies a 50% probability of bar fracture. The median value is chosen in part because it is consistent with the basic premise of the FEMA P695 procedure, where the analysis model is calibrated to represent median values. Thus, were bar fracture to be simulated directly in the analyses, the bar model would be calibrated to fracture at *FI* = 1.0. In doing so, the FEMA P695 procedure incorporates the modeling uncertainties (which would presumably reflect the variability in fracture behavior) in the assumed dispersion in the overall collapse fragility curve. A more significant aspect of this assumption is that the first occurrence of bar fracture would trigger (or be synonymous with) collapse. While this is a potentially very conservative assumption, it is not unprecedented. How important the assumption is will also depend on the tendency for reinforcing bar fracture, which is generally low in seismically detailed structures. Moreover, it should be kept in mind that this assumption equally affects the analyses of models with conventional (Grade 60) and high strength (Grade 80 and 100) reinforcing bars. So, to the extent that the focus of this project is to identify the difference in safety between conventional and high strength reinforcement, the influence of the simplifying assumptions on the final outcome is mitigated.

Following this assumption, this study applies FEMA P695 methodology to assess the collapse fragility considering non-simulated bar-fracture failure modes. Figure 6.1 illustrates the approach of accounting for increase in collapse risk due to rebar fracture. Each curve in the left plot of Figure 6.1 represents the maximum fracture indices in columns under each ground motion at increasing intensity levels. Some of these curves stop short of *FI* = 1.0, where sidesway collapse (evident from large story drifts) occurs before the first bar fractures. On the other hand, bar-fracture failure points (defined at *FI* = 1.0) are observed for several of the ground motions and are mapped to the IDA curves (as plotted in the middle panel in Figure 6.1). These bar fracture may occur right before the simulated collapse point (e.g., the top red cycle) or much earlier than the simulated collapse point (e.g., the bottom red cycle). The latter will result in much lower collapse intensities if compared to the original collapse intensity without considering bar fracture. The resulting impact is shown in the right panel, where the collapse fragility including fracture-induced failures (in red) is shifted to a lower intensity side, as compared to the collapse fragility without fracture failures (in black).

Referring to Figure 6.1, this increase in collapse probability may not be significant at lower intensity because the strain demands are relatively low and no fracture-induced collapse case. This trend is generally true for most buildings evaluated in this study, although the significance of fracture increases for the shorter concrete walls (as discussed in detail in Chapter 7 and Chapter 8).

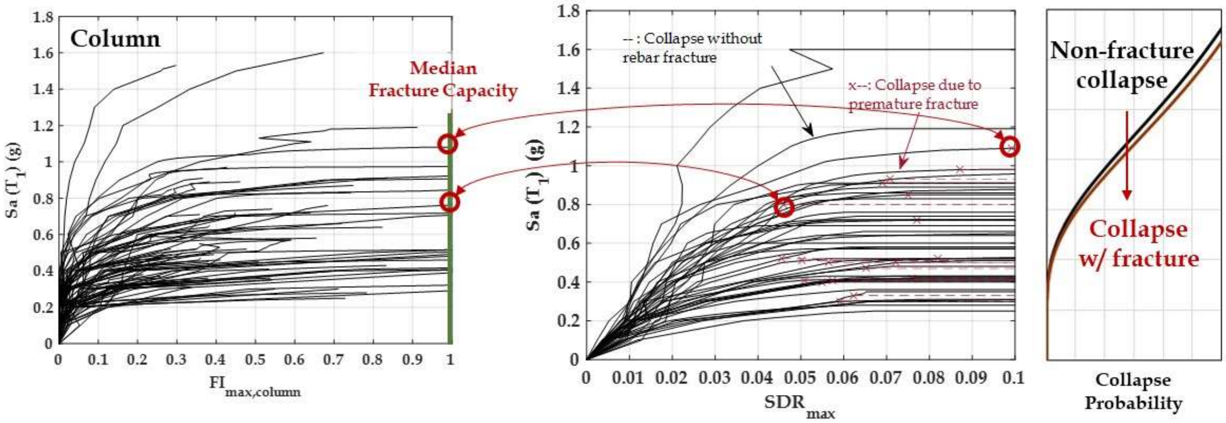

Figure 6.1. Incorporation of bar fracture into IDA calculation of FEMA P695 collapse assessment.

As per FEMA P695, the median collapse intensity (with or without fracture) is adjusted by the spectral shape factor (*SSF*) to represent site-specific spectral shape. The resulting collapse fragility curves have a fixed dispersion value of 0.5, which accounts for uncertainties in ground motions, modeling, and quality control/assurance. Comparison between the MCE_R collapse probabilities of the benchmark design (using Grade 60 with T/Y = 1.3 and s/d_b = 6) and designs using high-strength reinforcement are presented in Chapters 7 and 8. It is also noted that although the impact from ground motion duration are considered in computing the cumulative rebar strains and fracture indices, duration is not explicitly considered in the *SSF* adjustment, which is an inherent limitation of the FEMA P695 methodology.

6.3 MCE_R Demand Assessment by Hazard-Consistent Adjustment

In this section, a method for adjusting MCE_R structural response demands for site specific ground motion hazard is described. Figure 6.2 shows IDA curves of the benchmark 20-story frame (Grade 60 rebar with T/Y = 1.3 and s/d_b = 6). By taking horizontal cuts through the IDA curves, such as at the *Sa* = 0.24g level shown in the figure, story drift ratio demands (conditioned on the non-collapse cases) can be calculated at any intensity level. These maximum story drift demands can then be plotted with respect to the secondary ground motion characteristics to look for trends between the two. For example, shown in Figure 6.3 the trend between the spectral shape index, *SaRatio*, versus the maximum story drift demand for the Sa = 0.24g intensity level. The strong negative correlation between *SaRatio* and the drift demand is not surprising, since ground motions with larger *SaRatio*'s are known to be less damaging than ones with smaller ratios (Chandramohan et al., 2016a).

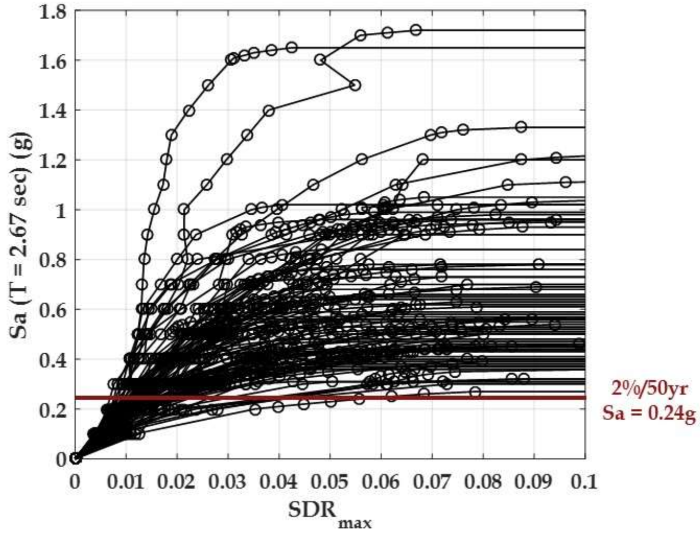

Figure 6.2. Original IDA curves (Gr. 60 T/Y = 1.3 at San Francisco).

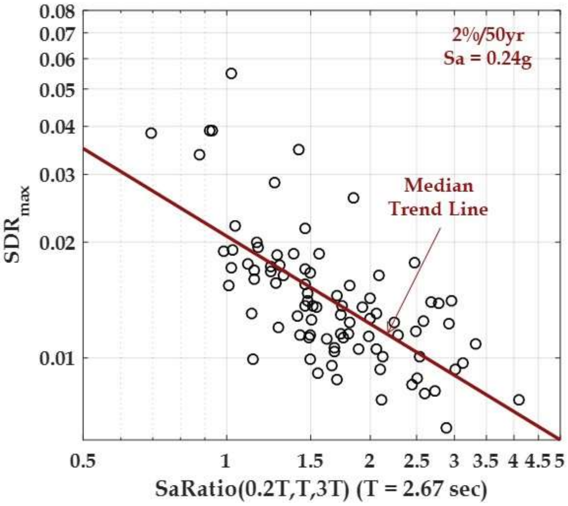

Figure 6.3. $SDR_{\max}$ vs. *SaRatio* under Sa = 0.24g.

Similar to Figure 6.3, Figure 6.4 shows the regressed median SDR_{max}-*SaRatio* functions given different intensities. If extended to consider the influence of both spectral shape (*SaRatio*) and significant duration ($Ds_{5\text{-}75}$), similar relationships could be achieved, by regress a median plane of SDR_{max} demands with respect to both *SaRatio* and $Ds_{5\text{-}75}$. Strictly speaking, the dispersion of response demands (in addition to the median values) also varies with the secondary parameters (*SaRatio* and $Ds_{5\text{-}75}$), but the data is generally insufficient for accurately estimating the second-order information (i.e., dispersion), especially for higher intensities where only a subset of ground motions does not collapse the structure. Therefore, as a practical measure, the dispersion is assumed constant over the range of secondary parameters. For example, shown in Figure 6.5 is an example to show how dispersion is assumed to be constant versus *SaRatio*, for the Sa = 0.24g intensity level. This allows one to estimate, through linear regression of lognormal model, the distribution of structural response demand at any intensity level from original IDA curves according to the following equation:

$$\ln\left(EDP\,|\,Sa\right)=a_0+a_1\ln\left(SaRatio\,|\,Sa\right)+a_2\ln\left(Ds_{5\text{–}75}\,|\,Sa\right)+\varepsilon,\varepsilon\sim N\left(0,\sigma^2\right) \tag{6.1}$$

Given the adjusted demand distribution $f_D(x)$ (Equation 6.1, where the EDP may be the fracture index FI) and the capacity distribution $F_C(x)$ (e.g., probability of fracture as a function of FI), the failure or limit state exceedance probability is defined by the following equation:

$$p_f=\int f_D\left(x\right)F_C\left(x\right)\cdot dx \tag{6.2}$$

where, x is the controlling factor (e.g., story drift, reinforcing bar strain, fracture index FI); $f_D(x)$ is the demand distribution; and $F_C(x)$ is the capacity distribution. In this study, the capacity function is consistent with the fracture fragility model calibrated in Chapter 3, where steel yield strength, *T/Y* ratio, and fracture strain were considered to influence the fracture resistance.

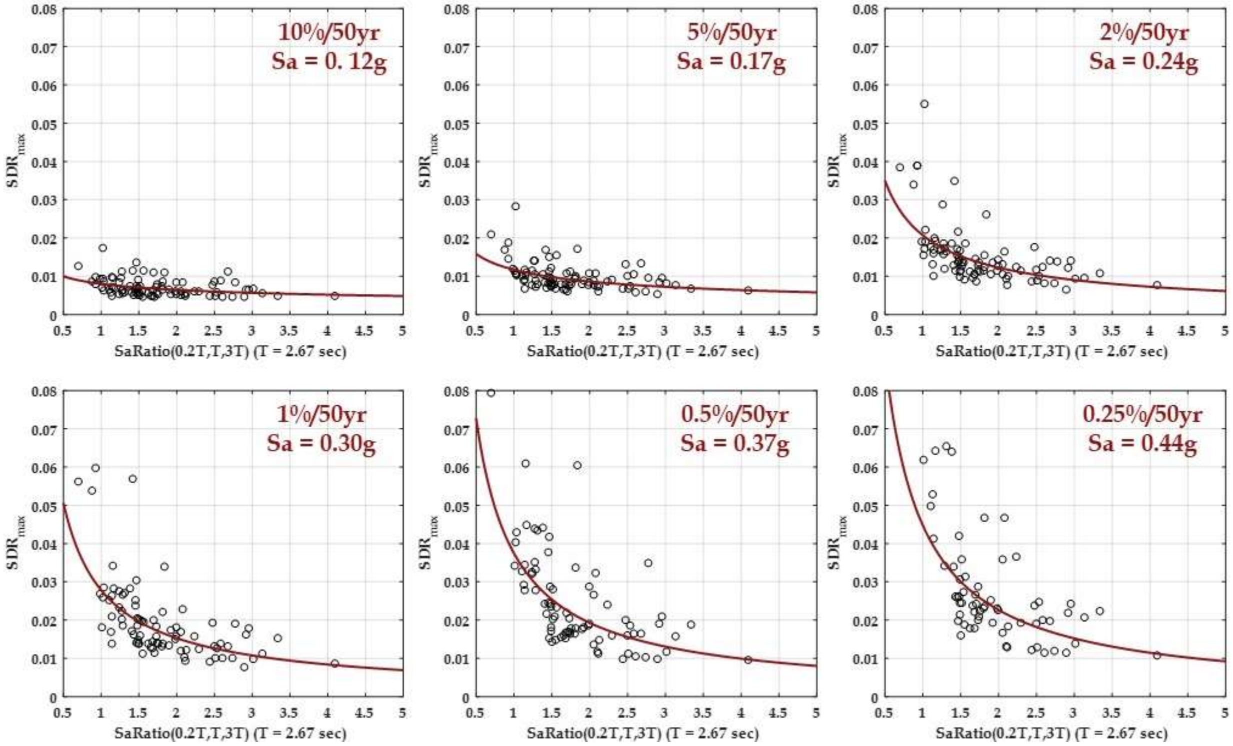

Figure 6.4. Median $SDR_{\max}$ demand versus *SaRatio* curves for different intensities.

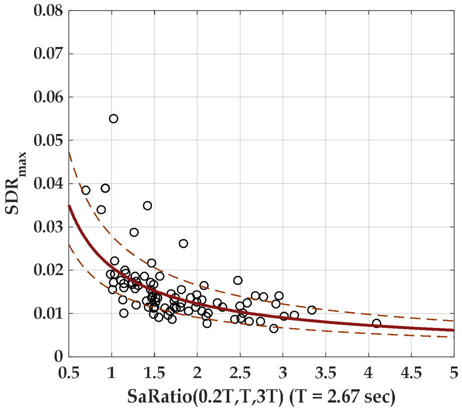

Figure 6.5. Plot of constant dispersion as a function of for *SaRatio* for a specific intensity level.

6.4 Ground Motion Hazard Characteristics

In the FEMA P695 method, the *SSF* factor is dependent on building inelastic deformation capacity and the spectral shape ε. Given the reference spectral shape value ε_0 is 1.5 for SDC D and the estimated period, the *SSF* can be computed for each structure. For 20-story and 4-story archetype frames the *SSF* values are 1.49 and 1.41, respectively. For 42-story and 8-story shear wall buildings the *SSF* values are 1.50 and 1.45, respectively. These *SSF* are used to assess the collapse risk for the frame and wall buildings for the MCE_R ground motion intensity for the building sites in San Francisco and Los Angeles.

For the MCE_R demand assessments, the site-specific hazard adjustments are based on the following intensity measures: spectral acceleration $Sa(T_1)$, significant duration $Ds_{5\text{-}75}$, and spectral shape measure

SaRatio. The Campbell and Bozorgnia (2008) ground motion prediction model is used to determine response spectral ordinates $Sa(T_1)$ for crustal earthquakes and the Abrahamson et al. (2016) model is used for the interface and in-slab earthquakes. Correlation coefficients for ε-values to evaluate the *SaRatio* (spectral shape) metric are determined using the Baker and Jayaram (2008) model for crustal and in-slab earthquakes and the Al Atik (2011) model was applied for interface earthquakes. The Abrahamson and Silva (1996) model is used to evaluate significant duration $Ds_{5\text{-}75}$. The Bradley (2011) model is employed to assess the covariance between the spectral ordinate and significant duration.

The site-specific IM joint distributions at three intensity levels (*DBE*, *MCE*, and 2% in 200 years) are illustrated in Figure 6.6 for the 20-story concrete frame building (T_1 = 2.67sec) at the San Francisco and Seattle building sites. The square dots are the median IM points and the cross bar represent the ±σ boundaries at each intensity level. The characteristics of 44 FEMA far-field ground motions and 44 spectrally-equivalent long-duration motions are plotted against the targets. The hazard targets shown for Seattle site represent the weighted mean value of three earthquake fault sources. Comparing the targets within each site, one can see that the duration and *SaRatio*'s tend to increase with increasing earthquake intensity. Comparing targets for the two sites, the Seattle motions have relatively longer durations but less damaging spectral shapes (i.e., larger *SaRatio*'s) as compared to the San Francisco site. Figure 6.7 compares the joint distributions at the MCE_R intensity level between the for three building periods (corresponding to Gr. 60, Gr. 80, and Gr. 100) at the two sites. Similar hazard data are utilized to define the hazard targets for the 4-story frame and 8-story and 42-story shear wall buildings at the San Francisco, Seattle and Los Angeles building sites.

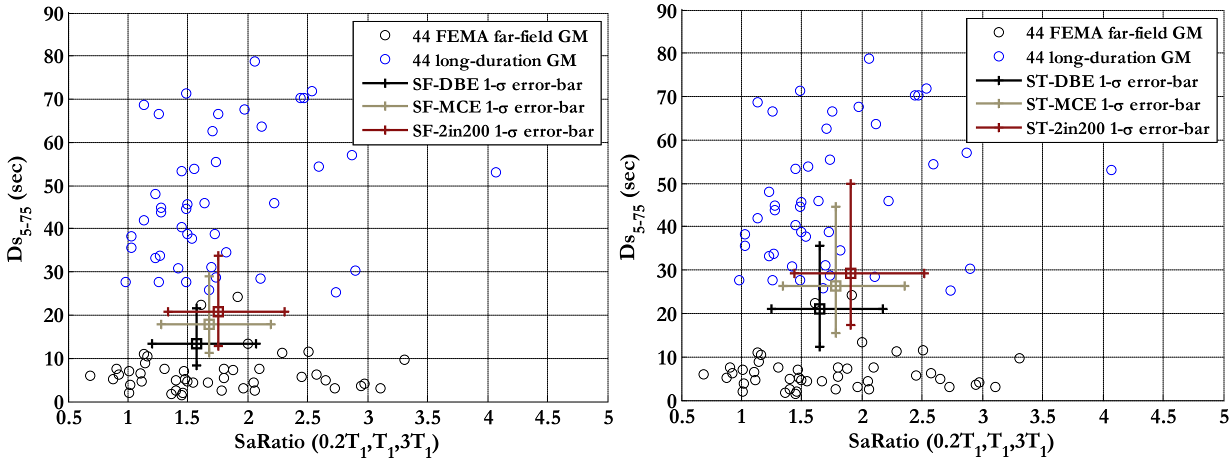

Figure 6.6. Site-specific information (±σ error-bar plots) against 88 ground motions' characteristics for T_1 = 2.67 sec. Left: San Francisco. Right: Seattle.

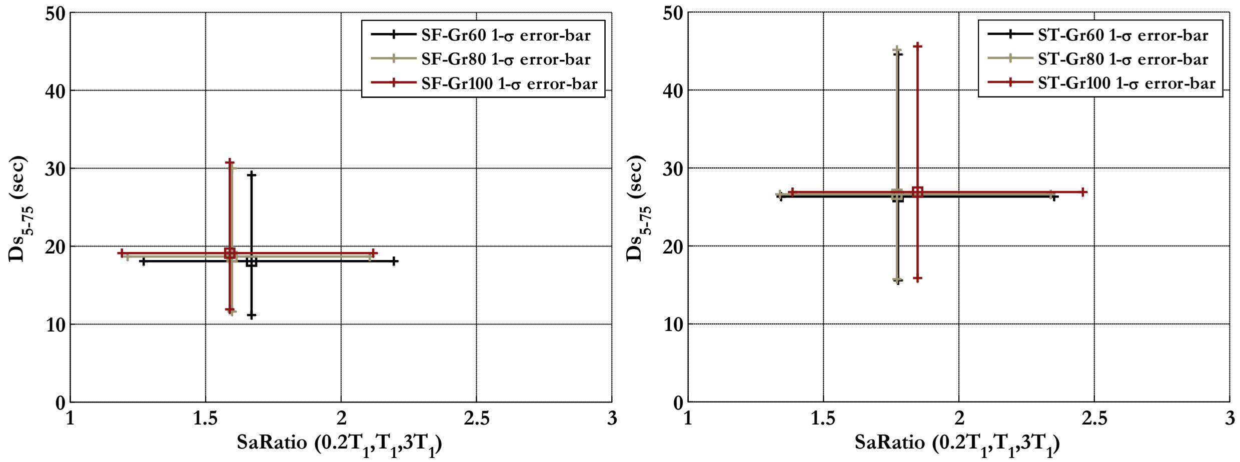

Figure 6.7. Site-specific information (±σ error-bar plots) against 88 ground motions' characteristics at *MCE* intensity level (Gr. 60: T_1 = 2.67 sec, Gr. 80: T_1 = 2.95 sec, Gr. 100: T_1 = 3.20 sec). Left: San Francisco. Right: Seattle.

7. FRAME CASE STUDY

7.1 Archetype Structures and Modeling

This chapter focuses on systematically evaluating reinforcing bar strain demands, bar-fracture and collapse risk for a 20-story and 4-story special moment frame building. These building designs were previously analyzed and documented in the FEMA P695 study on seismic performance factors (identified as frame IDs 1020 and 1003 in FEMA P695). These two archetypes are considered to represent prevailing standards and design practices for reinforced concrete special moment frames in the US. The 4-story frame represents low-rise short-period buildings that comply with the equivalent lateral force (ELF) method in ASCE 7. The 20-story frame represents mid-rise longer-period buildings whose designs are often controlled by drift (minimum stiffness) and minimum base shear (strength) requirements of ASCE 7.

The two original frame archetypes used Grade 60 reinforcement (Haselton et al., 2008), and were redesigned with higher grade (80 and 100) reinforcement to maintain the same nominal flexural member strengths (M_u). Each original archetype is further expanded to a 9-by-3 design matrix of design parameters, as shown in Table 7.1, to investigate of reinforcing bar hardening properties (T/Y ratio) and confinement tie spacings (s/d_b).

Each design case is identified by a unique code, defined as follows: story number – structural type – rebar grade – T/Y tag – column s/d_b tag. For example, the 20F060136 denotes the archetype 20-story frame using Grade 60 reinforcement with T/Y of 1.3 and column tie spacing s/d_b of 6 (note the s/d_b ratio for beams are fixed at 6 for all designs). The designs are configured to cover a wide range of possible hardening ratios (T/Y) and three tie spacing options. For instance, the Grade 100 reinforcement is examined at three median T/Y levels, from the high end of 1.3 to the low end 1.1, based on the range of T/Y ratios offered by the manufacturers of each steel grade. The designs using Grade 60 steel with the lowest T/Y ratio (1.3) and largest s/d_b spacing is selected as the benchmark case, as a point of comparison between performance permitted by current building code provisions for conventional steel reinforcement to designs with higher strength steel.

Table 7.1. Design matrix and ID of 20-story archetype frames.

Grade	*T/Y*	Tie spacing s/d_b		
		4	5	6
60	1.5	20F060154	20F060155	20F060156
	1.4	20F060144	20F060145	20F060146
	1.3	20F060134	20F060135	20F060136
80	1.4	20F080144	20F080145	20F080146
	1.3	20F080134	20F080135	20F080136
	1.2	20F080124	20F080125	20F080126
100	1.3	20F100134	20F100135	20F100136
	1.2	20F100124	20F100125	20F100126
	1.1	20F100114	20F100115	20F100116

For special moment frames, the current ACI standard (ACI 318-14) limits the maximum lateral reinforcement spacing in beams by the smallest value of (1) one-fourth of the beam depth, (2) six times the diameter of the smallest primary rebar, and (3) 6 in. The standard also limits the maximum transverse reinforcement spacing in columns by the smallest value of (1) one-fourth of the minimum section dimension, (2) six times the diameter of the smallest longitudinal bar, and (3) $s_0 = 4 + (14-h_x)/3$. In most conventional designs, the longitudinal bar sizes vary from #5 (d_b = 0.63 in) to #11 (d_b = 1.41 in), such that the tie spacing for small-size bars (up to #8) is usually restricted by the $6d_b$ limit, and the tie spacing for larger bars (over #8) is generally restricted by 6 in. In this case study, only #6 and #8 bars are used in designs, which means the $6d_b$ constraint is always active. Given that the fatigue-fracture failure of the reinforcing bars is closely related to bar buckling, the design matrix includes three tie spacings to evaluate benefits of tighter tie spacings on mitigating bar buckling and fracture.

Tables 7.2, 7.3, and 7.4 summarize section design details of the benchmark case (for the external columns, internal columns, and beams, respectively). The building is designed for Seismic Design Category D_{max} (SDC D_{max}). Member sizes are generally controlled by minimum strength and stiffness requirements, capacity design requirements (for columns), and minimum reinforcing ratio (in the upper stories).

Table 7.2. Design document for the external columns in 20F060136.

Story	H (in)	b (in)	h (in)	c (in)	f_c (ksi)	f_{yl} (ksi)	f_{yt} (ksi)	T/Y	ρ_l	ρ_{sh}	s/d_b
1	138	32	42	3	-7.2	67	67	1.3	0.0250	0.0103	6
2	114	32	42	3	-7.2	67	67	1.3	0.0180	0.0089	6
3	114	32	42	3	-7.2	67	67	1.3	0.0170	0.0089	6
4	114	32	42	3	-7.2	67	67	1.3	0.0160	0.0089	6
5	114	32	42	3	-7.2	67	67	1.3	0.0150	0.0089	6
6	114	32	42	3	-7.2	67	67	1.3	0.0145	0.0089	6
7	114	32	42	3	-7.2	67	67	1.3	0.0140	0.0089	6
8	114	32	42	3	-7.2	67	67	1.3	0.0130	0.0089	6
9	114	32	42	3	-7.2	67	67	1.3	0.0125	0.0089	6
10	114	32	42	3	-7.2	67	67	1.3	0.0120	0.0089	6
11	114	32	42	3	-6.0	67	67	1.3	0.0110	0.0089	6
12	114	32	42	3	-6.0	67	67	1.3	0.0100	0.0089	6
13	114	32	36	3	-6.0	67	67	1.3	0.0120	0.0075	6
14	114	32	36	3	-6.0	67	67	1.3	0.0120	0.0075	6
15	114	32	36	3	-6.0	67	67	1.3	0.0100	0.0075	6
16	114	32	36	3	-6.0	67	67	1.3	0.0100	0.0075	6
17	114	32	36	3	-6.0	67	67	1.3	0.0100	0.0075	6
18	114	32	36	3	-6.0	67	67	1.3	0.0100	0.0075	6
19	114	32	36	3	-6.0	67	67	1.3	0.0100	0.0075	6
20	114	32	36	3	-6.0	67	67	1.3	0.0100	0.0075	6

Table 7.3. Design document for the internal columns in 20F060136.

Story	*H* (in)	*b* (in)	*h* (in)	*c* (in)	f_c (ksi)	f_{yl} (ksi)	f_{yt} (ksi)	*T/Y*	ρ_l	ρ_{sh}	s/d_b
1	138	32	42	3	-7.2	67	67	1.3	0.0170	0.0089	6
2	114	32	42	3	-7.2	67	67	1.3	0.0170	0.0089	6
3	114	32	42	3	-7.2	67	67	1.3	0.0170	0.0089	6
4	114	32	42	3	-7.2	67	67	1.3	0.0170	0.0089	6
5	114	32	42	3	-7.2	67	67	1.3	0.0170	0.0089	6
6	114	32	42	3	-7.2	67	67	1.3	0.0170	0.0089	6
7	114	32	42	3	-7.2	67	67	1.3	0.0165	0.0089	6
8	114	32	42	3	-7.2	67	67	1.3	0.0160	0.0089	6
9	114	32	42	3	-7.2	67	67	1.3	0.0160	0.0089	6
10	114	32	42	3	-7.2	67	67	1.3	0.0160	0.0089	6
11	114	32	42	3	-6.0	67	67	1.3	0.0160	0.0089	6
12	114	32	42	3	-6.0	67	67	1.3	0.0160	0.0089	6
13	114	32	36	3	-6.0	67	67	1.3	0.0190	0.0075	6
14	114	32	36	3	-6.0	67	67	1.3	0.0180	0.0075	6
15	114	32	36	3	-6.0	67	67	1.3	0.0170	0.0075	6
16	114	32	36	3	-6.0	67	67	1.3	0.0160	0.0075	6
17	114	32	36	3	-6.0	67	67	1.3	0.0145	0.0075	6
18	114	32	36	3	-6.0	67	67	1.3	0.0130	0.0075	6
19	114	32	36	3	-6.0	67	67	1.3	0.0130	0.0075	6
20	114	32	36	3	-6.0	67	67	1.3	0.0120	0.0075	6

Table 7.4. Design document for the beams in 20F060136.

Story	*L* (in)	*b* (in)	*h* (in)	*c* (in)	f_c (ksi)	f_{yl} (ksi)	f_{yt} (ksi)	*T/Y*	ρ_l	ρ_{sh}	s/d_b
1	198	32	42	3	-6.0	67	67	1.3	0.0123	0.0049	6
2	198	32	42	3	-6.0	67	67	1.3	0.0135	0.0053	6
3	198	32	42	3	-6.0	67	67	1.3	0.0135	0.0053	6
4	198	32	42	3	-6.0	67	67	1.3	0.0133	0.0052	6
5	198	32	42	3	-6.0	67	67	1.3	0.0138	0.0054	6
6	198	32	42	3	-6.0	67	67	1.3	0.0133	0.0052	6
7	198	32	42	3	-6.0	67	67	1.3	0.0136	0.0053	6
8	198	32	42	3	-6.0	67	67	1.3	0.0128	0.0050	6
9	198	32	42	3	-6.0	67	67	1.3	0.0130	0.0051	6
10	198	32	42	3	-6.0	67	67	1.3	0.0123	0.0049	6
11	198	32	42	3	-6.0	67	67	1.3	0.0118	0.0047	6
12	198	32	42	3	-6.0	67	67	1.3	0.0113	0.0045	6
13	204	32	42	3	-6.0	67	67	1.3	0.0108	0.0042	6
14	204	32	42	3	-6.0	67	67	1.3	0.0100	0.0040	6
15	204	32	42	3	-6.0	67	67	1.3	0.0094	0.0038	6
16	204	32	42	3	-6.0	67	67	1.3	0.0084	0.0034	6
17	204	32	42	3	-6.0	67	67	1.3	0.0066	0.0029	6
18	204	32	42	3	-6.0	67	67	1.3	0.0066	0.0028	6
19	204	32	42	3	-6.0	67	67	1.3	0.0066	0.0028	6
20	204	32	42	3	-6.0	67	67	1.3	0.0066	0.0028	6

7.2 Results for 20-Story Frame

The design with Grade 60 reinforcement has a first-model period of the T_1 equal to 2.67 sec; and the seismic design base shear is governed by the minimum shear of 0.044g in ASCE-7 (versus a value of 0.028g, which would otherwise be implied by the design earthquake spectrum assuming a seismic response factor of R equal to 8). Member sizes in the original frame design are generally controlled by minimum strength and stiffness requirements, capacity design requirements (for columns), and minimum reinforcing ratio (in the upper stories).

The frame response is evaluated for seismic hazard characteristics at the San Francisco (Site Class D) and Seattle (Site Class C). The major reason to include the second site Seattle is to exam the reinforcement performance under long-duration earthquakes. Table 7.5 lists MCE_R values at these two selected sites, along with the seismic intensity Sa (T_1 = 2.67 s) at six return periods. The San Francisco Site Class D has the same MCE_R as used in the original design, which is about 30% higher than the spectral acceleration hazards at the Seattle site. However, to the extent that the ASCE-7 minimum base shear controls the design, the frame designs would not be expected to vary much at the between the sites.

Table 7.5. MCE_R and Sa (T_1 = 2.67 s) at different intensity levels.

Hazard Level (Return Period)	***Sa* (T_1 = 2.67 s) (g)**	
	San Francisco (Site Class D)	Seattle (Site Class C)
MCE_R	0.337	0.257
10%/50yrs	0.288	0.081
5%/50yrs	0.389	0.122
2%/50yrs	0.556	0.191
2%/100yrs	0.698	0.255
2%/200yrs	0.840	0.329
1%/200yrs	1.004	0.413

As summarized in Table 7.6, the frames using higher steel grades (Gr. 80 and 100) have longer periods than the original design (Gr. 60), mainly due to reduced steel areas and larger yield curvatures, which reduce the effective member stiffness. The periods for the Gr. 80 and 100 designs are about 10% and 20% longer, respectively, then the original design. Also tabulated are the corresponding values of period-dependent spectral intensities for the MCE_R and 2% in 50-year seismic hazard. In addition to spectral acceleration, the table summarizes the *SaRatio* (a measure of ground motion spectral shape) and $Ds_{5\text{-}75}$ (a measure of ground motion duration), where hazards with smaller *SaRatio* values and longer $Ds_{5\text{-}75}$ values tend to be more damaging. In terms of spectral shape, the San Francisco Site Class D location has the lower (more damaging) *SaRatio*, and Seattle has the higher (less damaging) *SaRatio*. On the other hand, Seattle has the longer (more damaging) duration, compared to San Francisco.

Table 7.6. Site-specific seismic hazard metrics for unique designs.

	San Francisco (Site Class D)			Seattle (Site Class C)		
Grade	60	80	100	60	80	100
Period (sec)	2.67	2.95	3.20	2.67	2.95	3.20
MCE (2% in 50 years) (g)	0.56	0.51	0.47	0.19	0.17	0.15
MCE_R (g)	0.34	0.31	0.28	0.26	0.23	0.21
$SaRatio$ ($0.2T_1$, T_1, $3.0T_1$)	1.64	1.60	1.58	1.78	1.77	1.75
$D_{S5\text{-}75}$ (sec)	16.6	17.1	17.6	26.2	26.6	26.8

7.2.1 Illustration of Response History for Gr. 60 and Gr. 100 Frames

All twenty-seven 20-story frame designs were analyzed under 88 ground motion records which are incrementally scaled up until collapse occurs (determined when the story drift ratio, $SDR_{max} > 0.1$). In this section, detail results from two of the archetype buildings are selected to (1) demonstrate the application of the assessment framework and (2) to provide an overview of how the response and safety risks (bar fracture and collapse) vary as a function of reinforcing bar properties. The comparison is between the 20-story frames with Gr. 60 (T/Y = 1.4) and 100 (T/Y = 1.2) bars, with s/d_b = 4, i.e., cases 20F060144 and 20F100124. Results are compared for one of the ground motions (YERMO270.th), as shown in Figure 7.1, which has a 5%-damped response spectrum that is close to the MCE_R spectrum per ASCE-7 for San Francisco (Site Class D).

Figure 7.2 shows the story drift ratio (SDR) histories for story 3, which experienced the maximum SDR under the YERMO270.th motion scaled to Sa (T_1 = 2.67s) = 0.40g, which is a bit higher than the MCE_R level for both structures (Table 7.5). The maximum SDR demand of 0.057 in the Gr. 100 building is roughly 20% higher than the demand of 0.047 in the Gr. 60 building. Interestingly, the difference in drifts roughly corresponds to the difference in building period, which is consistent with expected differences in the elastic spectral displacement. Note that these drifts are at the high end of what is considered acceptable for new buildings, where for example, chapter 16 of ASCE 7-16 limits the average peak story drift at MCE_R to 0.04.

Following the procedure described in Section 4.2, the lateral story displacement history is applied to a fiber-based beam-column element to calculate the reinforcing bar strains. The hysteresis loops of two external columns from Gr. 60 and Gr. 100 designs are compared in Figure 3, and the resulting strain demands are plotted in Figure 7.4. The two plots in Figure 7.4 represent the demands in reinforcing bars on opposite sides of the column.

The maximum steel strain of ~0.08 in the Gr. 100 column is roughly 15% more than the strain of ~0.07 in the Gr. 60 column. Substituting the steel strain histories of Figure 7.4 into the fatigue-fracture model (Chapter 3), the fracture index (FI) histories are computed and shown in Figures 7.5 and 7.6 for the Gr. 60 and Gr. 100 buildings, respectively. In spite of the large peak strain demands, the resulting bar fracture indices (FI = 0.5 to 0.6) and fracture probabilities (6% to 13%) are rather modest. This is explained by the relatively small number of large-amplitude loading cycles. As shown in the right-top plot of Figure 7.5 and 7.6, of the 21 half-cycles used in the rain-flow fracture calculations, only 3 excitations exhibit damaging plastic strain amplitudes (> 0.01). This is contrast to the large number of high strain cycles resulting from common test protocols (like ACI 374.2R-13 or FEMA 461) used to evaluate RC test specimens.

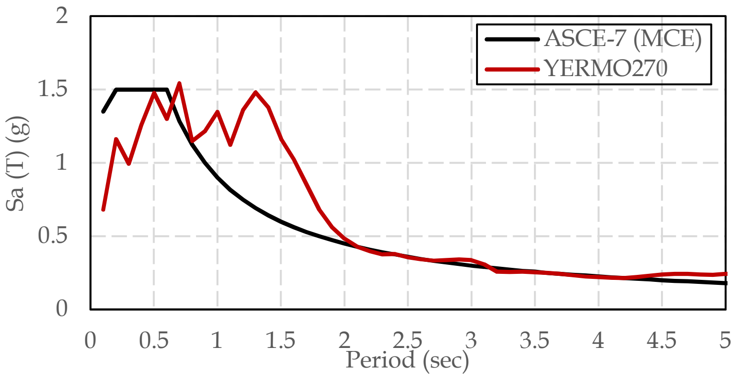

Figure 7.1. *MCE*R spectrum at San Francisco site and the scaled 5%-damped PSA of YERMO270.

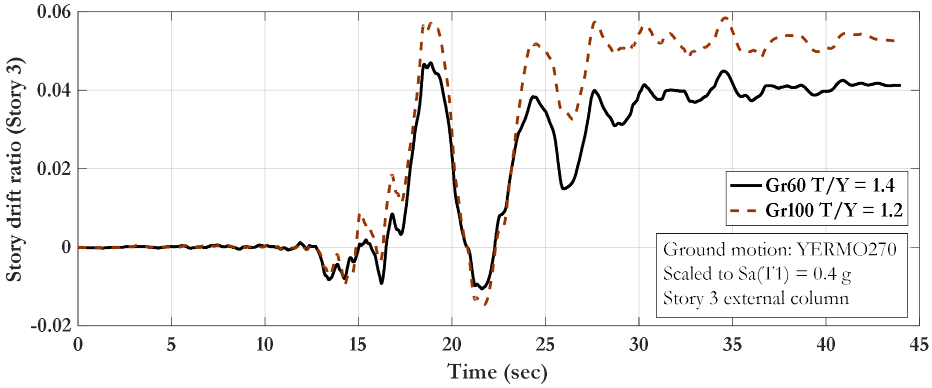

Figure 7.2. Story drift ratio histories of most-deformed story in 2 buildings under *Sa* = 0.4 g shaking by YERMO270.th

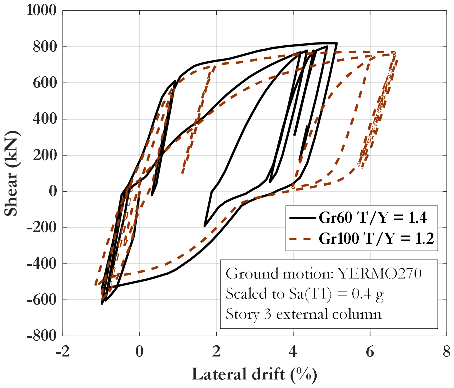

Figure 7.3. External column hysteretic behaviors under YERMO270.th (*Sa* = 0.4 g).

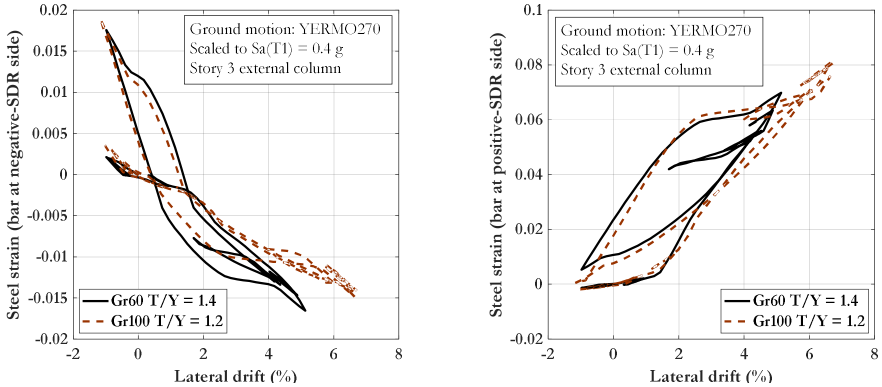

Figure 7.4. Steel strain vs. lateral drift ratio in the external column under YERMO270.th (*Sa* = 0.4 g).

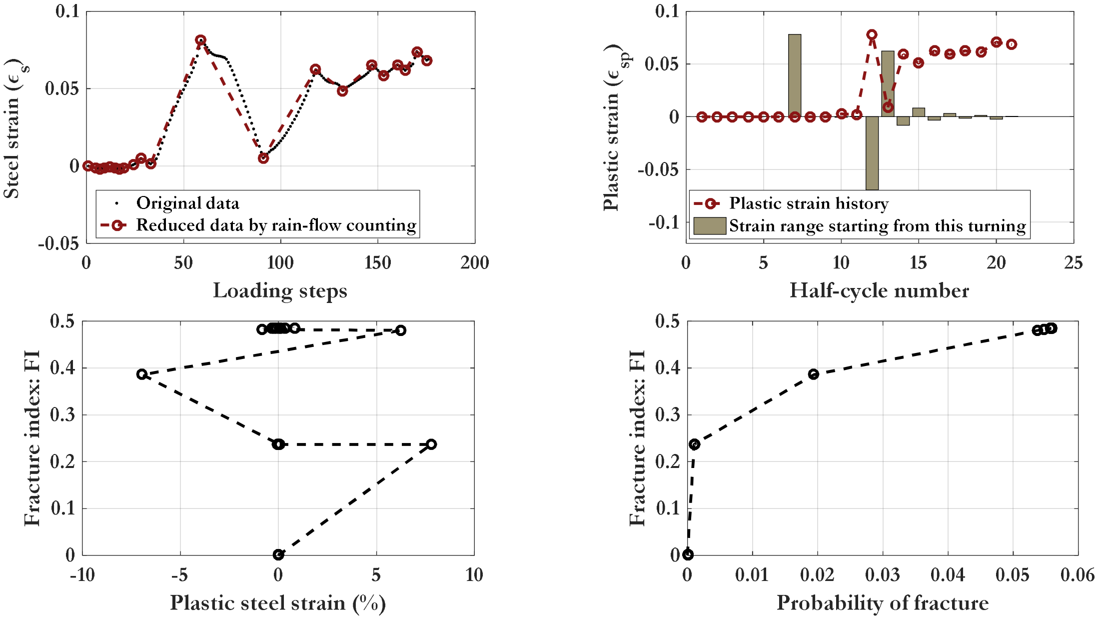

Figure 7.5. Fracture index (*FI*) history and the fracture probability in the worst column in the 20F060144.

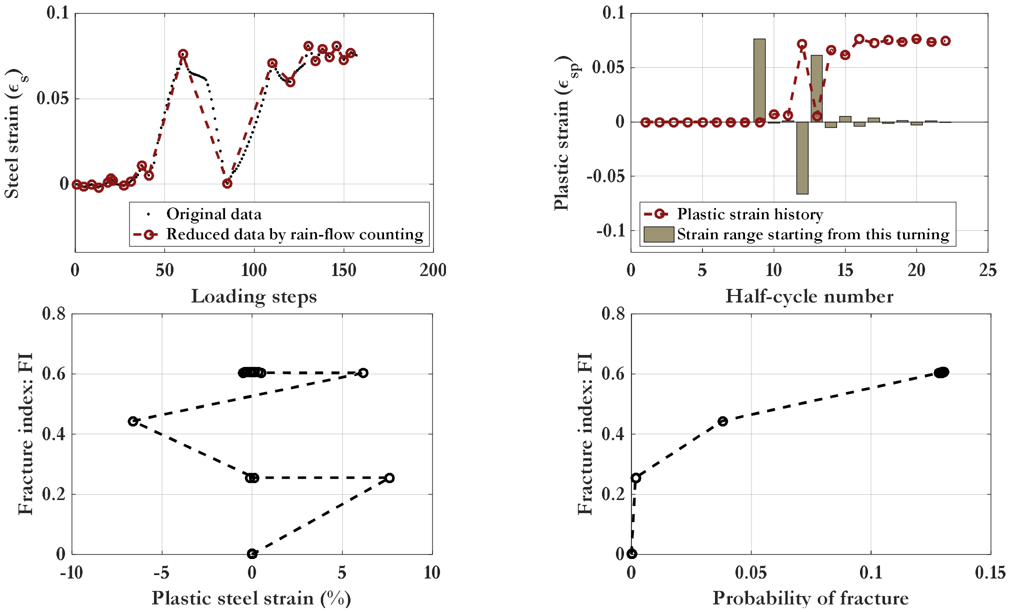

Figure 7.6. Fracture index (*FI*) history and the fracture probability in the worst column in the 20F100124.

7.2.2 Peak Story Drift Ratio

The peak (or maximum) story drift ratio (SDR_{max}) is defined as the largest lateral story drift along the building height under a given ground motion. Figure 7.7 plots the SDR_{max} against the ground motion intensity $Sa(T)$ for all 88 records. Instead of taking vertical slice of IDA curves at 10% drift to create a collapse fragility curve (e.g., as done in the FEMA P695 procedure), horizontal stripes of SDR_{max} data can be extracted at specific Sa intensity levels. Following the procedure described in Chapter 6, the drift demands from the raw incremental dynamic analysis (IDA) curve are then adjusted using the hazard-consistent procedure to represent the site-specific ground motion spectral shape and duration. To simplify comparisons of response between the buildings, the results for the three building designs with variable steel grades (60, 80 and 100) are adjusted and reported in terms of a consistent hazard intensity based on the fundamental period of the Gr. 60 building, T_1 = 2.67 sec.

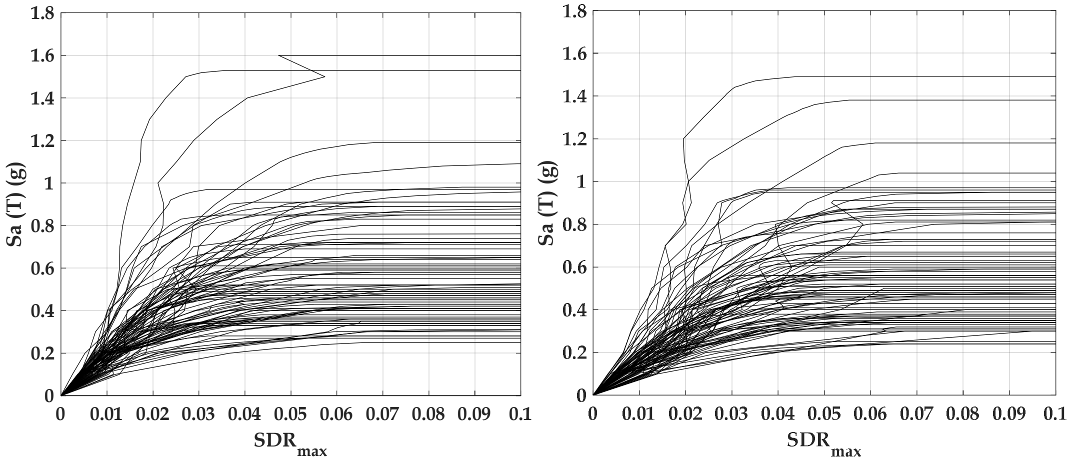

Figure 7.7. IDA curves under 88 ground motions. Left: 20F060136. Right: 20F100125.

Summarized in Table 7.7 are the adjusted mean SDR_{max} under MCE_R intensity ground motions for all of the 20-story archetype building designs. Note that the drift statistic calculations exclude the raw IDA results that exhibit excessive (collapse) drifts at the specified intensity level. So, for example, the mean SDR_{max} values for the buildings at the San Francisco Site Class D location exclude data from 16% to 26% of the ground motions, which exhibited excessive (collapse) drifts in these analyses. Note, because these data are from the raw (unadjusted) IDA results (without the hazard-consistent spectral shape adjustment), the ground motions with excessive drift do not correspond to actual MCE_R collapse rates. Rather, collapse rates are addressed separately using the FEMA P695 procedure.

Referring to Table 7.7, the Gr. 80 and Gr. 100 buildings have drifts that are roughly 7 to 13% and 10 to 20% larger than the baseline case 20F060136, which has average drifts of ~0.025 for the San Francisco site and ~0.015 for the Seattle site. The increased drifts for the buildings with higher grade steel are primarily attributed to the differences in initial stiffness and periods in those designs (e.g., see building periods in Table 7.3). Overall, these average peak MCE_R drifts are well within the range that is considered acceptable by ASCE 7 and the PEER TBI guidelines (e.g., Chapter 16 of ASCE 7-16 limits the average $SDR_{max,MCE}$ to 0.04, and PEER TBI limits the drift to 0.03). The T/Y ratios have a negligible effect on the drifts, which is not surprising given the moderate amount of frame yielding expected at these drift values.

Table 7.7. Mean SDR_{max} demands of 20-story archetypes at MCE_R intensity level.

	San Francisco (Site Class D) MCE_R = 0.34g			Seattle (Site Class C) MCE_R = 0.26g		
	$s/d_b = 4$	$s/d_b = 5$	$s/d_b = 6$	$s/d_b = 4$	$s/d_b = 5$	$s/d_b = 6$
20F06015-	0.0254	0.0246	0.0245	0.0155	0.0153	0.0153
20F06014-	0.0251	0.0246	0.0245	0.0156	0.0154	0.0154
20F06013-	0.0254	0.0246	0.0240	0.0158	0.0156	0.0156
20F08014-	0.0275	0.0268	0.0267	0.0166	0.0167	0.0167
20F08013-	0.0271	0.0271	0.0269	0.0168	0.0169	0.0169
20F08012-	0.0266	0.0266	0.0266	0.0170	0.0171	0.0171
20F10013-	0.0280	0.0283	0.0282	0.0178	0.0181	0.0181
20F10012-	0.0285	0.0286	0.0285	0.0180	0.0184	0.0184
20F10011-	0.0280	0.0284	0.0284	0.0182	0.0185	0.0185

7.2.3 Cumulative Plastic Strain

As noted previously, the reinforcing bar strain histories are obtained by converting the story drift history to equivalent chord rotation history (subtracting out joint rotations) which are input to the fiber beam-column analyses. The resulting strains are based on a nominal 8-inch gage length in the plastic hinge regions. Figure 7.8 shows the cumulative plastic strain demand (*CPD*) plots of both the most deformed beam and column in the benchmark 20F060136. Table 7.8 summarizes the maximum *CPD's* in all twenty-seven building design variants at the San Francisco (Site Class D) under MCE_R level earthquakes. Under the MCE_R the *CPDs* range from 0.10 to 0.13 for the Gr. 60 designs, with relatively slight increases (less than 10%) for the Gr. 80 and 100 designs. The *CPDs* are reported as absolute strain values. When normalized by the yield strains (~0.0021 for Gr. 60 up to ~0.0034 for Gr. 100), the normalized average *CPDs* are in fact smaller for the higher strength steels - on the order of 62 (0.13/0.0021) for Gr. 60 and 41 (0.14/0.0034) for Gr. 100.

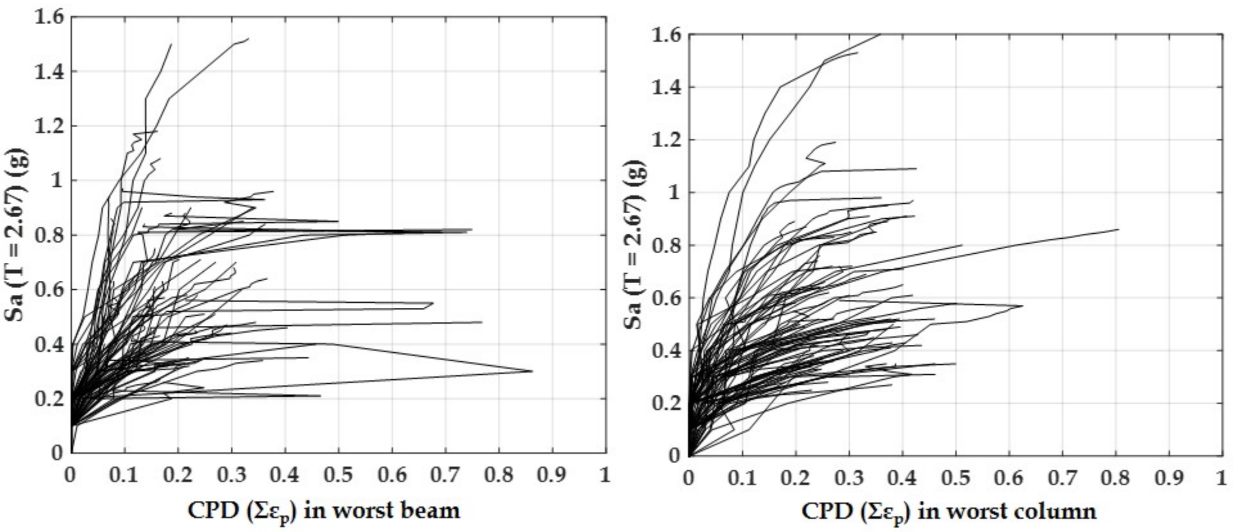

Figure 7.8. Cumulative plastic strain in the worst beam/column in the benchmark 20F060136.

Table 7.8. CPD_{max} of 20-story archetypes at San Francisco (Site Class D) MCE_R intensity level.

	San Francisco (Site Class D) MCE_R = 0.34g		
	s/d_b = 4	s/d_b = 5	s/d_b = 6
20F06015-	0.10	0.10	0.11
20F06014-	0.11	0.11	0.12
20F06013-	0.12	0.12	0.13
20F08014-	0.10	0.10	0.10
20F08013-	0.11	0.11	0.12
20F08012-	0.12	0.12	0.13
20F10013-	0.10	0.10	0.11
20F10012-	0.11	0.11	0.13
20F10011-	0.12	0.12	0.14

7.2.4 Maximum Fracture Index and Fracture Probability

Using the reinforcing bar strain histories from the members with the largest drift/deformation demands, reinforcing bar fracture indices (*FI*) and fracture probabilities are obtained using the fracture model described in Chapter 3. Figure 7.9 shows IDA type plots of the maximum *FI* for one 20-story frame (Gr. 60 *T/Y* = 1.4) which was subjected to the 88 ground motions. Note that all the *FI*-IDA curves in Figure 7.9 terminate when building collapse is detected based on excessive story drifts (SDR_{max} > 0.1). When the maximum *FI* at the end of the *FI*-IDA curve is much less than 1.0, then the collapse is deemed to be triggered by other failure modes rather than the rebar fracture. However, if the FI_{max} is considerable (e.g., approaching or exceeding 1.0), then there is a non-negligible risk of collapse triggered by reinforcing bar fractures. While fracture is not modeled directly in the nonlinear frame analyses, it is considered in evaluating the total collapse risk (further details of this are reported later).

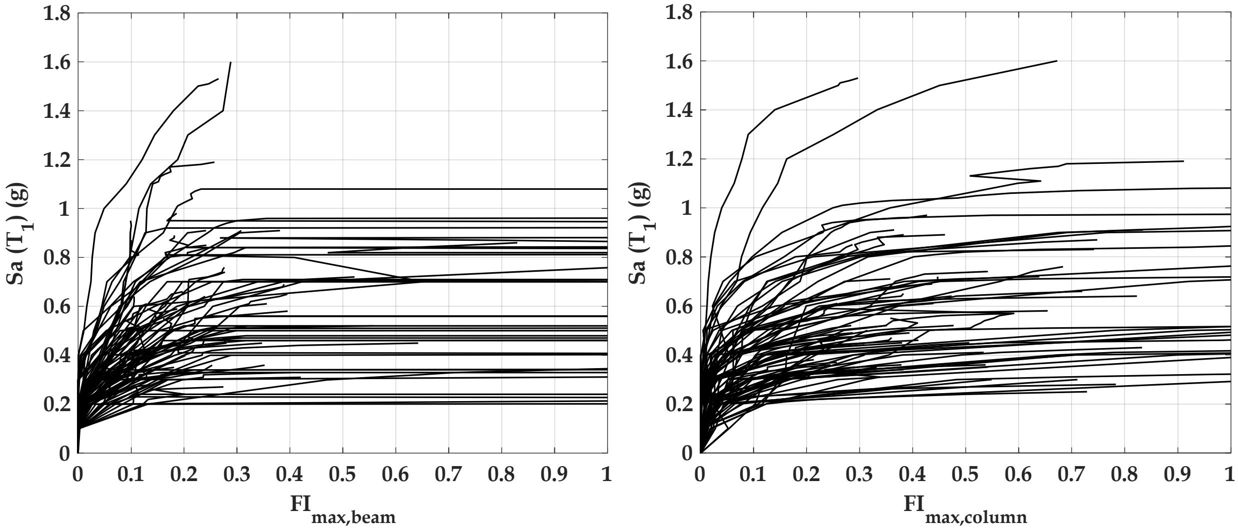

Figure 7.9. *FI*-IDA plots of the 20F060136 (baseline case) under 88 ground motions. Left: maximum *FI* in beams. Right: maximum *FI* in columns.

The median FI_{max} demands in columns under the site-specific MCE_R intensity are summarized in Table 7.9. Following from how the MCE_R story drift and strain demands are computed, the *FI* demands are conditional on the non-collapse IDA data. As reported in Table 7.9, the FI_{max} demands are significantly higher for the San Francisco site, as compared to the Seattle site, owing to the higher spectral intensity and more damaging spectral shape in San Francisco. Thus, these spectral acceleration demands more than offset the effect of the longer duration ground motions in Seattle. Therefore, the following discussion will be focused only on the San Francisco site.

Although the overall bar *FI* is very small, even for the San Francisco site, three trends are observed: (1) FI_{max} increases as steel grade increases; (2) FI_{max} increases as *T/Y* decreases; and (3) FI_{max} increases as s/d_b increases. The last two trends are also shown in Figure 7.10, 7.11, and 7.12 for Gr. 60, Gr.80, and Gr. 100 archetypes, respectively.

Table 7.9. Estimated median FI_{max} in columns at MCE_R intensity levels.

	Site	San Francisco (Site Class D) $MCE_R = 0.34g$	Seattle (Site Class C) $MCE_R = 0.26g$
Archetype ID	20F060154	0.020	0.001
	20F060144	0.025	0.002
	20F060134	0.034	0.002
	20F060155	0.041	0.004
	20F060145	0.057	0.005
	20F060135	0.069	0.006
	20F060156	0.060	0.007
	20F060146	0.080	0.009
	20F060136*	0.087	0.010
	20F080144	0.038	0.004
	20F080134	0.047	0.005
	20F080124	0.052	0.005
	20F080145	0.064	0.006
	20F080135	0.084	0.007
	20F080125	0.091	0.008
	20F080146	0.092	0.009
	20F080136	0.113	0.011
	20F080126	0.129	0.013
	20F100134	0.048	0.004
	20F100124	0.063	0.005
	20F100114	0.088	0.007
	20F100135	0.074	0.007
	20F100125	0.091	0.009
	20F100115	0.108	0.010
	20F100136	0.092	0.012
	20F100126	0.114	0.015
	20F100116	0.144	0.016

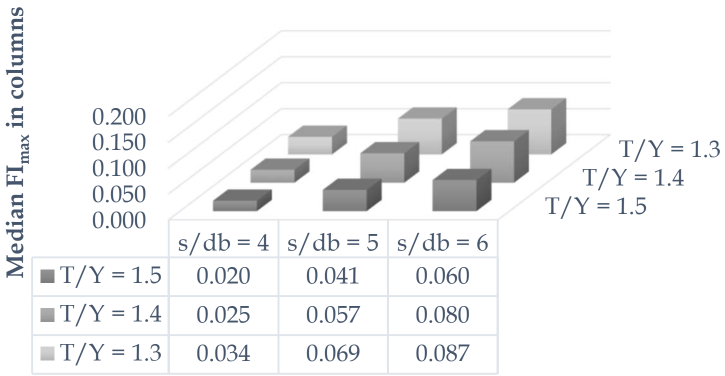

Figure 7.10. Median FI_{max} in columns of Gr. 60 archetypes at San Francisco (Site Class D, MCE_R).

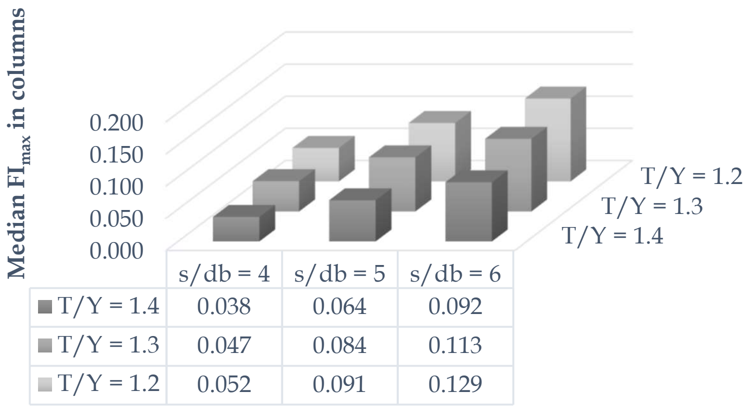

	s/db = 4	s/db = 5	s/db = 6
■ T/Y = 1.4	0.038	0.064	0.092
■ T/Y = 1.3	0.047	0.084	0.113
■ T/Y = 1.2	0.052	0.091	0.129

Figure 7.11 Median FI_{max} in columns of Gr. 80 archetypes at San Francisco (Site Class D, MCE_R).

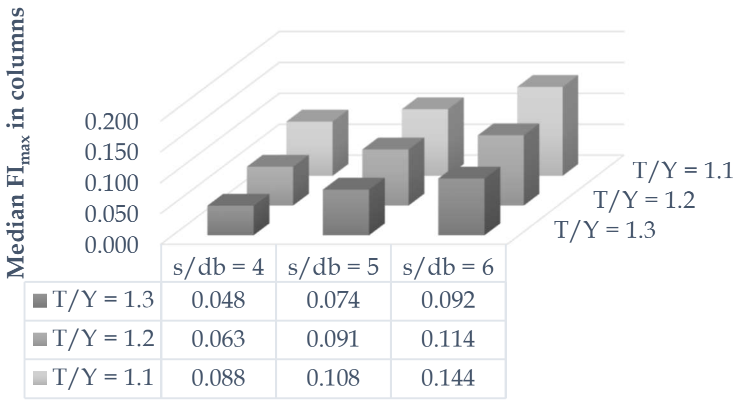

	s/db = 4	s/db = 5	s/db = 6
■ T/Y = 1.3	0.048	0.074	0.092
■ T/Y = 1.2	0.063	0.091	0.114
■ T/Y = 1.1	0.088	0.108	0.144

Figure 7.12. Median FI_{max} in columns of Gr. 100 archetypes at San Francisco (Site Class D, MCE_R).

Notwithstanding that the median MCE_R *FI* demands in all of the 20-story archetypes are small, roughly ranging from 0.02 to 0.15 as compared to the median *FI* of 1.0, the probabilities of fracture can still be determined using the fracture fragility model of Figure 3.12. Table 7.10 summarizes the resulting reinforcing bar fracture probabilities under the MCE_R ground motion hazard in San Francisco (Site Class D). The fracture probability of the benchmark case (frame # 20F060136) is 2.9%. The worst case among all twenty-seven archetypes is the 20F100116 case, whose fracture probability is roughly 4.2%. This increase in fracture probability is attributed to three contributing factors: (1) the Gr. 100 building is more flexible and subject to 15% to 20% more peak drift demands under the same level of shakings; (2) the smaller strain hardening (*T/Y* ratio) in 20F100116 leads to higher strain localization and cyclic strain demands; and (3) the smaller fracture-fatigue resistance in the Gr. 100 versus Gr. 60 bars, represented by the α_f and C_f in fatigue-fracture model.

The fracture probabilities for different combinations of steel grade, hardening (*T/Y*) ratios, and tie spacing (s/d_b) are compared in Figures 7.13 to 7.15. Assuming a goal (criteria) of not exceeding the fracture probability in the worst Gr. 60 case (*T/Y* = 1.3 and s/d_b=6) would lead to the following design limitations (recommendations) for frames with high strength reinfrocement : (1) limiting the minimum median hardening ratio (*T/Y*) to 1.2, and (2) limiting the maximum tie spacing ratio (s/d_d) to 5, as opposed to the current minimum of 6. Another observation from Figures 7.13 to 7.15 is that the fracture potential is slightly more sensitive towards the tie spacing as compared to the hardening ratio.

Table 7.10. Estimated rebar fracture probability under MCE_R

	Site	San Francisco (Site Class D), MCE_R = 0.34g
Archetype ID	20F060154	1.50%
	20F060144	1.68%
	20F060134	1.83%
	20F060155	1.82%
	20F060145	2.16%
	20F060135	2.41%
	20F060156	2.28%
	20F060146	2.69%
	20F060136*	2.87%
	20F080144	2.13%
	20F080134	2.28%
	20F080124	2.51%
	20F080145	2.22%
	20F080135	2.35%
	20F080125	2.72%
	20F080146	2.64%
	20F080136	2.82%
	20F080126	3.26%
	20F100134	1.99%
	20F100124	2.57%
	20F100114	3.51%
	20F100135	2.02%
	20F100125	2.83%
	20F100115	3.85%
	20F100136	3.15%
	20F100126	3.42%
	20F100116	4.20%

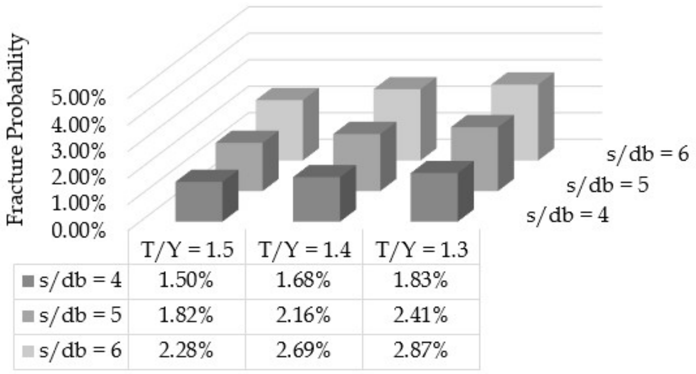

Figure 7.13. Fracture probability of Gr. 60 archetypes at San Francisco (Site Class D, MCE_R)

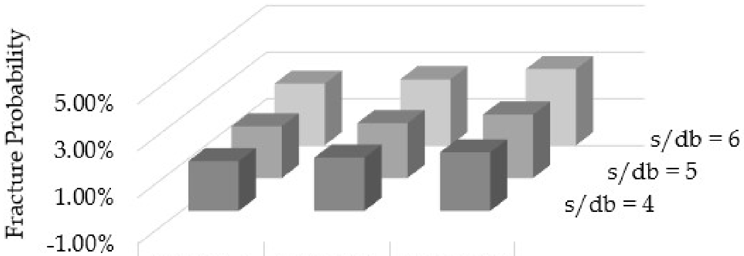

	T/Y = 1.4	T/Y = 1.3	T/Y = 1.2
■ s/db = 4	2.13%	2.28%	2.51%
■ s/db = 5	2.22%	2.35%	2.72%
■ s/db = 6	2.64%	2.82%	3.26%

Figure 7.14. Fracture probability of Gr. 80 archetypes at San Francisco (Site Class D, MCE_R)

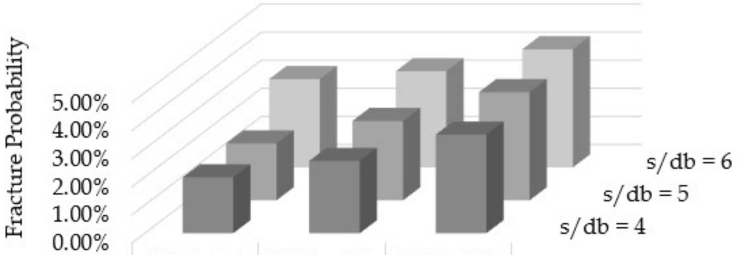

	T/Y = 1.3	T/Y = 1.2	T/Y = 1.1
■ s/db = 4	1.99%	2.57%	3.51%
■ s/db = 5	2.02%	2.83%	3.85%
■ s/db = 6	3.15%	3.42%	4.20%

Figure 7.15. Fracture probability of Gr. 100 archetypes at San Francisco (Site Class D, MCE_R)

7.2.5 Maximum Fracture Index vs. Maximum Story Drift Ratio (FI_{max}-SDR_{max})

As an alternative to evaluating the reinforcing bar *FI* and fracture probability at a specific ground motion intensity, the *FI* and fracture probability can be conditioned on the story drift demand, *SDR*. This comparison helps to minimize subjectivity of results to the specific archetype building design and would instead provide a more direct assessment relative to minimum building code criteria, i.e., maximum drifts permitted by the building code. Figure 7.16 shows the maximum fracture index versus the maximum story drift ratio under each non-collapse ground motion for the 20-story building with Gr. 60 bars (20F060136). The maximum fracture index is 0 before the first yield event occurs somewhere in the building, after which the FI_{max} increases as SDR_{max} increases. The FI_{max} of the worst beam grows faster than the FI_{max} of the worst column at relatively small story drift ratios (i.e., SDR_{max}<0.03 in 20F060136), which is consistent with the strong-column-weak-beam design philosophy. Under increasing drifts, FI_{max} demands for beams increase less quickly as compared to columns, which is related to the redistribution of plastic deformation demands and the larger bar-slip in the beams (which tends to reduce strain demands for a given deformation demand). The median FI_{max} in the building is roughly 0.3 at SDR_{max} of 0.04. As indicated in the fracture probability chart in Table 7.11, the fracture probability corresponding to *FI* equal to 0.3 is still less than 1%.

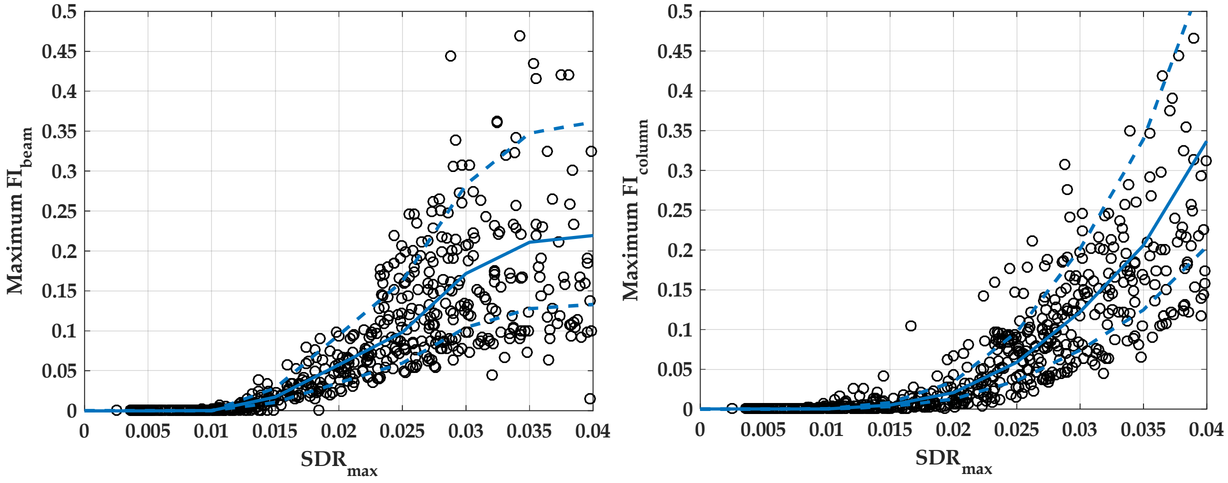

Figure 7.16. Maximum fracture index vs. Maximum story drift ratio in 20F060136 under all non-collapse ground motions. Left: fracture index in worst beams. Right: fracture index in worst columns.

Table 7.11. Fracture probability given fracture index value.

Fracture index	0.0	0.1	0.2	0.3	0.4	0.5	0.6	0.7	0.8	0.9	1.0
Fracture probability	0.0%	0.0%	0.1%	0.8%	3.3%	8.3%	15.3%	23.8%	32.8%	41.7%	50.0%

Figure 7.17 shows the median FI_{max} vs. SDR_{max} relations in Gr. 80 archetypes along with the benchmark case. Three buildings using Gr. 80 bars with T/Y of 1.4 tend to have lower fracture probabilities than the Gr. 60 benchmark (T/Y of 1.3) case. For Gr. 80 with T/Y of 1.3, the worst building is the one having s/d_b of 6 tie spacing, whose FI_{max} exceeds the benchmark value at large drifts. In the group of Gr. 80 with T/Y of 1.2, the building with s/d_b of 5 tie spacing has comparable FI_{max} to the benchmark; while the building with s/d_b of 6 tie spacing tends to have higher fracture potential when SDR_{max} exceeds 0.025.

Figure 7.18 shows the median FI_{max} vs. SDR_{max} relations in Gr. 100 archetypes along with the Gr. 60 benchmark case. Three buildings using Gr. 100 bars with T/Y of 1.3 generally have lower fracture demands than the benchmark. The worst case among Gr. 100 bars with T/Y of 1.2 is the building having s/d_b of 6 tie spacing, whose FI_{max} surpasses the benchmark at large drifts. In the group of Gr. 100 with T/Y of 1.1, both the buildings with s/d_b of 5 and 6 tie spacings have higher fracture demands when SDR_{max} exceeds 0.03.

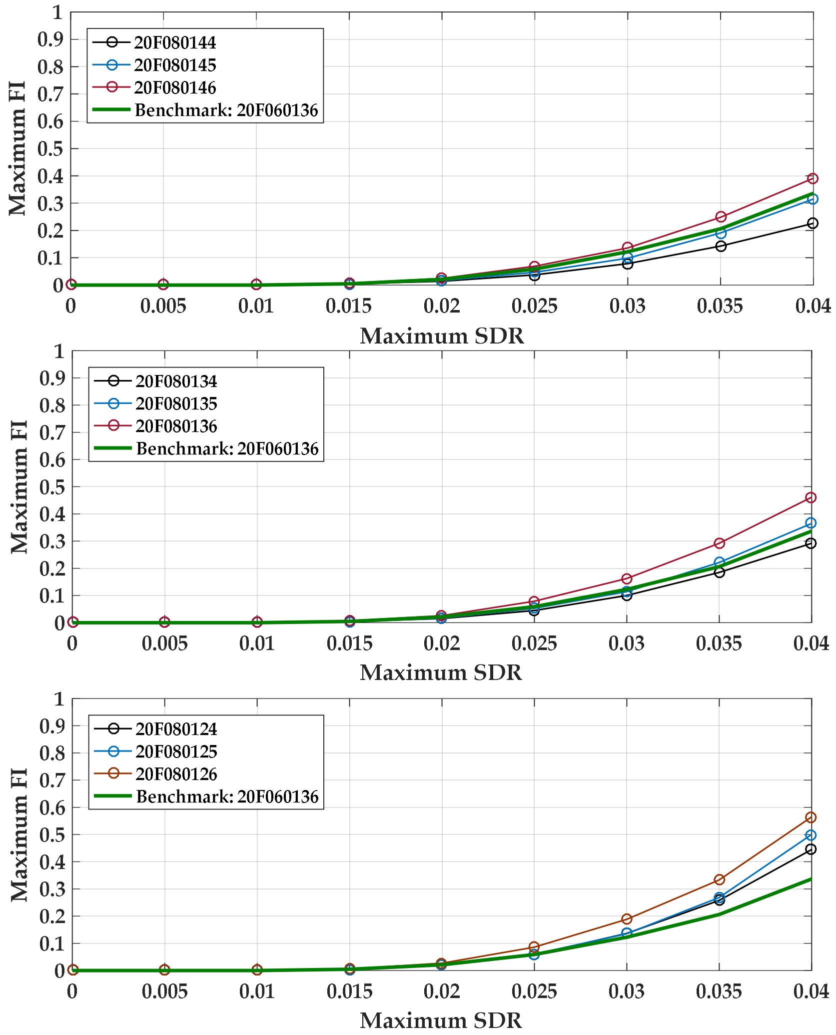

Figure 7.17. Median FI_{max} vs. SDR_{max}. Top: 20F08014X archetypes and the benchmark. Middle: 20F08013X and archetypes and the benchmark. Bottom: 20F08012X archetypes and the benchmark.

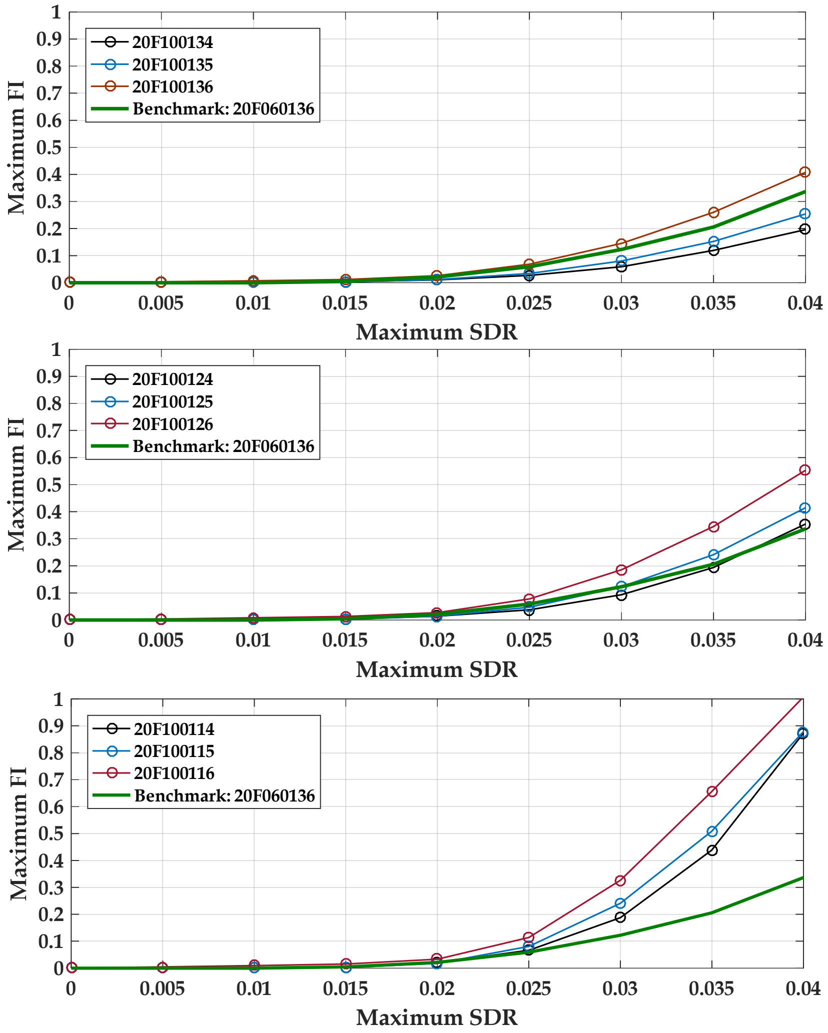

Figure 7.18. Median FI_{max} vs. SDR_{max}. Top: 20F10013X archetypes and the benchmark. Middle: 20F10012X and archetypes and the benchmark. Bottom: 20F10011X archetypes and the benchmark.

Another important observation is that for two building designs of equivalent strength, the design with high-strength reinforcement yields at a relatively larger drift ratio (SDR ~0.015) as compared to the Gr. 60 reinforcement (SDR ~0.010). This delayed yield point means potentially less plastic strain demand in those buildings under the same drift ratio as the benchmark (e.g, 20F100116 is a good but extreme example whose FI_{max} is smaller than the benchmark at SDR ~0.02). Nevertheless, it is also observed that buildings with high-strength bars tend to deform about 10% to 20% more under the same intensity ground motions. This provides an alternative solution dealing with low-T/Y and large-s/d_b designs, instead of enforcing stricter limits on T/Y and s/d_b, a stricter drift limit (e.g., $SDR_{max} < 0.03$) could be imposed on the overall system design.

Finally, it is useful to note that the slope of FI_{max}-SDR_{max} curve is an implicit measure of structural ductility with respect to fracture risk. The steeper the slope is, the faster the fracture index would reach at a critical value, and thus, the narrower the safety margin between the first yield and the fracture occurrence. From this perspective, an argument to minimize fracture risk could be made against permitting the 20-story frame with Gr. 100 steel with a low T/Y ratio (~1.1), i.e., frame ID 20F100114.

7.2.6 Collapse Risk

Collapse is deemed as a small probability risk for buildings designed per current building codes (e.g., 10% collapse probability under a MCE_R ground motions). So, comparison of collapse risk is helpful to evaluate the implications of changing design requirements, such as by allowing high strength reinforcement. FEMA P695 outlines a systematic methodology to evaluate the collapse fragility through adjusting IDA results by the period-dependent factor to account for spectral shape associated with extreme (MCE_R) ground motion hazard. Briefly, the procedure entails the following steps: (1) analyzing the structural responses under 44 incrementally scaled ground motions until collapse (i.e., maximum story drift ratio exceeding 10%); (2) determining the median collapse intensity from the IDA results, as shown in Figure 7.21 for example; (3) modifying the median collapse intensity by a spectral shape factor (*SSF*); (4) estimating the uncertainty of the collapse capacity including record-to-record (RTR), design requirements uncertainty (DR), test data uncertainty (TD), and modeling uncertainty (MDL), which leads to a total dispersion usually at 0.5~0.6; (5) examining the collapse probability under MCE_R per the 10% limitation; or alternatively checking the adjusted collapse margin ratio (*ACMR*) to the prescribed limit.

An additional concern in this study is whether premature reinforcing bar fracture failure would accelerate the strength deterioration and cause collapse of the building. The fracture-induced collapse is handled as the so-called non-simulated collapse modes, which is not modeled explicitly in the nonlinear analysis and instead is evaluated as a critical limit state in the analysis. This is done because, with current analysis technology, bar fracture is numerically difficult to directly simulate fracture failures in the incremental dynamic analysis.

Following the recommendation of FEMA P695, the non-simulated fracture limit state checks are conducted by evaluating bar fracture demands. For instance, the red x-points indicated in the IDA plots of Figure 7.19 correspond to limit points where the maximum fracture index in the building first exceeds its median capacity (or expected value), i.e., $FI_{max} > 1.0$. The median capacity limit on FI_{max} is consistent with using median parameters for modeling structural components in the nonlinear IDA. Assuming the first occurrence of fracture will lead to collapse of the structure, the red dashed lines result in lower collapse intensities for those ground motions. While the assumption that the first bar fracture triggers collapse is a conservative assumption, as shown in Figure 7.19 it does not dramatically shift the median collapse intensity. While not ideal, this is a practical approach that provides a consistent method for evaluating effects from fatigue-fracture failure and its impacts on collapse that are otherwise difficult (or practically impossible with existing software) to explicitly included in the analysis model.

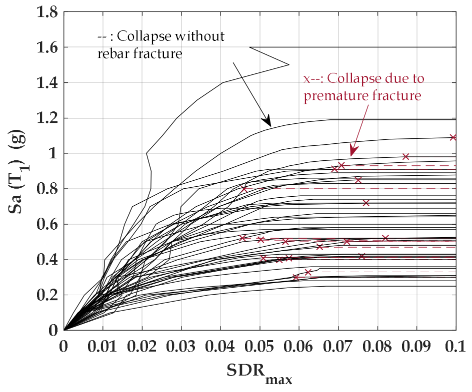

Figure 7.19. IDA results (under 44 FEMA P695 ground motions) integrated with non-simulated fracture-induced collapse modes for the benchmark (20F060136).

Table 7.12 summarizes the median collapse intensities (S_{CT}), along with *CMR*, *ACMR*, and adjusted median collapse intensities (S_{CT}*) for the twenty-seven archetype 20-story moment frame buildings. To simplify the comparison, the period-dependent ductility ratio and the spectral shape factor is fixed at 5.60 and 1.49, respectively, which are the same as the original (Gr. 60) design. Compared to the case excluding fracture-induced failures, the median collapse capacity reduces by 2% to 5%. Note that the S_{CT}'s listed here are at period of 3.36 sec, which is the code-based fundamental period of this 20-story frame. Considering the RTR and modeling uncertainty in estimating the collapse fragility, the dispersion is, as suggested by FEMA P695, fixed at 0.5 for all archetypes. Table 7.13 summarizes the estimated collapse probability under MCE_R at San Francisco (Site Class D), i.e., Sa (T_1 = 3.36) = 0.27g. Compared to the case excluding fracture-induced failures, the collapse probability under MCE_R ground motions increases by 0.5% to 2.0%. One average, bar fracture increases the MCE_R risk of collapse by about 0.9% in the Gr. 60 (5.9% → 6.8%), 1.2% in the Gr. 80 archetypes (6.0% → 7.2%), and 1.4% in the Gr. 100 archetypes (7.6% → 9.0%) under MCE_R.

Table 7.12. Adjustment of collapse fragility.

				Excluding fracture-induced collapse				Including fracture-induced collapse			
Archetype	μ_T	β_1	*SSF*	S_{CT} (g)	*CMR*	*ACMR*	S_{CT}* (g)	S_{CT} (g)	*CMR*	*ACMR*	S_{CT}* (g)
20F060154	5.60	0.27	1.49	0.42	1.65	2.45	0.62	0.41	1.60	2.39	0.60
20F060144	5.60	0.27	1.49	0.40	1.57	2.34	0.59	0.39	1.53	2.28	0.58
20F060134	5.60	0.27	1.49	0.38	1.50	2.23	0.57	0.37	1.46	2.17	0.55
20F060155	5.60	0.27	1.49	0.40	1.57	2.33	0.60	0.39	1.57	2.33	0.58
20F060145	5.60	0.27	1.49	0.39	1.53	2.28	0.58	0.38	1.49	2.22	0.56
20F060135	5.60	0.27	1.49	0.37	1.50	2.23	0.56	0.36	1.46	2.17	0.54
20F060156	5.60	0.27	1.49	0.40	1.57	2.33	0.60	0.39	1.57	2.33	0.58
20F060146	5.60	0.27	1.49	0.39	1.53	2.28	0.58	0.38	1.46	2.17	0.56
20F060136*	5.60	0.27	1.49	0.38	1.46	2.17	0.56	0.36	1.42	2.11	0.54
20F080144	5.60	0.27	1.49	0.41	1.59	2.38	0.61	0.39	1.57	2.33	0.59
20F080134	5.60	0.27	1.49	0.39	1.52	2.26	0.58	0.37	1.49	2.22	0.56
20F080124	5.60	0.27	1.49	0.37	1.43	2.14	0.55	0.36	1.38	1.97	0.53
20F080145	5.60	0.27	1.49	0.40	1.53	2.28	0.60	0.38	1.49	2.22	0.57
20F080135	5.60	0.27	1.49	0.38	1.49	2.22	0.57	0.37	1.42	2.11	0.55
20F080125	5.60	0.27	1.49	0.36	1.42	2.11	0.54	0.35	1.34	2.00	0.52
20F080146	5.60	0.27	1.49	0.40	1.53	2.28	0.60	0.38	1.49	2.22	0.57
20F080136	5.60	0.27	1.49	0.39	1.49	2.22	0.57	0.37	1.38	2.06	0.55
20F080126	5.60	0.27	1.49	0.37	1.42	2.11	0.54	0.35	1.34	2.00	0.52
20F100134	5.60	0.27	1.49	0.39	1.51	2.25	0.58	0.37	1.42	2.11	0.56
20F100124	5.60	0.27	1.49	0.37	1.42	2.12	0.55	0.36	1.38	2.06	0.53
20F100114	5.60	0.27	1.49	0.35	1.33	1.99	0.52	0.34	1.31	1.95	0.50
20F100135	5.60	0.27	1.49	0.39	1.46	2.17	0.58	0.37	1.38	2.06	0.56
20F100125	5.60	0.27	1.49	0.37	1.38	2.06	0.55	0.36	1.34	2.00	0.53
20F100115	5.60	0.27	1.49	0.35	1.31	1.95	0.52	0.33	1.27	1.89	0.50
20F100136	5.60	0.27	1.49	0.39	1.46	2.17	0.58	0.37	1.34	2.00	0.55
20F100126	5.60	0.27	1.49	0.37	1.38	2.06	0.55	0.35	1.31	1.95	0.52
20F100116	5.60	0.27	1.49	0.35	1.31	1.95	0.52	0.33	1.23	1.83	0.49

Table 7.13. Collapse probability under MCE_R (T = 3.36 sec) at San Francisco (Site Class D).

Archetype	Excluding fracture	Including fracture	Net impact
20F060154	4.71%	5.18%	0.47%
20F060144	5.57%	6.14%	0.56%
20F060134	6.54%	7.45%	0.91%
20F060155	5.30%	6.17%	0.87%
20F060145	6.10%	7.00%	0.90%
20F060135	7.12%	8.04%	0.92%
20F060156	5.29%	6.18%	0.89%
20F060146	6.01%	7.00%	0.99%
20F060136*	6.85%	7.89%	1.04%
20F080144	4.88%	5.83%	0.95%
20F080134	6.04%	7.10%	1.06%
20F080124	7.50%	8.70%	1.20%
20F080145	5.34%	6.50%	1.17%
20F080135	6.44%	7.68%	1.24%
20F080125	7.96%	9.23%	1.28%
20F080146	5.33%	6.60%	1.27%
20F080136	6.36%	7.70%	1.34%
20F080126	7.84%	9.21%	1.37%
20F100134	6.09%	7.15%	1.06%
20F100124	7.48%	8.60%	1.12%
20F100114	***9.42%***	***10.63%***	***1.20%***
20F100135	6.04%	7.10%	1.07%
20F100125	7.45%	8.68%	1.24%
20F100115	***9.39%***	***10.75%***	***1.36%***
20F100136	5.98%	7.27%	1.30%
20F100126	7.42%	9.03%	1.61%
20F100116	***9.36%***	***11.33%***	***1.97%***

Referring to Figure 7.20, excluding fracture, all of the archetypes pass the FEMA P695 seismic collapse criteria (10% collapse probability under MCE_R), where the three Gr. 100 frames with *T/Y* of 1.1 come closest to the boundary (~9%). When bar fracture is included, all archetypes still pass the FEMA P695 criteria with the notable exception of the Gr. 100 archetypes with *T/Y* = 1.1 steel (20F10011X's), which have collapse risks of ~11% that slightly exceed the 10% limit.

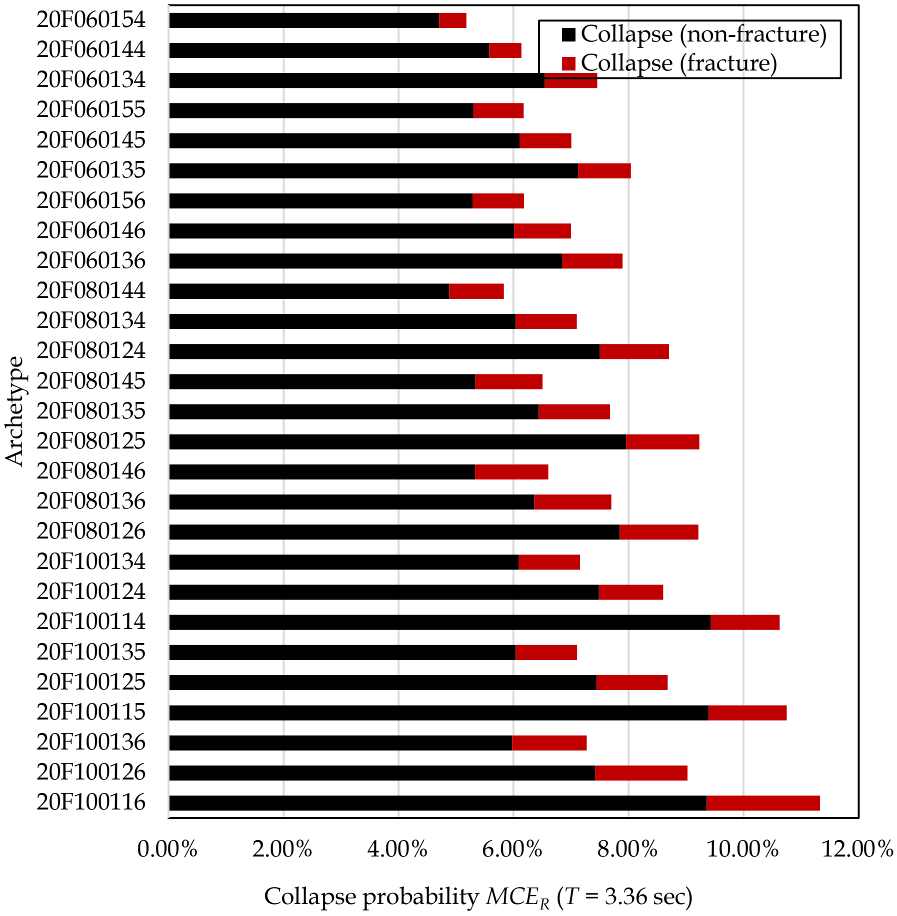

Figure 7.20. Collapse probability of all archetypes under MCE_R.

Figure 7.21 shows the collapse fragility curve of the Gr. 60 benchmark design (20F060136). The black curve represents the collapse fragility based on directly simulated failure modes. The grey curve shows the collapse probability due to non-simulated, fracture-induced failure modes. The red curve is the sum of the black and grey curves, and thus, is the total collapse fragility. These plots further illustrate the point that for this frame bar fracture has a small influence on the overall collapse risk.

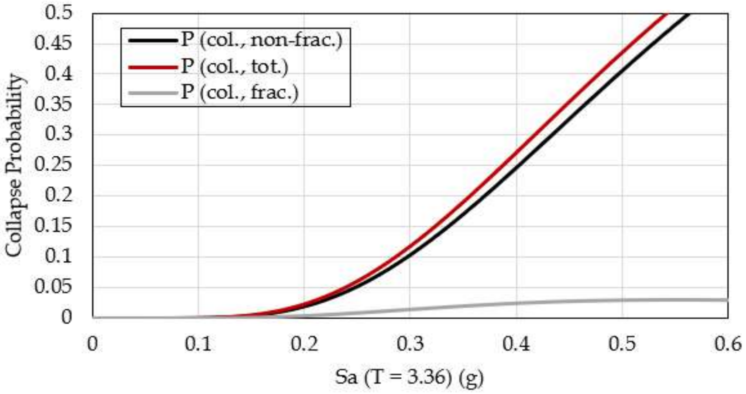

Figure 7.21. Collapse fragility curves (non-fracture, due-to-fracture, and total) of the benchmark 20F060136.

Figure 7.22 shows the comparison of collapse fragility curves for the "median case" of the three steel grades. The "median case" uses the middle value of *T/Y* (i.e., 1.4 for Gr.60, 1.3 for Gr. 80, or 1.2 for Gr. 100) and a tie spacing of 5. As indicated, while the collapse risk is slightly higher for the higher grade steels, all three curves are fairly close.

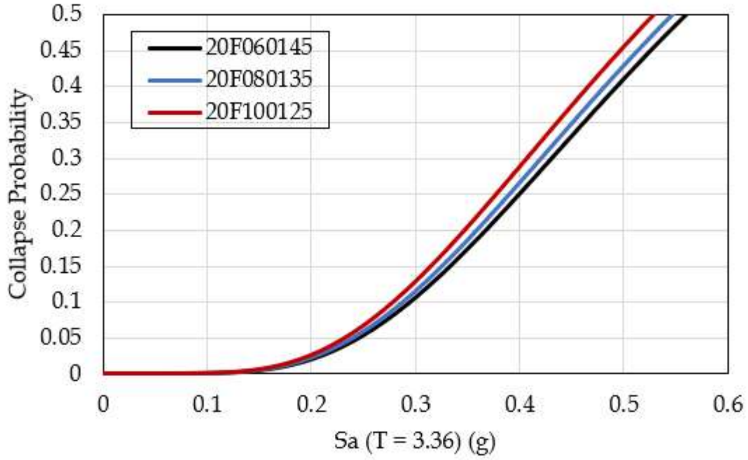

Figure 7.22. Total collapse fragility curves of 20F060145, 20F080135, and 20F100125.

Figure 7.23 isolates the effect of bar strain hardening (*T/Y* ratio), by comparing the collapse fragility curves for the three Gr. 100 archetypes, 20F100136, 20F100126, and 20F100116. The fragility curve for the Gr. 60 benchmark case is also shown. These plots demonstrate the negative impact of the smaller *T/Y* ratios, which cause strain-localization, which can aggravate material damage in the plastic hinge region, accelerate section strength deterioration, and increase the fracture potential.

Figure 7.24 isolates the effect of tie spacing by comparing the archetypes with Gr. 100 steel and s/d_b ratios of 4, 5 and 6 (archetypes20F100124, 20F100125, and 20F100126, plus the benchmark case 20F60136). As indicated, while the closer tie spacing offers some improvement in collapse safety, the effect of tie spacing on collapse is limited for this archetype.

The last comparison, shown in Figure 7.25, is between the collapse fragilities for two suggested minimum allowable design cases (Gr. 80 and 100 bars with *T/Y* = 1.2 and s/d_b = 5, archetypes 20F080125 and 20F100125) and a worst case (Gr. 100, *T/Y*=1.1 and s/d_b = 6, archetype 20F100116). The Gr. 60 benchmark case is also shown. The collapse fragilities of two minimum allowable cases are very close to each other and to the benchmark case. On the other hand, the more lenient Gr. 100 case (lower *T/Y*, larger tie spacing), has a markedly higher collapse risk.

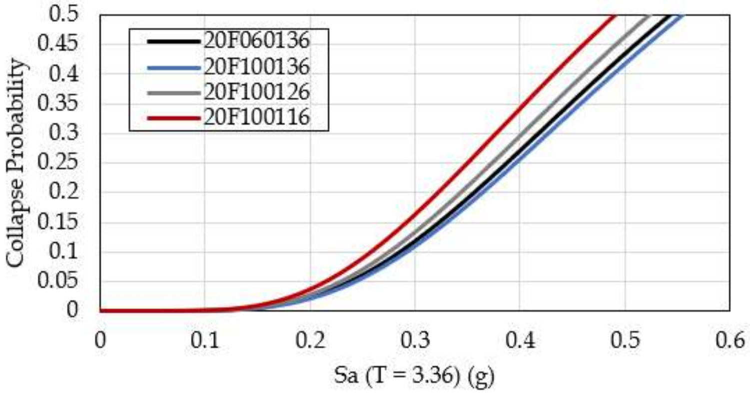

Figure 7.23. Total collapse fragility curves of the benchmark vs. Gr. 100 buildings with various *T/Y*'s.

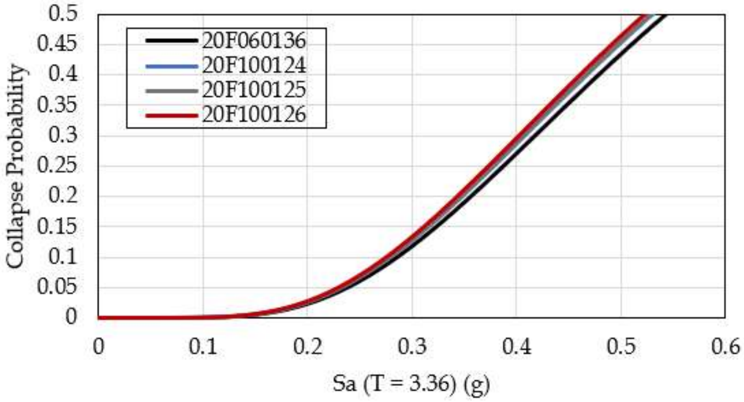

Figure 7.24. Total collapse fragility curves of the benchmark vs. Gr. 100 buildings with various s/d_b's.

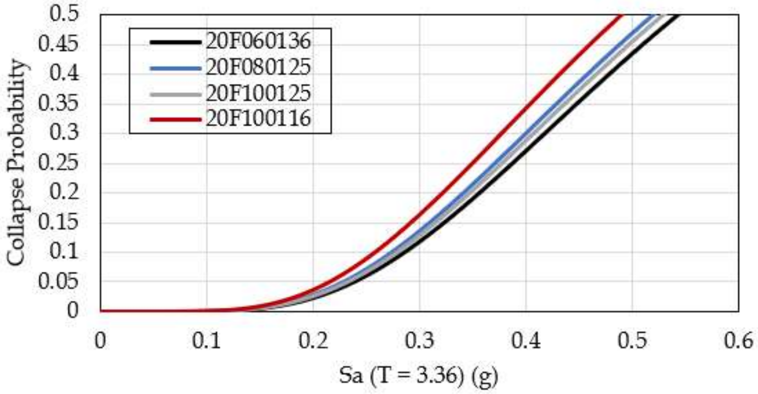

Figure 7.25. Total collapse fragility curves of the benchmark vs. 20F080125, 20F100125, and 20F100116.

7.2.7 Observations from 20-Story Frame Case Study

The following is a summary of major observations from the results of the 20-story frame study:

1. Buildings with high-strength reinforcement (and otherwise similar design strengths) tend to:

   a. experience larger drift ratios (about 10% to 20% higher drifts, for Gr. 80 and 100 respectively), primarily due to reduced transformed stiffness.
   b. experience slightly larger cumulative plastic strains (about 5% to 10% higher strains, for Gr. 80 and 100, respectively), primarily due to the combination of larger drifts/deformations and lower strain hardening.
   c. experience slightly higher probabilities of bar fracture, although the increased values for higher strength reinforcement is not due to the higher bar strength itself, but rather to the lower *T/Y* ratios and lower cyclic toughness that tend to be correlated with increasing bar strength. Interestingly, if *T/Y* is held constant, the probabilities of bar fracture are essentially the same for Gr. 60 and higher strength (Gr. 80 and 100) reinforcing bars.
2. Overall, the cumulative plastic strains, Fracture Indices (*FI*), and fracture probabilities for reinforcement in the 20-story moment frames are fairly low under MCE_R intensity ground motions. The average cumulative plastic strain demand (*CPD*) under MCE_R ground motions range from 0.10 to 0.14. When normalized by yield strain (CPD/ε_y), the plastic strain demand is on the order of 65 for Gr. 60, 45 for Gr. 80 and 35 for Gr. 100. While the total plastic strains are slightly larger with high strength reinforcing bars, the normalized plastic strains for high strength bars are significantly lower due to their higher yield strains. Owing to the relatively low strain demands, the average Fracture Indices and probability of bar fractures, under MCE_R ground motions, are similarly low, where the mean probability of fracture ranges from 1.5% to 2.9% (depending on *T/Y* and s/d_b) for Gr. 60 steel and up to 2.0% to 4.2% for Gr. 100 steel. By limiting the minimum *T/Y* to 1.2 and maximum s/d_b to 5, the fracture probabilities of the high strength bars are limited to 2.8%.
3. The probability of reinforcing bar fracture increases with decreasing *T/Y* and increasing tie spacing (s/d_b). To the extent that *T/Y* tends to be inversely correlated with bar strength, the risk of bar fracture tends to be higher for the higher strength bars, however bar strength is not the underlying cause. The higher fracture risk is primarily due to following factors (in order of significance): (1) lower strain hardening (*T/Y*), (2) reduced bar area and stiffness, leading to larger displacement demands, and (3) lower bar cyclic fracture toughness. Compared to the benchmark case (Gr. 60 with *T/Y* of 1.3 and s/d_b of 6), the fracture risk in the high strength bars can be well controlled by limiting the minimum allowable median *T/Y* to 1.2 and the maximum tie spacing to $5d_b$.
4. Collapse risks generally increase with decreasing *T/Y* and increasing rebar strength (grade) due to the combined effects of (1) less strain hardening, (2) reduced lateral stiffness, and (c) larger tendency for bar fracture (due to lower toughness). Reinforcing bar fracture contributes a small additional risk to collapse (about an increase of fracture risk by 1%, i.e., from 6% to 7% probability of collapse under MCE_R ground motions). Due to the combined effects of simulated sidesway collapse and reinforcing bar fracture, the collapse risk at MCE_R is calculated to increase by up to 1.2 times as a function of the reinforcing bar properties. Between the two effects of reinforcing bar strength and *T/Y* ratio, the latter has a more dominant effect. For example, for a constant *T/Y* of 1.3 and s/d_b ratio, there are negligible differences in the risk of bar fracture and collapse for frames with steel grades of 60, 80, and 100.

7.3 Results for 4-Story Frame

Similar to summary of data for the 20-story frames, in this section analysis results of 4-story buildings are summarized. Table 7.14 lists all twenty-seven archetypes considered for the 4-story frames. Based on the observations from 20-story frames, the primary structural safety and performance concerns are designs with small *T/Y*'s and large s/d_b's. Accordingly, only the benchmark case 04F060136 and those relatively vulnerable cases (as asterisked in the table) are analyzed and presented in this report. Table 7.15 summarizes MCE_R values at the two building sites in San Francisco and Seattle. The San Francisco Site Class D has the same MCE_R as used in the original archetype design, which is about 30% higher than the Seattle site. Thus, the 4-story archetype is somewhat over designed for the required base shear for Seattle site, but this analysis is still included to evaluate possible ground motion duration effects.

Table 7.14. Design matrix and ID of 4-story archetype frames.

Grade	*T/Y*	Tie spacing s/d_b		
		4	5	6
60	1.5	04F060154	04F060155	04F060156
	1.4	04F060144	04F060145	04F060146
	1.3	04F060134	04F060135	**04F060136***
80	1.4	04F080144	04F080145	**04F080146***
	1.3	04F080134	**04F080135***	**04F080136***
	1.2	**04F080124***	**04F080125***	**04F080126***
100	1.3	04F100134	04F100135	**04F100136***
	1.2	04F100124	**04F100125***	**04F100126***
	1.1	**04F100114***	**04F100115***	**04F100116***

Table 7.15. Sa (T_1 = 1.13 s) at different intensity levels.

Hazard Level (Return Period)	**Sa (T_1 = 1.26 s) (g)**	
	San Francisco (Site Class D)	Seattle (Site Class C)
MCE_R	0.71	0.54
10%/50yrs	0.55	0.22
5%/50yrs	0.71	0.31
2%/50yrs	0.95	0.46
2%/100yrs	1.15	0.59
2%/200yrs	1.36	0.74
1%/200yrs	1.57	0.91

Like the 20-story frame, the 4-story frame is designed following the provisions for special moment frames in ASCE-7 and ACI-318, based on an MCE_R intensity of SM_1 equal to 0.9g. The design with Gr. 60 reinforcement has a fundamental period of 1.26 s, with a seismic design base shear of 0.066g, equal to $(2/3)*S_{M1}/(T*R)$. Beam sizes are generally controlled by minimum strength and stiffness requirements, and columns are controlled by capacity design. In Table 7.16, the fundamental periods for the frames with higher grades (Gr. 80 and 100) are 5% and 20% longer, respectively, then the Gr. 60 design. Also tabulated are the *SaRatio* and $Ds_{5\text{-}75}$ based on the site hazard and calculated building periods.

Table 7.16. Site-specific seismic hazard metrics for unique designs.

	San Francisco (Site Class D)			**Seattle (Site Class C)**		
Grade	60	80	100	60	80	100
Period (sec)	1.26	1.33	1.54	1.26	1.33	1.54
***MCE* (2% in 50 years) (g)**	1.06	0.96	0.90	0.51	0.45	0.40
MCE_R (g)	0.71	0.68	0.58	0.54	0.52	0.45
SaRatio	1.67	1.71	1.75	2.01	1.96	1.92
$D_{S5\text{-}75}$ (sec)	10.4	11.1	11.6	19.7	21.4	22.5

7.3.1 Peak Story Drift Ratio (MCE_R)

Table 7.17 summarizes the mean peak drift ratio demands at MCE_R (SDR_{max}) in the 4-story archetype buildings. Drifts in the Gr. 60 and 80 frames are similar to each other, while the Gr. 100 buildings have drifts roughly 10%~15% more than the Gr. 60 benchmark. Again, this is mainly due to the decease of initial stiffness (i.e., a more flexible structure tends to move more at the same hazard level). A lower *T/Y* ratio is also found to slightly increase the story drift ratio demands.

Table 7.17. Peak story drift ratio demands of 4-story frames at MCE_R intensity level.

Archetype	San Francisco (Site Class D) MCE_R = 0.71g	Seattle (Site Class C) MCE_R = 0.54g
04F060136*	0.027	0.015
04F080124	0.028	0.016
04F080135	0.028	0.016
04F080125	0.028	0.016
04F080146	0.028	0.016
04F080136	0.028	0.016
04F080126	0.028	0.016
04F100114	0.029	0.017
04F100125	0.029	0.017
04F100115	0.029	0.017
04F100136	0.029	0.017
04F100126	0.029	0.017
04F100116	0.029	0.017

7.3.2 Cumulative Plastic Strain

Table 7.18 summarizes the maximum cumulative plastic strain in the 4-story archetypes under MCE_R seismic demands. Overall, the average cumulative strains are larger than in the 20-story archetypes, which is consistent with larger drift demands. The cumulative plastic strain demands of 0.19 to 0.22 at the San Francisco site correspond to normalized plastic strain demands (divided by the yield strain) of 95 (for Gr. 60) down to 65 (for Gr. 100). Although the absolute numbers are not in themselves a direct measure of fracture risk directly, two interestingly trends which are seemly in conflict with each other are observed. While the San Francisco (Site Class D) sees increases in cumulative plastic strain in buildings with higher grade steel, compared to the Gr. 60 benchmark; the buildings with higher grade reinforcement experience less cumulative plastic strain demands at the Seattle site. The contrary trend for the Seattle site is probably the result of the smaller drift and strain demands at that site, where the larger yield strains for the higher-grade steel have a more predominant effect on limiting the plastic strains.

Table 7.18. Maximum cumulative plastic strain in archetypes under MCE_R earthquakes.

Archetype	San Francisco (Site Class D) MCE_R = 0.71g	Seattle (Site Class C) MCE_R = 0.54g
04F060136*	0.19	0.09
04F080124	0.17	0.13
04F080135	0.16	0.13
04F080125	0.18	0.13
04F080146	0.15	0.07
04F080136	0.17	0.06
04F080126	0.18	0.07
04F100114	0.21	0.07
04F100125	0.18	0.06
04F100115	0.22	0.07
04F100136	0.16	0.06
04F100126	0.18	0.06
04F100116	0.22	0.07

7.3.3 Fracture Probability

Summarized in Tables 7.19 and 7.20 and Figures 7.26 and 7.27 are the rebar fracture probabilities, condition on non-collapse under MCE_R ground motion intensities, for all analyzed 4-story archetypes. As indicated in Figure 7.26-27, (1) the fracture probabilities are generally larger in the beams as compared to the columns, (2) the fracture probabilities of buildings with higher-strength reinforcement with T/Y >= 1.2 and s/d_b <= 5 are similar to that of the benchmark building at San Francisco (Site Class D). In Tables 7.19 and 7.20 it is interesting to note that the fracture probabilities are lower for the high strength bars at the Seattle site, which follows from the lower plastic strain demands resulting from the generally low overall demands and the higher yield strains of the high strength bars.

Compare to the 20-story archetype frames, the bar fracture risk of 4-story frames is generally higher. For example, for 20-story frames, the fracture probabilities in columns of the benchmark case and the 20F100116 are 2.9% and 4.2%, respectively. These two numbers increate to 3.8% and 5.1% for 4-story benchmark and the 04F100116, respectively. These increases in fracture probabilities follow from the larger drifts and cumulative plastic strains in the 4-story versus 20-story buildings.

Table 7.19. Estimated probability of rebar fracture in columns P (Column Frac. | non-collapse) under MCE_R.

Archetype	San Francisco (Site Class D) MCE_R = 0.71g	Seattle (Site Class C) MCE_R = 0.54g
04F060136	3.76%	1.56%
04F080124	2.60%	0.89%
04F080135	3.17%	1.04%
04F080125	3.54%	1.29%
04F080146	3.10%	1.01%
04F080136	3.38%	1.15%
04F080126	4.03%	1.36%
04F100114	3.23%	0.75%
04F100125	3.42%	0.81%
04F100115	4.00%	1.33%
04F100136	3.61%	0.92%
04F100126	4.11%	0.97%
04F100116	5.12%	1.05%

Table 7.20. Estimated probability of rebar fracture in beams P (Beam Frac. | non-collapse) under MCE_R.

Archetype	San Francisco (Site Class D) MCE_R = 0.71g	Seattle (Site Class C) MCE_R = 0.54g
04F060136	5.17%	1.89%
04F080124	3.38%	1.02%
04F080135	4.26%	1.22%
04F080125	4.78%	1.53%
04F080146	4.16%	1.18%
04F080136	4.57%	1.35%
04F080126	5.57%	1.63%
04F100114	4.32%	1.59%
04F100125	4.41%	0.86%
04F100115	5.27%	0.92%
04F100136	4.88%	1.06%
04F100126	5.65%	1.12%
04F100116	6.95%	1.23%

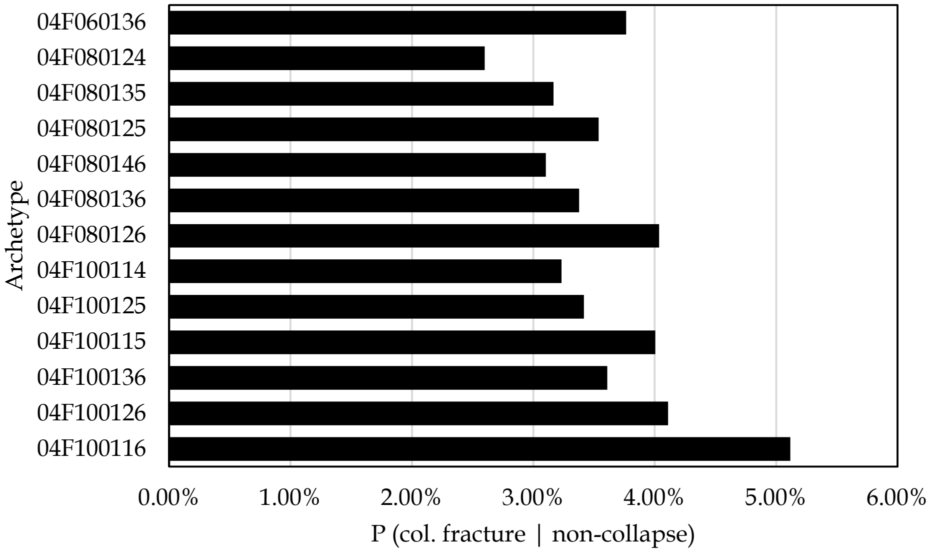

Figure 7.26. Probability of fracture in columns at MCE_R level at San Francisco (Site Class D).

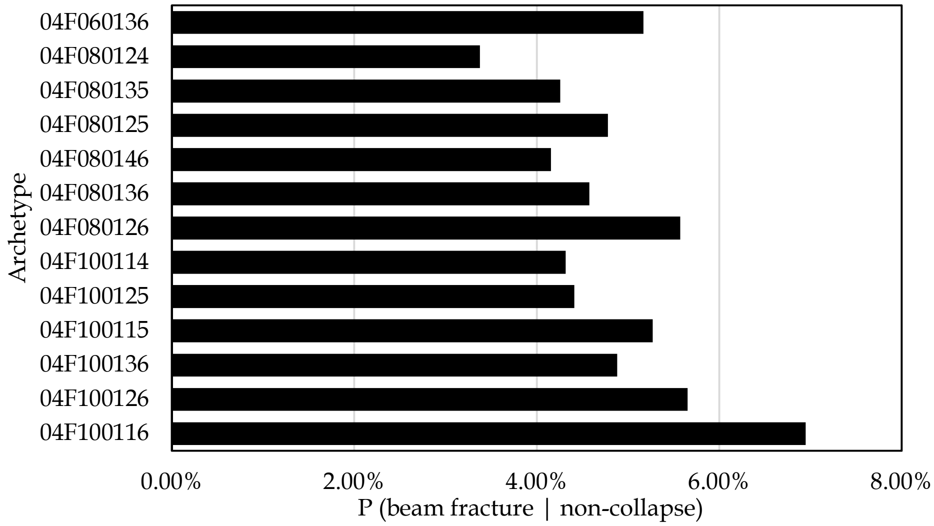

Figure 7.27. Probability of fracture in beams at MCE_R level at San Francisco (Site Class D).

7.3.4 FI_{max}-SDR_{max} Relation

Similar to the idea presented for the 20-story frames, the relation between maximum fracture index and maximum story drift ratio is helpful to understand the rebar fracture potential independent of the ground motion intensities. Figures 7.28 and 7.29 show the comparisons between Gr. 80 archetypes and the benchmark, and Figures 7.30 and 7.31 show the comparisons for the Gr. 100 archetypes.

A first observation is related the first-yield event in buildings. The fracture index in the Gr. 60 benchmark frame starts to accumulate at a story drift ratio of 0.01. Since reinforcing bar yield occurs at a larger strain for higher yield strength bars, the onset of increase in the fracture index is delayed to story drifts of roughly 0.015 for Gr. 80 buildings and between 0.015 to 0.02 for Gr. 100 buildings. As a result of this delayed yield point, frames with high-strength reinforcement tend to initially experience lower plastic strain demands than designs with Gr. 60 bars. However, this effect is eventually overcome by larger strain and fracture index values at larger drifts, due to the combined effects of lower *T/Y* ratios and lower fracture toughness in the higher strength reinforcement.

Referring again to Figures 7.28 to 7.31, under larger drifts the fracture index (FI) demands for the high strength bars increase at a faster rate than the Gr. 60 benchmark case. For example, under story drift demands of 0.03 to 0.04 (corresponding to the drift limits for MCE_R intensities), the FI_{max}-SDR_{max} curves of buildings with higher grade bars surpasses that of Gr. 60 benchmark case. If targeting the structural performance at the 4% story drift ratio (corresponding to the MCE_R limit in ASCE 7, Chapter 16), the data indicate that the fracture risk for the high strength bars can be maintained to the risk of Gr. 60 bars by requiring mean *T/Y* ratios of at least 1.2 and limiting the maximum s/d_b tie spacing ratio to 5 for Gr. 80 bars and 4 for Gr. 100 bars.

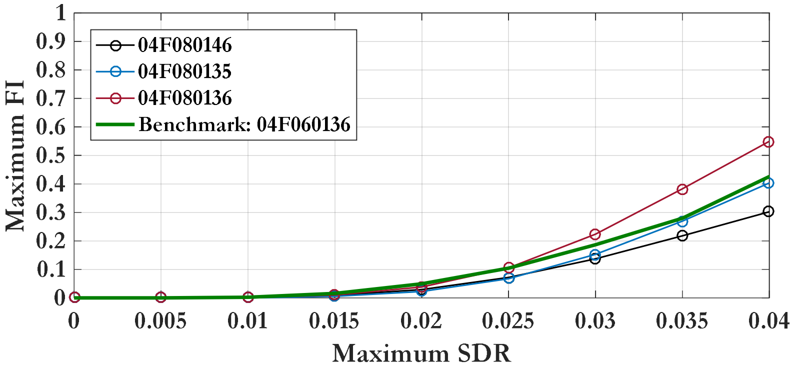

Figure 7.28. FI_{max}-SDR_{max} curves of Gr. 80 archetypes with higher *T/Y*'s and the benchmark.

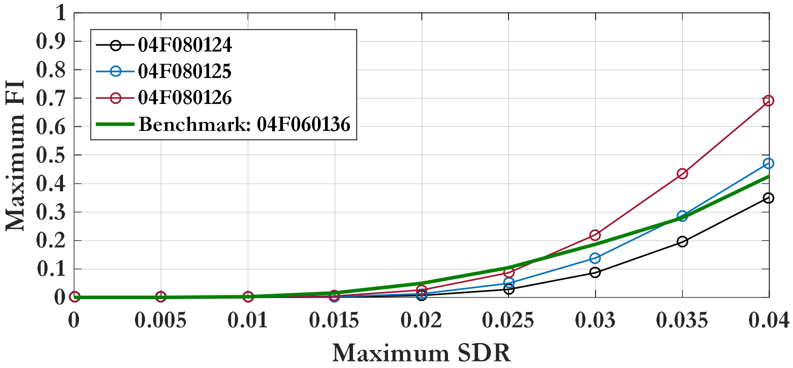

Figure 7.29. FI_{max}-SDR_{max} curves of Gr. 80 archetypes with the lowest *T/Y* and the benchmark.

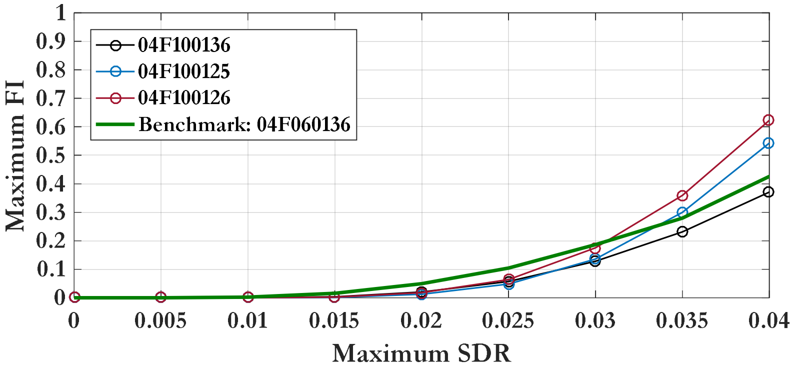

Figure 7.30. FI_{max}-SDR_{max} curves of Gr. 100 archetypes with the higher T/Y's and the benchmark.

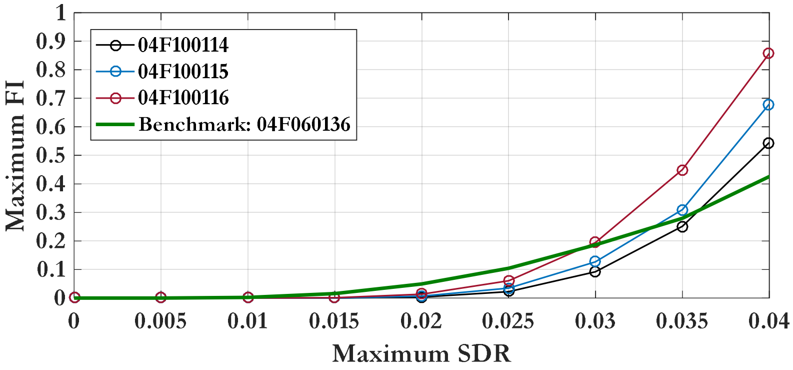

Figure 7.31. FI_{max}-SDR_{max} curves of Gr. 100 archetypes with the lowest T/Y and the benchmark.

7.3.5 Collapse Fragility

Table 7.21 summarize the median collapse intensities (S_{CT}), along with *CMR*, *ACMR*, and adjusted median collapse intensities (S_{CT}*) for twenty-seven 4-story archetype structures. To simplify the comparison, the period-dependent ductility ratio and the spectral shape factor is fixed at 10.9 and 1.41, respectively, which are the same as the original Gr. 60 design. Referring to the last column in Table 7.21, the median collapse capacity (S_{CT}*) of the Gr. 80 frames are about 4%~11% less than the Gr. 60 benchmark case, and the capacities for the Gr. 100 frames are about 10% to 19% less. As noted previously with respect to other metrics, the reductions in the higher-grade archetypes can be minimized by controlling the T/Y and s/d_b ratios.

Same as for the 20-story frames, the dispersion in the FEMA P695 collapse fragility curve is fixed at 0.5 for all archetypes. Using this dispersion and the median collapse intensities from Table 7.21, the estimated collapse probabilities under the MCE_R intensity at San Francisco (Site Class D), i.e., $Sa(T_1 = 0.81) = 1.11$g, are summarized in Table 7.22. The first column in Table 7.22 summarizes the MCE_R collapse probabilities without considering fracture, and the second column summarizes the probabilities including fracture (incorporated as a non-simulated collapse mode). The third column summarizes the increase in collapse risk due to fracture. In the Gr. 60 benchmark frame, the risk of bar fracture increases the probability of collapse by 0.6% (from 4.3% → 4.9%). In the Gr. 80 archetypes, the risk increases by about 1.4% due to fracture (5.3% → 6.7%), and in the Gr. 100 archetypes it increases by 1.7% (7.4% → 9.1%).

The MCE_R collapse probabilities from Table 7.22 are shown graphically in Figure 7.32. Compared to the FEMA P695 seismic collapse criteria (10% collapse probability under MCE_R), with the exception of the Gr. 100 cases with T/Y = 1.1, all of the other archetypes meet the 10% collapse risk. While none of the higher strength cases have as low collapse risk as the Gr. 60 benchmark case, the risks can be controlled in the higher-grade cases by limiting T/Y >= 1.2 and s/d_b <= 5.

Table 7.21. Collapse fragility table for all archetypical 4-story frames.

				Excluding fracture-induced collapse				Including fracture-induced collapse			
Archetype	μ_T	β_1	*SSF*	S_{CT} (g)	*CMR*	*ACMR*	S_{CT}* (g)	S_{CT} (g)	*CMR*	*ACMR*	S_{CT}* (g)
04F060136*	10.9	0.37	1.41	1.86	1.67	2.36	2.62	1.80	1.62	2.28	2.54
04F080124	10.9	0.37	1.41	1.78	1.60	2.26	2.51	1.70	1.53	2.16	2.40
04F080135	10.9	0.37	1.41	1.78	1.60	2.26	2.51	1.68	1.51	2.13	2.37
04F080125	10.9	0.37	1.41	1.77	1.59	2.25	2.50	1.64	1.48	2.08	2.31
04F080146	10.9	0.37	1.41	1.77	1.59	2.25	2.50	1.73	1.56	2.20	2.44
04F080136	10.9	0.37	1.41	1.76	1.58	2.23	2.48	1.65	1.49	2.09	2.33
04F080126	10.9	0.37	1.41	1.74	1.57	2.21	2.45	1.60	1.44	2.03	2.26
04F100114	10.9	0.37	1.41	1.62	1.46	2.06	2.28	1.54	1.39	1.95	2.17
04F100125	10.9	0.37	1.41	1.64	1.48	2.08	2.31	1.58	1.42	2.01	2.23
04F100115	10.9	0.37	1.41	1.61	1.45	2.04	2.27	1.48	1.33	1.88	2.09
04F100136	10.9	0.37	1.41	1.67	1.50	2.12	2.35	1.62	1.46	2.06	2.28
04F100126	10.9	0.37	1.41	1.62	1.46	2.06	2.28	1.56	1.40	1.98	2.20
04F100116	10.9	0.37	1.41	1.59	1.43	2.02	2.24	1.46	1.31	1.85	2.06

Table 7.22. Collapse probability of 4-story frames under MCE_R = 1.11g.

Archetype	Collapse (non-fracture)	Including fracture	Collapse (fracture)
04F060136	4.29%	4.93%	0.63%
04F080124	5.16%	6.21%	1.05%
04F080135	5.16%	6.50%	1.34%
04F080125	5.28%	7.13%	1.86%
04F080146	5.28%	5.79%	0.51%
04F080136	5.40%	6.97%	1.57%
04F080126	5.66%	7.83%	2.17%
04F100114	7.47%	9.01%	1.54%
04F100125	7.13%	8.21%	1.07%
04F100115	**7.65%**	**10.37%**	**2.72%**
04F100136	6.65%	7.47%	0.82%
04F100126	7.47%	8.60%	1.12%
04F100116	**8.02%**	**10.87%**	**2.86%**

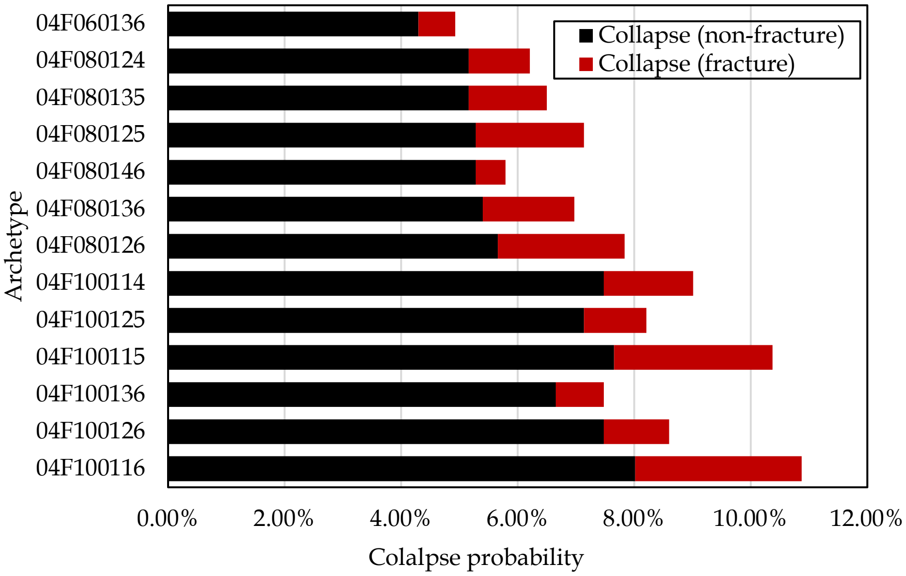

Figure 7.32. Collapse probability of 4-story frames without and with fracture under MCE_R earthquakes.

Figure 7.33 shows the collapse fragility of the benchmark 04F060136. Similar to the plots shown for the 20-story frame, the black curve represents the collapse fragility based on directly simulated failure modes, the grey curve shows the collapse probability due to non-simulated, fracture-induced failure modes, and the red curve is the total collapse fragility (obtained by summing the grey and black curves). Similar to the 20-story frame, the contribution of fracture to collapse is fairly small, contributing less than about 5% to the total collapse risk.

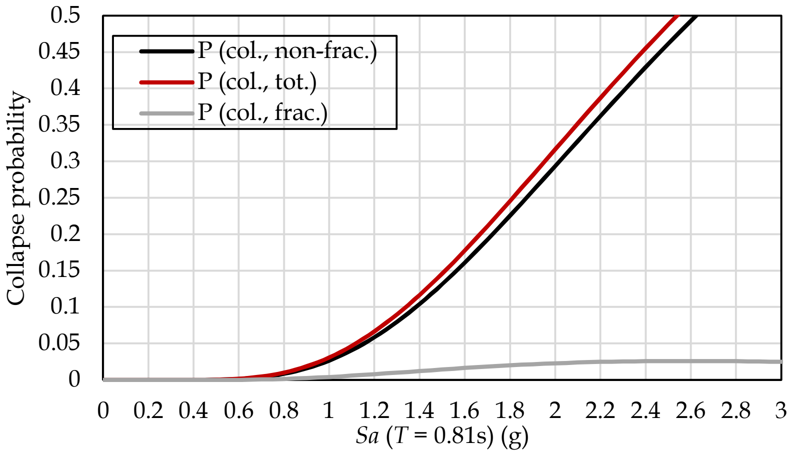

Figure 7.33. Collapse fragility curves (non-fracture, due-to-fracture, and total) of the benchmark 04F060136.

Figure 7.34 compares the performance of three Gr. 80 archetypes with different tie spacings (04F080124, 04F080125, and 04F080126). It is noted that these three frames have similar median collapse capacity, roughly 2.5g, when excluding the fracture risk. The difference in response is due to tie-spacing (s/d_b), which can have a measurable effect on the collapse safety.

Figure 7.35 compares the performance of three Gr. 100 archetypes with varying *T/Y* ratios (04F100136, 04F100126, and 04F100116). These plots demonstrate the significance of *T/Y* ratios, which changes the collapse risk due to: (1) influence of hardening on plastic strain concentration and material deterioration within the plastic-hinge region, (2) influence of hardening on the rebar fracture toughness.

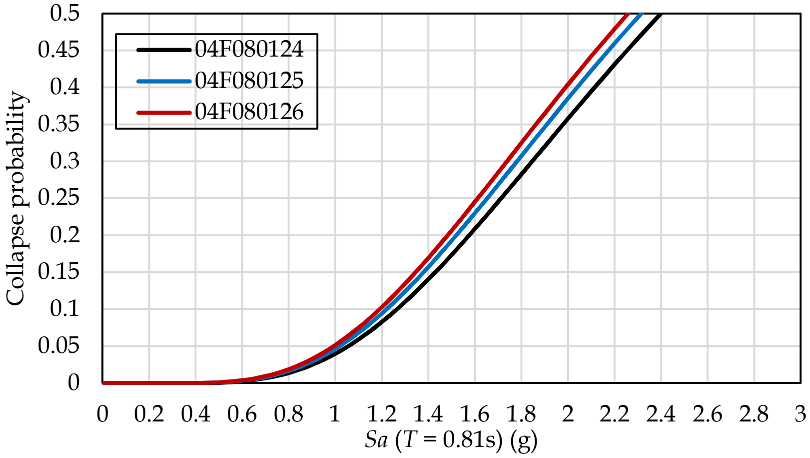

Figure 7.34. Total collapse fragility curves of the benchmark vs. Gr. 80 buildings with various s/d_b's.

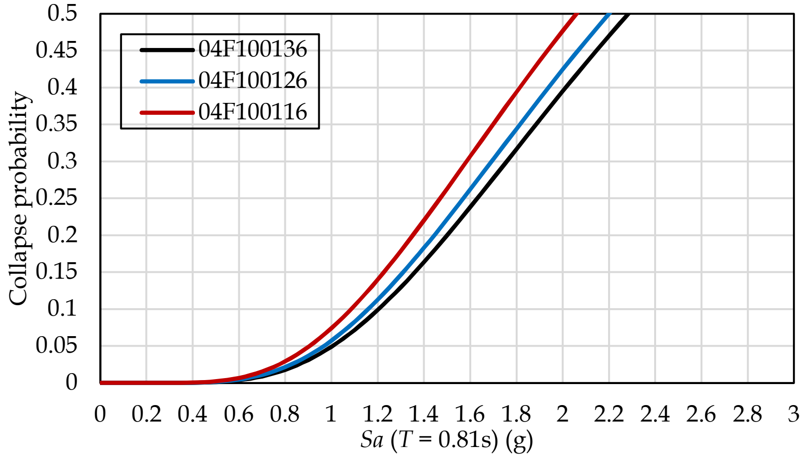

Figure 7.35. Total collapse fragility curves of the benchmark vs. Gr. 100 buildings with various *T/Y*'s.

7.3.6 Observations from 4-Story Frame Case Study

In general, the trends and observations from the 4-story frames are similar to those from the 20-story frames. Most significantly, these results support the prior recommendations to control the *T/Y* ratio (>= 1.2) and s/d_b tie spacing (<= 5) of frames with high strength reinforcement so as to achieve comparable collapse and bar fracture risks to the Gr. 60 benchmark frame.

Otherwise, it is noted that at similar story drifts, for instance 3%, the 4-story frames are generally subject to higher cumulative plastic strain demands compared to 20-story frames. The main reasons for this are (1) the shorter-period 4-story frame experiences more reversal cycles compared to longer-period 20-story frame, and (2) more localization of peak story drift demands in the 4-story frame.

7.4 Summary of Frame Analyses

In this chapter, the results of 4-story and 20-story moment frame analyses are summarized with special focus on the influence of reinforcing bar properties on maximum story drift ratio demands, cumulative plastic strain demands, bar fracture index demands, bar fracture probabilities, and collapse probabilities (with and without fracture) under different earthquake intensity levels. Earthquake demands were evaluated for two building sites in San Francisco and Seattle (the latter experiencing longer duration ground motions) and for the Seismic Design Category D_{max} hazard criterion in FEMA P695. While the peak story drift demands are similar in the 4-story and 12-story frames, the bar strain demands and bar fracture probabilities are larger in the 4-story archetype due to (1) a shorter period in the 4-story archetype, which results in a larger spectral demands and larger number of seismic loading excursions, and (2) more localization of peak story drift demands in the 4-story archetype. The following is a summary of the key observations and conclusions:

1. *Story Drift Demands:* Compared to the benchmark moment frame designs with Gr. 60 reinforcement, the MCE_R drift demands are about 10% higher with Gr. 80 reinforcement and about 20% larger with Gr. 100 reinforcement. These are based on designs where minimum strength is assumed to control the member sizes, such that the only change between conventional and high strength reinforcement is to reduce the reinforcing steel areas in proportion to the bar yield strengths. The difference in drift is roughly proportional to the difference in the transformed cross section stiffness, which suggests that, to achieve parity in designs limited by drift, the effective stiffness used in analysis should be based on the transformed section properties.

2. *Cumulative Plastic Strain Demands:* Nominal reinforcing bar strains and plastic strain demands are calculated assuming a nominal 8-inch gage length in the hinge regions of beams and columns. Note that these are nominal demands, which do not take into account amplification of strains due to local bar buckling. The average cumulative plastic strain demands (*CPD*) in the most critical frame member under MCE_R ground motions are about 0.12 in the 20-story frame and 0.19 in the 4-story frame. While the cumulative plastic strain demands are similar between the frames with conventional and high-strength steel, the normalized cumulative plastic strain demands (CPD/ε_y) are lower in the high strength bars due to the higher yield strains the high strength bars. For example, the normalized cumulative plastic strain demands in the 4-story frames are 95, 70, and 60 for Gr. 60, 80 and 100 bars.

3. *Reinforcing Bar Fracture Probability*: The probability of reinforcing bar fracture increases with decreasing tensile strength to yield ratio (*T/Y*) and increasing tie spacing (s/d_b). The strength of the reinforcement does not seem to affect the fracture probability, except insofar as the bar strength affects the frame stiffness (drift demands) and the reinforcing bar grade is related to the *T/Y* ratio, bar slenderness (s/d_b), and the inherent cyclic fracture toughness. To help maintain parity with the benchmark case with conventional grade steel (Gr. 60 with *T/Y* of 1.3 and s/d_b of 6), proposed requirements for higher grade still is to set the minimum allowable median *T/Y* to 1.2 and the maximum tie spacing to $5d_b$. By doing so, the probability of column bar fracture under MCE_R ground motions is about 4% for the 4-story frame of all three grades of steel (Gr. 60, 80 and 100) and about 3% for the 20-story frames. Bar fracture probabilities are roughly 1.3 times larger in the beams,

and without the limits on *T/Y* and *s/d*$_b$, the probability of bar fracture would increase to 5% in the columns and 7% in the beams.

4. *P695 Collapse Risk:* Collapse risks are evaluated using the FEMA P695 procedure, where the effect of reinforcing bar fracture is considered as a non-simulated failure mode. The collapse risk generally increases with decreasing *T/Y* and increasing rebar strength (grade) due to the combined effects of (1) reduced lateral stiffness, (2) less strain hardening, leading to more strain concentration, and (c) lower cyclic toughness. Similar to the point made with regard to bar fracture, to help maintain parity with the benchmark case with conventional grade steel (Gr. 60 with *T/Y* of 1.3 and *s/d*$_b$ of 6), proposed requirements for higher grade still is to set the minimum allowable median *T/Y* to 1.2 and the maximum tie spacing to 5*d*$_b$. Assuming these limits, the probabilities of collapse under *MCE*$_R$ motions for the 4-story archetypes, due to the combined effects of simulated sidesway collapse and reinforcing bar fracture, are 5%, 7% and 8% for the Gr. 60, 80, and 100 designs, respectively. The collapse risks for the 20-story archetypes are 8%, 9% and 9% for the Gr. 60, 80, and 100 designs, respectively. The risk of bar fracture contributes about 1% to 2% (absolute value) to these collapse probabilities. While the collapse probabilities are larger for the frames with higher grade (lower *T/Y* and fracture toughness) reinforcement, all are within the 10% *MCE*$_R$ collapse risk limit specified in ASCE 7. Without the limits of *T/Y* and *s/d*$_b$, the collapse risks for the Gr. 100 frame would increase to 11% (as compared to the 8% and 9% probabilities with the limits imposed), with a larger contribution (up to 3%) from fracture. Finally, it should be noted that the differences between the collapse probabilities for Gr. 60 and the Gr. 80 and 100 designs would likely be less if the frames with higher grade steels were redesigned (with transformed stiffness properties) to have the same *MCE*$_R$ drift demands.

8. SHEAR WALL CASE STUDY

8.1 Archetype Structures and Modeling

This chapter introduces two case studies on shear-wall structures: a 42-story C-shape wall archetype and an 8-story planar wall archetype.

The 42-story wall was originally studied in the PEER Tall Building Initiative (TBI) project (named as Building 1C) at Los Angeles Downtown (LADT, 118.25° W, 34.05° N, Site Class C[1]). It was a core-wall-only structure designed per the performance-based approach with higher performance objectives, including serviceability targets for coupling beams and wall piers. The minimum strength was initially calculated based on the maximum of the 43-year return earthquake and wind loads, and the performance was checked under MCE_R ground motions.

In this study, the 42-story building is analyzed using a simplified 2D model of the C-shaped wall for loading in the weak direction (i.e., EW direction), as highlighted in the plan drawing of Figure 8.1. The C-shaped wall with Grade 60 reinforcement (assuming a T/Y ratio of 1.3 and s/d_b of 6) is adopted as the benchmark design in this study. Table 8.1 summarizes the key design parameters of the benchmark wall structure, where h_w is the story height; l_w is the wall section height; b_w is the wall stem thickness; b_f is the flange width; t_f is the wall flange thickness; c is the cover depth; f_c is the concrete compressive strength; f_{yl} is the rebar yield strength; ρ_l is the vertical reinforcement design; ρ_{sh1} is the transverse reinforcement ratio in the wall stem; and ρ_{sh2} is the transverse reinforcement ratio in the wall flange.

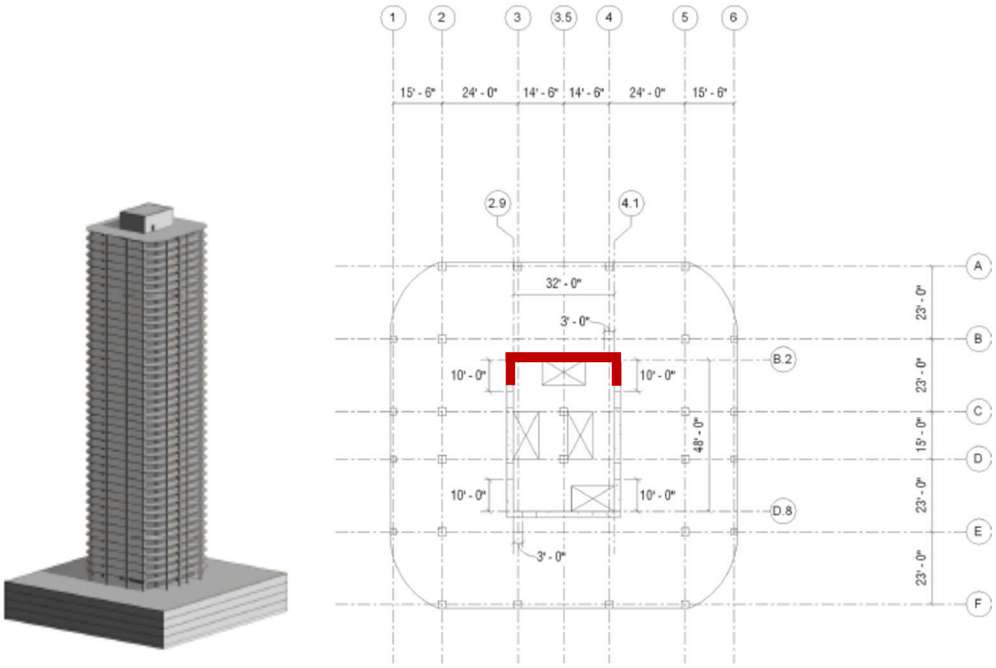

Figure 8.1. Building 1C tower plan (after Jack Moehle et al., 2011).

---

[1] The LADT site has a site class of C, and the soil velocity Vs30 is updated using the Cybershake data provided by the Southern California Earthquake Center (https://github.com/usgs/nshmp-haz/blob/master/etc/nshm/sites-cybershake-vs30-wills.csv).

Table 8.1. Design parameters of the 42-story benchmark wall 42W060136.

Story	h_w (in)	l_w (in)	b_w (in)	b_f (in)	c (in)	t_f (in)	f_c (ksi)	f_{yl} (ksi)	ρ_l	ρ_{sh1}	ρ_{sh2}
1	150	448	36	156	2	32	-10.4	67	#10 @ 6"	0.0139	0.0082
2	116	448	36	156	1.5	32	-10.4	67	#10 @ 6"	0.0093	0.0082
3	116	448	36	156	1.5	32	-10.4	67	#10 @ 6"	0.0093	0.0082
4	116	448	36	156	1.5	32	-10.4	67	#10 @ 6"	0.0093	0.0046
5	116	448	36	156	1.5	32	-10.4	67	#10 @ 6"	0.0093	0.0046
6	116	448	36	156	1.5	32	-10.4	67	#10 @ 6"	0.0093	0.0046
7	116	448	36	156	1.5	32	-10.4	67	#11 @ 6"	0.0073	0.0041
8	116	448	36	156	1.5	32	-10.4	67	# 11 @ 6"	0.0073	0.0041
9	116	448	36	156	1.5	32	-10.4	67	#11 @ 6"	0.0073	0.0041
10	116	448	36	156	1.5	32	-10.4	67	# 11 @ 6"	0.0073	0.0041
11	116	448	36	156	1.5	32	-10.4	67	#11 @ 6"	0.0073	0.0041
12	116	448	36	156	1.5	32	-10.4	67	# 11 @ 6"	0.0073	0.0041
13	116	432	24	144	1.5	24	-10.4	67	#10 @ 6"	0.0110	0.0055
14	116	432	24	144	1.5	24	-10.4	67	#10 @ 6"	0.0110	0.0055
15	116	432	24	144	1.5	24	-10.4	67	#10 @ 6"	0.0110	0.0055
16	116	432	24	144	1.5	24	-10.4	67	#10 @ 6"	0.0110	0.0055
17	116	432	24	144	1.5	24	-10.4	67	#10 @ 6"	0.0110	0.0055
18	116	432	24	144	1.5	24	-10.4	67	#10 @ 6"	0.0110	0.0055
19	116	432	24	144	1.5	24	-10.4	67	#9 @ 6"	0.0083	0.0042
20	116	432	24	144	1.5	24	-10.4	67	#9 @ 6"	0.0083	0.0042
21	116	432	24	144	1.5	24	-10.4	67	#9 @ 6"	0.0083	0.0042
22	116	432	24	144	1.5	24	-10.4	67	#9 @ 6"	0.0083	0.0042
23	116	432	24	144	1.5	24	-10.4	67	#9 @ 6"	0.0083	0.0042
24	116	432	24	144	1.5	24	-10.4	67	#9 @ 6"	0.0083	0.0042
25	116	432	24	144	1.5	24	-10.4	67	#8 @ 6"	0.0061	0.0042
26	116	432	24	144	1.5	24	-10.4	67	#8 @ 6"	0.0061	0.0042
27	116	432	24	144	1.5	24	-10.4	67	#8 @ 6"	0.0061	0.0042
28	116	432	24	144	1.5	24	-10.4	67	#8 @ 6"	0.0061	0.0042
29	116	432	24	144	1.5	24	-10.4	67	#8 @ 6"	0.0061	0.0042
30	116	432	24	144	1.5	24	-10.4	67	#8 @ 6"	0.0061	0.0042
31	116	426	21	141	1.5	21	-10.4	67	#7 @ 6"	0.0070	0.0048
32	116	426	21	141	1.5	21	-10.4	67	#7 @ 6"	0.0070	0.0048
33	116	426	21	141	1.5	21	-10.4	67	#7 @ 6"	0.0070	0.0048
34	116	426	21	141	1.5	21	-10.4	67	#7 @ 6"	0.0070	0.0048
35	116	426	21	141	1.5	21	-10.4	67	#7 @ 6"	0.0070	0.0048
36	116	426	21	141	1.5	21	-10.4	67	#7 @ 6"	0.0070	0.0048
37	116	426	21	141	1.5	21	-10.4	67	#6 @ 12"	0.0063	0.0035
38	116	426	21	141	1.5	21	-10.4	67	#6 @ 12"	0.0063	0.0035
39	116	426	21	141	1.5	21	-10.4	67	#6 @ 12"	0.0063	0.0035
40	116	426	21	141	1.5	21	-10.4	67	#6 @ 12"	0.0063	0.0035
41	116	426	21	141	1.5	21	-10.4	67	#6 @ 12"	0.0063	0.0035
42	128	426	21	141	1.5	21	-10.4	67	#6 @ 12"	0.0063	0.0035
Roof	240	426	21	141	1.5	21	-10.4	67	#5 @ 12"	0.0035	0.0035

The benchmark building is further expanded to alternative designs, by replacing Grade 60 rebar with higher grades steel and proportionally reducing the amount of reinforcement. All archetype designs are named by a unique identification code, similar to ones used for frames in Chapter 7. For example, 42W060136 denotes the archetype 42-story wall using Grade 60 reinforcement with *T/Y* of 1.3 and a lateral tie spacing of $6d_b$. Table 8.2 lists overall 19 archetype designs to investigate the influence from different combinations of bar hardening properties and tie spacings.

Table 8.2. Design matrix and ID of 42-story archetype walls.

Grade	*T/Y*	Tie spacing s/d_b		
		4	5	6
60	1.3	-	-	42W060136
80	1.4	42W080144	42W080145	42W080146
	1.3	42W080134	42W080135	42W080136
	1.2	42W080124	42W080125	42W080126
100	1.3	42W100134	42W100135	42W100136
	1.2	42W100124	42W100125	42W100126
	1.1	42W100114	42W100115	42W100116

The 8-story shear wall archetype, shown in Figure 8.2, was originally studied in ATC 123: *Improving Seismic Design of Buildings with Configuration Irregularities* (ATC 2018). The continuous planar wall was designed per SDC D for site class of C and a risk category of II. The lateral structural systems in each building axis are two planar walls in parallel, designed according to ASCE 7-10 and ACI 318-14. Following the equivalent lateral force method, the 8-story wall structure was designed with an *R* factor of 6 and a C_d factor of 5. The building was originally analyzed in OpenSees, the longitudinal reinforcement was designed to fulfill the required design overturning moment. Shear design was in accordance to 18.10.2 and 18.10.4 of ACI 318-14. The transverse reinforcement in the boundary elements were designed in accordance with ACI 318-14, 18.10.6.4 and related detailing requirements. The first period, as estimated by the simplified formula in ASCE 7, is 0.66 sec.

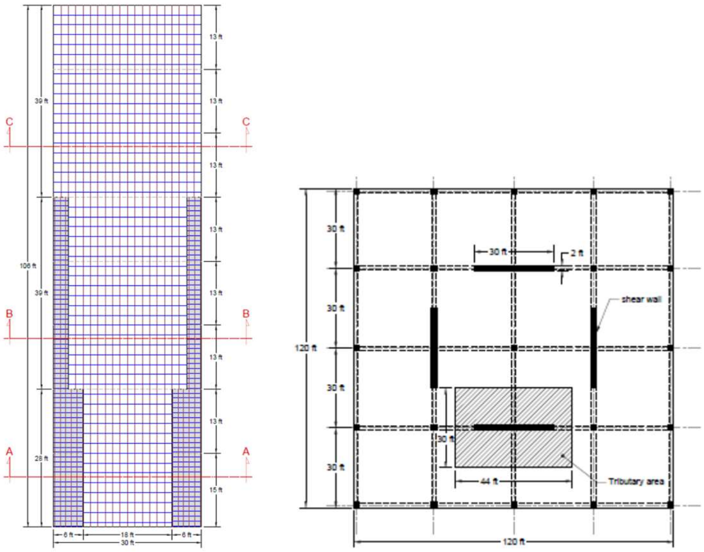

Figure 8.2. 8-story continuous planar wall, ELF method (after ATC 123., 2018).

For special wall structures, the current ACI standard (ACI 318-14) limits the maximum lateral reinforcement spacing for shear requirements by the smallest value of (1) three-times of the wall thickness, (2) 18 in, and (3) one-fifth of the wall length. It also limits the maximum transverse reinforcement spacing in boundary elements by the smallest value of (1) one-third of the least boundary element dimension, (2) six times the diameter of the smallest longitudinal bar, and (3) s_0 = 4 + (14-h_x)/3. For the purpose of parameter analyses and the consistency with the previous chapter, the only tie spacing limit considered in this study is one based on the ratio of s/d_b.

All walls are modeled using OpenSees with force-based fiber flexural (beam-column) elements, following the procedure introduced in Chapter 5. As shown in Figure 8.3, a leaning column is added to simulate P-Δ effects on the gravity columns. Each story is modeled with one fiber element with N integration points, where N is determined to have the equivalent integration length of the end integration point most close to 8 inches. The Concrete02 material, with the Kent-Park constitutive law, and the Reinforcingsteel material, without the fatigue and buckling options, are used to model the section properties. Following the suggestion by Pugh et. al. 2015, the softening (unloading) branch in the concrete material constitutive model is regularized to ease the mesh-dependency. At each integration point, one nonlinear shear section model (per ATC-114) is aggregated to the basic flexure section. At the base of the entire wall, one extra zero-length section element is inserted to simulate the strain penetration due to bar slippage behavior, following the modeling approach proposed by Zhao and Sritharan, 2007.

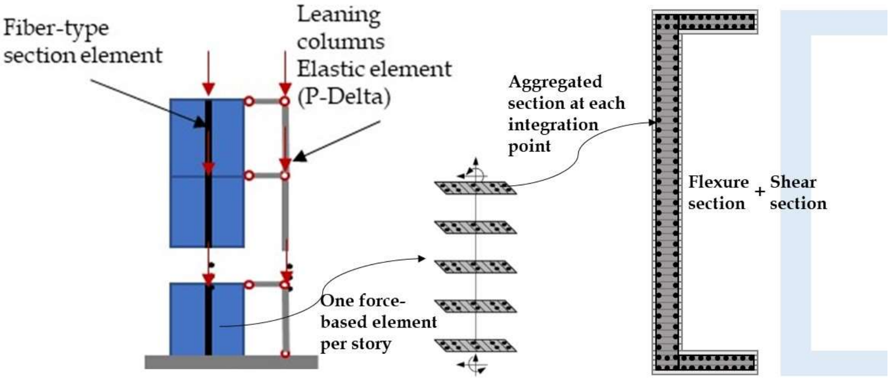

Figure 8.3. Simplified 2D wall model: fiber-based elements for walls and leaning columns for the gravity system.

The Rayleigh damping model with the tangent stiffness is used in this study. As suggested by PEER TBI tall building guidelines, a damping ratio of 2.5% is adopted for the 42-story model, which fixes the Rayleigh damping model at the first and second mode periods (i.e., 4 sec and 1 sec, respectively). It is a general trend that the damping ratio increases as decreasing the building height. Following the damping model by ATC-72-1, a damping ratio of 4.0% is used in analyses for the 8-story wall model.

8.2 Results for 42-Story Wall

The 42-story wall design with Grade 60 reinforcement has a first-model period of the T_1 equal to 4.2 sec. The wall response is evaluated for seismic hazard characteristics at LADT site. Table 8.3 lists MCE_R values at this site, along with the seismic intensity Sa (T_1 = 4.2 s) at six return periods.

As summarized in Table 8.4, the wall designs for the higher steel grades (Gr. 80 and 100) have longer periods than the original design (Gr. 60), due to reduced steel areas (and effective member stiffness). The periods for the Gr. 80 and 100 designs are about 5% and 10% longer, respectively, than the original design.

Also tabulated are the corresponding values of period-dependent spectral intensities for the MCE_R and 2% in 50-year seismic hazard. In addition to spectral acceleration, the *SaRatio* (a measure of ground motion spectral shape) and $Ds_{5\text{-}75}$ (a measure of ground motion duration) are also considered, where hazards with smaller *SaRatio* values and longer $Ds_{5\text{-}75}$ values tend to be more damaging. The period elongation does not change the seismic hazard significantly, which is partially due to the 1/T relationship of the hazard spectrum. Therefore, to simplify the comparisons, all reported results have been regularized to the fundamental period of the benchmark, i.e., 4.2 sec, in the following sections.

Table 8.3. MCE_R and Sa (T_1 = 4.2 s) at different intensity levels.

Hazard Level (Return Period)	Sa (T_1 = 4.2 s) (g)
	LADT (Site Class C)
MCE_R	0.186
10%/50yrs	0.071
5%/50yrs	0.092
2%/50yrs	0.130
2%/100yrs	0.148
2%/200yrs	0.170
1%/200yrs	0.194

Table 8.4. Site-specific seismic hazard metrics for unique designs.

	LADT (Site Class C)		
Grade	60	80	100
Period (sec)	4.2	4.4	4.6
***MCE* (2% in 50 years) (g)**	0.13	0.12	0.12
MCE_R **(g)**	0.19	0.18	0.17
SaRatio **(**$0.2T_1, T_1, 3.0T_1$**)**	1.44	1.40	1.38
$D_{S5\text{-}75}$ **(sec)**	7.30	7.40	7.50

8.2.1 Peak Story Drift Ratio

The peak (or maximum) story drift ratios (SDR_{max}) are plotted versus the first-mode period ground motion intensity Sa (T) in Figure 8.4 for the 88 ground motion records. As introduced in Chapter 6, the drift demands are extracted by taking horizontal stripes of SDR_{max} data from the raw IDA results, which are subsequently adjusted using the hazard-consistent procedure to represent the site-specific ground motion spectral shape and duration.

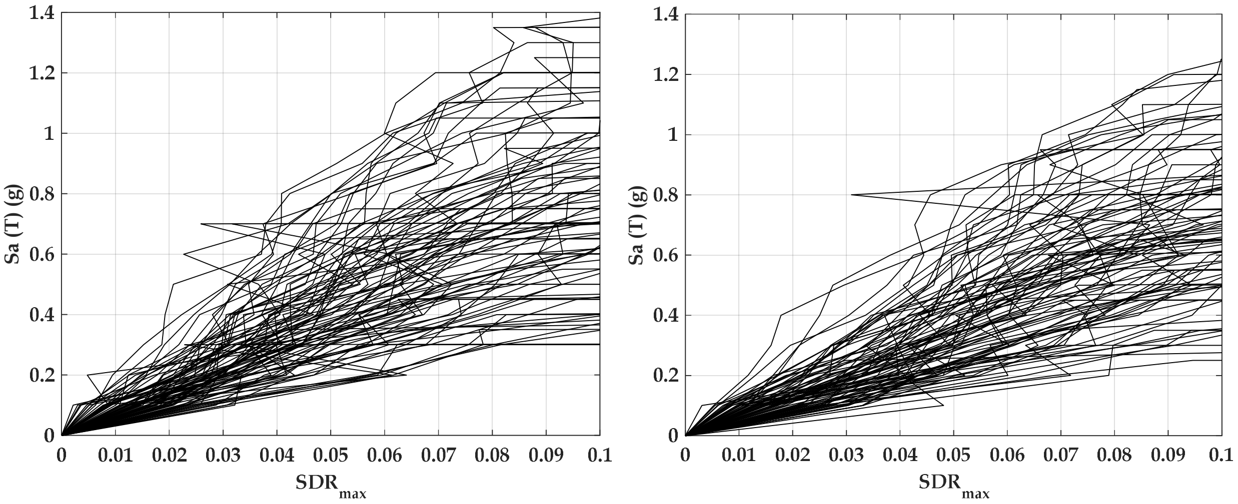

Figure 8.4. IDA curves under 88 ground motions. Left: 42W060136. Right: 42W100126.

Median values of the adjusted SDR_{max} data for all of the archetypes under six seismic hazard levels at the LA site are summarized in Table 8.5. One initial observation is that the story drift demands are only slightly sensitive to the steel grade and not at all sensitive to the *T/Y* ratio or tie spacing. Figure 8.5 shows the comparison of SDR_{max} demands between different steel grades. Compared to the Gr. 60 benchmark case (42W060136), the SDR_{max} of archetypes with the high strength rebars are about by 5%~10% higher.

Table 8.5. Median SDR_{max} (HCIDA-adjusted) of archetypes (LADT, Site Class C/D).

	Hazard level	10%/50yr	5%/50yr	2%/50yr	1%/50yr	0.5%/50yr	0.25%/50yr
	Sa (T_1) (g)	0.12	0.17	0.24	0.30	0.37	0.44
Archetype ID	42W060136*	0.013	0.018	0.025	0.028	0.031	0.035
	42W080144	0.014	0.019	0.027	0.031	0.035	0.039
	42W080134	0.016	0.020	0.027	0.030	0.034	0.038
	42W080124	0.015	0.020	0.027	0.030	0.034	0.038
	42W080145	0.015	0.020	0.027	0.030	0.034	0.038
	42W080135	0.015	0.020	0.027	0.031	0.034	0.038
	42W080125	0.015	0.020	0.027	0.030	0.034	0.038
	42W080146	0.015	0.020	0.027	0.031	0.034	0.038
	42W080136	0.014	0.019	0.027	0.030	0.034	0.038
	42W080126	0.015	0.020	0.027	0.030	0.034	0.038
	42W100134	0.014	0.019	0.027	0.029	0.034	0.037
	42W100124	0.014	0.019	0.027	0.029	0.034	0.037
	42W100114	0.014	0.019	0.027	0.030	0.034	0.038
	42W100135	0.014	0.019	0.027	0.030	0.034	0.038
	42W100125	0.014	0.019	0.027	0.030	0.034	0.038
	42W100115	0.014	0.019	0.027	0.030	0.034	0.038
	42W100136	0.014	0.019	0.028	0.031	0.034	0.038
	42W100126	0.014	0.019	0.028	0.031	0.034	0.038
	42W100116	0.014	0.019	0.028	0.031	0.034	0.038

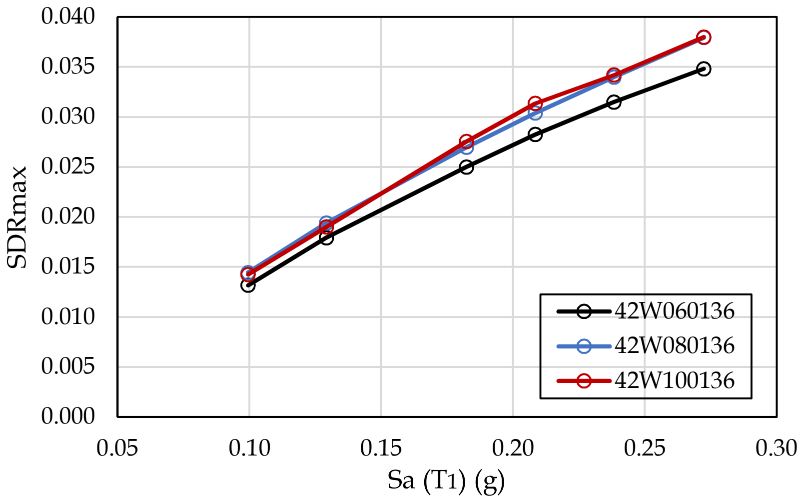

Figure 8.5. Comparison of SDR_{max} demands between different grades.

Summarized in Table 8.6 are the mean SDR_{max} under MCE_R intensity ground motions, where the drift statistics are calculated for the non-collapse data. Referring to Table 8.4, the Gr. 80 and Gr. 100 buildings have drifts that are roughly 7% larger than the baseline case 42W060136. These differences are primarily attributed to the differences in initial stiffness and periods in those designs. Overall, the peak drifts are within the 0.0.3 limit of the PEER TBI guidelines and well within the larger drift limit of Chapter 16 of ASCE 7. The *T/Y* ratios have a negligible effect on the drifts, which is not surprising given the modest amount of wall yielding at these drift values.

Table 8.6. Mean SDR_{max} demands of 42-story archetypes at MCE_R intensity level.

Archetype	LADT (Site Class C) MCE_R = 0.19 g
42W060136*	0.027
42W080144	0.029
42W080134	0.028
42W080124	0.029
42W080145	0.029
42W080135	0.029
42W080125	0.029
42W080146	0.029
42W080136	0.029
42W080126	0.029
42W100134	0.029
42W100124	0.028
42W100114	0.028
42W100135	0.029
42W100125	0.028
42W100115	0.028
42W100136	0.029
42W100126	0.029
42W100116	0.029

8.2.2 Cumulative Plastic Strain (MCE_R)

Table 8.7 summarizes the maximum cumulative plastic strain demand (*CPD*) in the reinforcement of the 42-story archetypes under MCE_R level ground motions. Similar to the frame archetypes, the reported values are nominal strains, calculated over an 8-inch gage length, where the *CPD* range from 0.125 to 0.155. Designs with higher strength steels have *CPD* roughly 10% to 15% larger than the benchmark design, except for the Gr. 100 bars with low *T/Y* ratios (42W100115 and 42W100116), which has strains 25% higher than the benchmark case (42W060136). For the Gr. 80 and 100 cases with *T/Y* equal to 1.2 and s/d_b equal to 5, the *CPDs* are 3% and 10%, respectively, larger than the benchmark case. For these cases, the normalized demands (CPD/ε_y) are 62, 48, and 41 for the Gr. 60, 80 and 100 cases, respectively.

Table 8.7. Maximum cumulative plastic strain in 42-story archetypes under MCE_R earthquakes.

Archetype	LADT (Site Class C) MCE_R = 0.19 g
42W060136*	0.125
42W080144	0.123
42W080134	0.124
42W080124	0.127
42W080145	0.122
42W080135	0.122
42W080125	0.129
42W080146	0.124
42W080136	0.129
42W080126	0.138
42W100134	0.135
42W100124	0.135
42W100114	0.139
42W100135	0.138
42W100125	0.138
42W100115	0.155
42W100136	0.134
42W100126	0.138
42W100116	0.151

8.2.3 Maximum Fracture Index and Fracture Probability (MCE_R)

As described in Chapter 5, the steel strain history demands are interpreted using a rain-flow counting algorithm to determine the fracture index, *FI*. Table 8.8 summarizes the median FI_{max} for the longitudinal wall reinforcement under the MCE_R ground motion intensity. Due to the relatively small strain demands, the FI_{max} values are extremely low, relative to the median (50% probability of reinforcing bar fracture) at *FI* equal to 1.0. Nevertheless, the following trends can be observed in the data (1) FI_{max} increases as steel grade increases; (2) FI_{max} increases as *T/Y* decreases; and (3) FI_{max} increases as s/d_b increases.

Table 8.8. Estimated median FI_{max} at MCE_R intensity levels.

Archetype	LADT (Site Class C) MCE_R = 0.19 g
42W060136*	0.035
42W080144	0.004
42W080134	0.008
42W080124	0.009
42W080145	0.013
42W080135	0.013
42W080125	0.019
42W080146	0.027
42W080136	0.027
42W080126	0.037
42W100134	0.010
42W100124	0.013
42W100114	0.016
42W100135	0.021
42W100125	0.028
42W100115	0.039
42W100136	0.042
42W100126	0.043
42W100116	0.055

Following the standard reliability integral, the probability of reinforcement fracture (conditioned on the non-collapse data) can be calculated as follows:

$$P(\text{fracture}\,|\,\text{non}-\text{collpase}) = \int f_D(x) F_C(x)\,dx \tag{8.1}$$

where f_D(x) is the probability density function (PDF) of *FI*, which is presumed as a lognormal distribution with the median and dispersion determined by HC-IDA method. The F_C(x) is the cumulative distribution function (CDF) of fatigue-fracture resistance, which is calibrated as a lognormal distribution with the median of 1.0 and dispersion of 0.5 (Chapter 3).

Table 8.9 summarizes the resulting rebar fracture probability under MCE_R ground motion intensity. The fracture probability of the benchmark case, 42W060136, is 2.16%, and for comparable Gr. 80 and 100 cases (42W080136, 42W100136) the fracture probabilities are 1.89% and 2.39%. Interestingly, the fracture probability for the Gr. 80 case is less than the benchmark case, due to the higher yield strain and lower normalized strain demand in the Gr. 80 bars. The worst case among all archetypes is the 42W100116, whose fracture probability is roughly 2.84%.

Plotted in Figure 8.6 and 8.7 are estimated fracture probabilities given different combinations of hardening ratios and tie spacings. In general, the fracture probability increases as *T/Y* decreases or tie spacing increases. Similar to the archetype frames, the fracture probability in the Gr. 100 case can be limited to achieve parity with the Gr. 60 benchmark case by (1) requiring a median *T/Y* of at least 1.2 and (2) limiting the tie spacing to s/d_b of 5.

Table 8.9. Estimated rebar fracture probability P (fracture | non-collapse) under MCE_R.

Archetype	**LADT (Site Class C) MCE_R = 0.19 g**
42W060136*	2.16%
42W080144	0.89%
42W080134	1.11%
42W080124	1.13%
42W080145	1.33%
42W080135	1.36%
42W080125	1.58%
42W080146	1.90%
42W080136	1.89%
42W080126	2.26%
42W100134	1.23%
42W100124	1.33%
42W100114	1.47%
42W100135	1.67%
42W100125	1.91%
42W100115	2.30%
42W100136	2.39%
42W100126	2.43%
42W100116	2.84%

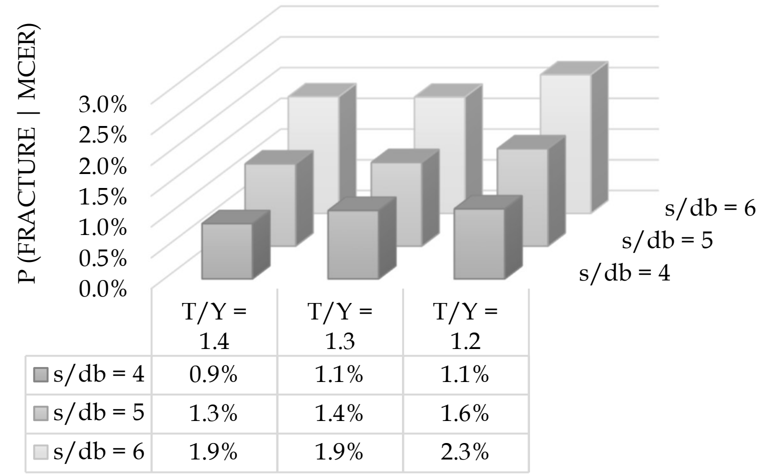

Figure 8.6. Fracture probability of Gr. 80 archetypes at LADT (Site Class C, MCE_R).

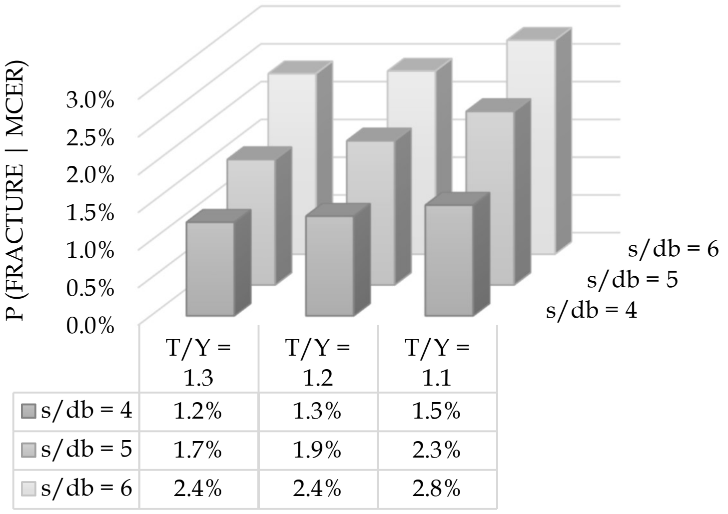

	T/Y = 1.3	T/Y = 1.2	T/Y = 1.1
▨ s/db = 4	1.2%	1.3%	1.5%
▨ s/db = 5	1.7%	1.9%	2.3%
☐ s/db = 6	2.4%	2.4%	2.8%

Figure 8.7. Fracture probability of Gr. 100 archetypes at LADT (Site Class C, MCE_R).

8.2.4 Maximum Fracture Index vs. Maximum Story Drift Ratio (FI_{max}-SDR_{max})

In previous section, the fracture probability is evaluated for the MCE_R intensity. To further evaluate the fracture risk relative to drift demands. Figure 8.8 shows the maximum fracture index versus the maximum story drift ratio under each non-collapse ground motion for the benchmark building (42W060136). The median FI_{max} in the building is roughly 0.2 at an SDR_{max} of 0.04, which is the maximum SDR permitted by ASCE 7-16 under MCE_R ground motions. As indicated by the fracture probability relationships in Table 8.10, the fracture probability is still less than 1% at FI equal to 0.2.

Table 8.10. Fracture probability given fracture index value.

Fracture index	0.0	0.1	0.2	0.3	0.4	0.5	0.6	0.7	0.8	0.9	1.0
Fracture probability	0.0%	0.0%	0.1%	0.8%	3.3%	8.3%	15.3%	23.8%	32.8%	41.7%	50.0%

Figure 8.9 compares the median FI_{max} vs. SDR_{max} relations for the Gr. 80 archetypes with varying T/Y and s/d_b ratios to the benchmark case. Three buildings using Gr. 80 bars with T/Y of 1.4 generally behavior better than the benchmark, in terms of fracture risk. The worst case using Gr. 80 bars with T/Y of 1.3 is the building having $6d_b$ tie spacing, whose FI_{max} surpasses the benchmark at large drifts. In the group of Gr. 80 with T/Y of 1.2, the building with $5d_b$ tie spacing has comparable FI_{max} to the benchmark; while the building using $6d_b$ tie spacing tends to have higher fracture potential when SDR_{max} exceeds 0.025.

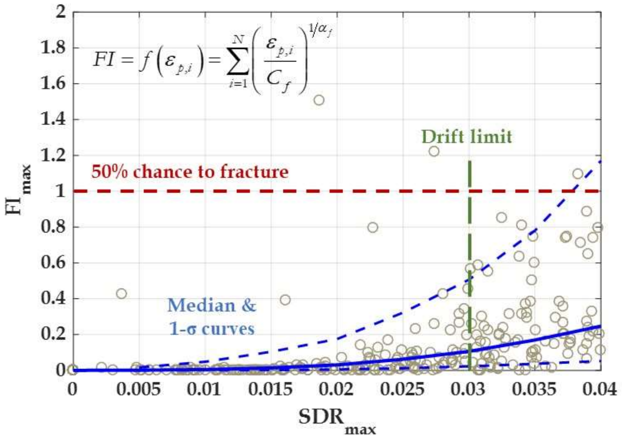

Figure 8.8. Maximum fracture index vs. Maximum story drift ratio in 42W060136 under non-collapse earthquakes.

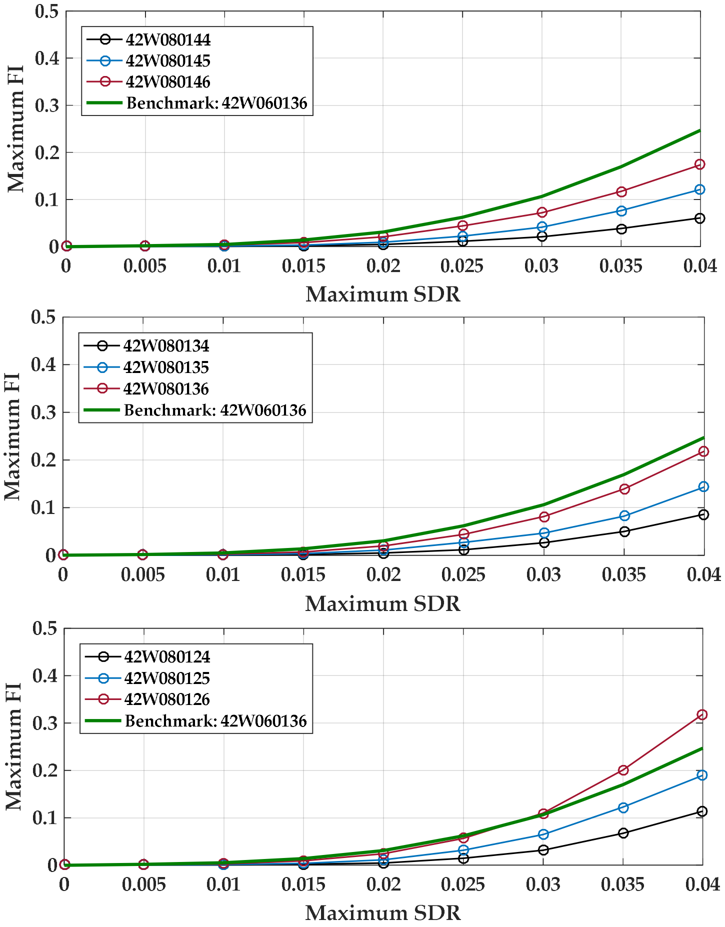

Figure 8.9. Median FI_{max} vs. SDR_{max}. (a) 42W08014X archetypes and the benchmark. Middle: 42W08013X and archetypes and the benchmark. Bottom: 42W08012X archetypes and the benchmark.

Figure 8.10 shows the median FI_{max} vs. SDR_{max} relations in Gr. 100 archetypes along with the benchmark case. Three buildings using Gr. 100 bars with *T/Y* of 1.3 generally behavior better than the benchmark, in terms of fracture risk. The worst case using Gr. 100 bars with *T/Y* of 1.2 is the building having $6d_b$ tie spacing, whose FI_{max} surpasses the benchmark at large drifts. In the group of Gr. 100 with *T/Y* of 1.1, both the buildings with $5d_b$ and $6d_b$ tie spacing bear higher fracture potential when SDR_{max} exceeds 0.03.

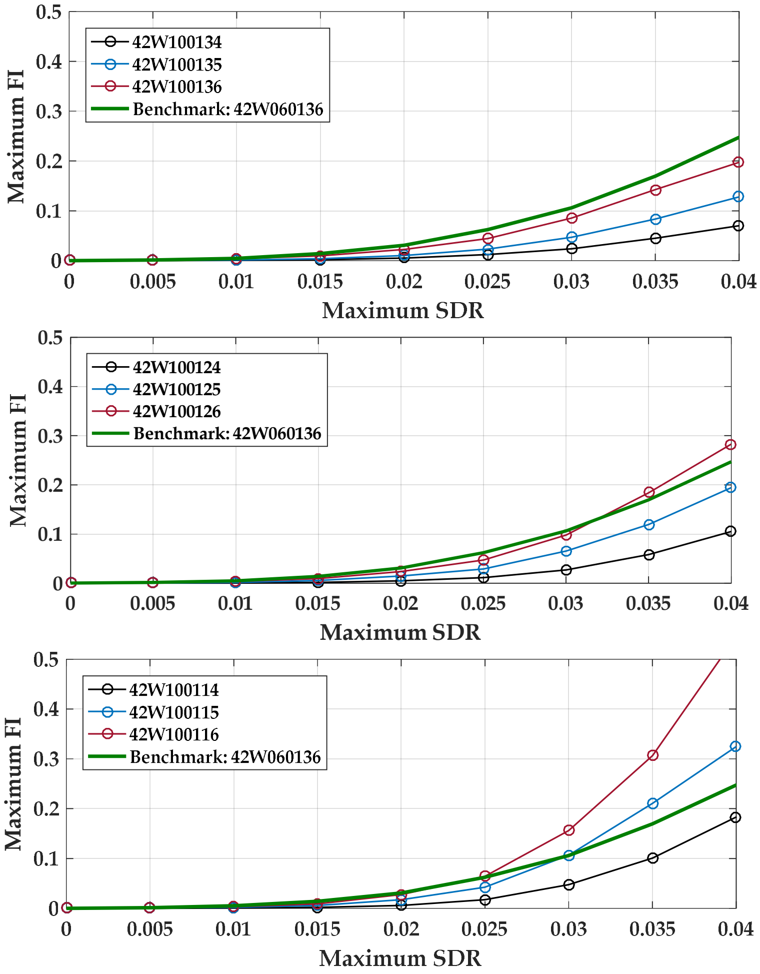

Figure 8.10. Median FI_{max} vs. SDR_{max}. Top: 42W10013X archetypes and the benchmark. Middle: 42W10012X and archetypes and the benchmark. Bottom: 42W10011X archetypes and the benchmark.

Another interesting observation from the analyses is that, given two equivalent-strength designs, the high-strength reinforcement is found to yield at a relatively larger drift ratio (about 1.0%), if compared to the Grade 60 reinforcement (at about 0.5%). This delayed yield point means potentially less plastic strain demand in those buildings under the small drift ratios. This favorable trend is negated somewhat by the fact buildings with high-strength bars tend to have larger drifts/deformations (about 10%~20% more) under the same intensity ground motions. In addition, the slopes of FI_{max}-SDR_{max} for some archetypes with Gr. 100 reinforcement (e.g., 42W100115 and 42W100116) are much steeper than the benchmark curve. This means the damage and the risk of bar fracture tends to accumulate faster in those Gr. 100 buildings.

8.2.5 Collapse Risk

Table 8.11 summarizes the median collapse intensities (S_{CT}), *CMR*, *ACMR*, and adjusted median collapse intensities (S_{CT}*) for the 42-story archetypes. To simplify the comparison, the spectral shape factor is fixed 1.5 for all designs. Compared to the benchmark case, the median collapse capacity, excluding fractures

(S_{CT}* in column 6 of Table 8.11) is about 5%~10% lower for the archetypes with higher strength steel. Accounting for bar fracture (S_{CT}* in column 10) reduces the median collapse intensity of the benchmark frame by about 5%, and the collapse capacities of the Gr. 80 and Gr. 100 archetypes are about 7% lower, on average, than the Gr. 60 benchmark case.

Table 8.11. Collapse fragility table for all archetypical 42-story walls.

		Excluding fracture-induced collapse				Including fracture-induced collapse			
Archetype	*SSF*	S_{CT} (g)	*CMR*	*ACMR*	S_{CT}* (g)	S_{CT} (g)	*CMR*	*ACMR*	S_{CiT}* (g)
42W060156	1.5	0.66	3.08	4.62	0.99	0.59	2.75	4.13	0.89
42W060146	1.5	0.66	3.08	4.62	0.99	0.57	2.66	3.99	0.86
42W060136	1.5	0.65	3.03	4.55	0.98	0.52	2.43	3.64	0.78
42W080144	1.5	0.70	3.27	4.90	1.05	0.57	2.66	3.99	0.86
42W080134	1.5	0.64	2.99	4.48	0.96	0.59	2.75	4.13	0.89
42W080124	1.5	0.63	2.94	4.41	0.95	0.56	2.61	3.92	0.84
42W080145	1.5	0.63	2.94	4.41	0.95	0.62	2.89	4.34	0.93
42W080135	1.5	0.64	2.99	4.48	0.96	0.59	2.75	4.13	0.89
42W080125	1.5	0.61	2.85	4.27	0.92	0.54	2.52	3.78	0.81
42W080146	1.5	0.65	3.03	4.55	0.98	0.63	2.94	4.41	0.95
42W080136	1.5	0.65	3.03	4.55	0.98	0.59	2.75	4.13	0.89
42W080126	1.5	0.62	2.89	4.34	0.93	0.52	2.43	3.64	0.78
42W100134	1.5	0.63	2.94	4.41	0.95	0.60	2.80	4.20	0.90
42W100124	1.5	0.61	2.85	4.27	0.92	0.53	2.47	3.71	0.80
42W100114	1.5	0.62	2.89	4.34	0.93	0.48	2.24	3.36	0.72
42W100135	1.5	0.63	2.94	4.41	0.95	0.58	2.71	4.06	0.87
42W100125	1.5	0.62	2.89	4.34	0.93	0.52	2.40	3.61	0.77
42W100115	1.5	0.63	2.94	4.41	0.95	0.46	2.15	3.22	0.69
42W100136	1.5	0.63	2.94	4.41	0.95	0.57	2.66	3.99	0.86
42W100126	1.5	0.63	2.94	4.41	0.95	0.51	2.38	3.57	0.77
42W100116	1.5	0.62	2.89	4.34	0.93	0.42	1.96	2.94	0.63

Table 8.12 summarizes the resulting collapse probabilities under the MCE_R intensity for the Los Angeles site. Similar to the frame archetypes, these proposed are based on a fixed dispersion of 0.5 in the FEMA P695 collapse fragility curve for all archetypes. As shown in the last column of Table 8.12, including bar fracture increases the collapse probability by 0.2% to 1.7%. In the Gr. 60 benchmark archetype (42W060136), the fracture increases the collapse risk by 0.6% (0.3% → 0.9%). In the Gr. 80 and 100 archetypes with T/Y = 1.2 and s/d_b = 5, fracture increases the collapse risk by 0.3% (0.4% → 0.7%) and 0.5% (0.4% → 0.9%), respectively. Even in the worst case (Gr. 100 with T/Y = 1.1 and s/d_b = 6), all of the 42-story archetypes have collapse risks far below the ASCE 7 minimum criterion of 10%, which is consistent with general impressions on the performance of tall shear wall buildings.

Table 8.12. Collapse probability of 42-story walls under MCE_R = 0.19 g.

Archetype	Collapse (non-fracture)	Including fracture	Collapse (fracture)
42W060156	0.27%	0.47%	0.20%
42W060146	0.27%	0.55%	0.28%
42W060136	0.29%	0.85%	0.56%
42W080144	0.20%	0.55%	0.36%
42W080134	0.31%	0.47%	0.16%
42W080124	0.34%	0.60%	0.26%
42W080145	0.34%	0.37%	0.03%
42W080135	0.31%	0.47%	0.16%
42W080125	0.40%	0.71%	0.31%
42W080146	0.29%	0.34%	0.05%
42W080136	0.29%	0.47%	0.18%
42W080126	0.37%	0.85%	0.48%
42W100134	0.34%	0.43%	0.09%
42W100124	0.40%	0.78%	0.38%
42W100114	0.37%	1.21%	0.84%
42W100135	0.34%	0.51%	0.17%
42W100125	0.37%	0.88%	0.52%
42W100115	0.34%	1.45%	1.11%
42W100136	0.34%	0.55%	0.21%
42W100126	0.34%	0.92%	0.59%
42W100116	0.37%	2.10%	1.74%

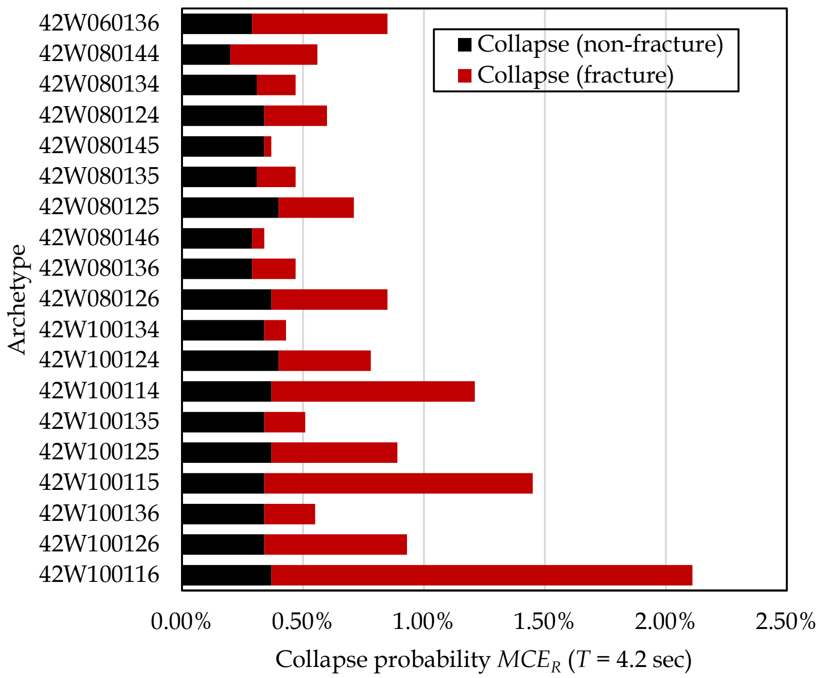

Figure 8.11. Collapse probability without and with fracture under MCE_R earthquakes.

Figure 8.12 shows the collapse fragility of the benchmark 42W060136. While this plot and the similar plots shown in Figures 8.13 to 8.15 consider responses well in excess of the MCE_R intensity of 0.19g, they are instructive to help understand the relative importance of fracture under larger earthquake ground motions and drift demands. The black curve represents the collapse fragility based on directly simulated failure modes. The grey curve shows the collapse probability due to non-simulated, fracture-induced failure modes. The red curve is the sum of the black and grey curves, and thus, is the total collapse fragility. In contrast to the frame archetypes, for the shear walls the fracture limit state plays a significant contribution to collapse risk relative to the sidesway collapse limit state. Of course, it is important to note that the assumption that fracture triggers collapse is a conservative.

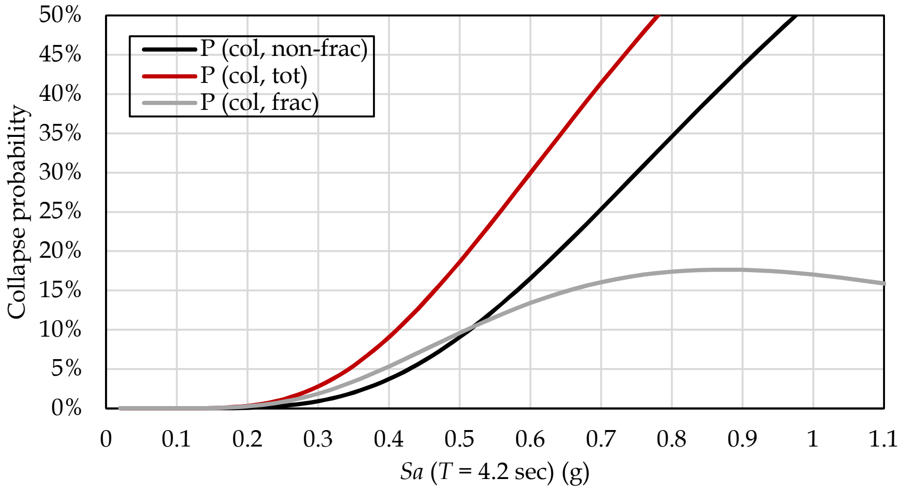

Figure 8.12. Collapse fragility curves (non-fracture, due-to-fracture, and total) of the benchmark 42W060136.

Figure 8.13 compares the collapse fragility curves for Gr. 100 shear wall archetypes with various *T/Y* ratios and the benchmark. The Gr. 100 case with *T/Y* equal to 1.2 and s/d_b equal to 5 (42W100125) has a similar collapse fragility as the benchmark. Decreasing the *T/Y* ratio to 1.1, increases the collapse risk, while increasing the ratio to 1.3 reduces the risk of the Gr. 100 archetype, relative to the benchmark case.

Figure 8.14 compares the collapse fragilities under different tie spacings. While the collapse probability is slightly affected by the tie spacing, compared to *T/Y* the effect of tie spacing is fairly negligible for the *Sa*(*T*) values considered.

Finally, Figure 8.15 compares the collapse fragilities of the benchmark case with one Gr. 80 archetype (42W080125) and two Gr. 100 archetypes (42W100125 and 42W100116). The first two walls comply with the proposed design requirements of *T/Y* >= 1.2 and s/d_b <= 5. Their collapse fragilities are very close to the benchmark case. The third fragility curve, plotted in red, is the worst case among all analyzed 42-story walls, whose collapse probability is 2.1% under MCE_R.

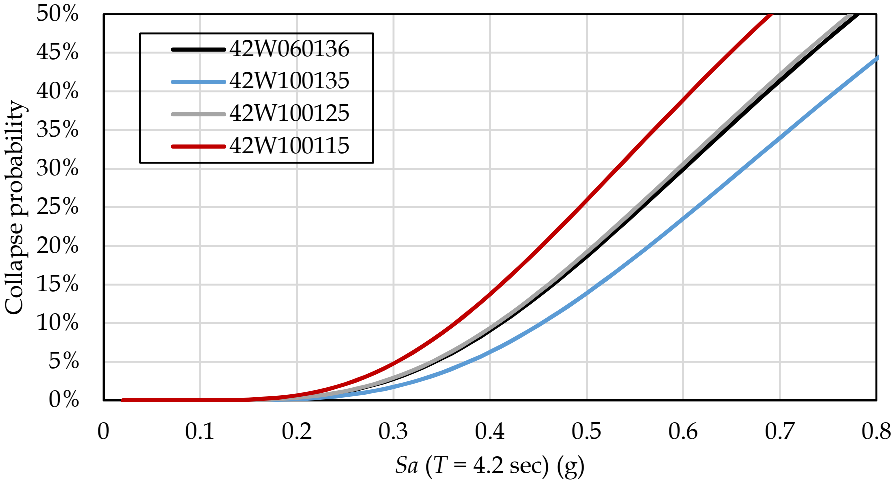

Figure 8.13. Total collapse fragility curves of the benchmark vs. Gr. 100 buildings with various *T/Y*'s.

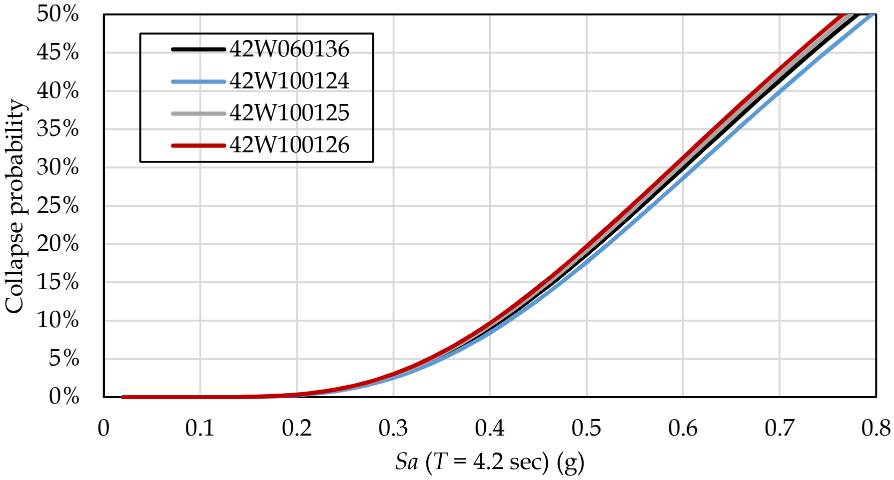

Figure 8.14. Total collapse fragility curves of the benchmark vs. Gr. 100 buildings with various s/d_b's.

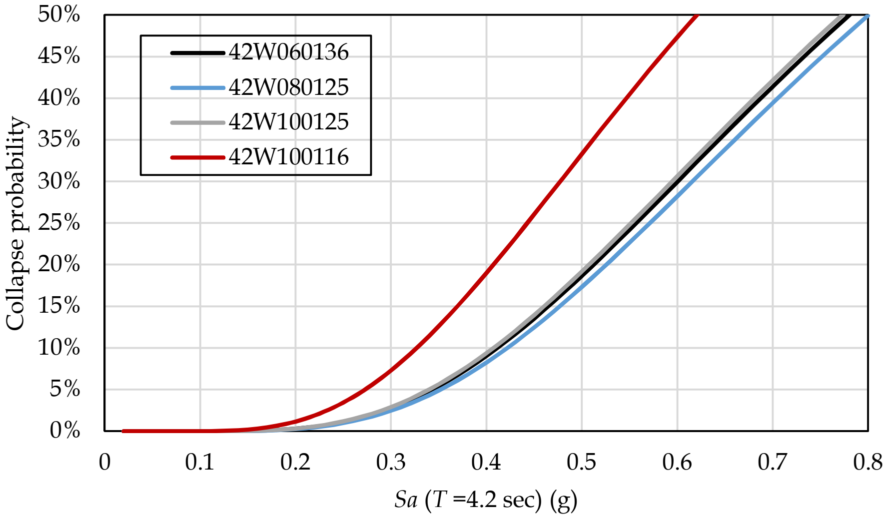

Figure 8.15. Total collapse fragility curves of the benchmark vs. 42W080125, 42W100125, and 42W100116.

8.2.6 Observations from 42-Story Wall Case Study

Overall, the 42-story archetypes all performed well in terms of having low risk of bar fracture or collapse. The following is a summary of detailed observations from the results of the 42-story frame study:

1. Buildings with high-strength reinforcement tend to experience larger drift ratios (about 7% more), primarily due to reduced transformed and effective stiffness.
2. Cumulative plastic strain demands for the walls with high strength bars are about 5% to 10% larger than the wall with conventional Gr. 60 steel (for cases with *T/Y* >= 1.2). When divided by their respective yield strain, the normalized cumulative plastic strain demands (CPD/ε_y) for the walls with high strength reinforcement is in fact less than for Gr. 60 steel, i.e., CPD/ε_y of about 60 for Gr. 60 steel and between 40 to 50 for Gr. 80 and 100 steel.
3. As with the frame archetypes, the probability of reinforcing bar fracture increases with decreasing *T/Y*, and increasing tie spacing (s/d_b). But, overall the probability of bar fractures under MCE_R ground motions (even with average maximum story drift ratios on the order of 0.03) are very small, typically less than 2% when *T/Y* >= 1.2 and maximum tie spacing is limited to $5d_b$. Even when the limits on *T/Y* and s/d_b are relaxed, the fracture probabilities are still less than 3%.
4. Collapse risks under MCE_R ground motions are small for the 42-story archetype, generally less than 2%. Nevertheless, trends similar to those in moment frames are observed, where decreasing *T/Y* and increasing tie spacing (s/d_b) contribute to increasing the collapse risk.

8.3 Results for 8-Story Wall

Similar to summary of data for the 42-story walls in Section 8.2, this section concludes analysis results of 8-story buildings. Table 8.13 lists all seventeen archetypes with various grades, hardening ratios, and tie spacings. Based on the observations from 42-story walls: the structural safety in concerns are designs with small *T/Y*'s but large s/d_b's. Herein, archetypes that are not deemed to be extreme (e.g., 08W080144) are not analyzed.

Table 8.13. Design matrix and ID of 8-story archetype walls.

Grade	*T/Y*	Tie spacing s/d_b		
		4	5	6
60	1.5	-	-	08W060156
	1.4	-	-	08W060146
	1.3	-	-	08W060136*
80	1.4	-	-	08W080146
	1.3	08W080134	08W080135	08W080136
	1.2	08W080124	08W080125	08W080126
100	1.3	-	-	08W100136
	1.2	08W100124	08W100125	08W100126
	1.1	08W100114	08W100115	08W100116

Like the 42-story wall, the 8-story wall is designed following the provisions for special walls in ASCE-7 and ACI-318, based on an MCE_R intensity of SM_1 equal to 0.6g. The design with Gr. 60 reinforcement has a fundamental period of 1.15 s. Table 8.14 summarizes MCE_R values at LADT (Site Class C), along with Sa (T_1 = 1.15 s) at six hazard levels. In Table 8.15, the fundamental periods of the walls with higher grades (Gr. 80 and 100) are nearly the same as the fundamental period of the benchmark Gr. 60 wall. Also tabulated are the *SaRatio* and $Ds_{5\text{-}75}$ based on the site hazard and calculated building periods. In following sections, the seismic performance is going to be assessed conditionally at T_1 = 1.15 sec.

Table 8.14. MCE_R and *Sa* (T_1 = 1.15 s) at different intensity levels.

Hazard Level (Return Period)	***Sa* (T_1 = 1.15 s) (g)**
	LADT (Site Class C)
MCE_R	0.52
10%/50yrs	0.45
5%/50yrs	0.61
2%/50yrs	0.89
2%/100yrs	1.03
2%/200yrs	1.19
1%/200yrs	1.38

Table 8.15. Site-specific seismic hazard metrics for unique designs.

	LADT (Site Class C)		
Grade	60	80	100
Period (sec)	1.15	1.16	1.17
MCE_R (g)	0.52	0.52	0.51
***SaRatio* ($0.2T_1, T_1, 3.0T_1$)**	1.86	1.85	1.84
$D_{S5\text{-}75}$ (sec)	3.90	3.92	3.94

8.3.1 Peak Story Drift Ratio (MCE_R)

Table 8.16 summarizes the mean peak story drift ratio demands at MCE_R (SDR_{max}) in the 8-story wall archetypes. Remarkably, these story drifts, ranging from 0.015 to 0.017, are considerably smaller than the drift ratios of 0.03 and 0.04, permitted by the PEER TBI guidelines or the ASCE 7 requirements, respectively. While not unexpected, this point is important to keep in mind when later reviewing the bar strain and fracture demands. The drifts in the Gr. 80 and 100 archetypes are about 5% and 10% larger than in the Gr. 60 benchmark case. Again, this is mainly due to the decease of initial stiffness (i.e., a more flexible structure tends to move more at the same hazard level). A lower *T/Y* ratio is also found to slightly increase the story drift ratio demands, however, these differences and impacts from different tie spacings are negligible.

Table 8.16. Mean peak story drift ratio demands of 8-story walls at MCE_R intensity level.

	Site	LADT (Site Class C) $MCE_R = 0.52$ g
Archetype ID	08W060156	0.015
	08W060146	0.015
	08W060136*	0.015
	08W080134	0.016
	08W080124	0.017
	08W080135	0.016
	08W080125	0.016
	08W080146	0.016
	08W080136	0.017
	08W080126	0.016
	08W100124	0.017
	08W100114	0.017
	08W100125	0.017
	08W100115	0.017
	08W100136	0.017
	08W100126	0.017
	08W100116	0.017

8.3.2 Cumulative Plastic Strain (MCE_R)

Table 8.17 summarizes the maximum cumulative plastic strain demands (*CPD*) in the 8-story wall archetypes. The *CPDs* for the 8-story walls, on the order of 0.25 to 0.34, are significantly larger than the values in the frame or 42-story wall studies. These large strains are in spite of the relatively low drift ratios, owing to the geometric proportions of the wall. Similar to the other archetypes, while the *CPDs* tend to be slightly larger for the archetypes with higher strength rebars, the normalized *CPDs* are comparable. The normalized CPD/ε_y values for the Gr. 60 benchmark (08W060136) and the Gr. 80 and 100 archetypes with *T/Y* = 1.2 (08W080125, 08W100125) are 155, 109, and 91, respectively. As will be seen, these larger *CPD* demands lead to larger bar fracture probabilities than in the other moment frame and 42-story wall archetypes.

Table 8.17. Maximum cumulative plastic strain in archetypes under MCE_R earthquakes.

	Site	LADT (Site Class C) MCE_R = 0.52 g
Archetype ID	08W060156	0.249
	08W060146	0.274
	08W060136*	0.311
	08W080134	0.248
	08W080124	0.285
	08W080135	0.270
	08W080125	0.291
	08W080146	0.243
	08W080136	0.268
	08W080126	0.296
	08W100124	0.280
	08W100114	0.343
	08W100125	0.302
	08W100115	0.326
	08W100136	0.270
	08W100126	0.309
	08W100116	0.326

8.3.3 Fracture Probability (MCE_R)

Summarized in Table 8.18 and Figure 8.16 are the rebar fracture probabilities, condition on non-collapse for the 8-story wall archetypes under the MCE_R ground motions. The reinforcement in the benchmark building, 08W060136, has about a 15% probability of fracture. Increasing the *T/Y* ratio of Gr. 60 bars to 1.4 and 1.5, reduces the fracture probability to 11% and 7%, respectively. This influence of *T/Y* ratio is also observed for high-strength reinforcement archetypes. For instance, the fracture probability of the worst case, the Gr. 100 steel with *T/Y* equal to 1.1 (08W100116), which is about 27%, can be reduced to less than 6% by increasing the *T/Y* ratio up to 1.3. Tighter tie spacings also help to control the fracture risks. Taking the Gr. 100 archetype with *T/Y* equal to 1.2 and s/d_b of 6 (08W100126) as a baseline case, the fracture probability is about 10%. Using the same bars but a tie spacing of $5d_b$, the fracture probability decreases to 8%. Although both increasing *T/Y* ratio and decreasing s/d_b can reduce the rebar fracture probability in 8-story wall archetypes, increasing *T/Y* ratio is generally more effective. Interestingly, the archetypes with high strength reinforcing bars can do as well or better than the benchmark Gr. 60 case, presumably because the normalized cumulative plastic strain demands are less (due to the higher yield strains in the high strength bars). If limits are imposed on *T/Y* and s/d_b (median *T/Y* >= 1.2, s/d_b <=5), then the worst case archetype with high strength reinforcement (08W080125) has a fracture probability about 11%, which compares favorably with the risk of 15% in the Gr. 60 benchmark case. The corresponding Gr. 100 archetype (08W100125) performs even better with a bar fracture risk of 8%.

Table 8.18. Estimated probability of rebar fracture under *MCE_R*

	Site	LADT (Site Class C) MCE_R = 0.52 g
Archetype ID	08W060156	6.82%
	08W060146	10.40%
	08W060136*	15.32%
	08W080134	5.04%
	08W080124	6.17%
	08W080135	6.65%
	08W080125	11.27%
	08W080146	5.19%
	08W080136	8.63%
	08W080126	16.52%
	08W100124	7.57%
	08W100114	18.27%
	08W100125	8.11%
	08W100115	22.37%
	08W100136	6.39%
	08W100126	9.63%
	08W100116	27.24%

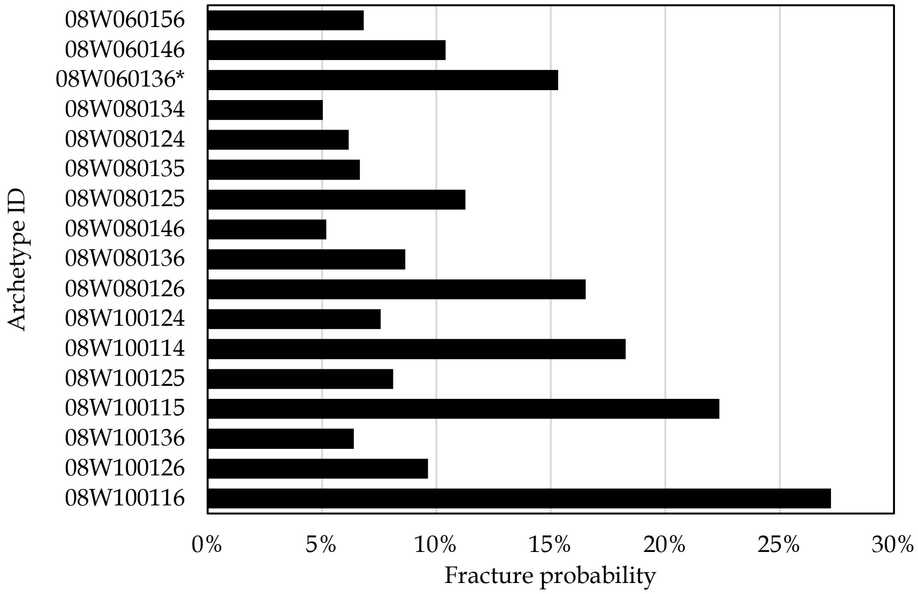

Figure 8.16. Probability of fracture under *MCE_R* at LADT (Site Class C)

8.3.4 FI_{max}-SDR_{max} Relation

Similar to the results presented for 42-story archetype, the relation between maximum fracture index and maximum story drift ratio is helpful to understand the rebar fracture potential independent of the ground motion intensities. Figures 8.15 to 8.19 summarize the FI_{max}-SDR_{max} curves of all analyzed 8-story walls.

Comparing these plots back to the ones for the 42-story archetypes (Figures 8.9 and 8.10) highlights that the reinforcing bars in the 8-story archetype are much more prone to fracture at comparable peak SDR_{max} values. For example, in the Gr. 60 benchmark case, for a SDR_{max} of 0.03, the median *FI* in the 8-story archetype is 1.7 versus only 0.1 in the 42-story archetype. This is largely because the shear wall in the 42-story archetype is about 3.6 times as slender (height/width ratio) as in the 8-story archetype. So, for a given peak drift the wall curvatures are much larger in the 8-story archetype.

Figure 8.17 compares three Gr. 60 walls with different strain hardening properties. These plots confirm previous observations that the FI_{max} increases with decreasing *T/Y*. At a SDR_{max} limit of 0.03, the median values of FI_{max} are 0.7, 1.0, and 1.7 for *T/Y* ratios of 1.5, 1.4 and 1.3, respectively.

Figure 8.18 shows the FI_{max}-SDR_{max} curves of three Gr. 80 walls with median *T/Y* ratios of 1.3 and 1.4 with varying tie spacing. Compared to the benchmark case, which is plotted in green, all three Gr. 80 walls performance better in terms of avoiding bar fracture failures.

Figure 8.19 shows the FI_{max}-SDR_{max} curves of three Gr. 80 walls with the median *T/Y* ratio fixed at 1.2 with various tie spacings. Compared to the benchmark case, which is plotted in green, all three Gr. 80 walls perform better at low drifts, but then cross over at SDR_{max} of ~0.02. This reflects the fact that at lower drifts the higher yield strain provides a benefit to the Gr. 80 bars before the benefit diminishes at higher drifts.

Figure 8.20 shows the FI_{max}-SDR_{max} curves of three Gr. 100 walls with median *T/Y* ratios or 1.2 and 1.3. Compared to the benchmark case, all three Gr. 100 walls performance better in terms of avoiding bar fracture failures.

Finally, Figure 8.21 shows the FI_{max}-SDR_{max} curves of three Gr. 100 walls with median *T/Y* ratio of 1.1 and with various tie spacings. Compared to the benchmark case, all three Gr. 100 walls have dramatically higher fracture indices once the SDR_{max} exceeding 1.0%, emphasizing the importance of maintaining a minimum requirement on the *T/Y* ratio.

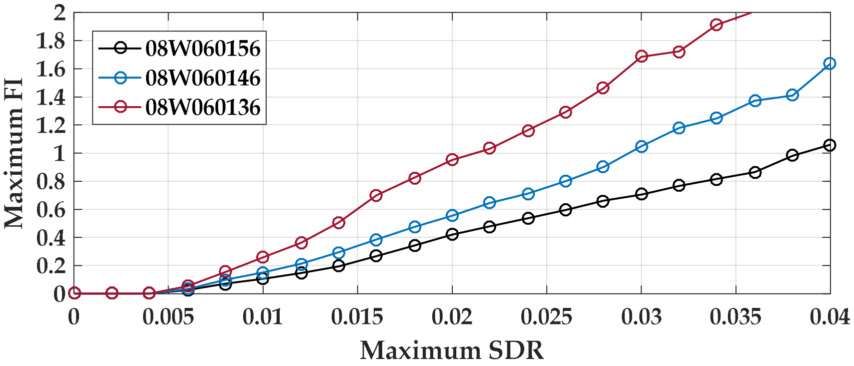

Figure 8.17. FI_{max}-SDR_{max} curves of Gr. 60 archetypes with different *T/Y*'s.

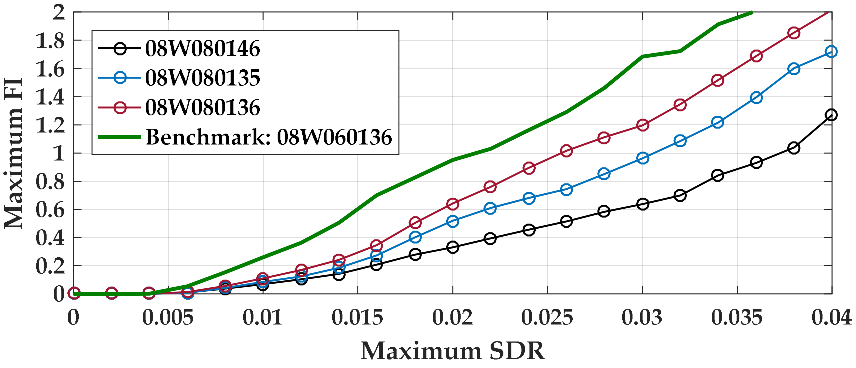

Figure 8.18. FI_{max}-SDR_{max} curves of Gr. 80 archetypes with the higher *T/Y* and the benchmark.

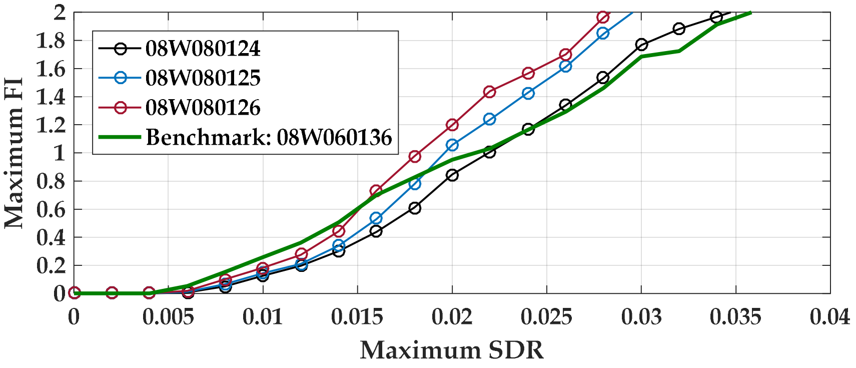

Figure 8.19. FI_{max}-SDR_{max} curves of Gr. 80 archetypes with the lowest *T/Y*'s and the benchmark.

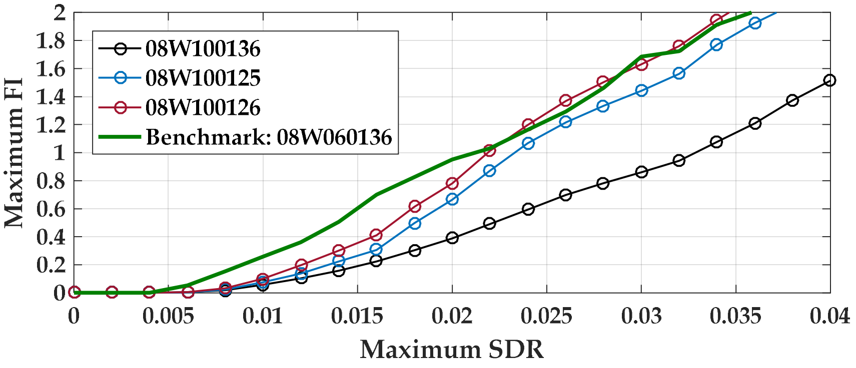

Figure 8.20. FI_{max}-SDR_{max} curves of Gr. 100 archetypes with the higher *T/Y* and the benchmark.

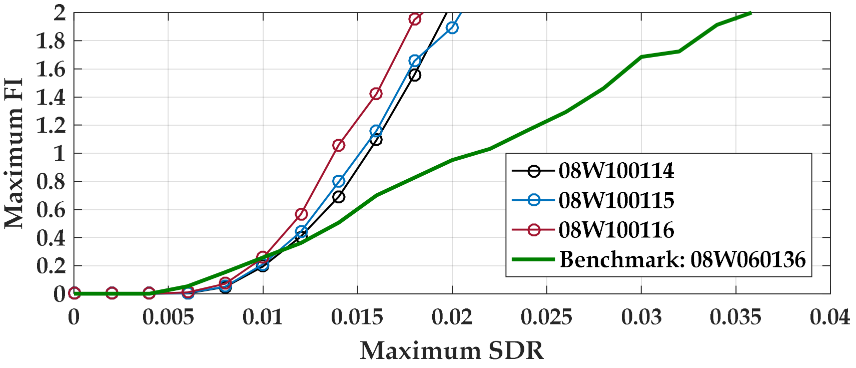

Figure 8.21. FI_{max}-SDR_{max} curves of Gr. 100 archetypes with the lowest *T/Y* and the benchmark.

8.3.5 Collapse Fragility

Table 8.19 summarizes the median collapse intensities (S_{CT}), along with *CMR*, *ACMR*, and adjusted median collapse intensities (S_{CT}*) for the 8-story wall archetypes, and Table 8.20 summarizes the corresponding MCE_R collapse probabilities. Similar to the assessment of other systems, the period-dependent ductility ratio and the spectral shape factor is fixed at 8.6 and 1.45, respectively, which are the same as the original 8-story wall design (after ATC 123 report). In addition, following the approach of FEMA P695, the ground motion spectral intensities are defined in terms of the simplified code formula for period, which in this structure is T equal to 0.66 sec, as opposed to the analysis model period of T_1 equal to 1.15 sec used in the previously reported analyses. The corresponding *MCE* values are Sa(T) equal to 0.91g, based on T=0.66 sec, and Sa(T_1) equal to 0.52g, based on T_1 = 1.15sec (both of which correspond to the same *MCE* intensity, assuming a $1/_T$ relationship between Sa and T).

Excluding the fracture-induced failure limit state, all archetypes have large median collapse intensities (S_{CT}* varying from 3.36g to 3.84g in Table 8.19) with correspondingly low collapse probabilities (MCE_R collapse probabilities below 1% in the second column of Table 8.20). Excluding the fracture failures, the collapse probabilities are so small that there is no clear trend with regard to reinforcing bar strengths.

On the other hand, when fracture-induced failures are included, and conservatively assuming that structural collapse occurs when FI_{max} = 1.0, the collapse probabilities increase significantly. The fourth column in Table 8.20 includes the probability of collapse due to fracture, and the third column indicates the total probability of collapse (the sum of columns two and four). The probability of collapse in the Gr. 60 benchmark archetype (08W060136) increases from about 0.7%, without considering fracture, to 5.8% including fracture. While the increase is significant, the total probability is still less than the FEMA P695 and ASCE 7 limit of 10%.

In walls using high-strength bars with a median *T/Y* of 1.2 and s/d_b equal to 5, the maximum MCE_R collapse capacities are on the order of the limiting value of 10%. The Gr. 80 case (08W080125) has a collapse probability of 11.2% and the Gr. 100 case (08W100125) has a probability of 10.3%. Further limiting of s/d_b to 4 achieves less than 10% collapse probabilities for both grades. At the other extreme, for the Gr. 100 cases with *T/Y* = 1.1, the probabilities of fracture-induced collapse shoot up to values of about 30%. Thus, these analyses lend further support to the proposal to limit *T/Y* of 1.2 and s/d_b equal to 4 or 5 so as to achieve performance consistent with FEMA P695 and ASCE 7. Of course, it should also be recognized that these statistics are predicated on the assumption that the first reinforcing bar fracture will trigger collapse, which is likely to be very conservative (especially for walls that are not heavily loaded in compression by gravity).

Table 8.19. Collapse fragility table for all archetypical 8-story walls.

			Excluding fracture-induced collapse				Including fracture-induced collapse			
Archetype	μ_T	*SSF*	S_{CT} (g)	*CMR*	*ACMR*	S_{CT}* (g)	S_{CT} (g)	*CMR*	*ACMR*	S_{CT}* (g)
08W060156	8.6	1.45	2.72	2.99	4.34	3.94	2.25	2.48	3.59	3.26
08W060146	8.6	1.45	2.71	2.98	4.32	3.93	1.99	2.19	3.17	2.89
08W060136*	8.6	1.45	2.71	2.98	4.32	3.93	1.61	1.77	2.57	2.33
08W080134	8.6	1.45	2.70	2.97	4.31	3.92	1.86	2.05	2.97	2.70
08W080124	8.6	1.45	2.71	2.98	4.32	3.93	1.36	1.50	2.17	1.97
08W080135	8.6	1.45	2.71	2.98	4.32	3.93	1.73	1.90	2.76	2.51
08W080125	8.6	1.45	2.71	2.98	4.32	3.93	1.30	1.43	2.07	1.89
08W080146	8.6	1.45	2.70	2.97	4.31	3.92	2.08	2.29	3.32	3.02
08W080136	8.6	1.45	2.71	2.98	4.32	3.93	1.65	1.82	2.63	2.39
08W080126	8.6	1.45	2.72	2.99	4.34	3.94	1.26	1.39	2.01	1.83
08W100124	8.6	1.45	2.68	2.95	4.27	3.89	1.40	1.54	2.23	2.03
08W100114	8.6	1.45	2.66	2.93	4.24	3.86	0.89	0.98	1.42	1.29
08W100125	8.6	1.45	2.65	2.92	4.23	3.84	1.34	1.47	2.14	1.94
08W100115	8.6	1.45	2.62	2.88	4.18	3.80	0.87	0.96	1.39	1.26
08W100136	8.6	1.45	2.65	2.92	4.23	3.84	1.66	1.83	2.65	2.41
08W100126	8.6	1.45	2.65	2.92	4.23	3.84	1.28	1.41	2.04	1.86
08W100116	8.6	1.45	2.46	2.71	3.92	3.57	0.84	0.92	1.34	1.22

Table 8.20. Collapse probability of 8-story walls under MCE_R = 0.91g.

Archetype	Collapse (non-fracture)	Including fracture	Collapse (fracture)
08W060156	0.72%	1.66%	0.94%
08W060146	0.73%	2.71%	1.98%
08W060136*	0.73%	5.80%	5.06%
08W080134	0.75%	3.50%	2.75%
08W080124	0.73%	9.84%	9.11%
08W080135	0.73%	4.54%	3.80%
08W080125	***0.73%***	***11.21%***	***10.48%***
08W080146	0.75%	2.28%	1.53%
08W080136	0.73%	5.34%	4.60%
08W080126	***0.72%***	***12.24%***	***11.51%***
08W100124	0.77%	9.03%	8.26%
08W100114	***0.80%***	***27.96%***	***27.16%***
08W100125	***0.81%***	***10.28%***	***9.46%***
08W100115	***0.86%***	***29.25%***	***28.39%***
08W100136	0.81%	5.23%	4.42%
08W100126	***0.81%***	***11.71%***	***10.90%***
08W100116	***1.14%***	***31.29%***	***30.16%***

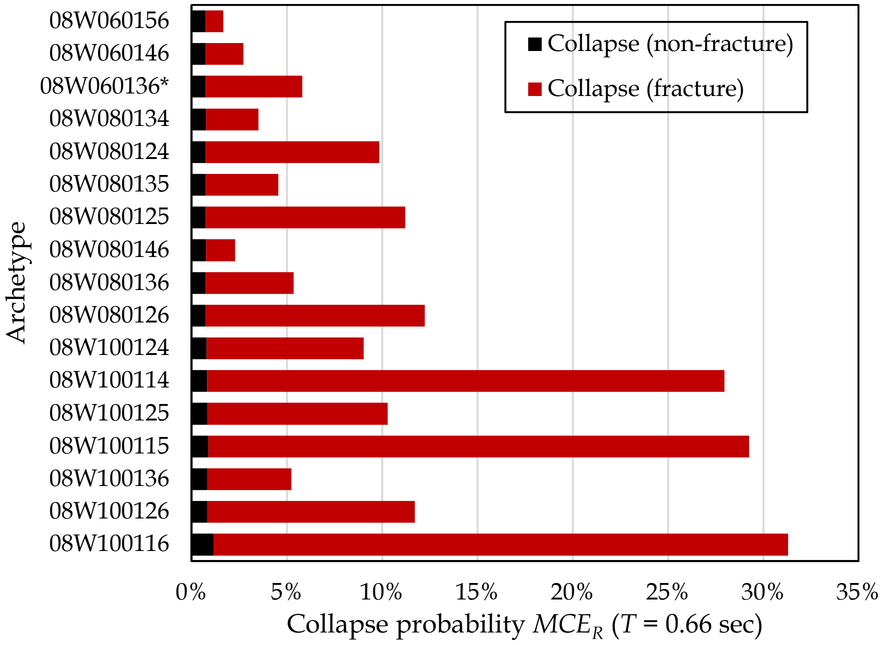

Figure 8.22. Collapse probability without and with fracture under MCE_R earthquakes.

Figure 8.23 shows the collapse fragility of the Gr. 60 benchmark building (08W060136). The black curve represents the collapse fragility based on directly simulated failure modes. The grey curve shows the collapse probability due to non-simulated, fracture-induced failure modes. The red curve is the sum of the black and grey curves, and thus, is the total collapse fragility. The contribution from fracture-induced failure is prominent, especially at lower intensities. Based on the T equal to 0.66sec, the *MCE* intensity is 0.91g, which corresponds to just under a 5% probability of collapse, nearly all attributed to fracture.

Figure 8.24 compares the performance of three Gr. 100 archetypes with varying *T/Y* (08F100136, 08W100126, and 04F100116) along with a Gr. 60 frame Excluding the fracture risk, these three structures have very close median collapse capacities, roughly 2.3 to 2.6g. However, including fracture-induced collapse, the probabilities of collapse for the cases with *T/Y* of 1.2 and 1.1 increase significantly above the Gr. 60 benchmark. The worst among these three Gr. 100 cases with *T/Y* equal to 1.1 (08W100116) only has about a half of the median collapse capacity of the benchmark.

Figure 8.25 compares the performance of three Gr. 100 archetypes with *T/Y* of 1.2 and varying tie spacing (08W100124, 08W100125, and 08W100126). The tighter tie spacing confines the core concrete and limits local buckle of longitudinal bars, all of which improve performance. None of the Gr. 100 cases perform as well as the benchmark case, but the one with tie spacing of s/d_b equal to 4 (08W100124) comes closest.

Figure 8.26 compares the performance of three archetypes with varying grade, *T/Y* and bar spacing (08W080125, 08W100125, and 08W100116), including two that conform with the purposed requirements of *T/Y* >= 1.2 and s/d_b <= 5. While none of the high strength cases are as good as the Gr. 60 benchmark, the ones with the tighter control on *T/Y* and s/d_b perform best. The third curve with *T/Y* = 1.2 and s/d_b =6, plotted in red, is the worst case among all analyzed 8-story walls, with a collapse probability of roughly 30% under MCE_R (0.91g).

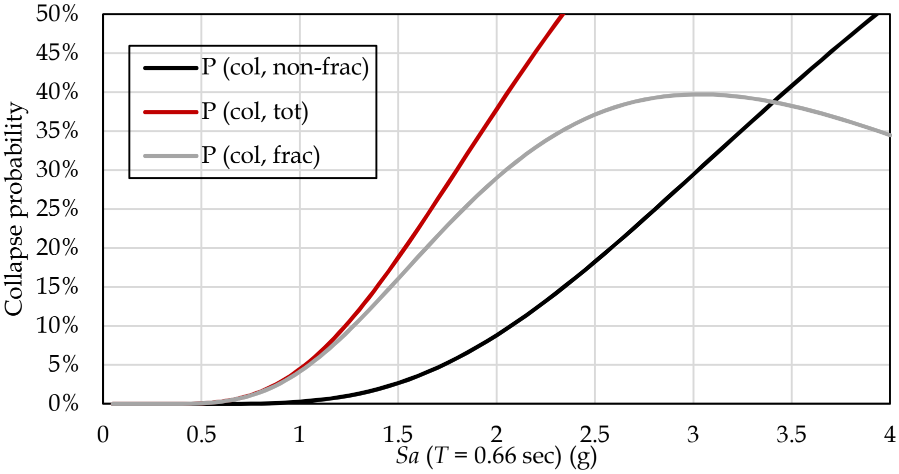

Figure 8.23. Collapse fragility curves (non-fracture, due-to-fracture, and total) of the benchmark 08W060136.

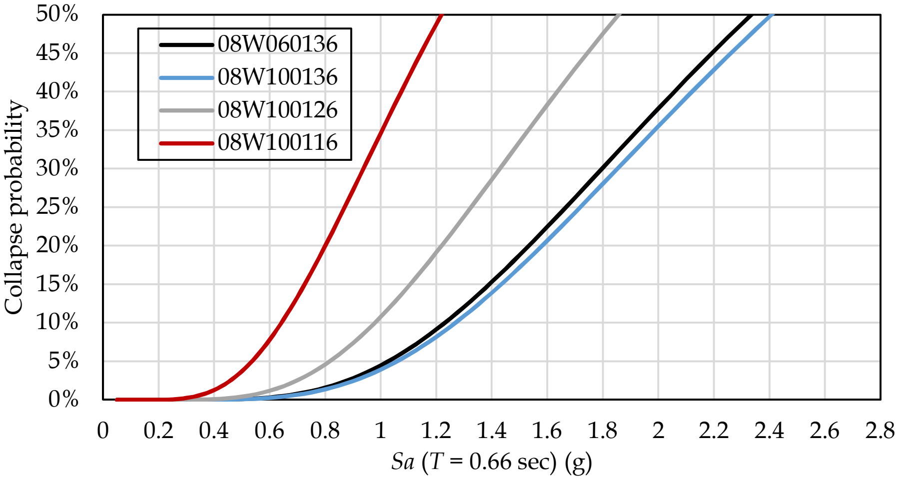

Figure 8.24. Total collapse fragility curves of the benchmark vs. Gr. 100 buildings with various *T/Y*'s.

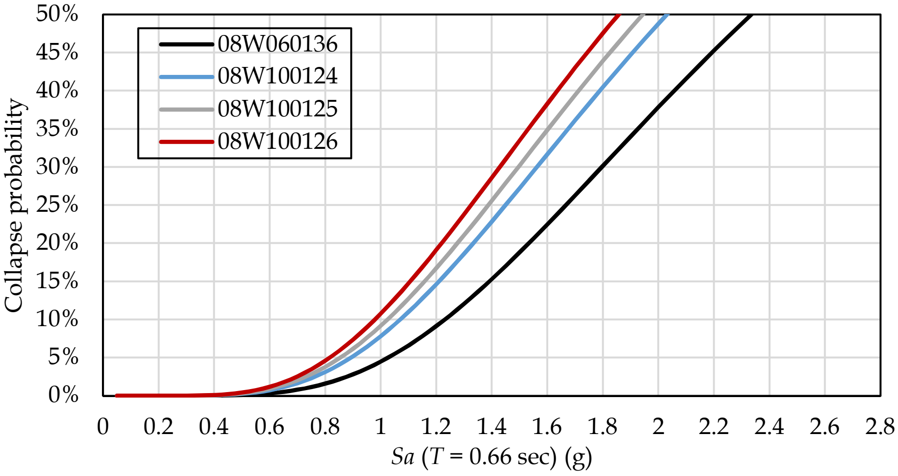

Figure 8.25. Total collapse fragility curves of the benchmark vs. Gr. 100 buildings with various s/d_b's.

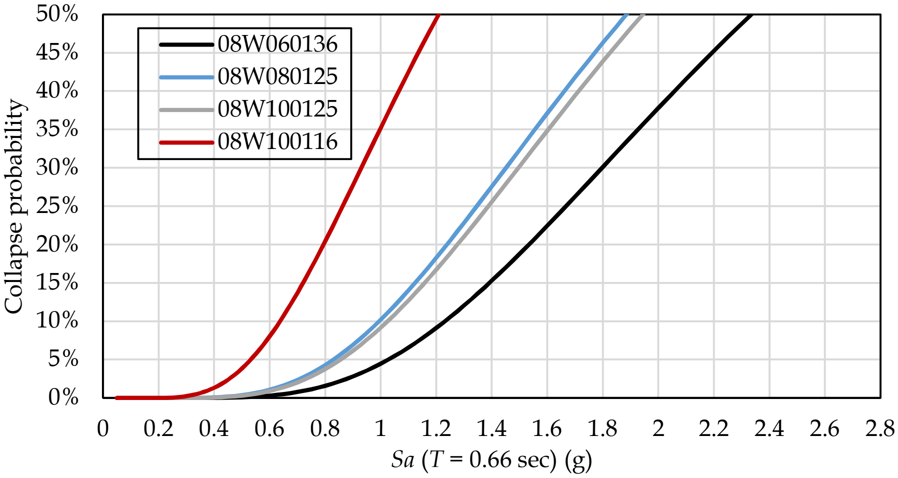

Figure 8.26. Total collapse fragility curves of the benchmark vs. 08W080125, 08W100125, and 08W100116.

8.3.6 Observations from 8-Story Wall Case Study

The following is a summary of major observations from the results of the 8-story wall study:

1. Most observations from the 42-story wall case study apply as well to the 8-story walls, in spite of the fact that the probabilities of bar fracture are significantly larger for the 8-story structure. Nevertheless, the results provide further support to the recommendation to set the minimum allowable median *T/Y* as 1.2 and to limit the tie spacing to $5d_b$ (and possibly $4d_b$) for the high strength reinforcing bars.
2. In general, the cumulative plastic strain demands in the 8-story walls are about 2 to 2.5 times larger than comparable cases (i.e., same reinforcing bar grade, *T/Y* ratio, tie spacing) than the 42-story wall case The probabilities of bar fracture under MCE_R ground motions are 4 to 7 times higher in the 8-story walls as compared to the comparable 42-story walls. There are two main reasons for the differences. First, he fundamental period of the 8-story wall is about 1.2 sec which is about one-third of the first period of the 42-story wall, which translates to a larger number of loading cycles in the 8-story wall. Second, while the maximum story drift demands (SDR_{max}) are larger in the 42-story building, the curvature demands (and hence the bar strain demands) are much larger in the 8-story wall. In this sense, the rate of change in story drift ratio between one floor and another, would be more indicative of the strain demands experienced by the walls.
3. Interestingly, at lower earthquake intensities, the walls with high-strength reinforcement often behavior better than with conventional strength reinforcement, due to the larger yield strains (and yield curvatures) in the walls with higher strength bars. However, this advantage is temporary, since the plastic strain demands and fracture indices increase more rapidly in the cases with high strength reinforcement for drifts (curvatures) beyond the yield point.

8.4 Summary of Results and Trends for HS bars in Walls

In this chapter, the results of 8-story and 42-story shear wall building analyses are summarized with special focus on the influence of reinforcing bar properties on maximum story drift ratio demands, cumulative plastic strain demands, bar fracture index demands, bar fracture probabilities, and collapse probabilities (with and without fracture) under different earthquake intensity levels. In general, the earthquake demands in the 8-story archetype are more severe than those in the 42-story archetype, due to a combination of factors, including (1) a shorter period in the 8-story archetype, which results in a larger spectral demands and larger number of seismic loading excursions, and (2) a smaller aspect ratio, which implies larger curvatures and reinforcing bar strains for a given peak story drift. The following is a summary of the key observations and conclusions:

Story Drift Demands: The peak average MCE_R story drift demands for the 8-story walls are 0.015 to 0.017, which is well below the maximum building code criteria. On the other hand, the drifts in the 42-story walls are 0.027 to 0.029, which is close the 0.03 limit permitted by the PEER TBI guidelines. Compared to the benchmark moment frame designs with Gr. 60 reinforcement, the MCE_R drift demands are about 5% higher with Gr. 80 reinforcement and about 10% larger with Gr. 100 reinforcement. These are assuming the only change in designs to reduce the flexural reinforcing steel areas in proportion to the bar yield strengths. The difference in drifts is roughly proportional to the difference in the transformed cross section stiffness.

Cumulative Plastic Strain Demands: Nominal reinforcing bar strains and plastic strain demands are calculated assuming a nominal 8-inch gage length in the hinge regions at the base of the walls. The average cumulative plastic strain demands (*CPD*) in the most critical wall reinforcement under MCE_R ground motions are about 0.30 in the 8-story wall and 0.14 in the 42-story wall. Similar to the frame systems, the maximum cumulative plastic strain demands are similar between the frames with conventional and high-strength steel, but the normalized cumulative plastic strain demands (CPD/ε_y) are lower in the high strength bars due to the higher yield strains the high strength bars. For example, cumulative normalized plastic strain demands in the 8-story walls are 150, 110, and 90 for Gr. 60, 80 and 100 bars.

Reinforcing Bar Fracture Probability: In the 42-story wall, average probabilities of bar fracture under MCE_R ground motions are very low, about 2% to 3% for all of the steel grades. The probabilities of fracture are much larger in the 8-story wall, ranging from 15% for the Gr. 60 benchmark case (Gr. 60 with *T/Y* of 1.3 and s/d_b of 6) up to 27% in the worst Gr. 100 case (Gr. 100 with *T/Y* of 1.1 and s/d_b of 6). By limiting the minimum allowable median *T/Y* to 1.2 and the maximum tie spacing to $5d_b$, the probabilities of bar fracture for Gr. 80 and 100 bars in the 8-story walls are 11% and 8%, which are in fact, lower than the benchmark case. The fracture probabilities are lower for the high strength bars, presumably due to the higher yield strains in the high strength bars, which result in lower plastic strain demands.

P695 Collapse Risk: Collapse risks are evaluated using the FEMA P695 procedure, where the effect of reinforcing bar fracture is considered as a non-simulated failure mode. The probabilities of collapse under MCE_R motions Collapse risks for the 42-story shear wall are very low, typically less than 1%, even when the fracture-induced collapse mode is considered. The one exception is the case of Gr. 100 bars with *T/Y* of 1.1 and s/d_b of 6, where the collapse risk increases to 2%. The collapse probabilities for the 8-story wall due to sideway (excluding fracture) is very small, all less than 1%. Including fracture, the probabilities increase to 6% for the Gr. 60 benchmark case and 11% for the Gr. 80 and 100 cases with the limits on $T/Y >= 1.2$ and $s/d_b <=5$. Without these limits, the probability of collapse including fracture increases to 31% for the worst Gr. 100 case (Gr. 100 with *T/Y* of 1.1 and s/d_b of 6). Thus, these data again support the limit on minimum *T/Y* and maximum tie bar spacing.

9. SUMMARY, CONCLUSIONS AND LIMITATIONS

9.1 Summary

This report summarizes work to integrate results from experimental laboratory tests and computational simulations of archetype buildings to evaluate seismic design requirements for high strength reinforcing bars. The three main components of the study are (1) development and calibration of a model to evaluate reinforcing bar fracture under random cyclic loading (Chapter 3), (2) development, calibration and validation of models to simulate the nonlinear response of concrete structures, with sufficient resolution and capabilities to differentiate the effects of reinforcing bar properties on structural deformations, reinforcing bar strains and reinforcing bar fracture (Chapters 4 and 5), and (3) nonlinear dynamic analyses of reinforced concrete moment frame and shear wall systems to assess seismic strain demands and fracture limit states for reinforcing bars and overall system performance (Chapters 7 and 8). An overall framework for integrating these three components and methods for characterizing site-specific earthquake hazard and demand parameters are outlined in Chapters 2 and 6, respectively.

9.1.1 Reinforcing Bar Fracture Model

Based on the available rebar monotonic tensile and cyclic test data (Slavin and Ghannoum, 2015; Zhao and Ghannoum, 2016), a parametric reinforcement fatigue-fracture model (Equation 9.1) is proposed in this study. Three material parameters (α_f, C_f, and ε_f) are calibrated to best capture the observed trends in tests, where fracture-fatigue resistance is negatively correlated with steel grade and tie spacing and positively correlated with tensile-to-yield strength ratio. Data reduction and linear regressions are performed to establish and calibrate a parametric model that is defined using standard bar material properties. Based on Miner's Law and rain-flow counting, the fracture index (*FI*, Equation 9.2) can be computed for a specific plastic strain history with known material parameters. Comparisons between the fracture index and 206 cyclic bar tests are conducted to verify the model accuracy. The resulting fracture indices are statistically related to the observed bar fractures, as described by the lognormal cumulative distribution (fragility) function in Figure 9.1 with a median *FI* value of 1.0 and a dispersion of 0.5. Details of the fracture-fatigue model are presented in Chapter 3.

$$\left\{ \begin{array}{c} \varepsilon_p = C_f \left(2N_f\right)^{-\alpha_f} \\ where, \quad \alpha_f = 0.080 - 0.045 \cdot \left(f_y / 60ksi\right) + 0.027 \cdot \left(s/d_b\right) + 0.129 \cdot \left(T/Y\right) \\ C_f = 0.5^{\alpha_f} \cdot \left(\varepsilon_f - f_y / E_s\right) \\ \varepsilon_f = f_y / E_s - 0.043 \cdot \left(f_y / 60ksi\right) + 0.128 \cdot \left(T/Y\right) + 0.018 \cdot \left(d_b / 1in\right) \end{array} \right. \tag{9.1}$$

$$FI = \sum_{i=1}^{N} \left(\varepsilon_{pi} / C_f\right)^{1/\alpha_f} \tag{9.2}$$

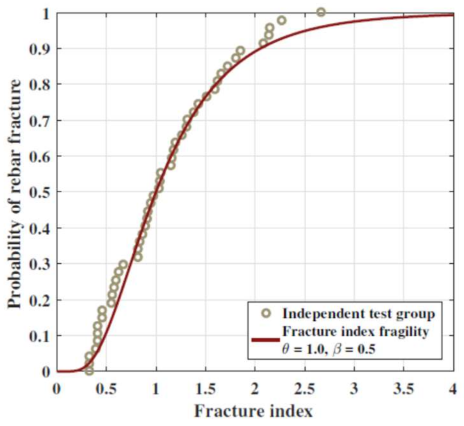

Figure 9.1. Reinforcement fracture fragility function.

Fiber-based beam-column models are used to simulate the detailed nonlinear response of beam, column, and slender shear walls. Reinforcing bar strain histories from the fiber-based models are used as input to the proposed fatigue-fracture model is used to compute fracture indices (*FI*) and the resulting probability of reinforcing bar fractures. The fiber-based model and fatigue-facture model are validated using tests of twelve reinforced concrete subassembly tests of beams (To and Moehle, 2017), columns (Sokoli et al., 2017), and walls (Huq et al., 2017). As shown in Figure 9.2, the computed *FIs* at the end of the cycle having the first reported bar fracture have an average value of 1.15; while the average fracture index at the end of non-fracture tests is 0.70. Thus, the model is slightly conservative in predicting the failure point in these tests, especially for the MMFX steel in columns (i.e., C4). However, the results are well within the acceptable statistical bounds, considering the inherent variability in the fatigue-fracture behavior and other complexities in the member response modeling. Details of the fiber-based models and validation studies are presented in Sections 4.2, 4.3 and Chapter 5.

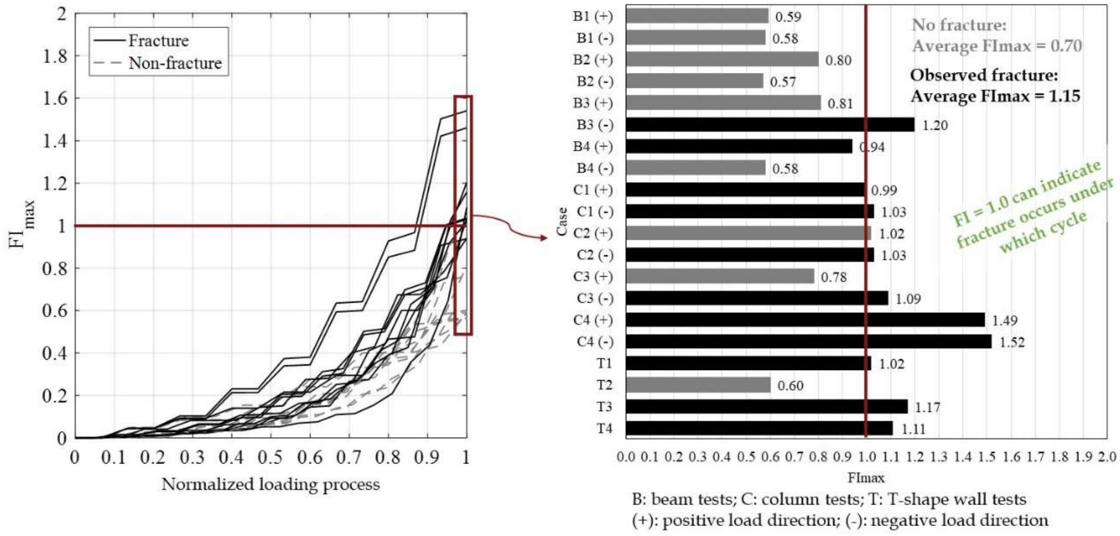

Figure 9.2. Validation of proposed fatigue-fracture model in subassembly cyclic tests.

9.1.2 Nonlinear Seismic Resisting System Analyses

As summarized in Chapter 5, the slender reinforced concrete wall systems are analyzed using fiber-based flexural models. The nonlinear concrete and steel material properties are input directly into the fiber cross section to simulate flexural response, taking care to regularize the concrete constitutive model to avoid strain localization. Shear deformations are combined with the flexural model, based on an idealized tri-linear model of wall shear force versus average shear strain. Bond-slip effects at the base of the wall are incorporated with a zero-length inelastic cross section fiber model, where the equivalent bar properties are based on a model by Zhao and Sritharan (2007). Numerical integration points along the member are defined to characterize reinforcing bar strains over an eight-inch gage length, which is consistent with the nominal strain input to the bar fracture model. Shown in Figure 9.3 (extracted from Figure 5.5) is an example of the comparison of simulated versus measured wall response for CPF wall test T2 (Huq et al., 2017).

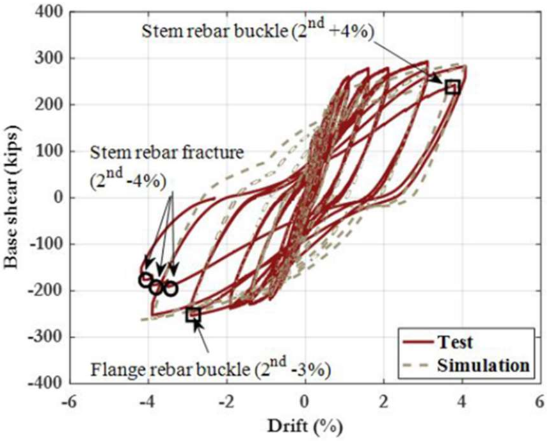

Figure 9.3. Comparison of simulated versus test data for fiber-based wall model of CPF wall specimen T4.

The reinforced concrete moment frames are simulated using beam-column elements with concentrated inelastic hinges, which are calibrated to simulate cyclic strength and stiffness degradation. As described in the overall assessment framework of Chapter 2, member deformation histories from the overall frame analyses are subsequently input to detailed fiber-based component models to calculate reinforcing bar strain histories that are input to the bar fracture models. The concentrated hinge models (as opposed to fiber-based models) are used to simulate the overall frame response for computational efficiency (for systems with many plastic hinge locations) and to pick up strength and stiffness degradation due to reinforcing bar buckling and combined shear-flexure interaction that is not captured well in the fiber-based models.

The concentrated hinges are modeled using the IMK model (Ibarra et al., 2005), which has been calibrated and used in prior seismic performance studies of reinforced concrete moment frames (Haselton et al. 2007, 2016). To reliably simulate the influence of reinforcing bar properties on the concentrated hinge models, a new approach is proposed for determining parameters of the IMK model. The 5 backbone-curve parameters of the IMK model are determined by first performing fiber-based cross-section analysis to obtain the flexure M-θ relation and aggregating shear and bar-slip relations, including reinforcing bar properties that reflect the yield strength and strain hardening response. As described in Section 4.2, the cyclic deterioration factor of the IMK model is calibrated to data from over 100 beam-column tests to best capture the observed trends in test data and regressed as a function of the reinforcing bar properties and member parameters. The resulting λ parameter is described by the parametric Equation 9.3, details of which are provided in Section 4.1. The model calibration includes data from the four beam and four column tests with high strength reinforcement conducted as part of other CPF projects (To and Moehle, 2017; Sokoli et al., 2017).

$$\lambda = (253.09)(0.17)^{\nu}(0.92)^{L/h}(1.10)^{T/Y}(1.38)^{\rho_{sh,eff}}(0.94)^{s_n} \tag{9.3}$$

Examples of the resulting calibration of the concentrated hinge model and the fiber-based model are shown in Figure 9.5 (extracted from Figures 4.10 and 4.20) for CPF beam test UBC #3 (To and Moehle, 2017).

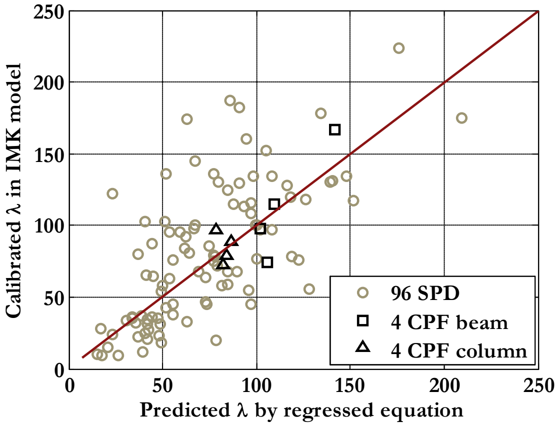

Figure 9.4. Comparison: predicted λ vs. calibrated λ.

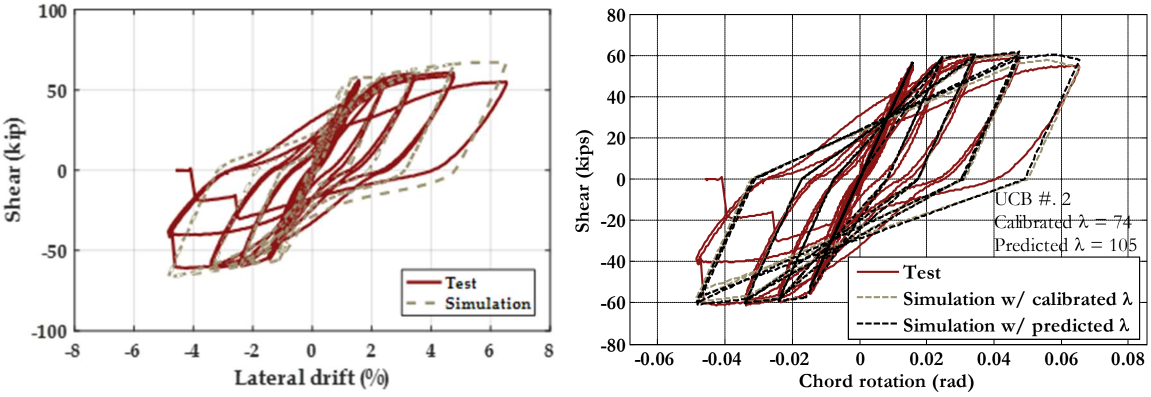

Figure 9.5. Comparison of simulated versus test data for fiber-based (left) and concentrated hinge (right) models of CPF beam specimen UCB #2.

9.1.3 Seismic Demands on Moment Frame and Shear Wall Buildings

Four archetype building designs were analyzed using the nonlinear analysis and bar fracture-fatigue model to assess the effect of reinforcing bar properties on their performance, including bar strain demands and the risk of bar fracture. The study includes 4-story and 20-story special moment frames and 8-story and 42-story shear walls with Gr. 60, 80, and 100 reinforcing bars. The analysis is conducted using an Incremental Dynamic Analysis (IDA) procedure, where a reliability-based framework is used to characterize the site-specific seismic hazard and systematically assess the risk of reinforcing bar fracture. Collapse risk is assessed using the FEMA P695 methodology, where reinforcing bar fracture is considered as a critical limit state.

Reinforcing bar properties and design parameters are considered by parametrically varying reinforcing bar yield strength (*Fy*) and tensile-to-yield strength ratio (*T/Y*) and longitudinal bar slenderness (through tie-spacing to bar diameter, s/d_b). Based on reported reinforcing bar properties, three *T/Y* ratios are considered for each steel grade (1.3, 1,4, and 1.5 for Gr. 60; 1.2, 1.3, and 1.4 for Gr. 80; 1.1, 1.2, 1.3 for Gr. 100). Three reinforcing bar tie spacings (s/d_b of 4, 5, and 6) are considered for each type of steel. In total, there are 27 different combinations of *Fy*, *T/Y* and s/d_b possible for each structural system. The full design space was evaluated for the 20-story moment frame at two building sites (based on seismic hazards in San Francisco and Seattle). Based on the observed trends and with a focus on the most critical combinations, the number of design variables was reduced to 13 combinations for the 4-story frame, 17 for the 8-story wall, and 21 for the 42-story wall.

Detailed results and observations are presented for the building systems in Chapters 7 and 8. A summary of key demand parameters for a subset of the system design variants is included in Table 9.1. Probabilities of reinforcing bar fracture under MCE_R intensity ground motions are compared in Figure 9.6, and probabilities of system collapse under MCE_R intensity ground motions, based on the FEMA P695 methodology, are compared in Figure 9.7. In Figures 9.6 and 9.7, the system variant designations follow the naming convention describe earlier based on *#stories|system|steel grade|T/Y ratio|*s/d_b *ratio*, where for example 20F06136 corresponds to a 20-story frame with Gr. 60 reinforcement with *T/Y* =1.3 and s/d_b = 6.

The following is a summary of the major observations are highlighted as follows:

> *Story Drift Demands:* As summarized in Table 9.1, the average peak story drift demands under MCE_R ground motions are approaching 0.03 (the limiting drift criteria in PEER TBI) for the moment frames and the 42-story shear wall, and the drifts are significantly less (on the order of 0.015 to 0.107) for the 8-story shear wall. In all cases the drifts tend to be larger for the designs with high strength reinforcement, which is related to their smaller steel areas and reduced transformed elastic stiffness values. Compared to the designs with Gr. 60 reinforcement, the MCE_R drift demands in the frame systems are about 10% to 20% larger with Gr. 80 and 100 steel, respectively, and the drift demands in the wall systems are around 5% and 10% larger with Gr. 80 and 100 steel, respectively. These data suggest that parity in the drift demands for designs with higher strength reinforcement could be achieved by basing the design drift calculations based on transformed section properties, as opposed to the traditional approach of using gross section properties.
>
> *Cumulative Plastic Strain Demands:* Cumulative plastic strain demands (*CPD*) are obtained by summing the nominal reinforcing plastic strain demands, assuming a nominal 8-inch gage length in the yielding regions. As summarized in Table 9.1, the *CPD* demands are fairly constant within each system type and not affected much by the steel grade, *T/Y* ratio or s/d_b ratio. The average cumulative plastic strain demands (*CPD*) in the most critical locations under MCE_R ground motions are about 0.12 to 0.14 in the 20-story frame and 42-story wall building. The average *CPDs* are somewhat larger, about 0.018, in the 4-story frame, and considerably larger, about 0.30, in the 8-story wall. As a point of reference, the *CPDs* corresponding fracture in the bare bar tests, based on similar nominal strains measurements (Ghannoum and Slavin, 2016), range from 0.60 to 1.82. It is important to recognize, however, that the *CPD* is a very approximate index of bar fracture since it does not differentiate between the strain amplitude and loading sequence, which significantly affect

fracture. This is in contrast to the fracture index, *FI*, and associated fracture fragility curve that account for strain amplitude, loading sequence, and other effects.

Reinforcing Bar Fracture Probability: As illustrated in Figure 9.6, the probability of reinforcing bar fracture under MCE_R ground motions tends to generally increase for higher strength reinforcement, but the increases are more systematically correlated with decreasing tensile strength to yield ratio (*T/Y*) and increasing tie spacing (s/d_b). As indicated by the subset of cases reported in Table 9.1, parity between the fracture probabilities for high strength bars with the benchmark case with conventional grade steel (Gr. 60 with *T/Y* of 1.3 and s/d_b of 6) can be achieved by limiting minimum allowable *T/Y* to 1.2 and the maximum tie spacing to $5d_b$. By doing so, the probability of column bar fracture for all three grades of steel (Gr. 60, 80 and 100) under MCE_R ground motions is between 3% and 4% for the moment frames, about 2% in the 42-story shear walls, and less than 15% in the 8-story shear walls. The 8-story shear wall is particularly interesting for two reasons. First, the fracture probabilities (and *CPDs*) are generally much higher than in the other cases, in spite of the lower drift demands in the 8-story wall. This is primarily due to the relatively squat aspect ratio of the 8-story wall (height/width = 3.5) that leads to large curvature and bar strain demands. Second, with the limits on *T/Y* and s/d_b, the bar fracture probabilities are in fact smaller for the high strength bars (11% for Gr. 80 and 8% for Gr. 100) than the conventional bars (15% for Gr. 60). This is probably due to the larger yield strains in the high strength bars, relative to the earthquake drift/strain demands. As shown by Figure 8.20, at larger drift demands the fracture probabilities in the 8-story wall would tend to converge for the three grades of steel.

P695 Collapse Risk: As illustrated in Figure 9.7 and Table 9.1, similar to the trends observed for bar fracture in Figure 9.6, the collapse risk under MCE_R ground motions generally tends to increase for higher strength reinforcement, but the increases are more systematically correlated with decreasing tensile strength to yield ratio (*T/Y*) and increasing tie spacing (s/d_b). In the frame systems, reinforcing bar fracture contributes relatively little to the collapse risk, and in the 42-story wall the probabilities of collapse are practically negligible. In contrast, the bar fracture limit state is a major contributor to the risk of collapse in the 8-story wall. Similar to the point made with regard to bar fracture, parity with the benchmark case with conventional grade steel (Gr. 60 with *T/Y* of 1.3 and s/d_b of 6) is generally achieved by limiting *T/Y* to 1.2 and the maximum tie spacing to $5d_b$. Assuming these limits, the probabilities of collapse under MCE_R motions for the frames and 42-story wall systems all are well within the 10% MCE_R collapse risk limit specified in ASCE 7, and the 8-story wall structure (with 11% probability for Gr. 80 and 100) comes very close to satisfying the limit. The 8-story cases would come in below 10% with a tighter $4d_b$ tie bar spacing. Without the limits of *T/Y* and s/d_b, the collapse risks for the higher grade steels would increase to unacceptable levels.

Table 9.1 Summary of seismic demands and performance metrics of archetype structural systems.

	Moment Frame		Shear Wall	
Reinforcing Bar	4-story	20-story	8-story	42-story
Grade	Period (s) | Story Drift Ratio at MCE_R			
60	1.3s | 2.7%	2.7s | 2.4%	1.2s | 1.5%	4.2s | 2.7%
80	1.4s | 2.8%	3.0s | 2.7%	1.2s | 1.6%	4.4s | 2.9%
100	1.5s | 2.9%	3.2s | 2.9%	1.2s | 1.7%	4.6s | 2.9%
Grade – *T/Y* – s/d_b	*CPD* at MCE_R | P(Fracture) at MCE_R			
60 - 1.3 - 6	0.19 | 3.8%	0.13 | 2.9%	0.31 | 15.3%	0.13 | 2.2%
80 - 1.2 - 5	0.18 | 3.5%	0.12 | 2.7%	0.29 | 11.3%	0.13 | 1.6%
80 - 1.2 - 6	0.18 | 4.0%	0.13 | 3.3%	0.30 | 16.5%	0.14 | 2.3%
100 - 1.2 - 5	0.18 | 3.4%	0.11 | 2.8%	0.30 | 8.1%	0.14 | 1.9%
100 - 1.1 - 6	0.22 | 5.1%	0.14 | 4.2%	0.33 | 27.2%	0.15 | 2.8%
	P(Collapse, w/o fracture) | P(Collapse, total) at MCE_R			
60 - 1.3 - 6	4% | 5%	7% | 8%	<1% | 6%	<1% | <1%
80 - 1.2 - 5	5% | 7%	8% | 9%	<1% | 11%	<1% | <1%
80 - 1.2 - 6	6% | 8%	8% | 9%	<1% | 12%	<1% | <1%
100 - 1.2 - 5	7% | 8%	8% | 9%	<1% | 11%	<1% | <1%
100 - 1.1 - 6	8% | 11%	9% | 11%	1% | 31%	<1% | 2%

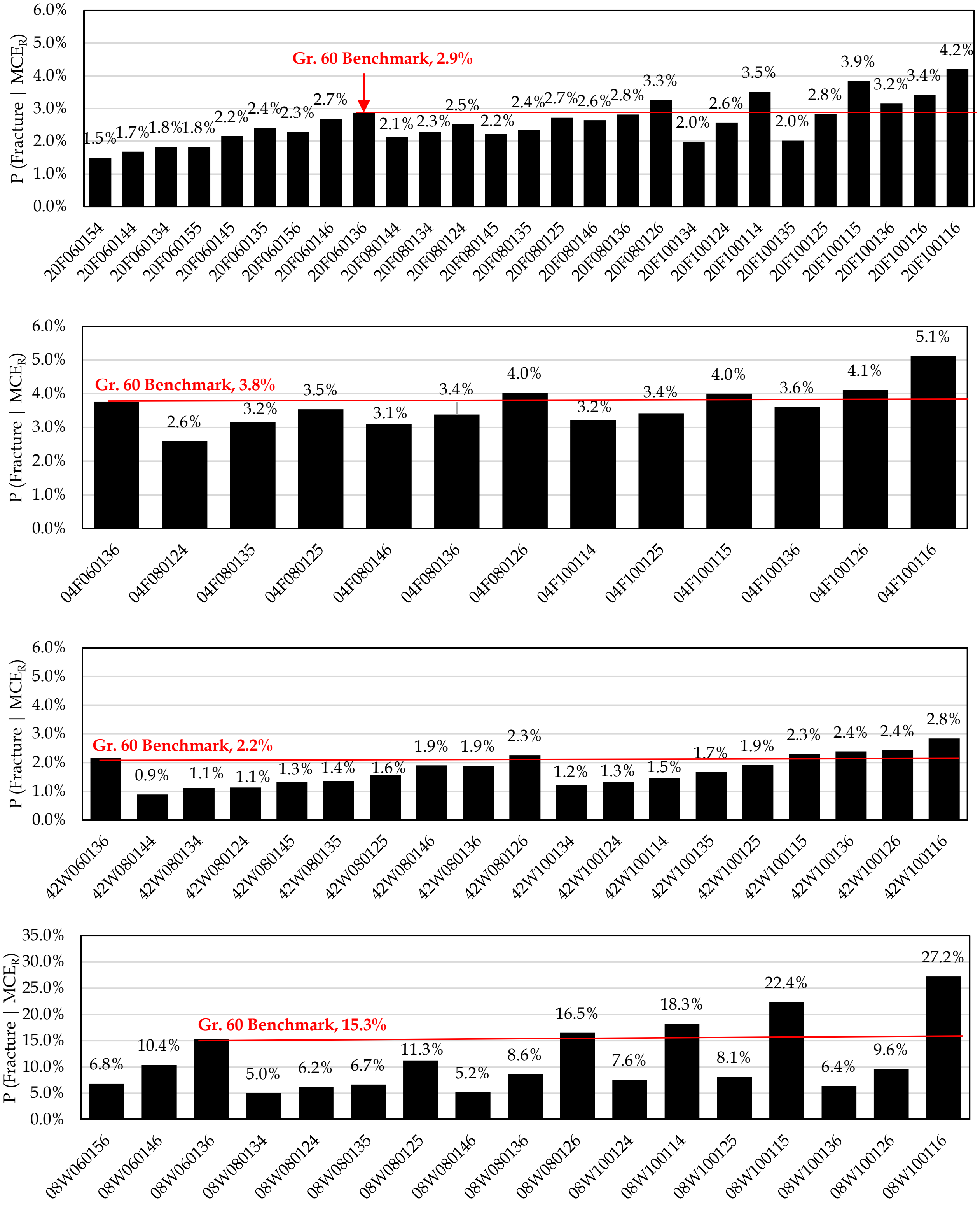

Figure 9.6. Fracture probabilities of most highly strained reinforcing bars under *MCE*$_R$ intensity ground motions

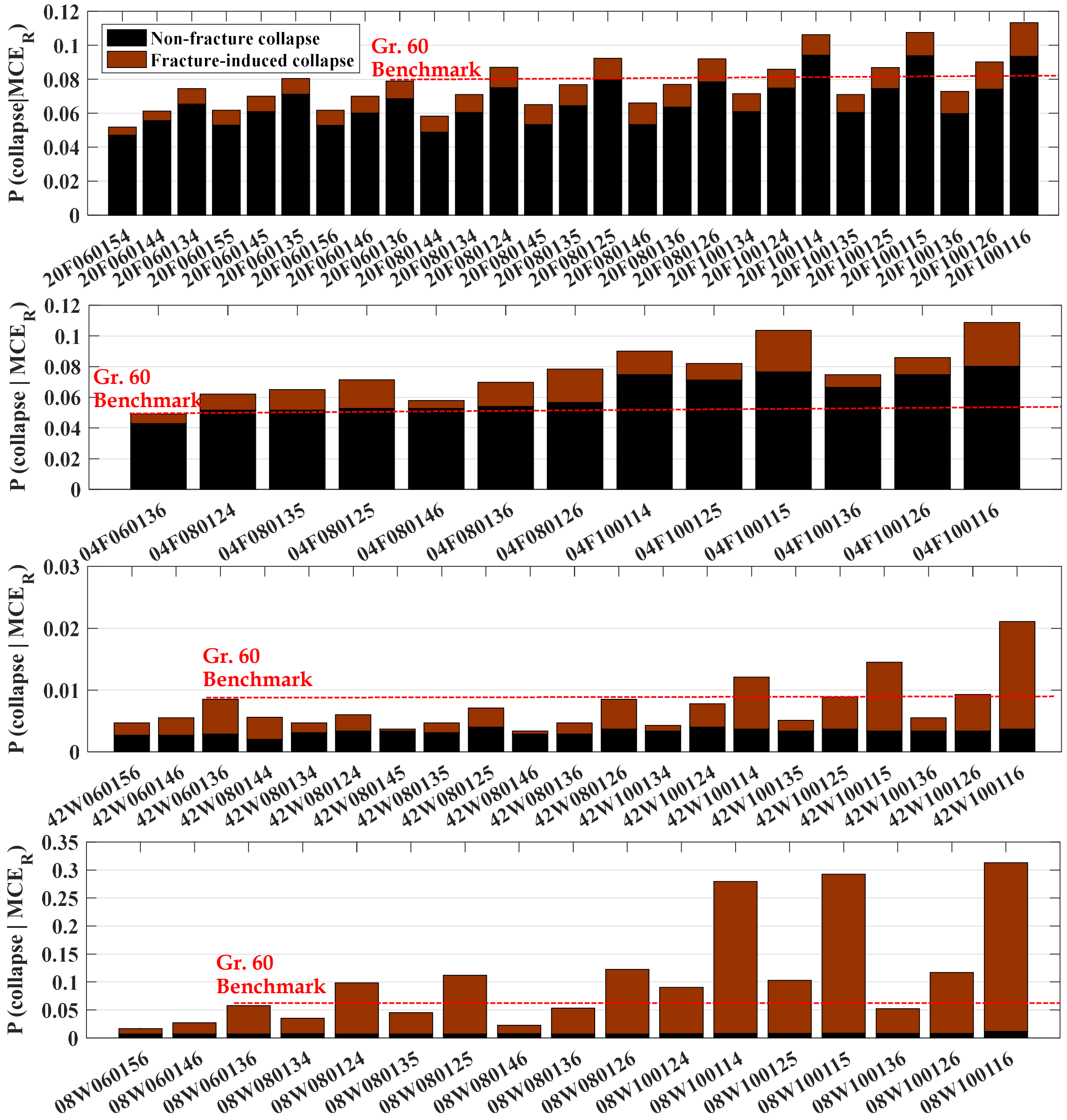

Figure 9.7. Collapse probabilities conditioned on MCE_R intensities from FEMA P695 analyses.

9.2 Implications for Use of High Strength Reinforcement for Seismic Design

The proposed fracture-fatigue model and nonlinear analyses of structural components and systems presented in this report: (1) generally confirm the basic understanding on the effects of reinforcing bar properties on the inelastic response of concrete structures, and (2) provide data to quantify these effects as related to the use of high strength reinforcement for seismic design. Based on these results, the following are major conclusions (or recommendations) to help ensure the satisfactory seismic performance of structures with high strength (Gr. 80 and 100) reinforcement:

1) It is recommended to have a minimum allowable median *T/Y* of 1.2 for Gr. 80 and 100 that ensures the sufficient strain hardening. Note that from a statistical standpoint, the proposed median *T/Y* value of 1.2 is considered to be satisfied with a minimum specified *T/Y* value of 1.17 (=1/0.85).
2) It is recommended to limit the tie spacing around Gr. 80 and 100 longitudinal bars in seismic resistant systems to a maximum distance of $5d_b$, where d_b is the longitudinal bar size.
3) In some cases, such as flexural walls or members with low aspect ratios (e.g., shear-span height/depth ratios less than 4), it could be argued to impose a tighter spacing limit of $4d_b$, or alternatively to require more stringent story drift limits than current building codes.
4) It is recommended to require the use of transformed section properties in estimating the seismic story drift demands. This is intended to help ensure parity in minimum stiffness criteria (maximum seismic drift demands) between buildings designed with different steel grades (Gr. 60, 80 and 100).
5) To the extent that satisfactory seismic performance is predicated on having reinforcing bars from a population that is represented by the fatigue-fracture model (Eq. 9.1 and Figure 9.1), this model can be used as the basis for developing acceptance criteria for qualification tests to establish the fatigue-fracture resistance of reinforcing bars.

9.3 Limitations

The following is a summary of several limitations on this study, which if addressed would improve the reliability of the system performance evaluation:

1. The current fatigue-fracture model is calibrated based on monotonic tensile tests and cyclic tests with strain ranges of 4% and 5%. To the extent that the peak steel strain demand in earthquakes can exceed 5%, the model resolution can be improved if provided more cyclic test data with strain ranges greater than 5% (i.e., to better constrain the fatigue model as shown in Figures 3.5 to 3.7)
2. Due to the limitations of existing nonlinear analysis software, the current FEMA P695 collapse analyses treat reinforcing bar fracture as a non-simulated collapse mode. To the extent that this may provide an overly conservative measure of fracture-induced collapse risk, the FEMA P695 evaluation of system archetype designs would be improved by using a nonlinear analysis model that explicitly simulates reinforcing bar fracture and its effect on overall systems response.
3. The uncertainty in the fracture-fatigue resistance of the reinforcing bars (as reflected by the dispersion of 0.5 in the fracture index) is large relative to the variability in other steel material parameters. compared to other structural steel. This large dispersion reflects (1) the inherent variability in the fracture-fatigue resistance of the bars, and (2) the variability introduced by bar parameters that are not explicitly represented in the fracture-fatigue model (such as bar deformation patterns, bar chemistry and processing that is not otherwise captured by f_y or *T/Y*, etc.). The reliability of reinforced concrete structures would be improved by bar manufacturing practices that reduce this variability by better controls on bar properties that affect their fracture-fatigue response. In addition, larger data sets on bar fracture-fatigue resistance could permit explicit tracking and consideration of bar parameters that are not in the current fracture-fatigue model.

REFERENCE

Abdalla J A, Hawileh R A, Oudah F, et al. (2009). Energy-based prediction of low-cycle fatigue life of BS 460B and BS B500B steel bars[J]. Materials & Design, 30(10): 4405-4413.4

Abrahamson N, Gregor N, Addo K. (2016). BC Hydro ground motion prediction equations for subduction earthquakes[J]. Earthquake Spectra, 32(1): 23-44.

Abrahamson N A, Silva W J. (1996). Empirical ground motion models[J]. Report to Brookhaven National Laboratory.

Al Atik L. (2011). Correlation of spectral acceleration values for subduction and crustal models[J]. COSMOS Technical Session.

American Concrete Institute. (2014). Building Code Requirements for Structural Concrete: ACI 318-14[M].

American Society of Civil Engineers. (2017). Minimum design loads and associated criteria for buildings and other structures: ASCE/SEI 7-16[M].

American Society of Civil Engineers. (2017). Seismic Evaluation and Retrofit of Existing Buildings: ASCE 41-17[M].

Aoyama H. (2001). Design of modern highrise reinforced concrete structures[M]. World Scientific.

Applied Technology Council. (2014). Roadmap for the Use of High-Strength Reinforcement in Reinforced Concrete Design[M]. US Department of Homeland Security, FEMA.

Applied Technology Council. (2017). Development of Accurate Models and Efficient Simulation Capabilities for Collapse Analysis to Support Implementation of Performance Based Seismic Engineering[M]. US Department of Homeland Security, FEMA.

Applied Technology Council. (2018). Improving Seismic Design of Buildings with Configuration Irregularities[M]. US Department of Homeland Security, FEMA.

Applied Technology Council. (2009). Quantification of building seismic performance factors[M]. US Department of Homeland Security, FEMA.

Applied Technology Council. (2017). Seismic Analysis, Design, and Installation of Nonstructural Components and Systems – Background and Recommendations for Future Work: NIST GCR 17-917-44[M]. US Department of Homeland Security, FEMA.

Baker J W, Cornell C A. (2008). Uncertainty propagation in probabilistic seismic loss estimation[J]. Structural Safety, 30(3): 236-252.

Baker J W, Jayaram N. (2008). Correlation of spectral acceleration values from NGA ground motion models[J]. Earthquake Spectra, 24(1): 299-317.

Baker J W. (2010). Conditional mean spectrum: Tool for ground-motion selection[J]. Journal of Structural Engineering, 137(3): 322-331.

Barbosa A R, Link T, Trejo D. (2015). Seismic performance of high-strength steel RC bridge columns[J]. Journal of Bridge Engineering, 21(2): 04015044.

Benzerga A A, Besson J, Pineau A. (2004). Anisotropic ductile fracture: Part I: experiments[J]. Acta Materialia, 52(15): 4623-4638.

Birely A C. (2012). Seismic performance of slender reinforced concrete structural walls[D]. University of Washington.

Bradley B A. (2010). A generalized conditional intensity measure approach and holistic ground-motion selection[J]. Earthquake Engineering & Structural Dynamics, 39(12): 1321-1342.

Bradley B A. (2011). Correlation of significant duration with amplitude and cumulative intensity measures and its use in ground motion selection[J]. Journal of Earthquake Engineering, 15(6): 809-832.

Brown J, Kunnath S K. (2000). Low-cycle fatigue behavior of longitudinal reinforcement in reinforced concrete bridge columns[J].

Brown J, Kunnath S K. (2004). Low-cycle fatigue failure of reinforcing steel bars[J]. Materials Journal, 101(6): 457-466.

Campbell K W, Bozorgnia Y. (2014). NGA-West2 ground motion model for the average horizontal components of PGA, PGV, and 5% damped linear acceleration response spectra[J]. Earthquake Spectra, 30(3): 1087-1115.

Chandramohan R, Baker J W, Deierlein G G. (2016). Quantifying the influence of ground motion duration on structural collapse capacity using spectrally equivalent records[J]. Earthquake Spectra, 32(2): 927-950.

Chandramohan R, Baker J W, Deierlein G G. (2016). Impact of hazard-consistent ground motion duration in structural collapse risk assessment[J]. Earthquake Engineering & Structural Dynamics, 45(8): 1357-1379.

Chang G A, Mander J B. (1994). Seismic energy based fatigue damage analysis of bridge columns: Part 1: Evaluation of seismic capacity[M]//Technical Report. US National Center for Earthquake Engineering Research.

Coffin Jr L F. (1954). A study of the effects of cyclic thermal stresses on a ductile metal[J]. Transactions of the American Society of Mechanical Engineers, New York, 76: 931-950.

Coleman J, Spacone E. (2001). Localization issues in force-based frame elements[J]. Journal of Structural Engineering, 127(11): 1257-1265.

Dhakal R P, Maekawa K. (2002). Modeling for postyield buckling of reinforcement[J]. Journal of structural engineering, 128(9): 1139-1147.

Downing S D, Socie D F. (1982). Simple rainflow counting algorithms[J]. International journal of fatigue, 4(1): 31-40.

Eads L, Miranda E, Lignos D G. (2015). Average spectral acceleration as an intensity measure for collapse risk assessment[J]. Earthquake Engineering & Structural Dynamics, 44(12): 2057-2073.

Eligehausen R, Popov E P, Bertero V V. (1982). Local bond stress-slip relationships of deformed bars under generalized excitations[J]. Proceedings of the 7th European Conference on Earthquake Engineering. Vol. 4. Athens : Techn. Chamber of Greece, 1982, S. 69-80

Elwood K J, Eberhard M O. (2009). Effective Stiffness of Reinforced Concrete Columns[J]. ACI Structural Journal, 106(4).

Fash J, Socie D F. (1982). Fatigue behaviour and mean effects in grey cast iron[J]. International Journal of Fatigue, 4(3): 137-142.

Fell B V, Kanvinde A M, Deierlein G G, et al. (2009). Experimental investigation of inelastic cyclic buckling and fracture of steel braces[J]. Journal of structural engineering, 135(1): 19-32.

Filippou F. (2010). "Concrete 02 Material – Linear Tension Softening". http://OpenSees.berkeley.edu/wiki/index.php/Concrete02_Material_--_Linear_Tension_Softening. OpenSeesWiki.

Ghee A B, Priestley M J N, Paulay T. (1989). Seismic shear strength of circular reinforced concrete columns[J]. Structural Journal, 86(1): 45-59.

Gill, W. D., Park, R., and Priestley, M.J.N. (1979). Ductility of Rectangular Reinforced Concrete Columns with Axial Load[R]. Report 79-1, Department of Civil Engineering, University of Canterbury, Christchurch, New Zealand.

Hancock J W, Mackenzie A C. (1976). On the mechanisms of ductile failure in high-strength steels subjected to multi-axial stress-states[J]. Journal of the Mechanics and Physics of Solids, 24(2-3): 147-160.

Haselton C B, Liel A B, Dean B S, et al. (2007). Seismic collapse safety and behavior of modern reinforced concrete moment frame buildings[M]//Structural engineering research frontiers. 2007: 1-14.

Haselton C B. (2008). Beam-column element model calibrated for predicting flexural response leading to global collapse of RC frame buildings[R]. Pacific Earthquake Engineering Research Center.

Haselton C B, Liel A B, Taylor-Lange S C, Deierlein G G. (2016). Calibration of Model to Simulate Response of Reinforced Concrete Beam-Columns to Collapse[J], ACI Structural Journal. Nov/Dec2016, Vol. 113 Issue 6, p1141-1152.

Hassan M, El-Tawil S. (2003). Tension flange effective width in reinforced concrete shear walls[J]. Structural Journal, 100(3): 349-356.

Hawileh R A, Abdalla J A, Oudah F, et al. (2010). Low-cycle fatigue life behaviour of BS 460B and BS B500B steel reinforcing bars[J]. Fatigue & Fracture of Engineering Materials & Structures, 33(7): 397-407.

Huq M S, Weber-Kamin A S, Ameen S, Lequesne R D, Lepage A. (2017). High-Strength Steel Bars in Reinforced Concrete Walls: Influence of Steel Mechanical Properties on Deformation Capacity[R]. Charles Pankow Foundation.

Ibarra L F, Medina R A, Krawinkler H. (2005). Hysteretic models that incorporate strength and stiffness deterioration[J]. Earthquake engineering & structural dynamics, 34(12): 1489-1511.

Jayaram N, Lin T, Baker J W. (2011). A computationally efficient ground-motion selection algorithm for matching a target response spectrum mean and variance[J]. Earthquake Spectra. 27(3): 797-815.

Johnson G R, Cook W H. (1985). Fracture characteristics of three metals subjected to various strains, strain rates, temperatures and pressures[J]. Engineering fracture mechanics, 21(1): 31-48.

Kanvinde A M, Deierlein G G. (2007). Cyclic void growth model to assess ductile fracture initiation in structural steels due to ultra low cycle fatigue[J]. Journal of engineering mechanics, 133(6): 701-712.

Kanvinde A M, Deierlein G G. (2008). Validation of cyclic void growth model for fracture initiation in blunt notch and dogbone steel specimens[J]. Journal of structural engineering, 134(9): 1528-1537.

Kelly D, Lepage A, Mar D, et al. (2014). Use of High-Strength Reinforcement for Earthquake-Resistant Concrete Structures[C]//Tenth US National Conference on Earthquake Engineering, Anchorage, AK.

Kent D C, Park R. (1971). Flexural members with confined concrete[J]. Journal of the Structural Division.

Khosrovaneh A K, Dowling N E. (1990). Fatigue loading history reconstruction based on the rainflow technique[J]. international journal of fatigue, 12(2): 99-106.

Koh S K, Stephens R I. (1991). Mean stress effects on low cycle fatigue for a high strength steel[J]. Fatigue & Fracture of Engineering Materials & Structures, 14(4): 413-428.

Langer B F. (1937). Fatigue failure from stress cycles of varying amplitude[J]. Journal of Applied Mechanics, 59: A160-A162.

Legeron F, Paultre P. (2000). Behavior of high-strength concrete columns under cyclic flexure and constant axial load[J]. Structural Journal, 97(4): 591-601.

Lehman D E, Moehle J P. (2000). Seismic performance of well confined concrete bridge columns[R]. PEER Report 1998/01[J]. University of California, Berkeley.

Liel A B, Haselton C B, Deierlein G G, et al. (2009). Incorporating modeling uncertainties in the assessment of seismic collapse risk of buildings[J]. Structural Safety, 31(2): 197-211.

Limantono A A. (2016). Modeling Strain Demands in Longitudinal Steel Bars of Concrete Columns[D]. University of Texas Austin.

Lin T, Baker J W. (2013). Introducing adaptive incremental dynamic analysis: a new tool for linking ground motion selection and structural response assessment[J].

Lorenzo F, Laird C. (1984). A new approach to predicting fatigue life behavior under the action of mean stresses[J]. Materials Science and Engineering, 62(2): 205-210.

Lutes L D, Corazao M, Hu S J, Zimmerman J. (1984). Stochastic fatigue damage accumulation[J]. Journal of Structural Engineering, 110(11): 2585-2601.

Mander J B, Priestley M J N, Park R. (1988). Theoretical stress-strain model for confined concrete[J]. Journal of structural engineering, 114(8): 1804-1826.

Mander J B, Panthaki F D, Kasalanati A. (1994). Low-cycle fatigue behavior of reinforcing steel[J]. Journal of Materials in Civil Engineering, 6(4): 453-468.

Manson S S. (1954). Behavior of materials under conditions of thermal stress[J].

Marini B, Mudry F, Pineau A. (1985). Ductile rupture of A508 steel under nonradial loading[J]. Engineering Fracture Mechanics, 22(3): 375-386.

Mazzoni S, McKenna F, Scott M H, et al. (2006). OpenSees command language manual[J]. Pacific Earthquake Engineering Research (PEER) Center, 264.

Miner M A. (1945). Cumulative Damage in Fatigue Journal of Applied Mechanics 12 (1945) No. 3, pp[J]. A159-A164.

Mitra N, Lowes L N. (2007). Evaluation, calibration, and verification of a reinforced concrete beam–column joint model[J]. Journal of Structural Engineering, 133(1): 105-120.

Mo Y L, Wang S J. (2000). Seismic behavior of RC columns with various tie configurations[J]. Journal of Structural Engineering, 126(10): 1122-1130.

Mohle J, Kunnath S. (2010). "Reinforcing Steel Material.", http://OpenSees.berkeley.edu/wiki/index.php/Reinforcing_Steel_Material. OpenSeesWiki.

Moore H F, Kommers J B. (1927). The fatigue of metals[M]. New York: McGraw-Hill.

Morrow J, Johnson T A. (1965). Correlation between cyclic strain range and low-cycle fatigue life of metals[J]. Materials Research and Standards, 5(1): 30-&.

National Institute of Standards and Technology. (2014). Use of High-Strength Reinforcement in Earthquake-Resistant Concrete Structures[M].

Nihei M, Heuler P, Boller C, et al. (1986). Evaluation of mean stress effect on fatigue life by use of damage parameters[J]. International journal of fatigue, 8(3): 119-126.

Pacific Earthquake Engineering Research Center. (2004). PEER Structural Performance Database, http://nisee.berkeley.edu/spd/.

Pacific Earthquake Engineering Research Center. (2017). Guidelines for Performance-Based Seismic Design of Tall Buildings (version 2.03) [R]. Pacific Earthquake Engineering Research Center, College of Engineering, University of California: Berkeley.

Palmgren A. (1924). Durability of ball bearings[J]. ZVDI, 68(14): 339-341.

Panagiotakos T B, Fardis M N. (2001). Deformations of reinforced concrete members at yielding and ultimate[J]. Structural Journal, 98(2): 135-148.

Paulay T, Priestley M J N. (1992). Seismic design of reinforced concrete and masonry buildings[M].

Pericoli V, Kanvinde A. (2018). Theoretical Study of Ductile Fracture in Steel Structures in the Presence of Spatial Variability in Toughness[J]. Journal of Structural Engineering, 144(5): 04018024.

Pugh J S. (2012). Numerical simulation of walls and seismic design recommendations for walled buildings[D].

Pugh J S, Lowes L N, Lehman D E. (2015). Nonlinear line-element modeling of flexural reinforced concrete walls[J]. Engineering Structures, 104: 174-192.

Rahnama M, Krawinkler H. (1993). Effects of soft soil and hysteresis model on seismic demands[R]. John A. Blume Earthquake Engineering Center Report No. 108. Department of CEE, Stanford University.

Ray A. (1999). Stochastic modeling of fatigue crack damage for risk analysis and remaining life prediction[J]. Journal of dynamic systems, measurement, and control, 121(3): 386-393.

Rice J R, Tracey D M. (1969). On the ductile enlargement of voids in triaxial stress fields[J]. Journal of the Mechanics and Physics of Solids, 17(3): 201-217.

Rychlik I. (1987). A new definition of the rainflow cycle counting method[J]. International journal of fatigue, 9(2): 119-121.

Rychlik I. (1988). Rain-Flow-Cycle distribution for ergodic load processes[J]. SIAM Journal on Applied Mathematics, 48(3): 662-679.

Shimokawa T, Tanaka S. (1980). A statistical consideration of Miner's rule[J]. International Journal of Fatigue, 2(4): 165-170.

Saatcioglu M, Alsiwat J M, Ozcebe G. (1992). Hysteretic behavior of anchorage slip in R/C members[J]. Journal of Structural Engineering, 118(9): 2439-2458.

Sezen H, Setzler E J. (2008). Reinforcement slip in reinforced concrete columns[J]. ACI Structural Journal, 105(3): 280.

Slavin C M, Ghannoum W M. (2015). Defining Structurally Acceptable Properties of High-Strength Steel Bars through Material and Column Testing – PART I: MATERIAL TESTING REPORT[R]. Charles Pankow Foundation.

Smith R W, Hirschberg M H, Manson S S. (1963). Fatigue behavior of materials under strain cycling in low and intermediate life range[R]. NATIONAL AERONAUTICS AND SPACE ADMINISTRATION CLEVELAND OH LEWIS RESEARCH CENTER.

Smith K N, Watson P, Topper T H. (1970). A Stress-Strain Function for the Fatigue of Metals[J]. Journal of Materials, 5(4): 767-778.

Soesianawati M T. (1986). Limited ductility design of reinforced concrete columns[J].

Sokoli D. (2014). Seismic performance of concrete columns reinforced with high strength steel[D]. University of Texas Austin.

Sokoli D, Limantono A, Ghannoum W M. (2017). Defining Structurally Acceptable Properties of High-Strength Steel Bars through Material and Column Testing – PART II: COLUMN TESTING REPORT[R]. Charles Pankow Foundation.

Tavernelli J F, Coffin L F. (1962). Experimental support for generalized equation predicting low cycle fatigue[J]. Journal of Basic Engineering, 84(4): 533-537.

To D V, Moehle J P. (2017). Seismic Performance Characterization of Beams with High-Strength Reinforcement[R]. Charles Pankow Foundation.

Topper T H, Sandor B I. (1970). Effects of mean stress and prestrain on fatigue-damage summation[M]//Effects of Environment and Complex Load History on Fatigue Life. ASTM International.

Trejo D, Barbosa A R, Link T. (2014). Seismic performance of circular reinforced concrete bridge columns constructed with grade 80 reinforcement[R].

Vamvatsikos D, Cornell C A. (2002). Incremental dynamic analysis[J]. Earthquake Engineering & Structural Dynamics, 31(3): 491-514.

Waugh J D. (2009). Nonlinear analysis of T-shaped concrete walls subjected to multi-directional displacements[D]. Iowa State University.

Wægter J. (2009) Stress range histories and rain flow counting[R]. Lecture note 5.1 for Advanced structural engineering of Aalborg University Denmark.

Weiss V. (1964). Analysis of crack propagation in strain-cycling fatigue[J]. Fatigue—An Interdisciplinary Approach: 179.

Wirsching P H, Light M C. (1980). Fatigue under wide band random stresses[J]. Journal of the Structural Division, 106(7): 1593-1607.

Yassin M H M. (1994). Nonlinear analysis of prestressed concrete structures under monotonic and cyclic loads[D]. University of California, Berkeley.

Zhao S D, Ghannoum W M. (2016). Setting Bar-Bending Requirements for High-Strength Steel Bars[R]. Charles Pankow Foundation.

Zhao J, Sritharan S. (2007). Modeling of strain penetration effects in fiber-based analysis of reinforced concrete structures[J]. ACI structural journal, 104(2): 133.